STUDIA UNIVERSITATIS
BABEŞ-BOLYAI

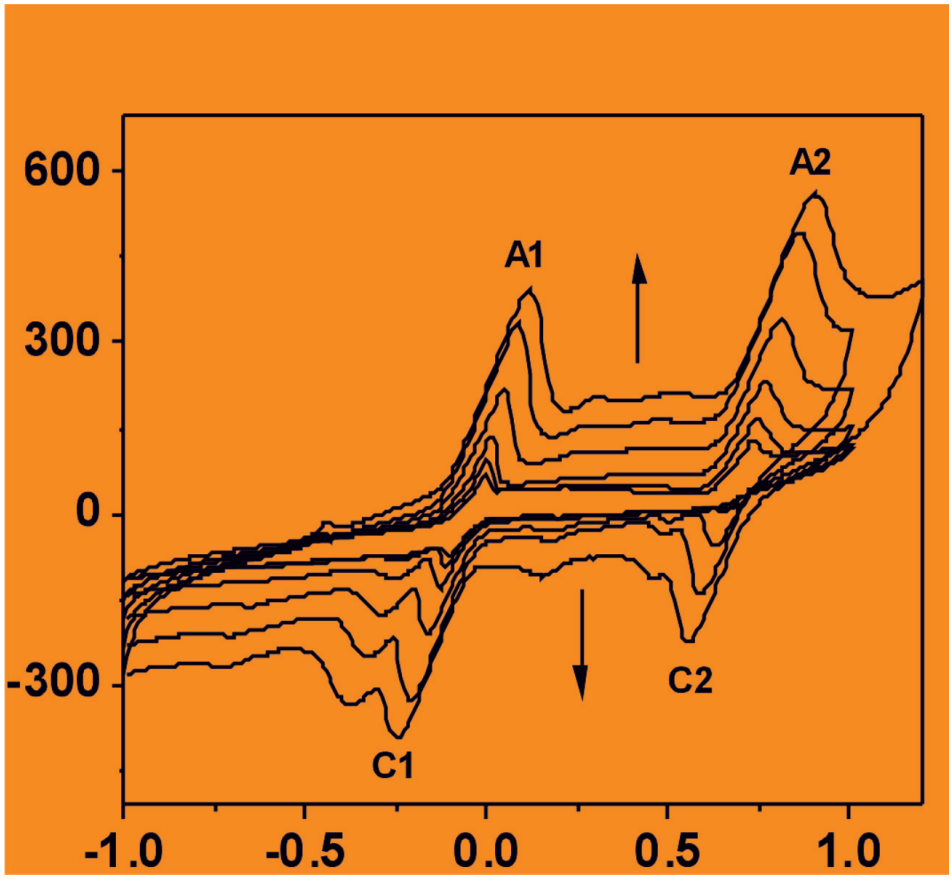

CHEMIA

3/2012

YEAR **(LVII) 2012**
MONTH **SEPTEMBER**
ISSUE **3**

S T U D I A
UNIVERSITATIS BABEŞ–BOLYAI
CHEMIA
3

Desktop Editing Office: 51ST B.P. Hasdeu, Cluj-Napoca, Romania, Phone + 40 264-40.53.52

CUPRINS – CONTENT – SOMMAIRE – INHALT

Studia Universitatis Babes-Bolyai Chemia has been selected for coverage in Thomson Reuters products and custom information services. Beginning with V. 53 (1) 2008, this publication is indexed and abstracted in the following:

- Science Citation Index Expanded (also known as SciSearch®)
- Chemistry Citation Index®
- Journal Citation Reports/Science Edition

STUDIA UBB CHEMIA, LVII, 3, 2012 (p. 5 – 13)
(RECOMMENDED CITATION)

POROSITY CHANGE BY RESIN IMPREGNATION IN STRUCTURES OBTAINED BY SELECTIVE LASER SINTERING TECHNOLOGY

RĂZVAN PĂCURAR[1], ANCUŢA PĂCURAR[1], PETRE BERCE[1], NICOLAE BÂLC[1], OVIDIU NEMEŞ[2,*]

ABSTRACT. The manufacturing of the injection moulding tools is one of the most important industrial applications of Selective Laser Sintering (SLS) technology. The resulted porosity after post-processing stage in the oven (bronze infiltration) has an important influence over the mechanical properties of the resulted SLS metallic matrix. In order to reduce the porosity, a new post-processing method has been developed as compared to the classical one, consisting in a supplementary resin impregnation after the bronze infiltrating process. This new stage will have a significant influence not only onto the resulted porosity within the material structure, but also onto the chemical composition of the material. In consequence, the mechanical behaviour of the final parts will be significantly influenced.

Keywords: *selective laser sintering, post-processing, porosity, epoxy resin.*

INTRODUCTION

Within the Selective Laser Sintering (SLS) process, there are a number of input parameters that can be controlled and modified in order to get different characteristics of the sintered parts [1]. Some of this input factors pertain to the laser beam (e.g. laser power, laser scan spacing, etc.), while others refers to the metallic powder properties (e.g. particle size, percentage composition of the constituent materials, etc.) or to the sintering parameters (e.g. layer thickness, scanning speed, etc.) (Figure 1) Output parameters of interest might be hardness, density, strength, porosity, etc. [2].

A considerable amount of work has been done and reported in this field, some of them mentioned bellow. Miler et al have carried out factorial

[1] *Universitatea Tehnică din Cluj-Napoca, Facultatea de Construcţii de Maşini, B-dul Muncii, Nr. 103-105, RO-400641 Cluj-Napoca, România*
[2] *Universitatea Tehnică din Cluj-Napoca, Facultatea de Ingineria Materialelor şi a Mediului, B-dul Muncii, Nr. 103-105, RO-400641 Cluj-Napoca, România, * ovidiu.nemes@sim.utcluj.ro*

experiments to express the strength of a sintered sample as a function of laser power, scanning speed and fill scan spacing and their respective interaction terms. The model developed takes into account the variation of small and large beam spot sizes and effect of heat loss on strength of sintered samples [3].

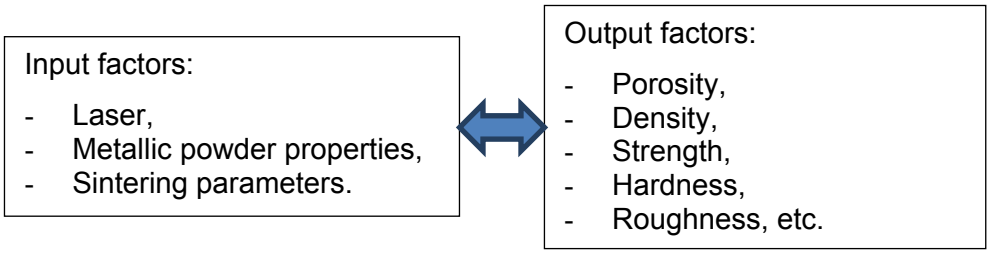

Figure 1. Input and output factors in selective laser sintering

The Song paper states the influence of laser parameters like laser beam power and experimental parameters like scanning speed on various properties of a laser sintered bronze product. It is reported that density increases while material porosity decreases with scanning speed decrease [4].

Hardro et al determined the optimal process parameters for SLS of an elastomeric polymer using an experimental design approach. Laser power, laser scan spacing and part bed temperature were the factors under consideration, while dimensional accuracy and material strength of the sintered samples were the response characteristics. It was concluded that all the factors as well as their interactions are statistically significant [5].

There are also other researches done by the authors with the aim of controlling better the selective laser sintering process in order to obtain a fully dense metal part at the end [6 – 10].

But, in order to turn the SLS process into a production technique for real components, some conditions still have to be fulfilled. Firstly, the process must guarantee consistency on the entire product life cycle [11]. Secondly, process accuracy, surface roughness and the possibility to fabricate geometrical features like overhanging surfaces and internal structures become very important for manufacturing [12]. Finally, the breakthrough of SLS process will depend on reliability, performance and economical aspects like production time and cost [13 – 15].

The current paper was not focused on the process control possibilities, but mainly on the metallic material porosity decreasing after the selective laser sintering process is completed. The influence of chemical elements of the metallic matrix and their influence onto the mechanical behaviour of the SLS injection moulding tools are also being analysed.

RESULTS AND DISCUSSION

The alloy elements that are present within the material structure of the metallic parts manufactured by SLS consist basically on two types of alloy elements – iron and cooper (see Figure 2). The percent of iron within the material structure on the pre-processing process is 53%, as carbon is present in the material structure in a percentage of 35%, while the part is in the "green stage". After the post-processing process, when bronze it is infiltrated into the parts, the matrix will be based mainly on iron (approximately 50%) and cooper (approximately 30%). There are other alloy elements in the matrix structure, such tin, chromium or carbon, having a significant influence as well.

Actually, the combination of iron and cooper is interesting due to the fact that it is not forming any intermediary stage. The cooper can be easily substituted within the iron-based matrix to a temperature of approximately 1500 °C.

The cooper it is known as having excellent diffusion properties within the matrixes that are based mainly on iron material. The easiness of breaking through the material structure, while being in a liquid state makes this type of material to be placed within the preferred material, in the case of matrixes based on iron material. The increased mechanical strength of this type of material it is also a very important analysis criteria, especially in the case when the resulted matrix it is mechanically stressed as it is the case of injection molding tools made by selective laser sintering technology. The thermal conductivity of the iron-cooper matrix is also very important, not only within the infiltrating process, but the injection molding process, as well.

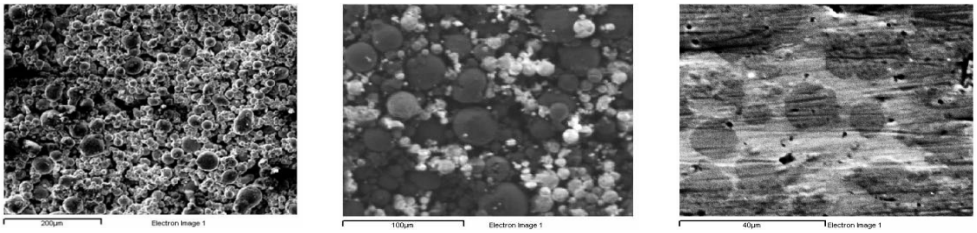

1) 2) 3)

Figure 2. SEM-EDX analysis of the SLS manufactured samples:
1) green stage; 2) after bronze infiltration; 3) after resin impregnation

As related to the other chemical components that are present within the matrix structure (chromium, tin), one of their consequence is the one of decreasing the solubility of cooper material.

Meanwhile, there are also positive aspects that could be mentioned, such as the increasing of corrosion resistance, the hardness or fracture strength of the resulted matrix. All these characteristics are very important in the case of injection moulding tools made by selective laser sintering.

The presence of aluminum and silicium in the matrix after the impregnating process in small quantities is not having a high impact on the overall characteristics of the matrix, even if there are few positive aspects that could be mentioned as advantages, such as the oxidation resistance.

Beside the chemical composition of the metallic matrix, by analyzing the SEM images, it was possible to do some estimations regarding the grains spread onto the material structure, in all three phases of analysis: in green stage, after infiltrating with bronze and after resin impregnation (see Figure 3 and Table 1). This analysis was made based on the images taken from the JEOL JSM - 5600 LV from the Technical University of Cluj-Napoca. As it is possible to observe by analyzing the results presented in Table 1, there is a non-uniform distribution of pores on all three stages. \the possibility to obtain a uniform structure still remains in consequence a difficult task to be solved. It is difficult also to make appreciations on the materials porosity, based on these selected SEM images. That is why it was necessary to do some suplementary calculus, by using formula 1. The results of the made calculus based on this formula proved that it is possible to speak about a porosity decrease from a value of approximately 34 % in the case of sample infiltrated with bronze to a value of approximately 25 % in the case of epoxy resin impregnation (see Table 2), but there are still many other aspects to be analyzed in the future, such as the study of the impregnation procedure in accordance with the size and the shape of the metallic part to be impregnated with resin and type of epoxy resin to be used within the impregnation process.

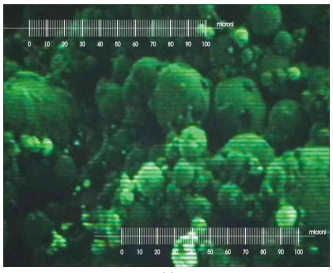

1)

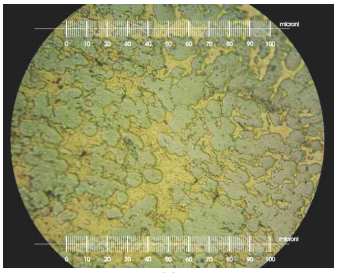

2)

Figure 3. SEM images of the sample:
1) in green stage; 2) after bronze infiltration process

Table 1. Grains distribution of samples

Sample in green stage			Sample infiltrated with bronze			Sample impregnated with epoxy resin		
Diam. [µm]	No.	Spread [%]	Diam. [µm]	No.	Spread [%]	Diam. [µm]	No.	Spread [%]
1	10	17.2	1	-	-	1	-	-
5	19	32.7	5	20	30.7	5	8	21.6
10	15	25.8	10	22	33.8	10	16	43.2
20	7	12	20	15	23.07	20	8	21.6
30	4	6.8	30	6	9.2	30	3	8.1
40	2	3.4	40	2	3.07	40	1	2.7
50	1	1.7	50	-	-	50	1	2.7
Total	58	99.6	Total	65	99.84	Total	37	99.9

Table 2. Aparent density and calculated porosity

	Sample 1			Sample 2		
	Green stage	After bronze infiltration	After resin impregnation	Green stage	After bronze infiltration	After resin impregnation
Apparent density ρ [g/cm^3]	4.84	4.80	5.34	5.07	5.03	5.6
Porosity p [%]	37.05	34.62	29.00	34.07	34.58	25.5

CONCLUSIONS

Researches that were made regarding post-processing stage of injection moulding tools by selective laser sintering (SLS) technology revealed that resin impregnation is a reliable alternative when speaking about decreasing the porosity of these type of tools made by Laserform St-100 metallic powder material. In the case when Ropoxid R510 epoxy resin material has been used as impregnating material, the porosity was decreased from 34% to a value up to 25%, with positive consequences over the mechanical behaviour of such active elements used within the injection moulding process. Meanwhile, the chemical analysis that has been made proved the fact that the metallic matrix is based on the iron-cooper alloyed material, with positive consequences not only for the selective laser sintering process (cooper being easiness to be braked through the material structure), but also for the injection moulding process, due to the thermal conductivity of the material. Still, there are many other aspects to be analyzed in the future, such as the study of the impregnation procedure in accordance with the size and the shape of the

metallic part to be impregnated with resin and the type of epoxy resin to be used within the impregnation process, but as demonstrated, the solution of supplementary epoxy resin impregnation process could be an alternative in the case when the porosity of a metallic part manufactured by selective laser sintering process still have to be decreased afterwards.

EXPERIMENTAL SECTION

The LaserForm St-100 material, which is used for manufacturing metallic parts by using the selective laser sintering technology is a stainless steel powder mixed with an epoxy resin for binding the grains. The part is manufactured based on the layer-by-layer manufacturing technique, every slice being scanned by a CO_2 laser with a maximum power up to 50 W. The polymer that is surrounding the grains is melted and welded together, so as the part in "green stage" it will be obtained. In order to obtain a fully dense metal part, a second stage is obligatory needed in the oven, when, at 1070 ˚C, the binder is burned out and under the capillarity effect, bronze is infiltrated. While post processing in the oven, the metallic part follows the next steps:

- Melting (burning out) the polymer (at 450 °C – 650 °C), which was surrounding the metal grains
- Get fully sintered metal parts, while increasing the temperature to about 700°C
- Infiltrating with bronze, at about 1050 °C – 1070 °C
- Cooling down the parts (natural / slow cooling).

The selective laser sintering process seems well controlled, but in fact there are some limitations, such as the possibility of porosity control. The level of porosity, the shape, the size and the non-uniform porosity distribution into the porous material structure have an important influence over the mechanical and technological characteristics of the metallic parts that are manufactured. If the possibilities of controlling the porosity are limited, the possibilities of decreasing the level of porosity after the selective laser sintering process are not limited.

In order to study the possibility of decreasing the porosity within the material structure, the schematic method presented in Figure 4 has been used, consisting basically in vacuum impregnation equipment.

A sintered die for the lid button of a grass cutting machine has been manufactured using the Sinterstation 2000 equipment from the National Center of Rapid Prototyping – Technical University of Cluj-Napoca, being then split into four pieces by using a side mill. Every sample has been weighted in air and water before on every stage of the manufacturing. For the impregnation process, the epoxy resin ROPOXID R510 has been successfully used. The

aim of resin impregnation under the vacuum is to fill all the existing blanks in the model structure. Half litter of resin has been used with 5% hardener in order to reduce the polymerization process of the resins (see Table 3). The resin and the hardener were mixed until the air was completely sucked by the vacuum. After 8 minutes under the vacuum a boiling phenomenon appears. Total time of maintaining under the vacuum was 56 minutes. After taking out from the vacuum impregnation equipment, the samples were introduced into the oven, as illustrated in Table 3. The samples were dried in the oven for 72 hours.

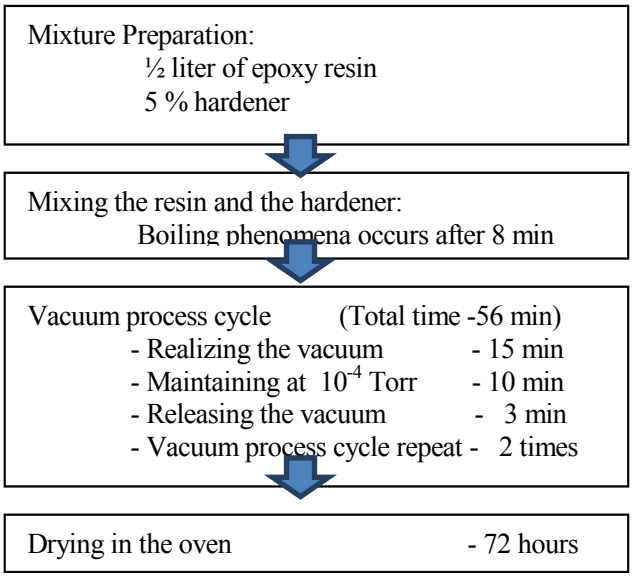

Figure 4. Process Flow for Resin impregnation

The porosity of the material was calculated using the following formula:

$$P_d = \frac{(m_2 - m_1)\cdot \rho_w}{(m_2 - m_3)\cdot \rho_L}\cdot 100 \quad (1)$$

where: m_1 – is the sample mass, weighted in air before resin impregnation, m_2 – is the sample mass, weighted in air after the impregnation, m_3 – is the sample mass weighted in water, ρ_W is the water density (g/cm^3), ρ_L is the resin density (g/cm^3).

At the end of the experiment, some estimation were made regarding the chemical structure and porosity of the sintered die in all stages: in “green stage”, after infiltration with bronze and after resin impregnation, based on the SEM images analyzed with the TESLA BS-300 and JEOL JSM - 5600 LV microscope from the Technical University of Cluj-Napoca.

ACKNOWLEDGMENTS

This paper was financially suported by the project "Development and support of multidisciplinary postdoctoral programmes in major technical areas of national strategy of Research Development - Innovation" 4D-POSTDOC, contract no. POSDRU/89/1.5/S/52603, the project "Progress and development through post-doctoral research and innovation in engineering and applied sciences – PRiDE – Contract no. POSDRU/89/1.5/S/57083", both co-funded from European Social Fund through Sectorial Operational Program Human Resources 2007-2013, by the project BIOMAPIM National Research Grant PCCE no. 5/2010, and project PCCE 140/2008 - Metallomics funded by UEFISCSU.

REFERENCES

1. A.N. Chatterjee, S. Kumar, P. Saha, P.K. Mishra, A. Roy Choudhury, *Journal of Materials Processing Technology,* **200**3, *136*, 151.
2. T.H.C. Childs, M. Berzins, G.R. Ryder, A. Tontowi, *Journal of Engineering manufacture,* **1999**, *213*, 333.
3. P.J. Hardro, J.-H. Wang, B.E. Stucker, *Proceedings of the 5th Int. Conference on Automation Technology*, Chiao Tung University, Taipei, **1998**.
4. D. Miller, C. Deckard, J. Williams, *Rapid Prototyping Journal,* **1997**, *3*, 4.
5. Y. Song, *CIRP Annals Manufacturing Technology,* **1997**, *46*, 127.
6. M. Dewidar, J.K. Lim, K.W Dalgarno, *Journal of Materials and Science Technology*, **2008**, *24*, 227.
7. H.T. Liao, J.R. Shie, *Rapid Prototyping Journal*, **2007**, *13*, 156.
8. K.J. Prashant, M.P. Pulak, P.V.M. Rao, *The International Journal of Advanced Manufacturing Technology*, **2009**, *43*, 117.
9. K. Senthilkumaran, P.M. Pandey, P.V.M. Rao, *Materials and Design*, **2009**, *30*, 2946.
10. J.H. Liu*,* Y.S. Shi, Z.L. Lu, Y. Xu, K.H. Chen, S.H. Huang*, Materials Science and Engineering A*, **2007**, *444*, 146.

11. M. Ablani, A. Bagchi, *Transactions of the North American Manufacturing Research Institution of SME*, **1995**, *23*, 319.
12. J.R. Woodzaik, G.M. Fade, C. Kirschman, *Proceedings of the 5th International Conference on RP*, **1994**.
13. X. Wang, *Rapid Prototyping Journal,* **1999**, *5*, 129.
14. B. Donnchadha, A. Tansey, *Journal of Materials Processing Technology*, **2004**, *153*, 28.
15. P. Berce, N. Bâlc, M. Ancău, *Academic Journal of Manufacturing Engineering*, **2006**, *4*, 13.

STUDIA UBB CHEMIA, LVII, 3, 2012 (p. 15 – 21)
(RECOMMENDED CITATION)

PHOTODEGRADATION STUDY OF SOME INDOOR AIR POLLUTANTS IN THE PRESENCE OF UV-VIS IRRADIATION AND TiO_2 PHOTOCATALYST

GABRIELLA SCHMUTZER[1], IOANA FEHER[1], OLIVIAN MARINCAS[1], VERONICA AVRAM[1], MELINDA H. KOVACS[1], LEONTIN DAVID[2], VIRGINIA DANCIU[3], ZAHARIE MOLDOVAN[1]

ABSTRACT. In the present study, two selected volatile organic compounds (VOCs) were exposed to UV-VIS irradiation – produced by common fluorescent tubes - under controlled humidity and different temperature conditions and their photocatalytic oxidation was quantitatively studied in the presence of TiO_2. Using the inexpensive UV-VIS light source a significant photochemical degradation of toluene and chlorobenzene was obtained. The removal of studied compounds was investigated, in the presence of two different TiO_2 catalysts (Degussa P25 TiO_2 and aerogel TiO_2), whose activity was not affected by the high humidity conditions. In all experiments the degradation rate for toluene was higher than for chlorobenzene. At 70 % relative humidity and room temperature conditions, Degussa P25 TiO_2 shows a major photodegradation effect, comparatively to aerogel TiO_2. Increasing the temperature up to 50 °C and maintaining the relative humidity at the same level, the photocatalytic degradation in the presence of the aerogel TiO_2 increase significantly, therefore the photocatalytic activities for both TiO_2 catalysts are comparable, as well in the case of toluene as for chlorobenzene.

Keywords: *photocatalytic oxidation, toluene, chlorobenzene, degradation rate*

INTRODUCTION

Common indoor air pollutants, namely volatile organic compounds (VOCs) arise from paints, solvents, preservatives, automobile exhaust gas, industrial facilities et al and they are found in the indoor air of residences as well as in office buildings. Due to the absence of air current and aeration of the indoors, the concentration of the total VOCs can be 2-5 fold higher than

[1] *National Institute of Research and Development for Isotopic and Molecular Technology (INCDTIM), Str. Donath Nr. 65-103, RO-400293 Cluj-Napoca, Romania, gabriella.schmutzer@itim-cj.ro*
[2] *Babeş-Bolyai University, Faculty of Physics,, Str. Kogălniceanu, Nr. 1, RO-400084 Cluj-Napoca, Romania*
[3] *Babeş-Bolyai University, Faculty of Chemistry and Chemical Engineering, Str. M. Kogălniceanu, Nr. 1, RO-400084 Cluj-Napoca, Romania*

in outdoor air and can have unwholesome effects [1]. The destruction of various VOCs from polluted air can be performed in different ways: activated carbon adsorption methods, photochemical oxidation and photocatalytic oxidation (PCO) [1-3].

Recently, titanium dioxide(TiO_2)-mediated photocatalysis used to achieve the degradation of VOCs pollutants has been receiving an accentuated attention [1, 4, 5]. The pollutants were fairly decomposed by ozone and hydroxyl radicals produced by UV irradiation [6], and the photodegradation was enhanced by the presence of TiO_2. Semiconductors, in our cause TiO_2 are widely used as photocatalysts, due to their specific characteristics: photochemical stability, lack of toxicity and low cost. Another advantage of the TiO_2 assisted photodegradation is the possibility to operate under atmospheric pressure and room temperature. Despite these advantages, the application of photocatalytic oxidation has some concerns. A limiting factor of the PCO is that one compound may promote or inhibit the removal rate of other compounds [7-9]. In literature contradictory results are presented on: the inhibitory effect of water molecules, which can be attributed to the competition for adsorption on semiconductor surface between pollutants and water molecules [10, 11], respectively the enhancement effect of H_2O, due to formation of active species of hydroxyl radicals, which inhibit deactivation of catalyst [1, 2, 12, 13].

Toluene is a major indoor air pollutant and extensively studied. It is frequently used as an industrial feedstock and as a solvent. For toluene low degradation rates were reported, due to catalyst deactivation [14, 15], in spite of humid air conditions, namely the water molecules can assist to the regeneration of surface: under UV irradiation give rise the highly oxidative hydroxyl radicals involved in the photocatalytic oxidation process [12]. Chlorobenzene is a typical halogenated aromatic VOC that is widely used in industrial fields and in agriculture [16], and the removal rate and the quantum yield could be enhanced working under higher air humidity conditions [17].

The aim of the present paper was to investigate the removal efficiency by photochemical oxidation and photocatalysis of toluene and chlorobenzene under different experimental conditions, using the UV-VIS irradiation. Generally UV irradiation is used for PCO studies, but in the present paper UV-VIS light was used, because it is a very common illumination system of indoors. The photodegradation under controlled humid air conditions at 25 °C and at 50 °C, and the photocatalytic oxidation on the TiO_2 Degussa P25 and TiO_2 aerogel surfaces were investigated and compared. The high humidity condition was chosen to study the role of water molecules in the PCO process. The photochemical oxidation was also evaluated in the presence of irradiation with UV-VIS light, without photocatalyst, too, in order to verify the efficiency of the irradiation with UV-VIS light.

RESULTS AND DISCUSSION

Under dry air condition, reactive oxygen species are generated due to exposure to UV-VIS light, via gas-phase reaction [1]. The generated oxygen species react with the H_2O molecules from humid air, in this way a large number of hydroxyl radicals are formed. The formation of hydroxyl radicals takes place by direct interaction of the H_2O molecules with the irradiation. The generated reactive species, having a strong oxidative effect, induce the photochemical oxidation of the VOCs in the gas phase. The experiments performed confirm the theory about the enhancement effect of water, therefore in this paper are presented results obtained for high (70 %) relative humidity (RH) conditions.

In case of experiments performed at 25 °C, in the absence of TiO_2 and after 150 min irradiation a significant removal of toluene (20.3 %) was observed (see **Table 1.**). This photochemical degradation can be attributed to the oxidation effects of reactive radicals formed in humid air conditions under UV-VIS irradiation. For chlorobenzene the degradation rate under UV-VIS light treatment was lower relative to toluene (8.1 %, after 150 min irradiation), which can be correlated with the chemical structure of the compounds. Therefore the common fluorescent tubes can produce a significant degradation of the studied VOCs and the costs are much lower, than in the case of ozone producing UV lamps.

On the other hand, in the reaction of TiO_2 with UV-VIS light there are photoinduced electrons (e^-) and positive holes (h^+) on the semiconductor surface [18]. The electrons and holes produced can further generate hydroxyl and oxygen reactive species, under appropriate conditions. Due to the high reactivity of the generated species, the mechanism is contributing to the oxidation of organic pollutants and leads to the photocatalytic oxidation of VOCs. In the present study the activity of two different TiO_2 was evaluated: the commercial available Degussa P25 and aerogel TiO_2.

In the presence of photocatalyst and UV-VIS light, according to the theory described above, a significant enhancement of the photodegradation is expected. The degradation rate in photocatalytic oxidation of studied compounds is relevant at 25 °C temperature, in the presence of the commercial semiconductor, Degussa P25 TiO_2. In spite of high humidity conditions (RH=70%), no deactivation of TiO_2 was observed. Under these experimental conditions for toluene the degradation rate, attributed to the photocatalytic oxidation activity of the Degussa P25 TiO_2, was increased by 10.4 %, as compared to photochemical oxidation (without TiO_2), and for chlorobenzene by 9.4 % (see **Table 1.**).

By increasing the photoreactor temperature up to 50 °C, the photocatalytic activity of Degussa P25 TiO_2 did not change, the removal of toluene (31.1 % degradation, after 150 min) and chlorobenzene (17.1 % degradation, after 150 min) remaining at about the same level as for 25 °C (see **Table 1**). The Degussa P25 TiO_2 photocatalytic activity was not affected by a 25 °C increase of temperature, so in these conditions the semiconductor properties were conserved.

Table 1. Photodegradation of toluene and chlorobenzene under UV-VIS irradiation, after 150 min exposure, at 70 % RH, for different temperature conditions (25 °C and 50 °C), in the presence of two type of photocatalyst (Degussa P25 and Aerogel), respectively in the absence of photocatalyst (without TiO_2)

Compound	Photoreactor temperature [ºC]	TiO_2 Photocatalyst	Degdaration rate at 150 min [%]
Toluene	25	Degussa P25	30.7
		Aerogel	22.4
		without TiO_2	20.3
	50	Degussa P25	31.1
		Aerogel	28.6
		without TiO_2	20.9
Chlorobenzene	25	Degussa P25	17.5
		Aerogel	10.7
		without TiO_2	8.1
	50	Degussa P25	17.1
		Aerogel	16.2
		without TiO_2	9.0

The photocatalytic activity of the second semiconductor, aerogel TiO_2 catalyst under UV-VIS light, at 25 °C was much lower than the Degussa P25 TiO_2 activity under the same experimental conditions. The toluene photodegradation, by UV-VIS irradiation and in the presence of aerogel TiO_2 after 150 min, was 22.4 %, by 8.3 % less than in the case of Degussa P25 TiO_2, and being just by 2.1 % higher than in the absence of photocatalyst. The photodegradation rate by UV-VIS light and aerogel TiO_2, for chlorobenzene was 10.7 %, a much lower value in comparison with photocatalytic activity of Degussa P25 TiO_2 (17.5 %), and only little higher than under UV-VIS irradiation (8.1 %). It may be concluded that the photocatalytic activity of aerogel TiO_2 semiconductor is the same for toluene and chlorobenzene degradation. The differences between the degradation rate for toluene and chlorobenzene were attributed to the differences in the chemical structures of the studied VOCs.

The photocatalytic activity of the aerogel TiO_2 under UV-VIS light exposure was significantly increased by the temperature increase of the photoreactor (**Figure 1.**) and was comparable with the photocatalytic activity of Degussa P25 TiO_2. For high humidity condition (RH = 70 %), at 50 °C, under UV-VIS irradiation the photocatalytic activity of aerogel TiO_2 for the toluene degradation was 28.6 %, and for chlorobenzene degradation 16.2 %. The degradation rates presented were very similar to those reported for Degussa P25 TiO_2 under similar conditions. The higher photocatalytic activity of aerogel TiO_2 at 50 °C can be correlated with a structural modification of the titanium dioxide following an increase in temperature.

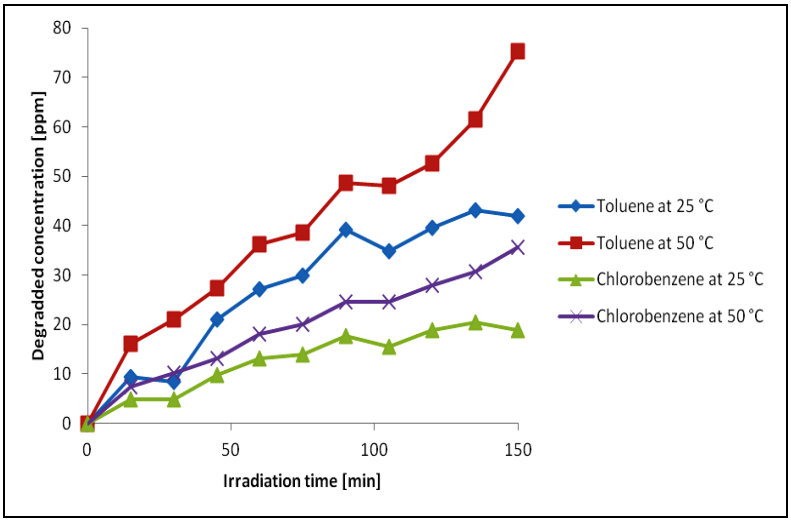

Figure 1. Evaluation as a function of time (from 0 min to 150 min irradiation) of the photocatalytic activity of aerogel TiO_2 for toluene and chlorobenzen at different temperature conditions (25 °C and 50 °C)

CONCLUSIONS

Using common UV-VIS emitting fluorescent tubes a relevant degradation of toluene and chlorobenzene was obtained, permitting also a significant reduction of costs. Higher removal was observed in the presence of semiconductors: Degussa P25 and aerogel; and the high humidity conditions did not produce a TiO_2 deactivation. Due to the chemical structure differences between toluene and chlorobenzene, for toluene a higher degradation rate was found, in all experimental conditions.

For the closed photoreactor operated at 25 °C the degradation rate in the presence of Degussa P25 was much higher than the degradation in the presence of aerogel TiO_2. By increasing the temperature of the reactor up to 50 °C, an increase in the photocatalytic activity of the aerogel TiO_2 was observed. It may be concluded that Degussa P25 has a stable semiconductore structure, while the aerogel TiO_2 photocatalyst structure was modified due to 25 °C temperature increasing.

EXPERIMENTAL SECTION

A closed photoreactor (0.410 l volume) of cylindrical shape, having an internal air-blower - which maintains a homogenous flow of the compounds - was used. In opposite position to the air-blower was set a sample collection

point with a rubber septum system. The dipping procedure – repeated at nine times - was used to deposit the Degussa P25 TiO_2 catalyst and aerogel TiO_2 catalyst on the surface of three glass plates, followed by a drying procedure. The glass plates having a total area of 250 cm^2 coated with the TiO_2 catalyst, were located in the center of the reactor.

Irradiation was made with two straight fluorescent daylight 13W tubes, situated at the two opposite parts of the glass plates, in order to obtain an adequate illumination. Irradiation with fluorescent lamps, instead of UV irradiation was preferred, because in case of extension of the method to a large scale, it can reduce significantly the costs. On the other hand the fluorescent tube has an intensive emission at 434 nm, which contribute to electron transfer from the valence band to the conduction band, on the TiO_2 semiconductor surface [19].

The experiments were carried out at a temperature of 25 °C measured inside of the photoreactor. The temperature of 25 °C was obtained using a cooling air stream. Without air cooling, the temperature increases and stabilizes at 50 °C. Photocatalysis was studied under both temperature conditions.

The relative humidity (RH) was maintained at constant level, RH = 70 % by introducing a suitable quantity of water into the reactor, to supply the H_2O molecules as needed. The initial concentrations of toluene and chlorobenzene in the photoreactor were 400 ppm (v/v) of each compound. After equilibration, 0.2 ml of gas samples were collected from the reactor for analysis at every 15 min intervals and the concentration measurements of the target compound were performed over a time interval of 150 min. The quantitative determination was achieved using a Perkin Elmer Gas Chromatograph (GC), equipped with a flame ionization detector (FID). A stainless steel column with a phenyl-methyl silicone packing was used, of 2 m length and 2.2 mm i. d., maintained in isothermal conditions at 125 °C. The temperatures of injector and manifold were set to 225 °C. The concentrations of the studied compounds were calculated from chromatographic peak areas.

ACKNOWLEDGMENTS

This study was supported by a National Plan II Programmers' Grant (No. 71-136) from the Ministry of Education and Research, National Authority for Scientific Research (ANCS). The authors thank Dr. Nicolae Palibroda for his valuable comments and suggestions.

REFERENCES

1. J. Jeong, K. Sekiguchi, W. Lee, K. Sakamoto, *J. Photochem. and Photobiol. A Chem.*, **2005**, *169,* 279.
2. T. Sano, N. Negishi, K. Takeuchi, S. Matsuzawa, *Solar Energy,* **2004**, *77*, 543.
3. O. Carp, C.L. Huisman, A. Reller, *Prog. Solid State Chem.*, **2004**, *32*, 33.
4. C.C. Chena, C.S. Lua, Y.C. Chungb, J.L. Jan, *J. Hazard. Mater.*, **2007**, *141*, 520.
5. C.H. Ao, S.C. Lee, J.Z. Yu, J.H. Xu, *Appl. Catal. B: Environ.*, **2004**, *54*, 41.
6. J. Jeong, K. Sekiguchi, Mami Saito, Yungyu Lee, Y. Kimb, K. Sakamoto, *Chem. Eng. J*, **2006**, *118*, 127.
7. N.N. Lichtin, M. Avudaithai, E. Berman, A. Grayfer, *Solar Energy*, **1996**, *56*, 377.
8. C.H. Ao, S.C. Lee, S.C. Zou, C.L. Mak, *Applied Catalysis B: Environmental*, **2004**, *49*, 187.
9. R.M. Alberici, W.F. Jardim, *Appl. Catal. B - Environ*. **1997**, *14*, 55.
10. J. Van Durme, J. Dewulf, W. Sysmans, C. Leys, H. Van Langenhove, *Chemosphere*, **2007**, *68*, 1821.
11. A.K. Boulamanti, C.J. Philippopoulos, *Atmospheric Environment*, **2009**, *43*, 3168.
12. F. Fresno, M.D. Hernandez-Alonso, D. Tudela, J.M. Coronado, J. Soria, *Appl. Catal. B: Environ.*, **2008**, *84*, 598.
13. T. Guo, Z. Bai, C. Wu, T. Zhu, *Appl. Catal. B: Environ.*, **2008**, *79*, 171.
14. M.C. Blount, J.L. Falconer, *Appl. Catal. B*: *Environ.,* **2002***, 39*, *39*.
15. M. Lewandowski, D.F. Ollis, *Appl. Catal. B: Environ.*, **2003**, *43*, 309.
16. C. Wang, JY. Xi, H.Y. Hu, *Chemosphere*, **2008**, *73*, 1167.
17. C. Wang, JY. Xi, H.Y. Hu, *J. Air Waste Manag. Assoc.*, **2009**, *59*, 386.
18. Y. Xu, C.H. Langford, *J. Photochem. Photobiol. A Chem.*, **2000**, *133*, 67.
19. M. Kaneko, I. Okura, "Photocatalysis: science and technology" (Biological and Medical Physics Series), Springer-Verlag Berlin Heidelberg, New York, **2002**.

STUDIA UBB CHEMIA, LVII, 3, 2012 (p. 23 – 30)
(RECOMMENDED CITATION)

GAS ANALYSIS OF MUNICIPAL LANDFILL EMISSIONS

MICHAELA BIANCA VAC (SOPORAN)[1], VASILE FILIP SOPORAN[1], EMANUELA ADINA COCIŞ[1], GHEORGHE BĂTRÎNESCU[2], OVIDIU NEMEŞ[1,*]

ABSTRACT. The article presents a method of measurements and analysis of gas emissions from municipal landfills, especially for the nonconforming ones. Based on measurements made from Pata Rat landfill, Cluj-Napoca, a methodology is presented for interpreting the results in order to assess the current energetic potential of the deposit. Experimental data are the main basis for determining the energetic potential of the deposit. Applying the methodology of setting the stage energy deposit, shows that the best period for using Pata Rat landfill was exceeded, but the methane concentration and the flow rate, resulted from the last measurements, indicates that the site should continue to be monitored in terms of gas emissions.

Keywords: *landfill, gas emissions, gas analysis*

INTRODUCTION

The European Municipal waste management system of our days, according to European documents [1-3], faces a situation caused by increased of stored waste volume (because 49% are stored, 18% incinerated and 43% recycled or composted). In EU there is a greater distribution of landfilling compared to other waste treatments. Thus, there are states storing in 90%, while others are storing less than 10%.

Landfills with historical significance were built before the adoption of regulations which set restrictions on avoiding implementation of environmental impact of leachate and landfill gas. Many of these sites are now sources of pollution by leakage. Particularly, landfill gas can be dangerous because its main component, methane, can reach explosive concentrations. This problem is accentuated by many large landfills built near residential areas, or, sometimes, residential neighborhoods were built on or near closed landfills. On the other hand, methane gas from landfills is also a "greenhouse gas", which leads to global warming and it is approximately 30 times more harmful than carbon dioxide.

[1] *Universitatea Tehnică din Cluj-Napoca, Facultatea de Ingineria Materialelor şi a Mediului, B-dul Muncii, Nr. 103-105, RO-400641, Cluj-Napoca, Romania, e-mail: ovidiu.nemes@sim.utcluj.ro*
[2] *Institutul Naţional de Cercetare-Dezvoltare pentru Ecologie Industrială INCD-ECOIND, Str. Drumul Podu Dâmboviţei, nr. 71-73, Sector 6, RO-060652, Bucureşti, România*

In terms of energy recovery are important phases are phase fourth and fifth. Based on this, we will analyze the gas emissions from the municipal landfill Pata Rat, Cluj-Napoca.

The issue of waste disposal has two aspects: the recovery of potential energy and solving environmental problems in terms of emissions. This paper aims to determine the energy potential for the deposits with historical significance. This goal is achieved by monitoring gaseous emissions.

RESULTS AND DISCUSSION

The landfill "Pata Rat" located near Cluj – Napoca, was open in 1973 and has been designed and sized, considering a period of 30 years for exploitation. Basically, storage capacity was exceeded, considering 2003 as the deadline year for the operation of the landfill. However, according to Government Decision 349 of 2005, closing date was fixed for 16.07.2010. The deposit area is 8.94 ha. Minimum distance from residential areas is 1.5 km.

Table 1. Experimental data

Measurement points	Depth [cm]	CH_4 [%]	CO_2 [%]	O_2 [%]	H_2S [ppm]	CO [ppm]	Bal [%]
P001	60	0.2	69.2	1.1	29	500	29.5
P002	60	50.7	67.1	0	33	500	0
P003	60	24.8	45.7	0	0	526	29.5
P004	60	47.5	65.3	0	500	500	0
P005	60	52.8	65.2	0	500	183	0
P006	60	52.7	65.3	0	500	209	0
P007	60	43	62.7	0	500	296	0
P008	60	16.7	42.4	0	33	500	40.9
P009	60	11,9	34,1	1,3	0	46	54.7
P010	60	42.4	63.8	0.5	9	200	9
P011	60	45.5	56.6	0	156	73	0
P012	60	48.7	68.4	0.1	1	183	0
P013	60	51.3	64.7	0.5	122	388	0
P014	60	54	61.1	0.7	4	34	0
P015	60	44.3	56.7	1.5	500	478	0
P016	60	25	54.2	5.5	19	78	15.3
P017	60	34.6	86.6	0.1	87	276	0
P018	60	51.1	62.6	1,1	500	500	0
P019	60	39.7	76.8	0.3	500	473	0
P020	60	62	46.2	3.1	38	36	0
P021	60	1.8	20.6	8.7	9	77	68.9
P022	60	45.4	54.4	0.2	500	91	0
P023	60	0	12.6	11.7	5	2	75.7
P024	60	10.3	3.6	9.9	19	500	76.2

Measurements were made in the research program VALENDEM, during a period of three years, 2009 – 2011. The first measurements were explorers, following the determination of potential energy.

In the beginning, in 2009, a set of data was obtained. For this purpose on the deposit surface were chosen some points (Fig. 1) placed at equal distances from each other. Then we did the measurements with GA 2000.

The obtained experimental data are presented in Table 1. Table contains results obtained in 20.11.2009, when weather conditions were: sky clear, temperature 15 °C and atmospheric pressure of 986 mbar.

The distribution charts of methane, carbon dioxide, oxygen, hydrogen sulfide and carbon monoxide are represented in Figure 1.

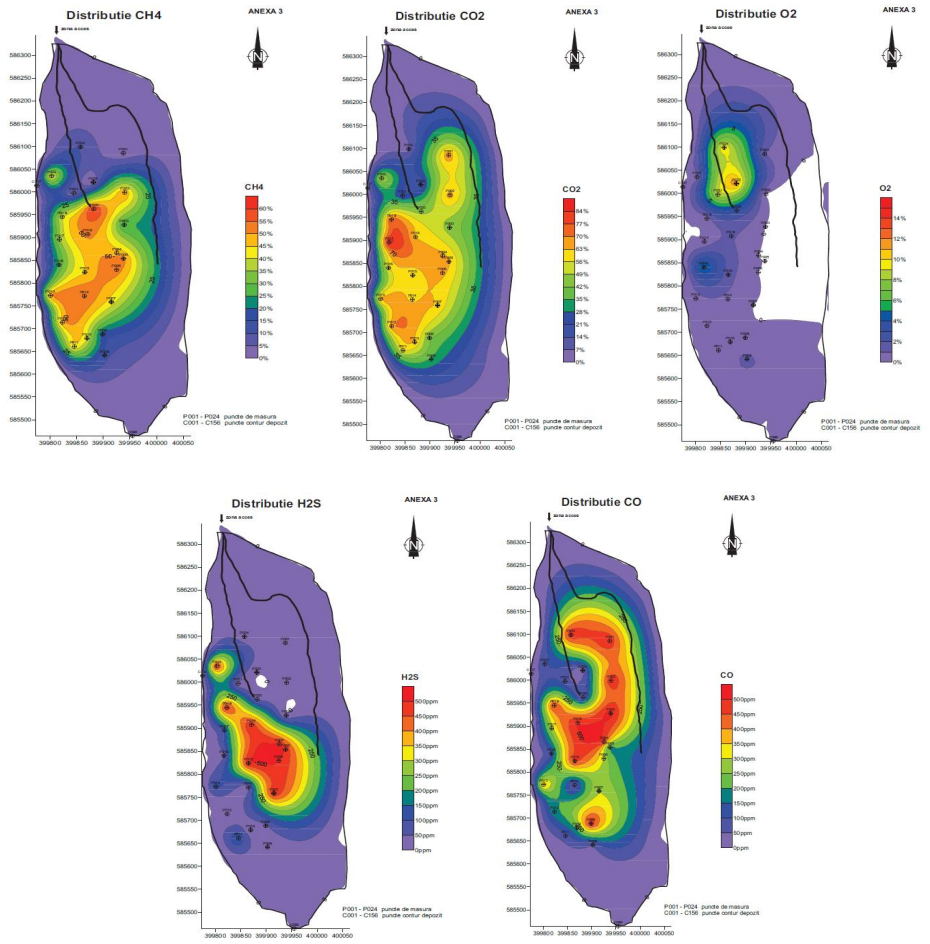

Figure 1. Experimental points and gas distribution maps.

In order to determine the energy capacity of Pata Rat landfill in Cluj-Napoca, measurements were executive in April 2011. The obtained values are detailed in Table 2.

Table 2. Experimental data obtained at the municipal landfill Pata Rat

DAY: 04.04.2011			**WEATHER CONDITIONS: Clear, sunny, light wind, low precipitation**									
No.	**Hour**	**Ext. temp. [°C]**	**Drill. temp. [°C]**	**Pres. atmos. [mbar]**	**Rel. pres. [mbar]**	**Q [l/h]**	**CH_4 [%]**	**CO_2 [%]**	**O_2 [%]**	**Bal. [%]**	**H_2S [ppm]**	**CO [ppm]**
1	$15^{\underline{00}}$	17.5	12.3	969	0.19	0.3	72.5	20.6	0.9	6.0	53	5
2	$17^{\underline{00}}$	16	12.4	969	0.23	0.2	71.6	21.3	0.7	6.4	39	4
DAY: 05.04.2011			**WEATHER CONDITIONS: Partly cloudy, light wind**									
1	$8^{\underline{00}}$	8.3	11.6	972	0.14	0.3	69.3	22.5	1.2	7.0	29	2
2	$10^{\underline{00}}$	12.7	11.9	972	0.01	0.3	70.4	22.0	1.1	6.5	46	3
3	$12^{\underline{00}}$	15.9	12.1	972	0.11	0.4	71.2	23.9	0.8	4.1	38	1
4	$14^{\underline{00}}$	17.4	12.4	972	0.14	0.4	72.8	23.1	0.3	3.8	27	3
5	$16^{\underline{00}}$	18.6	12.3	973	0.09	0.3	70.6	22.1	1.1	6.2	32	4
6	$18^{\underline{00}}$	19.2	12.3	973	0.11	0.2	69.8	23.2	1.9	5.1	41	2
DAY: 06.04.2011			**WEATHER CONDITIONS: Variable, mostly clear, light wind**									
1	$8^{\underline{00}}$	8.6	11,8	979	0.23	0.3	72.6	20.6	0.4	6.4	69	5
2	$10^{\underline{00}}$	13.1	12.0	979	0.09	0.3	71.5	22.2	0.5	5.8	87	2
3	$12^{\underline{00}}$	16.2	12.1	979	0.06	0.4	70.2	21.8	0.8	7.2	101	3
4	$14^{\underline{00}}$	17.6	12.3	979	0.12	0.2	71.9	22.9	0.3	4.9	72	3
5	$16^{\underline{00}}$	18.9	12.5	979	0.14	0.3	70.9	23.9	1.4	3.8	56	2
6	$18^{\underline{00}}$	20.1	12.3	979	0.11	0.3	71.2	23.1	0.6	5.1	62	3
DATA: 07.04.2011			**WEATHER CONDITIONS: Clear, sunny**									
1	$8^{\underline{00}}$	8.8	11.4	975	0.28	0.4	71.3	22.4	0.8	5.5	71	4

For measurements made in April 2011, where possible, averages were made for each day, obtaining the average value of the day. These are presented in Table 3.

Table 3. Average values of the day

Average	**Drilling temperature t_f [°C]**	**Atmospheric pressure p_a [mbar]**	**Flow Q [l/h]**	**Methane C_{CH4} [%]**
M1 - 04.04.11	16.75	969.00	0.250	72.050
M2 - 05.04.11	15.35	972.33	0.316	70.683
M3 - 06.04.11	15.75	979.00	0.300	71.383
Monthly average	15.95	973.44	0.289	71.372

Graphical representations of variation measures determined in a series of three days in April are as follows: flow - Figure 2, the methane concentration - Figure 3.

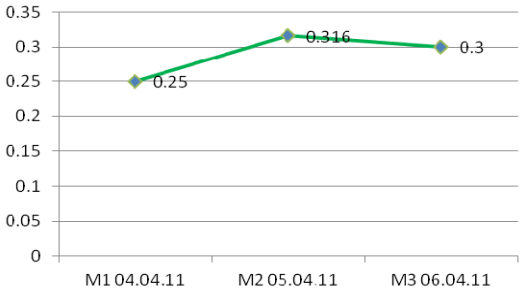

Figure 2. Average gas flow variation in April 2011 [l/h].

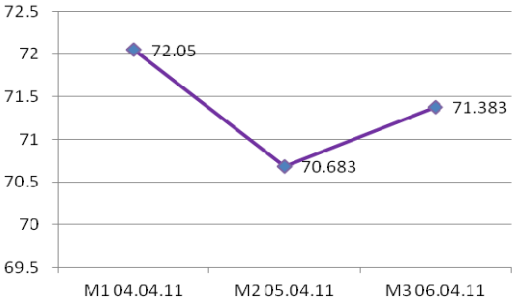

Figure 3. Methane average concentration variation in April 2011 [%].

Similarly, measurement results were processed in 2010 and 2011. The results average values of all measurements in the July 2010 - June 2011 interval are presented in Table 4.

Table 4. Average values for measurements in July 2010 - June 2011

Average	**Drilling temperature t_f [ºC]**	**Atmospheric pressure p_a [mbar]**	**Flow Q [l/h]**	**Methane C_{CH4} [%]**
Monthly average for July 2010	20.445	973.9	0.286	74.662
Monthly average for September 2010	18	982.4	0.299	73.804
Monthly average for April 2011	15.95	973.443	0.289	71.372

Average	Drilling temperature t_f [ºC]	Atmospheric pressure p_a [mbar]	Flow Q [l/h]	Methane C_{CH4} [%]
Monthly average for June 2011	21.46	977.222	0.254	68.388
Average	**18.963**	**976.741**	**0.282**	**72.056**

Graphical representation of values variation measured and expressed as the mean intervals are depicted as follows: average hourly flow of landfill gas - Figure 4, the average concentration of methane - Figure 5.

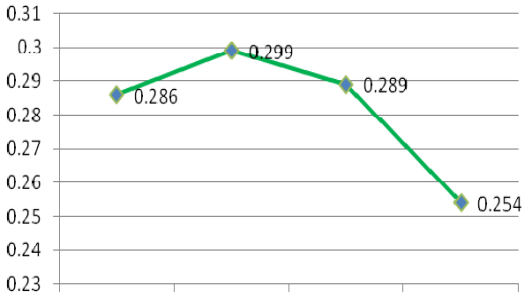

Figure 4. Measurements variations of hourly landfill gas flow for the period July 2010 - June 2011 [l/h]

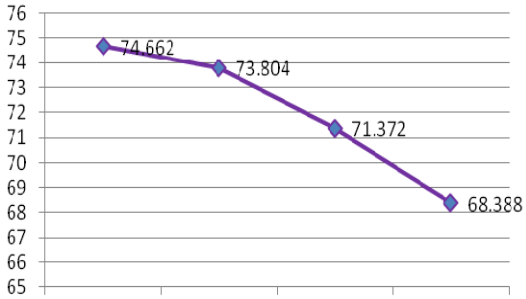

Figure 5. Variation of the average methane concentration measurements during July 2010 - June 2011 [%]

EXPERIMENTAL SECTION

To determine the composition of landfill gas in order to estimate their energy potential, preliminary experiments have been set on landfill gas characterization. Measurements were done during 2010-2011.

In order to determine the energy potential of the landfill gas emission from Pata Rat gaseous samples were collected from 24 drilling points (P001 to P024). A drilling in diameter of 160 mm was performed until a depth of 10 m. Perforated PVC tubes was introduced, for a good capture of landfill gas. On the surface, on the end of the tube, a concrete collar stiffener was made and a valve cover set at the end to install the gas composition meter GA 2000. Drilling position on landfill surface was determined using a GPS device and its coordinates are: N46° 46.075'; E23° 41.270'. Figure 6 shows the system for the gas capture in Pata Rat municipal landfill.

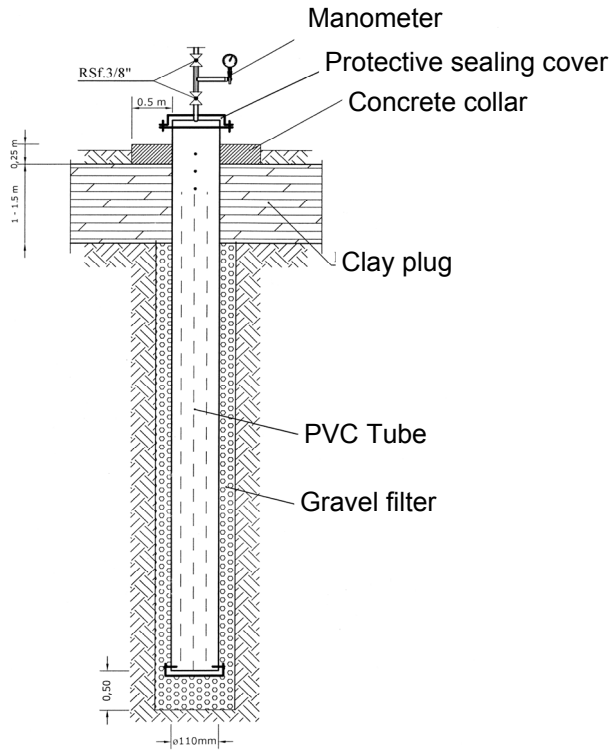

Figure 6. Gas captures equipment on Pata Rat municipal landfill.

CONCLUSIONS

In this paper, gas monitoring and analysis activities can lead to a methodology for measuring and proper interpretation of the data. Therefore, the monitoring of non-compliant landfills should include the following actions: Establishment of municipal landfill surface contour; Establishment of the exploratory measurement points set, so that they have an equal distance from each other and from the contour; Recording space and time of preliminary

measurements to determine the gas concentration of methane, carbon dioxide, oxygen, hydrogen sulfide and carbon monoxide; Interpretation of results and determination of the maximum energy potential area; Drilling coordinates definition in order to capture the landfill gas; Achieving drilling and attachment system for the capture and characterization of landfill gas; Making measurements at intervals determined; Quantification and interpretation of data to characterize landfill gas and the conditions under which measurements were made; Interpretation for a given range, in our case 3 years, for the measurements results; Interpretation of experimental data for the energy status of the deposit. The Methodology for determining the energy state is based on time tracking evolution of two quantities, namely methane flow and concentration. From Figure 4, results that maximum flow was measured in September 2010, the decrease being confirmed by measurements made in April and June 2011. Also, analyzing the variation of methane concentration (figure 5) it is observed that methane has a constantly decreasing evolution from June 2010 to June 2011.

Therefore, a methodology for assessing energy capacity of the landfill should include the following: Performing measurements for flow and methane concentration in the landfill gas for a given time interval; Quantifying the evolution in time of flow and methane concentration of the landfill gas; Determining the gas evolution and distribution.

In terms of applied methodologies we can say that Pata Rat deposit is beyond maximum levels of methane (gas flow and concentration).

ACKNOWLEDGMENTS

This paper was funded by the Project SIDOC - *PhD engineering sciences to develop knowledge-based society* POSDRU/88/1.5/S/60078 and VALENDEM - *Energy recovery Emissions from Municipal Landfills* nr.32/113/01.10.2008.

REFERENCES

1. V.F.Soporan, O. Nemes, V. Dan, M.B. Soporan, A. Gombos, A.I. Moldovan, “Gestiunea deseurilor in documente europene”, Colectia Documente Europene si Nationale, Ed. Casa Cartii de Stiinta, Cluj-Napoca, **2011**.
2. ***, Directiva 2008/98/CE a Parlamentului European si a Consiliului din 19 noiembrie 2008 privind deseurile si de abrogare a anumitor Directive, Jurnalul Oficial al Uniunii Europene L312, **2001**
3. ***, Directiva 76/2000/CE a Parlamentului si a Consiliului European din 04.12.2000 privind incinerarea deseurilor, **2000**.
4. L. Blasy, M. Lange, N. Hagen, D. Rosar, A. Atudorei., *Salubritatea*, **2006**, 4.

STUDIA UBB CHEMIA, LVII, 3, 2012 (p. 31 - 40)
(RECOMMENDED CITATION)

METALS LEACHING FROM WASTE PRINTED CIRCUIT BOARDS. PART I: EFFICIENCY AND SELECTIVITY IN $FeCl_3$ AND $CuCl_2$ ACIDIC SOLUTIONS

SZABOLCS FOGARASI[1], FLORICA IMRE-LUCACI[2], PETRU ILEA[1,*]

ABSTRACT. The leaching of metals from waste printed circuit boards (WPCBs) was investigated in different leaching systems using $FeCl_3$ or $CuCl_2$ as oxidants. The influence of solution speciation on the redox equilibria and process performances was studied in unstirred 1 M HCl solutions. The efficiency of these systems was compared on the basis of the extent of leaching of individual metals and total metal dissolution. It has been found that in chloride medium the leaching efficiency reaches a plateau at 0.4 M $CuCl_2$ concentration, while for $FeCl_3$ it is continuously increasing even at concentrations four times higher.

Keywords: *waste printed circuit boards, leaching systems, $FeCl_3$ and $CuCl_2$*

INTRODUCTION

In the recent years, the lifespan of consumer electronic devices has become relatively short, due to the rapid changes in equipment features and capabilities. This creates a large stream of waste electric and electronic equipment (WEEE) [1, 1]. Printed circuit boards (PCBs) are a key component in electronic equipments, representing about 3 % of the total amount of WEEE. In general, WPCBs contain approximately 30 % metals and 70 % non-metal materials [2, 3]. The typical metals in PCBs consist of copper (20 %), iron (8 %), tin (4 %), nickel (2 %), lead (2 %), zinc (1 %), silver (0.2 %), gold (0.1 %), and palladium (0.005 %) [2-7]. Hence, recycling of electronic waste is an important topic not only from the point of waste treatment but also from the recovery aspect of valuable materials. Therefore, in the past few years many investigations have been made to develop eco-friendly technologies with cost effective processing and without any negative impact on the environment [1, 2-8].

Electronic waste recycling technologies have several preliminary steps in order to separate and concentrate the valuable materials and thus increase the performance of the recycling process. The most important pre-treatments are mechanical processing, specific gravity separation, magnetic and

[1] *Babeş-Bolyai University, Faculty of Chemistry and Chemical Engineering, 11 Arany Janos Street, Cluj-Napoca, 400028, Romania*
[2] *Babeş-Bolyai University, Interdisciplinary Research Institute on Bio-Nano-Sciences, 42 Treboniu Laurian Street, Cluj-Napoca, 400271, Romania, * pilea@chem.ubbcluj.ro*

electrostatic separation [5-8]. These are followed by pyrometallurgical and hydrometallurgical technologies which are the main industrial scale processes for metal recovery from WEEE [5, 7]. Pyrometallurgical processing, especially open burning, incineration and smelting were the traditional methods for metal recovery from e-waste in the last two decades [2, 5, 7, 8]. These methods are simple but have major disadvantages like: non-selectivity, hazardous operating conditions and emission of toxic gases (dioxin, brominated flame retardants) and fumes metals (Hg, Pb and Cd) [1, 5-9]. The hydrometallurgical method is more predictable, and more easily controlled. The most important steps in hydrometallurgical processing consist of a series of acid or caustic leaching of metals from the WEEE depending upon the composition of the WPCBs and the variable chemical properties of the metals. The use of aerated cyanide leaching system for gold and silver has been banned in some countries due to environmental concerns [10]. This has resulted in the increase in research activities with non-cyanide ligands and more efficient oxidant than air [11-14]. However there are issues that need to be solved, such as: increasing leaching rate and selectivity while reducing the reagent consumption [8].

The aim of this work was to study the leaching of metals from WPCBs in acidic $FeCl_3$ or $CuCl_2$ solutions. The efficiency of the dissolution processes was evaluated based on the experimental results and possible redox equilibriums.

RESULTS AND DISCUSSION

The influence of oxidant concentration on overall metal dissolution

Analyzing the literature data for the Fe-Cl-H_2O and Cu-Cl-H_2O systems [15-20] it was found that, depending on chloride concentration, the following chemical species can be present in the solution: $FeCl_2^+$, Fe^{2+}, $CuCl_2(aq)$, $CuCl^+$, $CuCl_2^-$ and $CuCl_3^{2-}$. For the Fe^{3+}/Fe^{2+} redox couple, Cl^- concentration is ranging from 1.3 to 5.8 M, as a result, the predominant chemical species are $FeCl_2^+$ and Fe^{2+}. In the case of Cu^{2+}/Cu^+ when chloride concentration is lower than 2 M the predominant chemical species are $CuCl^+$ and $CuCl_2^-$, while at higher concentrations, $CuCl_2(aq)$ and $CuCl_3^{2-}$ are the predominant.

Considering the calculated equilibrium potentials (vs. NHE) for the standard redox systems (Fe^{3+}/Fe^{2+}, Cu^{2+}/Cu^+, Cu^{2+}/Cu, Cu^+/Cu):

$$Fe^{3+} + e^- \leftrightarrow Fe^{2+} \qquad E^0 = 0.775\ V \qquad (1)$$

$$Cu^{2+} + 2e^- \leftrightarrow Cu \qquad E^0 = 0.337\ V \qquad (2)$$

$$Cu^{2+} + e^- \leftrightarrow Cu^+ \qquad E^0 = 0.167\ V \qquad (3)$$

$$Cu^+ + e^- \leftrightarrow Cu \qquad E^0 = 0.506\ V \qquad (4)$$

The dissolution of metals involves the following redox reactions and equilibrium potentials for the oxidants:

$$FeCl_2^+ + e^- \leftrightarrow Fe^{2+} + 2Cl^- \qquad E^0 = 0.702\ V \qquad (5)$$

$$CuCl^+ + 2e^- \leftrightarrow Cu + Cl^- \qquad E^0 = 0.318\ V \qquad (6)$$

$$CuCl^+ + Cl^- + e^- \leftrightarrow CuCl_2^- \qquad E^0 = 0.466\ V \qquad (7)$$

$$CuCl_2^- + e^- \leftrightarrow Cu + 2Cl^- \qquad E^0 = 0.169\ V \qquad (8)$$

$$CuCl_{2(aq)} + 2e^- \leftrightarrow Cu + 2Cl^- \qquad E^0 = 0.319\ V \qquad (9)$$

$$CuCl_{2(aq)} + Cl^- + e^- \leftrightarrow CuCl_3^{2-} \qquad E^0 = 0.428\ V \qquad (10)$$

$$CuCl_3^{2-} + e^- \leftrightarrow Cu + 3Cl^- \qquad E^0 = 0.209\ V \qquad (11)$$

Comparing the standard reduction potential value of the Fe^{3+}/Fe^{2+} redox couple in chloride, eq. (5), and chloride free medium eq. (1) it can be seen that the formation of $FeCl_2^+$ does not influence significantly the oxidant power of Fe^{3+} ions. Similarly, for the Cu^{2+}/Cu redox couple the potential was not notably modified in chloride solution due to the low stability of Cu (II) chloro-complexes. Quite the opposite happens in the case of Cu^{2+}/Cu^+ (eq. 7, 10) for which the redox potential is shifted to more positive values, in the presence of chloride ions. This can be attributed to the formation of very stable Cu (I) chloro-complexes which, accordingly to the Nernst equation, will determine the increase of the redox potential. Figure 1 shows that the dependency of the global dissolution degree (defined as the ratio between the amount of dissolved metals and total amount of metals in the WPCB sample) on the oxidant concentration is more pronounced in the case of $FeCl_3$ than for $CuCl_2$.

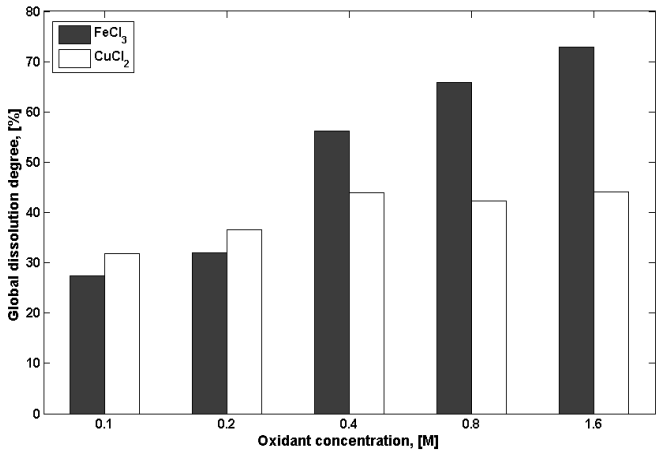

Figure 1. Global dissolution degree of metals in 1 M HCl using $FeCl_3$ and $CuCl_2$ as oxidants.

Hence, an increase of oxidant concentration by 16 times (0.1-1.6 M) enhances the global dissolution degree 2.6 times for $FeCl_3$ and 1.5 times for $CuCl_2$. This can be easily explained by considering the different standard reduction potentials eq. (1-11) of the studied redox systems Fe^{3+}/Fe^{2+},

Cu^{2+}/Cu^{+}, Cu^{2+}/Cu. As a result, at the same oxidant concentration Fe^{3+} is a more powerful oxidizing agent than Cu^{2+} or Cu^{+} in both chloride and chloride free mediums, due to the higher redox potential. However, the experimental results show that at low oxidant concentrations (0.1-0.2 M) it appears that $CuCl_2$ is more efficient oxidant in the dissolution of metals than $FeCl_3$.

In order to explain these results the influence of mass transport on the dissolution rate has to be considered. Since the leaching experiments are realized in stationary solutions the mass transport of the reactants and products will occur only by diffusion. Therefore the transport intensity of different chemical species is dependent on the diffusion coefficient which in turn depends on the molar volume (bulk) of the ions. Based on the discussions regarding the speciation of Fe^{3+}/Fe^{2+} and Cu^{2+}/Cu^{+} in aqua chloride medium it is obvious that the intensity of the mass transport will depend on the complexation of Fe^{3+}, Cu^{2+} and Cu^{+}. For this reason in the case of $FeCl_3$ the mass transport has the same rate throughout the experiments thanks to the formation of only one chloro-complex ($FeCl_2^+$) while for Cu^{2+}/Cu^{+} there are two situations. At lower $CuCl_2$ concentrations than 0.4 M the chemical species involved in the leaching process are $CuCl^+$ and $CuCl_2^-$, while at higher concentrations than 0.4 M the transport of $CuCl_{2(aq)}$ and $CuCl_3^{2-}$ has to be considered.

It is clear that the transport of copper chloro-complexes is even slower as the concentration of chloride ions increases due to the formation of more bulk species. Also, comparing the copper chloro-complexes with $FeCl_2^+$ it seems like at oxidant concentrations lower than 0.4 M the diffusion of Cu^{2+} is faster than that of Fe^{3+} because the $CuCl^+$ ion is smaller than $FeCl_2^+$ ion. For oxidant concentrations higher than 0.4 M the transport of Cu^{2+} is still the fastest due to the formation of $CuCl_{2(aq)}$ neutral species which diffuse more easily than $FeCl_2^+$ ions.

In order to reveal the chemical species which diffuse from the reaction zone to the bulk and their influence on the metals dissolution rate is essential to identify the reactions from which they have been resulted. Analyzing the possible redox reactions eq. (1-11) it is obvious that in the case of Fe^{3+}/Fe^{2+} there is a single main redox reaction eq. (5) which generates small ions (Fe^{2+}, Cl^-) as reaction products. In contrast, the Cu^{2+} can be reduced by parallel reactions to Cu or Cu^{+} depending on the $CuCl_2$ concentration and the molar ratio between the $CuCl_2$ and the metals from the WPCB sample. Therefore at low $CuCl_2$ concentrations (0.1-0.4 M) the Cu^{2+} ion is reduced by two competitive reactions eq. (6, 7). The redox equilibrium constant for eq. (6, 7) can be defined by the following equations:

$$K_1 = \frac{k_1}{k_{-1}} = e^{-\frac{\Delta_r G_1}{RT}} = \frac{[Cl^-]}{[CuCl^+]} = 5.72 \cdot 10^{10} \qquad (12)$$

$$K_2 = \frac{k_2}{k_{-2}} = e^{-\frac{\Delta_r G_2}{RT}} = \frac{[CuCl_2^-]}{[CuCl^+][Cl^-]} = 7.63 \cdot 10^7 \quad (13)$$

where K_1, K_2 are the redox equilibrium constants for eq. (6, 7); k_1, k_2 forward rate constants; k_{-1}, k_{-2} backward rate constants; $\Delta_r G_1$, $\Delta_r G_2$ standard free energy of reaction expressed in KJ/mol; *R* - universal gas constant in J/(mol K); *T* - temperature in K.

By comparing the redox equilibrium constants values of the two reactions it is evident that the ratio between the forward and backward rate constants is 750 times higher for the cementation of copper than for the reduction of $CuCl^+$ to $CuCl_2^-$. This means that $CuCl^+$ is consumed much faster when it is reduced to Cu than when it is reduced to $CuCl_2^-$. Given that the both mass transport and redox reaction are much faster in the case of eq. (6) it can be concluded that the contribution of eq. (7) to the dissolution of metals can be neglected in the range of 0.1-0.4 M $CuCl_2$ concentration.

It is also important to reveal that the increase of $CuCl_2$ concentration will affect the rate of copper cementation until the whole surface of the metals is covered by Cu. This also results from the experimental data showed in Figure 1, which confirm that the metals dissolution achieves a maximum at 0.4 M after which the increase of $CuCl_2$ concentration does not affect the dissolution rate due to the fact that the contact between the reagents is blocked by the cemented copper. In order to continue the dissolution of metals it is necessary to dissolve the cemented copper first. This can occur by eq. (14) at chloride concentrations below 2 M and by eq. (15) at chloride concentrations higher than 2 M:

$$Cu + 3Cl^- + CuCl^+ \leftrightarrow 2CuCl_2^- \qquad K_3 = 1.01 \cdot 10^5 \quad (14)$$

$$Cu + 4Cl^- + CuCl_{2\,(aq)} \leftrightarrow 2CuCl_3^{2-} \qquad K_4 = 5.13 \cdot 10^3 \quad (15)$$

The equilibrium constants values obtained for eq. (14, 15) indicates that the dissolution of cemented copper is less favored than the dissolution of metals through copper cementation eq. (12, 13) and is diminished by the increase of chloride concentration. Furthermore, the discussions regarding the influence of mass transport and thermodynamic equilibriums on the dissolution of metals explains why Cu^{2+} is more efficient at lower oxidant concentration than Fe^{3+}. Since the dissolution of metals in the case of $CuCl_2$ occurs only by cementation eq. (6, 8) it is evident that $CuCl_2$ can oxidize twice as much metal than $FeCl_3$. For this reason, as it is shown in Fig. 1, the global dissolution degree of metals is a bit higher for $CuCl_2$ when the oxidant concentration is ranging from 0.1-0.2 M. As for higher oxidant concentrations than 0.2 M, $FeCl_3$ turns out to be more efficient because the dissolution of metals with Fe^{3+} is not hindered by the formation of a solid phase like in the case of copper cementation.

The influence of oxidant concentration on individual metal dissolution

The individual dissolution degree was determined for each metal at the studied oxidant concentrations (0.1-1.6 M). Comparing the experimental results from Table 1 it is obvious that the leaching rate of Zn and Ni differ not only in values but also in their evolution with oxidant concentration.

Table 1. Individual dissolution degree of Zn, Ni and Cu in 1 M HCl using different oxidant concentrations

Oxidant concentration, M	Individual dissolution degree, %				
	Zn		Ni		Cu
	$FeCl_3$	$CuCl_2$	$FeCl_3$	$CuCl_2$	$FeCl_3$
0.1	93.3	92.5	18.1	26.9	52.8
0.2	93.2	89.3	22.1	33.7	71.1
0.4	95.3	71.6	51.1	43.9	91.9
0.8	95.1	64.1	65.2	43.5	90.7
1.6	94.2	64.1	74.9	45.3	90.8

First of all, this difference between Zn and Ni appears due the fact that Ni being a more noble metal than Zn the reaction with the oxidants occurs slower. It is also important to notice that the rate of the dissolution process also depends on the structure in which the two metals are present in the WPCBs. While Ni is used as thin layers in the corrosion protection of electric contacts and components, Zn is used as Cu-Zn alloys (brass). Therefore the dissolution of Zn is influenced by both oxidant concentration and Cu dissolution rate, while for Ni it depends only on the concentration of the leaching agents. In consequence the dissolution rate of Ni increases with the increase of $FeCl_3$ concentration due to the large contact area between the reactants, while for Zn the process is slightly affected, since the leaching of Zn, out of the brass lattice, leads to a porous structure in which the process can be limited by mass transport. However due to the fact that $FeCl_3$ dissolves efficiently even copper (Table 1) the dissolution degree of Zn is very high and practically limited not by diffusion but through the redox equilibrium established between the Fe^{3+} and the two metals. The pores influence on Zn dissolution is also sustained by the literature date [21] available for the dezincification of Cu-Zn alloys in various corrosive environments.

Similarly for the experiments with $CuCl_2$ it can be observed, from Table 1 that the dissolution degree of Zn and Ni varies in opposite direction with the increase of oxidant concentration. For Zn the dissolution rate decreases while for Ni increases with an increase of $CuCl_2$ concentration. This can be easily explained in view of the discussions regarding the global dissolution of the metals and the literature date [21] concerning the dezincification of Cu-Zn alloys. Considering that the dissolution of Zn involves the cementation of Cu it is clear that the number and size of the pores becomes even lower as the concentration of $CuCl_2$ is higher, reaching a minimum when the pores (access to Zn) are

completely blocked by cemented copper [21]. Therefore the dissolution of Zn in this case is limited by the mass transport in the pores due to the fact that $CuCl_2$ dissolves much slower copper from the pores walls than $FeCl_3$.

In other situations, concurrently with the dissolution process can occur the cementation of the same metal on less noble ones, due to the different standard reduction potentials of the metals. Such an example is the dissolution of silver and lead, which even if are very different in terms of chemical reactivity, their dissolution processes are similarly affected by the cementation on more reactive metals such as Ni and Zn. Therefore the accumulation rate of Ag^+ and Pb^{2+} ions in the solution is given by the difference between the rate of their dissolution and cementation.

In the case of $CuCl_2$ the leaching processes for Ag and Pb are more complicated because their cementation and dissolution is influenced by the cementation of copper as well. In contrast, when $FeCl_3$ is used, the dissolution and cementation of Ag and Pb is not affected so differently, because the reduction of Fe^{3+} those not involve the formation of a new phase. Therefore, at the same oxidant concentration the amount of Ag^+ and Pb^{2+} ions in the solution is higher for the $CuCl_2$ experiments than for the $FeCl_3$. This is also sustained by the experimental results obtained for Ag and Pb, as it is showed in Fig. 2-3.

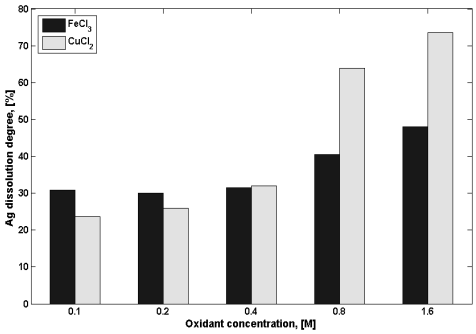

Figure 2. Individual dissolution degree of Ag in 1 M HCl using different concentrations of $FeCl_3$ and $CuCl_2$.

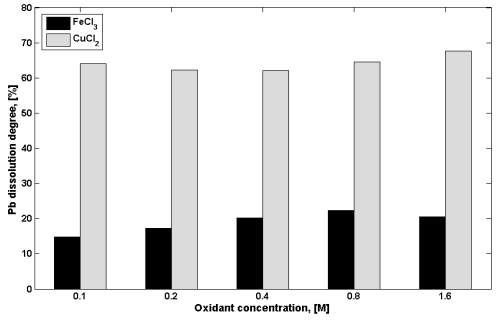

Figure 3. Individual dissolution degree of Pb in 1 M HCl using different concentrations of $FeCl_3$ and $CuCl_2$.

Also, comparing the dissolution degree for Ag and Pb it seems like the difference between the efficiency of the two oxidants is greater in the case of Pb. This is caused by the fact that silver can also react with the cemented copper while lead being a more reactive metal than copper is cementing only on Ni or Zn.

Differently from the previous metals, the reduction potential of Au^{+} and Au^{3+} in the presence of chloride ions is still higher than the ones obtained for the oxidants. As a result the chemical dissolution of gold is not possible in these experimental conditions. The presence of dissolved gold (Fig. 4) can be attributed to the formation of colloidal gold through the detachment of very small gold particles from the surface of dissolving metals. In consequence to achieve higher gold dissolution degrees it is necessary to use a more efficient ligand than chloride ions.

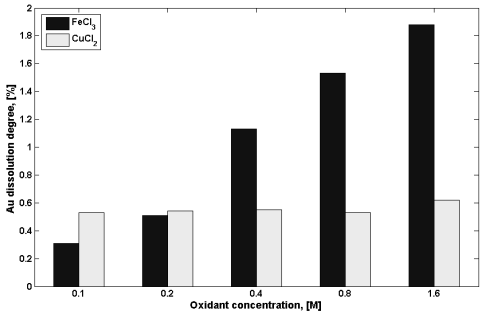

Figure 4. Individual dissolution degree of Au in 1 M HCl using different concentrations of $FeCl_3$ and $CuCl_2$.

CONCLUSIONS

The experimental results proved that the dissolution of metals from WPCBs occurs efficiently in acidic $FeCl_3$ and $CuCl_2$ solutions. However, the efficiency and selectivity of the leaching systems is very different and strongly depends on the oxidant concentration and solution speciation. The main differences between the oxidants are caused by the fact that the dissolution process with $CuCl_2$ is limited not by the redox equilibrium like for $FeCl_3$, but through the cementation of copper which blocks the surface of the metals. Nevertheless, until the metals are completely covered with copper the leaching process with $CuCl_2$ gives superior performances than the one with ferric chloride. For this reason the global metal dissolution degree is higher for copper chloride at oxidant concentrations below 0.2 M, while at higher concentrations $FeCl_3$ is more efficient, because it does not block the metals surface like cemented copper. In contrast the selectivity of the leaching systems is not modified significantly, compared to each other, with the increase of oxidant concentration. Therefore further investigations will be performed in the presence of more efficient ligands (thiourea, thiosulfate, and thiocyanate) in order to enhance the dissolution of metals and the selectivity of the process.

EXPERIMENTAL

Leaching tests were carried out using a special type of PCBs in which the support was made of a ceramic material and the conductive pathways between the electronic components consist of thin layers of Au, Ag and Pb. The solid material was characterized using XRD and EDAX.

The elemental assay of digested material in aqua regia was conducted using atomic absorption spectroscopy (Avanta PM, GBC-Australia). The mass of the WPCBs used in these experiments was 18.8 g. In order to ensure a large contact area between the reactants, they were crushed to smaller pieces (3.1-3.8 cm^2) in a preliminary mechanical step. Then Al was removed selectively from each sample by leaching the WPCBs with 50 mL solution of unstirred 2.5 M NaOH for 24 h. Next, the aluminium free samples were used to determine the extent of dissolution of overall and individual metals in different solutions. The oxidants used were hydrochloric acid and ferric (III)-chloride (Fluka) or copper (II)-chloride (Merck). All leaching experiments were conducted in 100 ml unstirred solution, at room temperature, over a period of 72 h. To prevent the precipitation of metal ions in all experimental situations the pH was kept in strong acid medium by using 1 M HCl acid (Merck). The solid:liquid ratio in the leaching experiments was 1:5. The concentration of metals in the leaching solutions and in the residue at the end of the experiments was determined by atomic adsorption spectroscopy.

The XRD analysis of the ceramic support shows that, instead of copper based boards a mixture of oxides (Al_2O_3, SiO_2) was used to manufacture the non-conductive substrate. Also the elemental composition of the ceramic substrate determined by EDAX indicates the presence of Al (51.89 %), Si (11.46 %) and O (35.69 %). The metallic composition of the WPCBs determined by atomic adsorption spectroscopy, after the pretreatment with NaOH, is shown in Table 2.

Table 2. Chemical composition (%) of the studied WPCB samples*

Ag	Au	Cu	Ni	Pb	Zn	Ceramic material
0.14	0.11	0.45	2.2	0.05	0.40	96.65

* Average data obtained from five different WPCB samples

ACKNOWLEDGEMENTS

The authors acknowledge the following project for financial support: *Investing in people!* Ph.D. scholarship, Project co-financed by the SECTORAL OPERATIONAL PROGRAM FOR HUMAN RESOURCES DEVELOPMENT 2007 – 2013. Priority Axis 1. "Education and training in support for growth and development of a knowledge based society". Key area of intervention 1.5:

Doctoral and post-doctoral programs in support of research. Contract nr.: POSDRU/88/1.5/S/60185 – “INNOVATIVE DOCTORAL STUDIES IN A KNOWLEDGE BASED SOCIETY”, Babeş-Bolyai University, Cluj-Napoca, Romania.

REFERENCES

1. I. Bereketli, M.E. Genevois, Y.E. Albayrak, M. Ozyol, *Expert Systems with Applications,* **2011**, *38*, 71.
2. H.Y. Kang, J.M. Schoenung, *Resources, Conservation and Recycling*, **2005**, *45*, 368.
3. K. Huang, J. Guo, Z. Xu, *Journal of Hazardous Materials*, **2009**, *164*, 399.
4. L. Longa, S. Sun, S. Zhong, W. Dai, J. Liu, W. Song, *Journal of Hazardous Materials*, **2010**, *177*, 626.
5. S. Ilyas, M.A. Anwar, S.B. Niazi, M.A. Ghauri, *Hydrometallurgy*, **2007**, *88*, 180.
6. W. Jiang, L. Jia, X. Zhen-Ming, *Journal of Hazardous Materials*, **2009**, *161*, 257.
7. R.V. Murugan, S. Bharat, A.P. Deshpande, S. Varughese, P. Haridoss, *Powder Technology*, **2008**, *183*, 169.
8. Y.J. Park, D.J., Fray, *Journal of Hazardous Materials*, **2009**, *164*, 1152.
9. J. Wang, J. Bai, J. Xu, B. Liang, *Journal of Hazardous Materials*, **2009**, *172*, 1100.
10. J. Cui, L. Zhang, *Journal of Hazardous Materials*, **2008**, *158*, 228.
11. G. Hilson, A.J. Monhemius, *Journal of Cleaner Production,* **2006**, *14*, 1158.
12. D. Feng, J.S.J. Van Deventer, *Hydrometallurgy*, **2011**, *106*, 38.
13. E.Y. Kim, M.S. Kim, J.C. Lee, J. Jeong, B.D. Pandey, *Hydrometallurgy*, **2011**, *107*, 124.
14. O.N. Starovoytov, N.S. Kim, K.N. Han, *Hydrometallurgy*, **2007**, *86*, 114.
15. O. Tsydenova, M. Bengtsson, *Waste Management*, **2011**, *31*, 45.
16. L. Barbieri, R. Giovanardi, I. Lancellotti, M. Michelazzi, *Environmental Chemistry Letters,* **2010**, *8*, 171.
17. B. Beverskog, *SKI Rapport 98*, Sweden, **1998**.
18. M.D. Muir, G. Senanayake, *Hydrometallurgy*, **2003**, *14*, 279.
19. G. Senanayake, D.M. Muir, *Metallurgical and Materials Transactions B*, **1988**, *19*, 37.
20. B.R. Tagirov, I.I. Diakonov, O.A. Devina, A.V. Zotov, *Chemical Geology*, **2000**, *162*, 193.
21. N.J. Welham, K.A. Malatt, S. Vukcevic, *Hydrometallurgy*, **2000**, 57, 209.
22. P.R. Roberge, *Handbook of Corrosion Engineering*, McGraw-Hill, New-York, **2000**, 451.

STUDIA UBB CHEMIA, LVII, 3, 2012 (p. 41 - 49)
(RECOMMENDED CITATION)

METALS LEACHING FROM WASTE PRINTED CIRCUIT BOARDS. PART II: INFLUENCE OF THIOUREA, THIOSULFATE AND THIOCYANATE CONCENTRATION ON THE LEACHING PROCESS

SZABOLCS FOGARASI[1], FLORICA IMRE-LUCACI[2], PETRU ILEA[1,*]

ABSTRACT. This paper presents the possibility of achieving high selectivity and efficiency at low $FeCl_3$ and $CuCl_2$ concentrations by adding small quantities of thiourea, thiosulfate and thiocyanate into the solution. The overall metal dissolution in the presence of 0.1 M thiosulfate, thiocyanate and thiourea is significantly higher (60 % compared to 32 %), than in chloride medium, for both oxidants. However, the increase of ligand concentration decreases the global metal dissolution degree, but improves the selectivity of the leaching processes. The results show that different oxidant and ligand combination promote the dissolution of one metal or another, making possible the use of these leaching systems for selective metal dissolution.

Keywords: *$FeCl_3$ and $CuCl_2$, leaching systems, thiosulfate, thiocyanate, thiourea*

INTRODUCTION

Recently, due to the stringent environmental regulations the researches focused on the development of eco-friendly and energy-saving processes for the separation of metals and alloys from hazardous and non-metallic materials [1-8]. These can be very complicated considering the complex composition of the WPCBs and the variable chemical properties of the metals. However the improvements made to hydrometallurgical methods in the past few decades, allow an efficient extraction of metals from WPCBs. The use of caustic and acidic leaching mediums along with strong oxidizing agents and different lixiviants can dissolve efficiently the metals and with high selectivity [8-13]. This is very important especially in the case of noble metals which have high chemical stability and lower concentration in WPCBs than base metals [14].

Thus, based on the available literature data, thiourea, thiosulfate and thiocyanate were identified as the most appropriate ligands for the dissolution of noble metals [15-18]. According to previous studies [17-19] the leaching of gold can occur five times faster in the presence of these ligands than in aerated

[1] *Babeş-Bolyai University, Faculty of Chemistry and Chemical Engineering, 11 Arany Janos Street, Cluj-Napoca, 400028, Romania*
[2] *Babeş-Bolyai University, Interdisciplinary Research Institute on Bio-Nano-Sciences, 42 Treboniu Laurian Street, Cluj-Napoca, 400271, Romania, * pilea@chem.ubbcluj.ro*

cyanide solution which has been banned in many countries. Moreover combining thiourea, thiosulfate and thiocyanate with more efficient oxidants like Fe^{3+} and Cu^{2+} researchers [19] obtained gold dissolution rates 25 times higher than in cyanide solution. It is also important to notice that these ligands can intensify the leaching process of base metals (Cu, Ni, Zn and Pb) too, by forming very stable complexes with some of them. However, there are possible several side reactions between these ligands and the oxidants (dissolved metals) which can hinder the leaching of metals. As a result the selectivity and efficiency of the dissolution processes will be very different from one metal to another when the oxidants ($CuCl_2$ and $FeCl_3$) are combined with thiourea, thiosulfate and thiocyanate [15-19].

The aim of this work was to study the beneficial effect of small additions of thiourea, thiosulfate and thiocyanate on the leaching of metals from WPCBs with $FeCl_3$ or $CuCl_2$. The results show the possibility of reducing the oxidant consumption and increasing the selective metal dissolution.

RESULTS AND DISCUSSION

In order to demonstrate that the addition of small quantities of ligands can enhance considerably the dissolution of metals, leaching tests were performed at different ligand concentrations (0.1-0.5 M), while the concentration of $CuCl_2$ and $FeCl_3$ was maintained constant at 0.2 M. The choice of 0.2 M oxidant concentration instead of 0.1 M was necessary in order to ensure a little higher amount of oxidant than the stoichiometrically required for the total dissolution of metals. As it can be seen, from the global dissolution degrees in Table 1, at the same oxidant concentration the dissolution of metals is faster in the presence of thiosulfate and thiocyanate and lower in the presence of thiourea.

Table 1. Global dissolution degree of metals in 1 M HCl and 0.2 M oxidant concentration using different concentrations of thiocyanate, thiosulfate and thiourea.

Ligand conc., M	$FeCl_3$			$CuCl_2$		
	NH_4SCN	$Na_2S_2O_3$	$CS(NH_2)_2$	NH_4SCN	$Na_2S_2O_3$	$CS(NH_2)_2$
	Global metal dissolution degree, %					
0		32			37	
0.1	51	60	27	49	52	39
0.2	46	38	26	46	37	35
0.3	38	32	25	45	39	35
0.4	40	25	23	42	38	35
0.5	41	24	19	41	26	22

Also, by comparing with the results presented in Part I of this series of papers, it seems that the leaching process is more efficient if rather using a high oxidant concentration we use a lower one but along with small amount of ligands.

These differences are more accentuated in the case of $CuCl_2$ because the formation of very stable Cu^+ complexes increases the dissolution rate of cemented copper, which is a crucial step in the leaching of metals with $CuCl_2$. This is also reflected by the following equilibrium constant values calculated for the dissolution of cooper, using the thermodynamic data [21, 19] for copper complexes:

$$Cu + 4S_2O_3^{2-} + CuCl^+ \leftrightarrow 2[Cu(S_2O_3)_2]^{3-} + Cl^- \qquad K_1 = 1.06 \cdot 10^{19} \qquad (1)$$

$$Cu + 4CS(NH_2)_2 + CuCl^+ \leftrightarrow 2[Cu(CS(NH_2)_2)_2]^+ + Cl^- \qquad K_2 = 1.93 \cdot 10^{18} \qquad (2)$$

Differently from the previously two ligands, in the case of thiocyanate the process is more complicated, because besides SCN^- ions the solution contains ammonium ions as well. Therefore the dissolution of copper or other metals will involve the formation of both copper-thiocyanate and copper-ammoniac complexes. Thus for copper the main reactions are the following:

$$Cu + 4SCN^- + CuCl^+ \leftrightarrow 2[Cu(SCN)_2]^- + Cl^- \qquad K_3 = 6.56 \cdot 10^{11} \qquad (3)$$

$$Cu + [Cu(NH_3)_4]^{2+} \leftrightarrow 2[Cu(NH_3)_2]^+ \qquad K_4 = 49.11 \qquad (4)$$

$$Cu + [Cu(NH_3)_4]^{2+} + 2SCN^- \leftrightarrow [Cu(NH_3)_2]^+ + [Cu(SCN)_2]^- + 2NH_{3(aq)} \qquad K_5 = 8.42 \cdot 10^8 \qquad (5)$$

$$Cu + [Cu(NH_3)_4]^{2+} + 4SCN^- \leftrightarrow 2[Cu(SCN)_2]^- + 4NH_3 \qquad K_6 = 1.44 \cdot 10^{16} \qquad (6)$$

It seems like the equilibrium constant values for copper dissolution eq. (1-3, 6) are much higher in the presence of these ligands than in chloride medium. Furthermore, it can be observed, that the equilibrium constant value for the cementation of copper, discussed in Part I of this series of papers, is smaller than for its dissolution eq. (1-2, 6). In consequence the influence of copper cementation on the dissolution process of the metals is negligible in these experimental conditions. Similarly conclusions can be found by comparing the redox potentials of Cu^{2+}/Cu^+ redox couple in chloride medium with the ones calculated in the case of thiourea, thiosulfate and thiocyanate complexes:

$$CuCl^+ + 2S_2O_3^{2-} + e^- \leftrightarrow [Cu(S_2O_3)_2]^{3-} + Cl^- \qquad E^0 = 0.879\ V \qquad (7)$$

$$CuCl^+ + 2CS(NH_2)_2 + e^- \leftrightarrow [Cu(CS(NH_2)_2)_2]^+ + Cl^- \qquad E^0 = 0.857\ V \qquad (8)$$

$$CuCl^+ + 2SCN^- + e^- \leftrightarrow [Cu(SCN)_2]^- + Cl^- \qquad E^0 = 0.666\ V \qquad (9)$$

$$[Cu(NH_3)_4]^{2+} + e^- \leftrightarrow [Cu(NH_3)_2]^+ + 2NH_{3(aq)} \qquad E^0 = 0.01\ V \qquad (10)$$

$$[Cu(NH_3)_4]^{2+} + 2SCN^- + e^- \leftrightarrow [Cu(SCN)_2]^- + 4NH_3 \qquad E^0 = 0.416\ V \qquad (11)$$

The redox potential values from eq. (7-8) confirm that the oxidizing power increases as the ratio between the stability constants of Cu^{+} and Cu^{2+} complexes is greater. Also it is remarkable that the redox potentials for Cu^{2+}/Cu^{+} eq. (7-11) not only that are higher than in chloride medium, but in the case of thiosulfate and thiourea they also exceed the ones obtained for the Fe^{3+}/Fe^{2+} redox couple as well. This can be attributed to the formation of more weakly complexes in the case of Fe^{3+}/Fe^{2+}, therefore the reduction of Fe^{3+} to Fe^{2+} occurs mainly by eq. (12) even in the presence of these ligands. Although, according to the literature [22], in parallel with eq. (5), there are also possible other reactions of which the most significant are the following:

$$[FeCl_2]^{+} + e^{-} \leftrightarrow Fe^{2+} + 2Cl^{-} \qquad E^{0} = 0.702 \ V \qquad (12)$$

$$[Fe(CS(NH_2)_2)_2]^{3+} + e^{-} \leftrightarrow Fe^{2+} + 2CS(NH_2)_2 \qquad E^{0} = 0.276 \ V \qquad (13)$$

$$[Fe(SCN)_2]^{+} + e^{-} \leftrightarrow Fe(SCN)^{+} + 2SCN^{-} \qquad E^{0} = 0.600 \ V \qquad (14)$$

Despite the lower redox potentials in the case of Fe^{3+}/Fe^{2+} (eq. 12-14), the results shown in Table 1, indicate the fact that for 0.1 M thiosulfate and thiocyanate concentration $FeCl_3$ is more efficient oxidant than $CuCl_2$, while at higher ligand concentrations $CuCl_2$ results in better performance. This can be attributed to the degradation of ligands, which becomes more pronounced with the increase of ligand concentration especially in $FeCl_3$ solutions due to the formation of more weakly Fe^{3+}/Fe^{2+} complexes. In contrast, in the case of thiourea since both oxidants form stable complexes their diffusion is affected similarly. As a result the global dissolution degree is greater when $CuCl_2$ is used, due to the higher reduction potential of the Cu^{2+}/Cu^{+} redox couple.

It is also important to note that the complexation of the oxidants and dissolved metals is strongly linked through the concentration of the ligands since they are competitive reactions. Given that initially the oxidants concentration is much higher, it is clear, that their complexation is faster and can lower the concentration of the ligands, more than the stability of the formed complexes is higher. Therefore, it is possible that the amount of free ligands, remained in the solution, is smaller than the required for the further complexation of the dissolving metals. In consequence the dissolution of the metals can be slower or in some cases quite impossible because their redox potential is more positive as the influence of metal complexation is weaker. However, for the most of the metals (ex. Zn, Ni) this competition between the two complexing processes has no influence on the dissolution degree, due to the fact, that their redox potential is sufficiently negative. On the other hand, there are particularly situations, like gold and silver, when

this influence on the dissolution process cannot be ignored. As it is showed in Table 2 the dissolution degree of gold is very different in the case of $FeCl_3$ and $CuCl_2$ with one exception, when thiosulfate was used.

Table 2. Gold dissolution degree in 1 M HCl and 0.2 M oxidant concentration using different concentrations of ligands

Ligand conc., M	$FeCl_3$			$CuCl_2$		
	NH_4SCN	$Na_2S_2O_3$	$CS(NH_2)_2$	NH_4SCN	$Na_2S_2O_3$	$CS(NH_2)_2$
	Global metal dissolution degree, %					
0.1	1.3	0.6	2	0.5	0.9	0.8
0.2	2.4	0.5	3.6	0.8	0.8	0.8
0.3	3.9	0.5	5.1	1.4	0.8	0.9
0.4	4.7	0.7	4.2	0.7	1	1.1
0.5	6.5	0.8	4.1	1.1	0.8	0.8

This differences appear due to the fact that Cu^{2+}/Cu^{+} decreases more the concentration of the ligands, since forms more stable complexes than Fe^{3+}/Fe^{2+}. In the case of thiosulfate it seems like both oxidants have the same efficiency in the dissolution of gold. This can be explained by the passivation of gold surface (similarly for other metals) due to the generation of different sulfur species in the reaction among the oxidants and thiosulfate [15-19]. The influences of similarly side reactions have also been reported for thiourea and thiocyanate [23-25]. However the degradation of these ligands is less pronounced thanks to their higher chemical stability. Moreover the presence of ammonium ions, in the experiments with thiocyanate, has a benefit effect on both ligand stabilization and metal dissolution. Therefore, in contrast with the other two ligands the global dissolution degree decreases the less with the increase of NH_4SCN concentration. Similarly, it seems like, the increase of thiocyanate concentration gives the best performances in the dissolution of gold as well.

The experimental results also highlight that the individual dissolution degree of metals differs more when the oxidants are used with these ligands instead of chloride ions. Furthermore, it seems like, these divergences become even more significant as the concentration of the ligands increases. Fig. 1-3 shows the experimental data for the dissolution of metals at the highest ligand concentration (0.5 M).

It can be observed that different oxidant and ligand combinations promote the dissolution of one or another of the metals. For example $FeCl_3$ with thiosulfate dissolves efficiently the majority of metals with the exception of Au, Ag, and Cu. Moreover the same oxidant in the presence of thiocyanate allows the separation of base metals from gold and copper. An even higher selectivity can be noticed in the case of $CS(NH_2)_2$ since $FeCl_3$ favors the dissolution of Ag while $CuCl_2$ dissolves more efficiently Zn. Therefore it can be concluded that by using the leaching systems in the most appropriate sequence, it is possible to selectively extract the metals from the WPCBs.

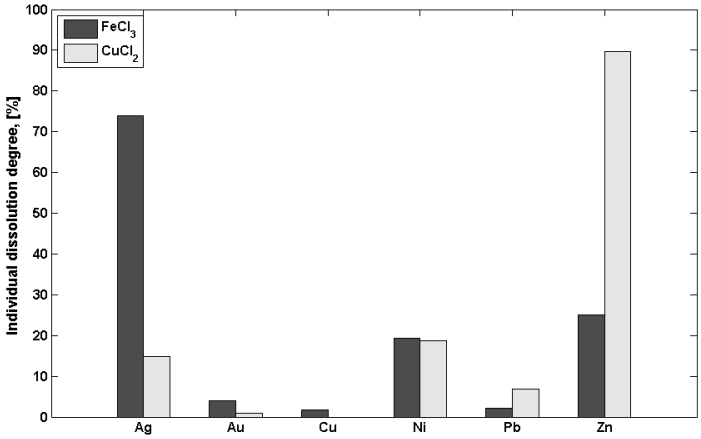

Figure 1. Individual metal disolution degree in 0.5 M $CS(NH_2)_2$ using 1 M HCl and 0.2 M oxidant concentration.

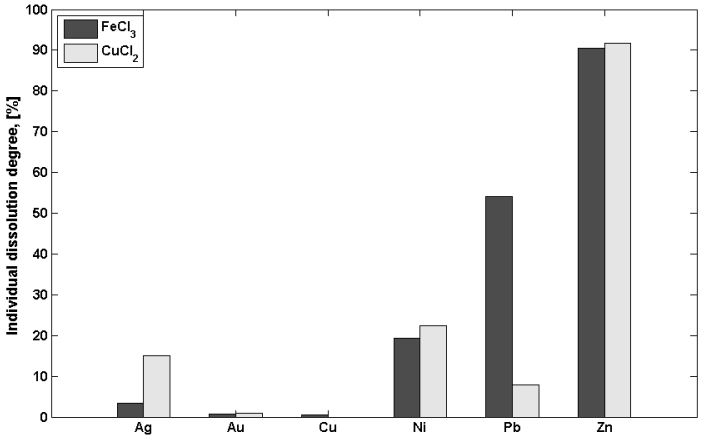

Figure 2. Individual metal dissolution degree in 0.5 M $Na_2S_2O_3$ using 1 M HCl and 0.2 M oxidant concentration.

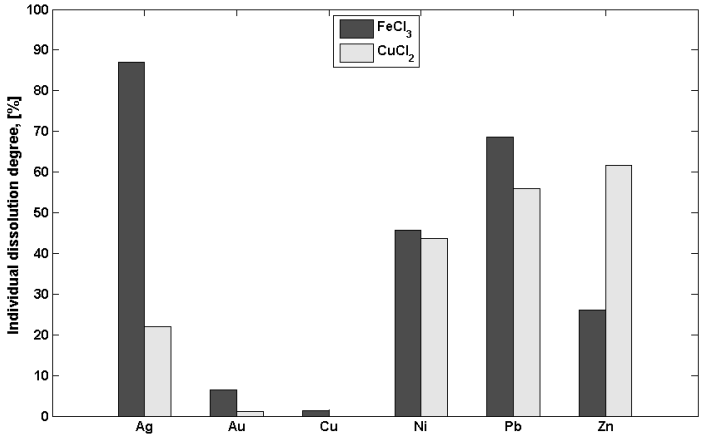

Figure 3. Individual metal dissolution degree in 0.5 M NH_4SCN using 1 M HCl and 0.2 M oxidant concentration.

CONCLUSIONS

The study presents the possibility of reducing the oxidant consumption and improving the selectivity of the process by adding small quantities of thiourea, thiosulfate and thiocyanate into the leach solution. At the same oxidant concentration the global dissolution degree is higher in the presence of these ligands than in their absence. It is also important to note that the increase of ligand concentration leads to several side reactions which decrease the global metal dissolution degree. The influence of ligand degradation is more pronounced for thiourea and thiosulfate and less for thiocyanate. The higher stability of thiocyanate is due to the presence of ammonium ions which have a catalytic effect on the process. This is the reason why the global metal dissolution degree decreases less with the increase of NH_4SCN concentration. On the other hand, it seems like high ligand concentrations are favorable for the selective leaching of metals. The experimental results show that $FeCl_3$ with thiosulfate dissolves efficiently the majority of metals with the exception of Au, Ag and Cu, while the presence of thiocyanate allows the separation of gold and copper from the rest of the metals. Similarly, in the case of thiourea, $FeCl_3$ favors the dissolution of Ag while $CuCl_2$ dissolves more efficiently Zn. From these results it can be concluded that by using the leaching systems in the most appropriate sequence, it is possible to selectively extract the metals from the WPCBs.

EXPERIMENTAL

Leaching tests were performed using the same WPCB samples characterized by XRD, EDAX spectra and metallic composition analysis in the first part of our study. Similarly to the previous studies the WPCBs were crushed to smaller pieces (3.1-3.8 cm^2) in a preliminary mechanical step followed by the selective leaching of Al in 50 mL solution of unstirred 2.5 M NaOH for 24 h. After that, the aluminium free samples were used to determine the extent of dissolution of overall and individual metals in different leaching solutions. The oxidants used were hydrochloric acid and ferric (III)-chloride (Fluka) or copper (II)-chloride (Merck) while the ligands were: thiourea (Merck), sodium thiosulfate pentahydrate and ammonium thiocyanate (Fluka). All leaching experiments were conducted in 100 ml unstirred solution, at room temperature, over a period of 72 h. The pH was kept in strong acid medium by using 1 M HCl acid (Merck). The solid liquid ratio in the leaching experiments was 1:5. The concentration of metals in the leaching solutions and in the residue at the end of the experiments was determined by atomic adsorption spectroscopy.

ACKNOWLEDGEMENTS

The authors acknowledge the following project for financial support: *Investing in people!* Ph.D. scholarship, Project co-financed by the SECTORAL OPERATIONAL PROGRAM FOR HUMAN RESOURCES DEVELOPMENT 2007 – 2013. Priority Axis 1. "Education and training in support for growth and development of a knowledge based society". Key area of intervention 1.5: Doctoral and post-doctoral programs in support of research. Contract nr.: POSDRU/ 88/1.5/S/60185 – “INNOVATIVE DOCTORAL STUDIES IN A KNOWLEDGE BASED SOCIETY”, Babeş-Bolyai University, Cluj-Napoca, Romania.

REFERENCES

1. J. Cui, L. Zhang, *Journal of Hazardous Materials*, **2008**, *158*, 228.
2. K. Huang, J. Guo, Z. Xu, *Journal of Hazardous Materials*, **2009**, *164*, 399.
3. I. Bereketli, M.E. Genevois, Y.E. Albayrak, M. Ozyol, *Expert Systems with Applications*, **2011**, *38*, 71.
4. L. Longa, S. Sun, S. Zhong, W. Dai, J. Liu, W. Song, *Journal of Hazardous Materials*, **2010**, *177*, 626.
5. I. Masavetas, A. Moutsatsou, E. Nikolaou, S. Spanou, A. Zoikis-Karathanasis, E.A. Pavlatou, N. Spyrellis, *Global NEST Journal*, **2009**, *11*, 241.

6. F. Imre-Lucaci, S.A. Dorneanu, P. Ilea, *Studia UBB Chemia,* **2009**, *LIV*, *Sp. Iss., 1*, 105.
7. Y. Zhou, K. Qiu, *Journal of Hazardous Materials***, 2010**, *175*, 823.
8. Z. Ping, F. ZeYun, L. Jie, L. Qiang, Q. GuangRen, Z. Ming, *Journal of Hazardous Materials*, **2009**, *166*, 746.
9. M.B.J.G. Freitas, V.G. Celante, M.K. Pietre, *Journal of Power Sources*, **2010**, *195*, 3309.
10. A. Janin, F. Zaviska, P. Drogui, J-F. Blais, G. Mercier, *Hydrometallurgy*, **2009**, *96*, 318.
11. A.T. Lima, A.B. Ribeiro, J.M. Rodriguez-Maroto, E.P. Mateus, A.M. Castro, L.M. Ottosen, *Journal of Applied Electrochemistry*, **2010**, *40*, 1689.
12. F. Imre-Lucaci, Sz. Fogarasi, P. Ilea, M. Tămăşan, *Environmental Engineering Management Journal*, **2012**, *accepted for publication*.
13. S. Ilyas, M.A. Anwar, S.B. Niazi, M.A. Ghauri, *Hydrometallurgy*, **2007**, *88*, 180.
14. L. Barbieri, R. Giovanardi, I. Lancellotti, M. Michelazzi, *Environmental Chemistry Letters*, **2010**, *8*, 171.
15. I. Chandra, M.I. Jeffrey, *Hydrometallurgy*, **2005**, *77*, 191.
16. D. Feng, J.S.J. Van Deventer, *Minerals Engineering*, **2010**, *23*, 399.
17. D. Feng, J.S.J. Van Deventer, *Hydrometallurgy*, **2011a**, *106*, 38.
18. D. Feng, J.S.J. Van Deventer, *Minerals Engineering*, **2011b**, *24*, 1022.
19. G. Senanayake, *Minerals Engineering*, **2004**, *17*, 785.
20. A.C. Grosse, G.W. Dicinoski, M.J. Shaw, P.R. Haddad, *Hydrometallurgy*, **2003**, *69*, 1.
21. B. Beverskog, *SKI Rapport 98*, Sweden, **1998**.
22. J. Li, J.D. Miller, *Hydrometallurgy*, **2007**, *89*, 279.
23. J. Li, M. Safarzadeh, M. Sadegh, S. Michael, J.D. Miller, K.M. LeVier, M. Dietrich, R.Y. Wan, *Hydrometallurgy*, **2011a**, doi: 10.1016/j.hydromet.2011.11.005.
24. J. Li, M. Safarzadeh, M. Sadegh, S. Michael, J.D. Miller, K.M. LeVier, M. Dietrich, R.Y. Wan, *Hydrometallurgy*, **2011b**, doi: 10.1016/j.hydromet.2011.11.009.
25. X. Yang, M.S. Moats, J.D. Miller, X. Wang, X. Shi, H. Xu, *Hydrometallurgy*, **2011**,*106*, 58.

STUDIA UBB CHEMIA, LVII, 3, 2012 (p. 51 - 58)
(RECOMMENDED CITATION)

DEPOSITION AND CHARACTERIZATION OF NANO CRYSTALLINE DIAMOND ON DIFFERENT SUBSTRATES BY PLASMA ENHANCED CVD TECHNIQUE

HASTI ATEFI[1], ZAHRA KHALAJ[1], MAHMOOD GHORANNEVISS[1,*]

ABSTRACT. In this paper, we report the results concerning characterization of the nanocrystalline diamond with different crystallite structures with the purpose of determining the parameters responsible for the texture, crystallinity, and surface morphology. Beyond the influence of the substrate on these characteristics, the role of the etching gas on diamond growth is studied. It is shown that the grain size is a strong function of the substrate's material. Crystalline grain size is estimated by broadening the X-ray diffraction peaks using the Scherer equation. Other techniques for structural and morphological characterization used in this study are Raman spectroscopy and Scanning electron microscopy and Fourier Transform Infrared spectroscopy.

Keywords: *Etching gas, Crystallinity, NCD.*

INTRODUCTION

Synthesis of Microcrystalline Diamond (MCD) films and Nanocrystalline Diamond films (NCD) by variety of Chemical Vapor Deposition (CVD) techniques, have generated a great interest. Scientists are interested on growth of NCD and MCD with carbon containing gas mixture such as CH_4/H_2, $H_2/CH_4/O_2$, $H_2/CH_4/N_2$ or other gases of different composition [1-8]. In the two last decades because of outstanding properties and useful applications of diamond films such as high thermal conductivity and low electrical conductivity or optical transparency, scientists studied about growing and using diamond coating for instruments such as cutting tools, modern biomedicine, or micro- and nano-electromechanical and optical systems [9-11]. It is believed that $C\text{-}H_x$ radicals played major roles in NCD growth the same as in MCD growth [12]. Most of the researches preparing nanocrystalline diamond thin films have been done by using plasma enhanced CVD, microwave and hot filament CVD process or pulsed laser deposition [13-20].The fundamental aspect of beneficial's Plasma Enhanced Chemical Vapor Deposition(PECVD) uses electron energy as the activation method to enable deposition to occur at low temperature and at reasonable rate [25]. Investigating the effect of substrate on crystallinity of the diamond films by DC-PECVD method is the

[1] *Plasma Physics Research Center, Science and Research Branch, Islamic Azad University, Tehran, Iran, P.O.BOX:14665-678; E-mail: Ghoranneviss@gmail.com*

purpose of this project. Using chemical or physical etching of substrate is another effective way to increase the diamond nucleation. Using hydrogen as etching gas provides suitable sites for nucleation and growth of CVD diamond. Besides, C.K. Lee et al in 2008 reported that Hydrogen plasma treatment of as-grown CVD diamond surfaces provide a smoother surface [21]. It is proved that nanocrystalline diamond thin films could be deposited on gold coated silicon as the best substrate in this study. We investigate surface morphology and the formation of diamond crystals. Scanning electron microscopy (SEM), X-ray diffraction (XRD), DEKTAK profilometer, Raman spectroscopy and Fourier transform infrared (FTIR) spectroscopy was used for analyzing the samples.

RESULTS AND DISCUSSION

The instrument used in this experiment for coating Au nanolayer was direct magnetron sputtering system. This system consists of a cylindrical glass tube with 18 cm high and 16 cm in diameter, and two parallel disks as cathode and anode in its chamber [15]. Argon was selected as a sputtering gas. A uniform magnetic field was induced for Au coating from outside. Silicon wafers were coated by gold for 8 minutes. The thickness of the gold catalyst layer for these substrates was 50 nm given by DEKTAK profilometer 3, version 2.13 that reveals in Figure 1.

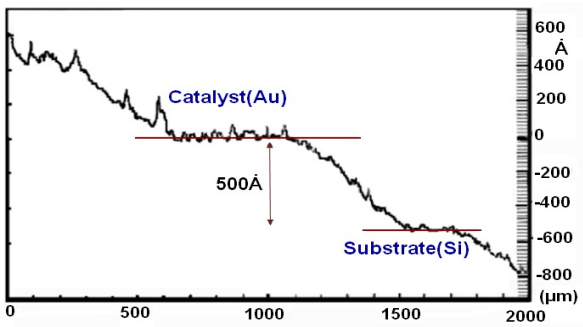

Figure 1. The thickness of gold coated silicon substrate measured by DEKTAK profilometer

The surface morphologies of the deposited films were investigated by scanning electron microscopy reveals that the morphology of nanocrystalline diamond. As shown in the Figure 2 (a-c), different nanocrystalline diamond grows in various substrates. NCD films grown on S_1 substrate can be seen in Fig. 2 (a). Because of the lower density of nano crystalline diamond and low distribution was obtained from this sample, this substrate was further declined [22]. Figure 2 (b) illustrates the NCD films grown on S_2 substrate. Finally, more concentrate NCD films are produced on the S_3 substrate (See Fig. 2 (c)).

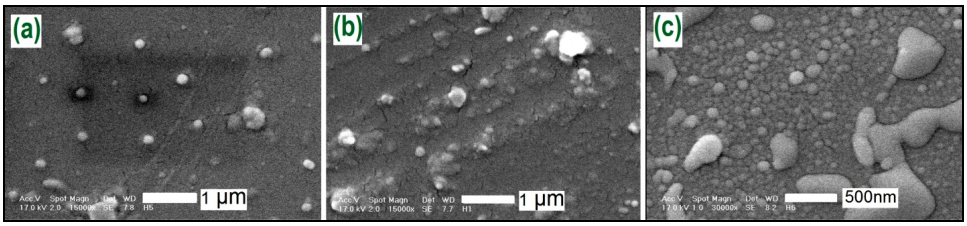

Figure 2. The surface morphology of the NCD films deposited on different substrates: (a) S_1, (b) S_2 and (c) S_3.

Diamond crystals can be investigated by means of X-ray diffraction spectroscopy, an imaging technique based on Bragg diffraction as shown in Figure 3(a–c). The crystal size varies from 14 nm to 50 nm, as deduced from the XRD spectra (Figure 3(a)).There is one peak at 2θ= 42.65º that indicates the diamond (102) on sample S_1. Oxygen in this sample reduces the diamond crystallite by increasing the sp^2 amorphous carbon phase content. According to the Scherrer formula, the grain size of the nanocrystalline diamonds, d, were calculated by $d = 0.9\lambda/\Delta(2\Theta)\cos\Theta$, where $\Delta(2\Theta)$ is the FWHM in radians and λ is the wavelength [23].

The grain size of NCD for S_1 was estimated 30 nanometers by using the Scherrer formula. Three peaks with relatively large FWHM at 42.61º and 66.50º and 90.26°are clearly observed for S_2 substrate. In addition, we note that the XRD pattern indicates the presence of diamond (102), (109), (202) crystallites structure (Figure 3(b)). For S_3, there are three main diffraction peaks at 2θ= 41.58º, 43.44º, 66.50º that give evidence for the diamond type (101), (008), (109), respectively (See Fig. 3 (c)). Using the Scherrer formula, the grain size was calculated as 30, 20 and 67 nm for sample S_3.

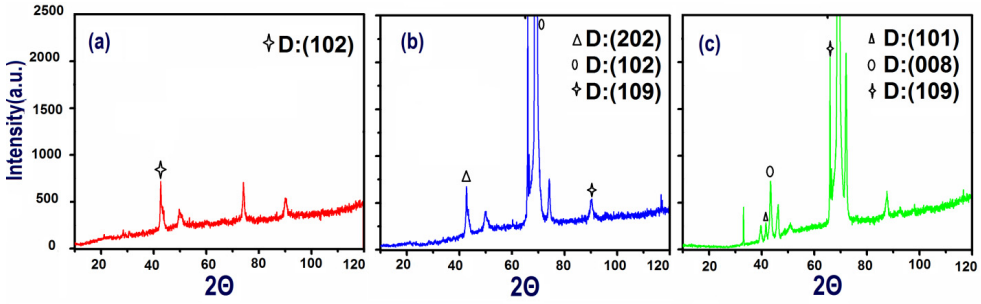

Figure 3. Representative XRD spectra of the NCD film grown on different substrates: (a) S_1, (b) S_2 and (c) S_3.

Raman scattering is one of the most important method to characterize the diamond quality which approximately 50 times more sensitive to small grain size or amorphous diamond and graphite, hence, it is frequently used to characterize CVD diamond films [25,26]. The Raman spectra of the diamond deposited films, measured by 628 nm excitation wave length of Nd: YLF laser are shown in Fig. 4. The Raman spectra of the NCD films grown on S_1 substrate display one major features at around 1150 cm^{-1}which are corresponding to diamond while a sharp peak at 1326 cm^{-1} that be observed for the NCD films deposited on S_2 substrate, both of them confirming that the major phase in the films is diamond and show variation of NCD films. Whereas, in Figure 4(c), the D peak for the grown NCD films on S_3 substrate is observed at 1332 cm^{-1}. One of the best factors for crystallite quality in Raman and XRD is Full Width Half Maximum (FWHM) of the patterns. In fact, sharp peaks with small FWHM indicate high crystal quality. The intensity of the Raman peaks increases from S_1 to S_3, however the FWHM of the peaks are reduced in this case. As can be seen verifies occurrence of the characteristic diamond and suggesting a better crystallite of sp^3 diamond phase, respectively that are finding agreeing well with literature data which is in good agreement with XRD measurement. Briefly, the Raman spectroscopy and XRD analysis reveals that the crystallites of the deposited films has changed by different substrates also indicated that a greater sp^2 bonded carbon component containing at sample S_1. Therefore, the crystallites and quality of the films increases in the following order, $S_1 < S_2 < S_3$.

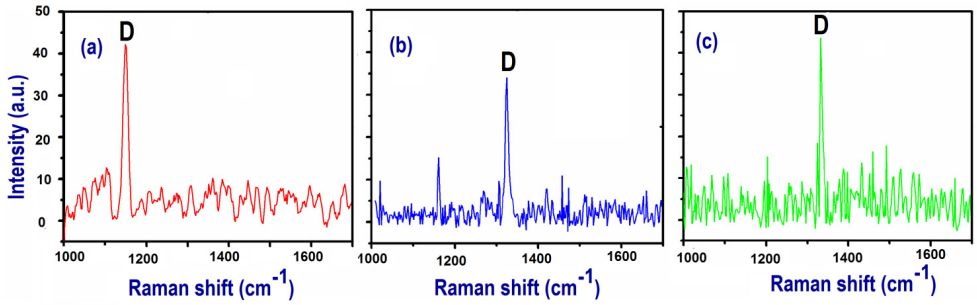

Figure 4. Raman spectrum of the deposited films on: (a) S_1, (b) S_2 and (c) S_3

Fourier Transform Infrared (FTIR) spectroscopy is a spectroscopic technique used to characterize the chemical bonds, molecular structures and C-H_n (n=1, 2, 3) bonding configurations in carbon materials. It is allowed to analyzing in more details the nature of chemical bonding in all tested carbon nanomaterials. The typical infrared spectra of the diamond films deposited on S_1, S_2 and S_3 substrates, in the range of 1000-4000 cm^{-1}, are shown in Figure 5. The peaks at 2852 cm^{-1} and 2921 cm^{-1} are related to the C–H_2 and

C–H_2 which refers to the symmetric and asymmetric stretch vibrations of C–H_2, respectively. These are reveals clearly the absorption bands of CVD diamond. For all samples there are no peaks in the region of 3000–3150 cm^{-1}, which would imply the presence of unsaturated hydrocarbons.

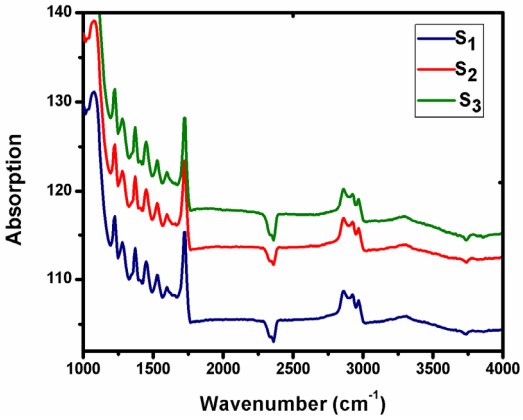

Figure 5. FTIR absorbance spectra of the diamond films grown on S_1, S_2 and S_3

CONCLUSIONS

In this paper, growth of nanocrystalline diamond films on different substrates was investigated by DC-PECVD method. Using gold coated silicon, good quality diamond nano crystals with different crystallite structures were grown on pretreated substrates. The XRD and Raman analysis patterns show that diamond nano crystals grown on Si covered Au has a higher quality due to their high intensity and small FWHM in diamond peaks. The FTIR analysis in this case shows an absorption band in CVD diamond with peaks at 2852 cm^{-1} and 2921 cm^{-1}, which are believed to be caused by symmetric and asymmetric stretch vibrations of C–H_2, vibrations. The results show that substrate pretreatments, hydrogen etching gas and coating gold nanolayer, have great influence on diamond nucleation and growth.

EXPERIMENTAL PROCEDURE FOR DEPOSITION OF DIAMOND FILMS

The NCD films have been synthesized by Plasma Enhanced Chemical Vapor Deposition (PECVD) system. The plasma glow discharge system consists of a cylindrical pyrex wall of vertical type reactor chamber having a diameter about 28 cm and length 45 cm. The substrate holder is a stainless steel plate square. A schematic of the deposition chamber is presented in Fig. 6 [26]. After getting the base pressure, a mixture of the gases inserted to the system.

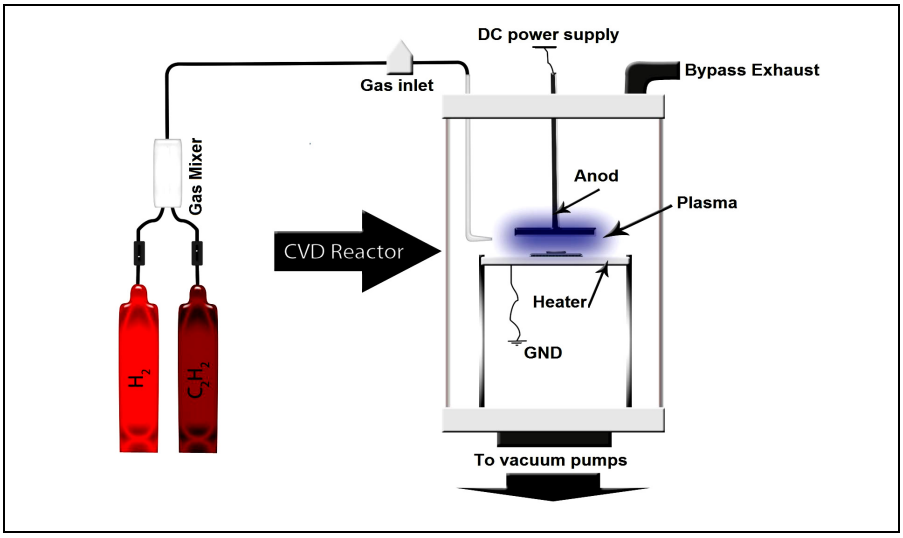

Figure 6. Schematic of the PECVD system which manufactured by our group in Plasma Physics Research Center

The inert gas and the reactive hydrocarbon precursor were premixed in a definite ratio and introduced into the deposition chamber from the top of cylinder. The plasma was produced by application of DC-supply between the substrate and the grounded wall of the deposition chamber.

EXPERIMENTAL PROCEDURE FOR DEPOSITION OF DIAMOND FILMS

The NCD films were deposited on glass, Si and Si coated with Au as catalysts layers by sputtering system which called S_1, S_2 and S_3 respectively. The silicon wafers which used in this study were P-typed with (100) orientation. The substrates were ultrasonically cleaned with acetone, ethanol and de-ionized water for 10 minutes separately before loading into the deposition chamber. The system was evacuated to the base pressure. Prior to deposition of the film, the substrate was etching treated by H_2 plasma at base pressure of 7 Torr with the flow rate about 210 Sccm for 15 minutes. The mixture of hydrogen and acetylene gas was introduced in the chamber and the pressure was adjusted to the required level. The ratio of H_2 and C_2H_2 gas was adjusted by controlling flow rate of these gases independently. DC voltage was applied to the plates after the pressure and flow rate of the gases fixed. The films were allowed to deposit for 1 hour. The substrate temperature and working pressure was kept ~280º C and 12 Torr respectively.

ACKNOWLEDGEMENT

The authors would like to thank Miss Somayeh Shams for design and fabrication of the PECVD system and also Miss Fatemeh Shahsavari for her cooperation.

REFERENCES

1. S.J. Askari, G.C. Chen, F. Akhtar, F.X. Lu, *Diamond Relat. Mater.*, **2008**, *17*, 294.
2. H. Yoshikawa, C. Morel, Y. Koga, *Diamond Relat. Mater.*, **2001**, *10*, 1588.
3. H. Zhang, J.M. Liu, F.X. Lu, *Appl. Surface Sci.*, **2007**, *253*, 3571.
4. Z.H. Shen, P. Hess, J.P. Huang, Y.C. Lin, K.H. Chen, *Ultrasonics*, **2006**, *44*, 1229.
5. Ying-Chieh Chen, Don-Ching Lee, Chao-Yang Hsiao, Yu-Fen Chung, Huang-Chin Chen, J.P. Thomas, Way-Faung Pong, Nyan-Hwa Tai, I-Nan Lin, Ing-Ming Chiu, *Biomater.*, **2009**, *30*, 3428.
6. K. Uppireddi, B.R. Weiner, G. Morell, *Diamond Relat. Mater.*, **2008**, *17*, 55.
7. F.R. Kloss, L.A. Francis, H. Sternschulte, F. Klauser, R. Gassner, M. Rasse, E. Bertel, T. Lechleitner, D. Steinmüller-Nethl, *Diamond Relat. Mater.*, **2008**, *17*, 1089.
8. Y. Hayashi, T. Soga, *Tribology Int.*, **2004**, *37*, 965.
9. X.M. Meng, W.Z. Tang, L.F. Hei, C.M. Li, S.J. Askari, G.C. Chen, F.X. Lu, *Int. J. Refract. Metals Hard Mater.*, **2008**, *26*, 485.
10. C.J. Tang, S.M.S. Pereira, A.J.S. Fernandes, A.J. Neves, J. Grácio, I.K. Bdikin, M.R. Soares, L.S. Fu, L.P.Gu, A.L. Kholkin, M.C. Carmo, *J. Crystal Growth*, **2009**, *311*, 2258.
11. Z.Z. Liang, H. Kanda, X. Jia, H.A. Ma, P.W. Zhu, Qing-Feng Guan, C.Y. Zang, *Carbon*, **2006**, *44*, 913.
12. H. Zhou, J. Watanabe, M. Miyake, A. Ogino, M. Nagatsu, R. Zhan, *Diamond Relat. Mater.,* **2007**, *16*, 675.
13. Z.Y. Chen, J.P. Zhao, T. Yano, T. Ooie, M. Yoneda, J. Sakakibara, *J. Crystal Growth,* **2001**, *226*, 62.
14. Sobia Allah Rakha, Guojun Yu, Jianqing Cao, Suixia He, Xingtai Zhou, *Diamond Relat. Mater.*, **2010**, *19*, 284.
15. Z. Khalaj, M. Ghoranneviss, S. Nasirilaheghi, Z. Ghoranneviss, R. Hatakeyama, *Chin. J. Chem. Phys*, **2010**, *23*, 689-692.
16. Z.Khalaj, S.Z.Taheri, S.N. Laheghi, P.A. Eslami, *IPJ*, **2009**, *3*, 19.
17. Sung-Pill Hong, H. Yoshikawa, K. Wazumi, Y. Koga, *Diamond Relat. Mater.*, **2002**, *11*, 877.

18. A. Stacey, I. Aharonovich, S. Prawer, J.E. Butler, *Diamond Relat. Mater.*, **2009**, *18*, 51.
19. T. Wang, H.W. Xin, Z.M. Zhang, Y.B. Dai, H.S. Shen, *Diamond Relat. Mater.*, **2004**, *13*, 6.
20. O.J.L. Fox, J. Ma, P.W. May, M.N.R. Ashfold, Yu.A. Mankelevich, *Diamond Relat. Mater.*, **2009**, *18*, 750.
21. C.K. Lee*, Appl. Surface Sci.*, **2008**, *254*, 4111.
22. J.H. Kim, S.K. Lee, O.M. Kwon, S.I. Hong, D.S. Lim, *Diamond Relat. Mater.*, **2009**,*18*, 1218.
23. A. Amorim, P.A.P. Nascente, V.J. Trava-Airoldi, E.J. Corat, A.R. Alves, J.R. Moro, *Vacum*, **2009**, *83*, 1054.
24. R. Haubner, B. Lux, *Int. J. Refract. Metals Hard Mater.*, **2002**, *20*, 93.
25. K.L.Choy, *Progress in Material Sience*, **2003**, *48*, 57.
26. Zahra Khalaj, Mahmood Ghoranneviss, Elnaz Vaghri, Amir Saghaleini and Mircea V. Diudea, *Acta Chim. Slov.*, **2012**, *59*, 338-343.

STUDIA UBB CHEMIA, LVII, 3, 2012 (p. 59 - 63)
(RECOMMENDED CITATION)

REVISED SZEGED INDEX OF $TC_4C_8(R)$ NANOTORUS

Z. MEHRANIAN[1], A.R. ASHRAFI[1], P.V. KHADIKAR[2], S. AZIZ[3], S. PANDIT[4], H. ACHRYA[4], B. SHAIK[4]

ABSTRACT. The revised Szeged index is a recently introduced topological index. In this paper, the revised Szeged index of $TC_4C_8(R)$ nanotorus is computed.

Keywords: *Rhombic $TC_4C_8(R)$ nanotorus, revised Szeged index.*

INTRODUCTION

A molecular graph is a simple graph such that its vertices correspond to the atoms and the edges to the bonds. A topological index is a number invariant under automorphisms of the considered graph.

It is easy to see that the vertex set V(G) equipped with the distance function d_G is a metric space and so the topological indices related to d_G carry important structural information on the molecule under consideration. The Szeged index is one of these topological indices and it was introduced by Ivan Gutman [1]. It is defined as

$$Sz(G) = \sum_{e=uv} n_u(e) n_v(e),$$

where $n_u(e)$ is the number vertices closer to u than v and $n_v(e)$ is defined analogously.

Milan Randić [2] presented a modification of this topological index to find better applications in chemistry. Later this modification was named the revised Szeged index. It is defined as

$$Sz^*(G) = \sum_{e=uv} \left[n_u(e) + \frac{n_0(e)}{2} \right] \times \left[n_v(e) + \frac{n_0(e)}{2} \right],$$

where $n_0(e)$ denotes the number of vertices equidistant from u and v. We refer the reader to [3] for mathematical notations used in this paper. The aim of this paper is to compute the revised Szeged index of a rhombic nanotorus

[1] *Department of Nanocomputing, Institute of Nanoscience and Nanotechnology, University of Kashan, Kashan 87317 – 51167, I. R. Iran*
[2] *Research Division, Laxmi Fumigation & Pest Control, PVT Ltd., 3 Khatipura, Indore 452007 India*
[3] *Department of Applied Sciences (Mathematics), Institute of Engineering and Technology, Devi Ahilya Vishwavidyalaya, Indore, Khandwa Road, Indore, India*
[4] *Department of Computer Engineering, Swami Vivekanand Collge of Engineering, Indore, India*

R[p,q] depicted in Figure 1. To do this, we first draw the molecular graph of nanotorus by HyperChem [3]. The same can be done by CVNET, by Diudea et al. [4,5]. Then we apply this HIN file to compute adjacency and distance matrix of the given nanotorus by TopoCluj software [6]. Finally, we prepare some programs by the computer algebra system GAP [7] to compute the revised Szeged index of some nanotori. This allowed to find some conjectures on our problem. Our final task is to prove these conjectures and compute the desired topological index.

Figure 1. 3D view of $TC_4C_8(R)[p,q]$

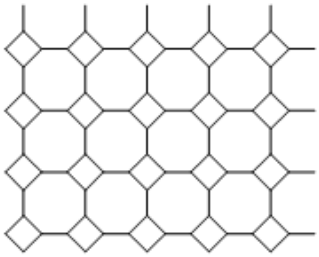

Figure 2. 2D view of R[5,4]

Our notations are taken from a recently published book of Diudea and Nagy [8]. A graph G is called bipartite if its vertex set can be partitioned into subsets A and B in such a way that each edge of G connects a vertex of A to a vertex of B. We encourage to the interested reader to see [9,10] for some applications in physics and chemistry. The aim of this paper is to compute the revised Szeged index of an arbitrary $TC_4C_8(R)[p,q]$ nanotorus, where p is the number of rhombs in each row and q is the number of rhombs in each column. The main result of this paper is the following theorem:

THEOREM: The revised Szeged index of $TC_4C_8(R) = TC_4C_8(R)[p,q]$, p is odd, is computed as follows

$$Sz^*(TC_4C_8(R)) = \begin{cases} 24p^3q^3 & q \ is \ odd \\ 24p^3q^3 - pq^3 & 2 \mid q \ \& \ q < p \\ 24p^3q^3 - p^3q & 2 \mid q \ \& \ q > p \end{cases}$$

RESULTS AND DISCUSSION

The unit rhombic cell U of the rhomb-octagonal lattice R has been chosen having the four vertices represented in Figure 2. This selection allows the generation of the complete 2–dimensional infinite lattice by pure translational operation along both lattice directions. We denote the obtained lattice by $TUC_4C_8(R)$ and in closed form by $TC_4C_8(R)$.

The aim of this section is to compute the revised Szeged index of an arbitrary $TC_4C_8(R)[p,q]$ nanotorus, when p is odd. To do this we first notice that the Szeged and revised Szeged indices of bipartite graphs are the same. In [11] the Szeged index of $TC_4C_8(R)$ nanotorus was computed in general. In fact, it is proved that the Szeged index of $TC_4C_8(R)$ is equal to $24p^3q^3$. Here we consider the cases that one of p and q are odd. Without loss of generality, we assume that p is odd.

From Figure 2, we can see that it is possible to partition the set of edges into three subsets A, B and C such that A is the set of all horizontal edges, Figure 3(a), B is the set of all vertical edges, Figure 3(b), and C is the set of all edges of rhombs of $TC_4C_8(R)$, Figure 3(c).

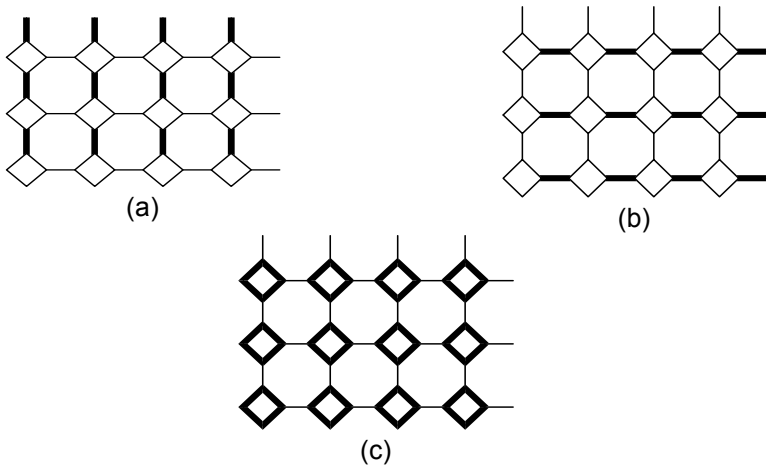

Figure 3. Three Types of Edges in $TC_4C_8(R)$.

For a given q we consider two cases that $p < q$ or $p \geq q$. If q is even then the quantities $n_u(e)$, $n_v(e)$ and $n_0(e)$ for each horizontal, vertical and rhombic edges of $TC_4C_8(R)$ are computed in Table 1. We notice that from the symmetry of $TC_4C_8(R)$ nanotorus these quantities are the same on each element of A. The same is correct for B and C. When q is odd, then it is possible to find an automorphism f of $TC_4C_8(R)$ such that f maps a vertical edge to a rhombic one. This shows that in this case the quantities n_u, n_v and n_0 for vertical and rhombic edges are the same. In Table 1, these quantities are recorded.

Table 1. The number of vertices closer to u than to v, the number of vertices closer to v than to u and equidistant vertices in $TC_4C_8(R)[p,q]$.

The number of vertices closer to u than to v, The number of vertices closer to v than to u and Equidistant vertices	***No of Vertices***	***p,q***
$\begin{cases} 2pq, 2pq, 0 \\ 2pq-2q+p, 2pq-2q+p, 4q-2p \\ 2pq, 2pq-p, p \end{cases}$	$\begin{cases} pq \\ pq \\ 4pq \end{cases}$	*p<q, 2|q*
$\begin{cases} 2pq, 2pq, 0 \\ 2pq-q, 2pq-q, 2q \\ 2pq, 2pq-q, q \end{cases}$	$\begin{cases} pq \\ pq \\ 4pq \end{cases}$	*p≥q, 2|q*
$\begin{cases} 2pq-2p+q, 2pq-2p+q, 4p-2q \\ 2pq-q, 2pq-q, 2q \end{cases}$	$\begin{cases} pq \\ 5pq \end{cases}$	*p ≥q, 2łq*
$\begin{cases} 2pq-2q+p, 2pq-2q+p, 4q-2p \\ 2pq-p, 2pq-p, 2p \end{cases}$	$\begin{cases} pq \\ 5pq \end{cases}$	*p<q, 2łq*

Also, some values of revised Szeged indices of this nanotorus are computed in Table 2.

Table 2. The revised Szeged indices of $TC_4C_8(R)$ nanotorus for some values of p and q.

p	**q**	**$Sz^*(TC_4C_8(R))$**
3	5	81000
5	4	191680
5	6	647250
5	2	23960

ACKNOLEDGEMENT. The research of the second author (ARA) is partially supported by the University of Kashan under grant no 159020/14.

REFERENCES

1. I. Gutman, *Graph Theory Notes New York*, **1994**, *27***,** 9.
2. M. Randić, *Acta Chim. Slov*., **2002**, *49*, 483.
3. HyperChem package Release 7.5 for Windows, Hypercube Inc., 1115 NW 4th Street, Gainesville, Florida 32601, USA, **2002**.
4. M. Stefu, M.V. Diudea, CVNET software, "Babes-Bolyai" University, Cluj, 2005.
5. Cs. L. Nagy, M.V. Diudea, Nano Studio software "Babes-Bolyai" University, Cluj, 2009.
6. M. V. Diudea, O. Ursu, GsL. Nagy, TOPOCLUJ, Babes-Bolyai University, Cluj, 2002.
7. The GAP Team, GAP, Groups, Algorithms and Programming, Lehrstuhl De fur Mathematik, RWTH, Aachen. **1992**.
8. M. V. Diudea, Cs. L. Nagy, "Periodic Nanostructures", Springer, Dordrecht, **2007**.
9. T. Doslic, A. Graovac, D. Vukicevic, F. Cataldo, O. Ori, A. Iranmanesh, A.R. Ashrafi, F. Koorepazan–Moftakhar, *Iranian J. Math. Chem*., **2010**, *1* 73.
10. A.R. Ashrafi, M Jalali, M Ghorbani, MV Diudea, *MATCH Commun. Math. Comput. Chem*., **2008**, *60* (3), 905.
11. A.R. Ashrafi, S. Yousefi, *Dig. J. Nanomat. Bios*. **2009**, *4*(3), 407.

STUDIA UBB CHEMIA, LVII, 3, 2012 (p. 65 – 72)
(RECOMMENDED CITATION)

DETECTION OF Cu(II) USING ITS REACTION WITH INDIGO CARMINE AND DIFFERENTIAL PULSE VOLTAMMETRY

MARIAME COULIBALY[1], LIANA MARIA MURESAN[2,*], IONEL CĂTĂLIN POPESCU[2]

ABSTRACT. An electrochemical method for Cu(II) determination based on its reaction with indigo carmine (IC) in alkaline medium and differential pulse voltammetry performed at graphite electrode, was elaborated. The experimental parameters affecting the Cu(II) - IC complex formation (reaction time and pH) were optimized. The linear range of the calibration curve, obtaining by representing the IC oxidation current (E_{appl} = 0.175 V *vs.* Ag/AgCl,KCl_{sat}) as function of the Cu(II) concentration (pH 10), was from 10 µM up to 70 µM Cu (II) and the detection limit was 4.74 µM.

Keywords: *Cu(II), indigo carmine, differential pulse voltammetry.*

INTRODUCTION

Copper is an essential trace element in biological systems [1]. Acute copper poisoning occurs when copper salts are ingested. The maximum tolerable daily intake for copper is 0.5 mg Cu / kg body weight [2]. Wilson's disease is a prototypical disease caused by copper toxicosis, affecting first the liver and later the central nervous system, kidneys and eyes. Consequently, monitoring trace of copper in natural environment, biological and other real samples is very important. For this reason, a sufficiently selective and sensitive method for reliable determination of copper would be of great interest.

Among the electrochemical techniques used for the trace analysis of metal ions, differential pulse voltammetry (DPV) is of great interest because of its low cost, easy operation, good sensitivity, high selectivity and accuracy [3].

Indigo carmine is a water soluble aromatic heterocyclic compound, used as redox indicator [4] and as a dye in food and cosmetic industries [5]. The reaction between copper and IC has been used for spectrophotometric determination of Cu(II) in pharmaceutical compounds [6].

[1] *Ecole Normale Supérieure, Laboratoire des Sciences Physiques Fondamentales et Appliquées, 08 BP 10 Abidjan, Côte d'Ivoire*
[2] *Babeş-Bolyai University, Faculty of Chemistry and Chemical Engineering, Department of Physical Chemistry, 11, Arany Janos St., RO-400028 Cluj-Napoca, Romania*
[*] *Corresponding author: limur@chem.ubbcluj.ro*

In this work, an electrochemical method for copper determination, based on Cu(II) reaction with IC [6] and using DPV measurements performed at graphite electrode, was proposed. The experimental parameters affecting the Cu(II) - IC complex formation (reaction time and pH) were optimized. Due to the electro-inactivity of Cu(II) - IC complex, the decrease of the IC oxidation current measured in alkaline medium (pH 10) at an applied potential of ~150 mV *vs*. Ag/AgCl,KCl_{sat}, was used to draw a calibration curve allowing the determination of Cu(II) concentrations.

RESULTS AND DISCUSSION

Electrochemical behavior of indigo carmine

Indigo carmine is an aromatic compound which, similarly to indigo, can be involved in a two steps redox reaction (see Scheme 1) [7-9]:

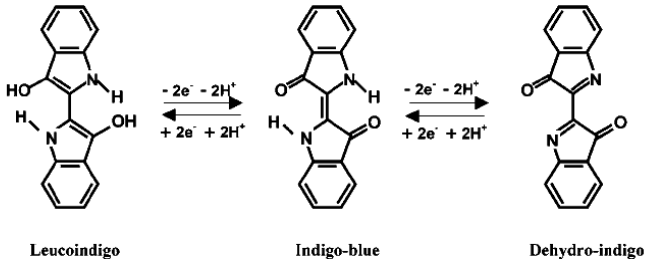

Scheme 1. Redox reactions involving indigo moiety [8]

As can be seen from Figure 1 and Table 1, the IC voltammetric response shows two well separated peak pairs, in good agreement with the literature data [7, 8, 10]. Taking into account that in alkaline media the A2/C2 peaks pair is better shaped than A1/C1, all further studies were carried out on A2/C2.

Table 1. Electrochemical parameters of the IC voltammetric response recorded at graphite electrode (scan rate 250 mV/s, pH 7).

Peaks pair	$*E^{0'}$ V *vs.* Ag/AgCl,KCl_{sat}	ΔE_p (mV)
A1/C1	-0.062	213
A2/C2	0.717	183

$*E^{0'} = (E_{pa} + E_{pc})/2$

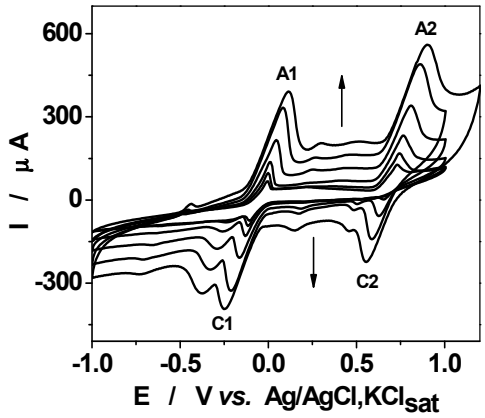

Figure 1. Cyclic voltammograms recorded at graphite electrode for 10^{-3} M IC. Experimental conditions: supporting electrolyte 0.1 M phosphate buffer (pH 7); start potential, -1.0 V *vs.* Ag/AgCl,KCl$_{sat}$; scan rates: 25, 50, 100, 250, 500 and 750 mV/s.

The log-log dependence of the peaks intensities corresponding to the A2/C2 redox couple on the scan rate (Figure 2) revealed that indigo carmine molecules (Scheme 1) are stronger adsorbed on graphite than dehydro-indigo carmine ones. Thus, the slope of this dependence observed for the A2 peak was 0.90 ± 0.02 (R^2 = 0.9939 for N = 10), being close to the theoretical value (1) expected for a surface-confined redox couple. At the same time, the corresponding slope for the C2 peak was 0.74 ± 0.02 (R^2 = 0.9903 for N = 10). This peculiar behavior could be explained by the differences existing between the configurations of IC and dehydro-indigo carmine molecules.

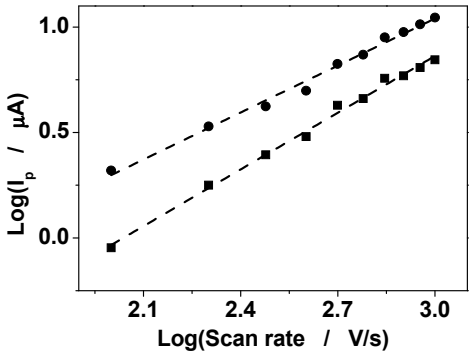

Figure 2. Log(I_p) *vs*. log(scan rate) dependence for A2/C2 peak pair. Experimental conditions: supporting electrolyte 0.1 M phosphate buffer (pH 10); (●) reduction and (■) oxidation.

PH influence on the IC redox response

Differential pulse voltammetry (DPV) measurements were carried out to investigate the pH effect on the redox couple A2/C2 from Figure 1. As expected for a redox process involving protons and electrons (Scheme 1), the pH increase induces a negative shift of the oxidation peak potential of IC, simultaneously with a monotone decrease of the peak currents (Figure 3).

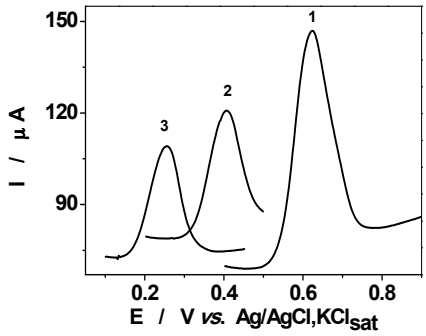

Figure 3. DPV response of IC recorded at graphite electrode. Experimental conditions: scan rate, 0.03 $V.s^{-1}$; pulse amplitude, 100 mV; supporting electrolytes, (1) acetate buffer (pH 2.5); (2) and (3) phosphate buffer pH 6 and pH 8.5, respectively; IC concentration, 10 $\mu mol.L^{-1}$.

Using DPV data for A2/C2 couple, a linear correlation between the anodic peak potential (E_{pa}), and the pH was found (Figure 4). This is described by the equation E_{pa} = 0.750 - 0.061*pH (R^2 =0.9933), which points out to an equal number of protons and electrons participating to this process and confirms once again the Scheme 1 regarding the redox reaction involving IC and dehydro-indigo.

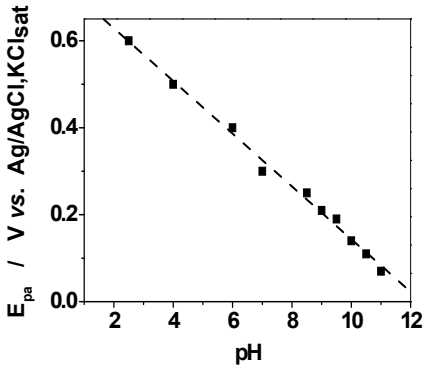

Figure 4. Anodic peak potential (E_{pa}) *vs*. pH dependence for A2/C2 couple.

DPV detection of Cu(II)

When Cu(II) ions are added to an alkaline solution of IC, the Cu_2IC complex is formed [6]. Because at the working potential this complex is electro-inactive, a decrease of the oxidation peak current will appear for A2/C2 redox couple. Moreover, as can be seen from Figure 5, the peak current decrease is depending on Cu(II) concentration in the μM range.

The main parameters influencing the Cu_2IC complex formation (reaction time and pH) were investigated. The influence of the solution pH on the Cu_2IC complex formation was investigated by measuring of the decrease of oxidation peak current (I_{pa}) of A2/C2 redox couple induced by Cu(II) addition at different pH values (results not shown). The maximum decrease of I_{pa} was observed at pH 11 (76%), but pH 10 was chosen as working pH, considering that: (i) at this pH the I_{pa} decrease was still significant (63%) and (ii) at pH 10 the buffering capacity of the carbonate solution is maximum. These results are in agreement with those reported for Cu(II) spectrophotometric determination [6].

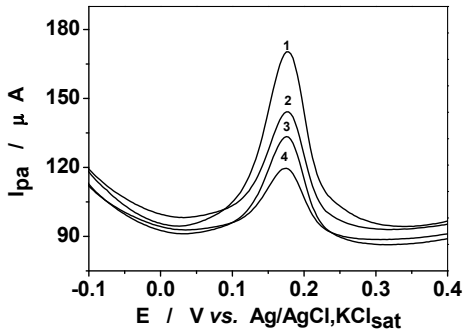

Figure 5. Typical DPV response obtained before (1) and after the addition of different Cu(II) ions concentrations in a solution containing 100 μmol.L^{-1} IC: (2) 40 μmol.L^{-1} Cu(II); (3) 80 μmol.L^{-1} Cu(II); (4) 100 μmol.L^{-1} Cu(II). Experimental conditions: supporting electrolyte, 0.1 M carbonate buffer (pH 10); scan rate 0.03 V/s; pulse amplitude, 100 mV.

Furthermore, in order to estimate the time required for the complex formation, Cu(II) ions were incubated with IC in alkaline medium (pH 10) for various periods of time (5 -120 min). The time evolution of the anodic peak current of A2/C2 redox couple is depicted in figure 6.

Using the data from Figure 6, first-order kinetics [k = (0.0081 ± 0.0006) min^{-1}] for the free IC concentration decrease due to the complex formation was found (R^2 = 0.9471; N = 11). Taking into account the time dependence of the Cu_2IC complex formation, all further measurements

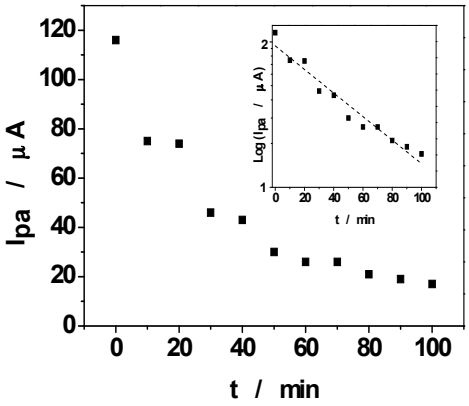

Figure 6. Time evolution of Cu_2IC complex formation. Inset illustrates the first-order kinetic linearization of the free IC concentration decrease. Experimental conditions: IC 10^{-3} mol.L^{-1}; 10^{-3} mol.L^{-1} Cu(II); other conditions as in figure 5.

were performed after a delay of 30 minutes, which was 50% higher than the value recommended by Zanoni *et al* [6] for Cu(II) detection from spectrophotometric measurements.

Under the optimal experimental conditions, the decrease of the oxidation peak current for A2/C2 redox couple due to Cu(II) addition into the alkaline (pH 10) IC solution and as a function of the copper ions concentration is depicted in Figure 7. The linear domain, from 10 up to 70 μM Cu(II), corresponds to the following regression equation: ΔI_{pa} = (1.63 ± 0.99)+ (0, 55 ± 0.03)*[Cu(II)]; R^2 = 0.9853, N = 7. The detection limit (DL) was estimated at 4.7 μM for a signal-to-noise ratio of 3.

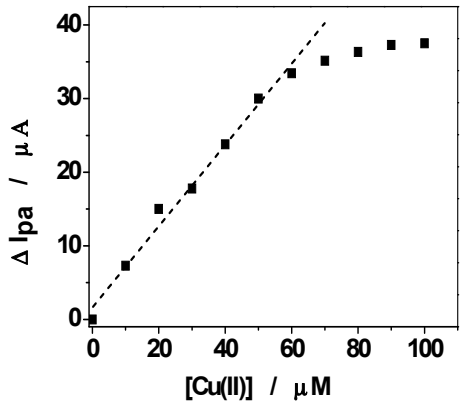

Figure 7. Calibration plot for Cu(II) DPV detection. Experimental conditions: 100 μM IC; electrolyte, 0.1M carbonate buffer (pH 10); reaction time, 30 min.

Conclusions

DPV measurements performed at graphite electrode were successfully used for copper determination, exploiting the Cu(II) reaction with IC in alkaline medium (pH 10). Due to the electro-inactivity of Cu(II) - IC complex, the decrease of the IC oxidation current, measured at an applied potential of ~150 mV *vs*. Ag/AgCl,KCl_{sat}, was used to draw a calibration curve allowing the determination of Cu(II) concentrations.

EXPERIMENTAL SECTION

Reagents

Indigo carmine (3,3 dioxo-2, 2 bis–indolyden-5,5-disulfonic acid disodium salt) was purchased from Sigma Aldrich (St. Louis, MO, USA). A 1 mM Cu (II) stock solution was prepared from $CuSO_4 \cdot 5H_2O$ (Microchim - Romania). All used chemicals were of analytical grade. Aqueous solutions were prepared with distilled water. All experiments were carried out at room temperature.

Electrochemical measurements

Cyclic and differential pulse voltammetric measurements were performed using a computer-controlled potentiostat (Autolab PGSTAT 10, Ecochemie, Utrecht, The Netherlands) and GPES 4.8 software. A conventional three electrodes cell (30 mL) consisting of a graphite electrode as working electrode, a Ag/AgCl,KCl_{sat} as reference electrode and a Pt wire as counter electrode, was used. Before using, the graphite electrode was cleaned by wet polishing with emery paper and filter paper, followed by 2 minutes ultrasonication, in an ultrasonic bath (Elma S10, Elmasonic, Germany). The solutions pH was measured using a digital pH meter (Hanna Instruments, USA). Each individual experiment was performed at least three times and the results were averaged.

ACKNOWLEDGMENTS

M.C. thanks to Agence Universitaire de la Francophonie and Romanian Government for Eugen Ionescu fellowship.

REFERENCES

[1]. G. Barceloux, *Clinical Toxicology*, **1999**, *37*, 217.

[2]. WHO Technical Report Series. *Evaluation of certain food additives and contaminants*, WHO, Geneva, **1982**, 683.

[3]. P.J.S. Barbeira, L.H. Mazo, N.R. Stradiotto, *Analyst*, **1995**, *120*, 1647.

[4]. E.H. Rodd, *Chemistry of carbon compounds*, 4th edition, Elsevier, Amsterdam, IVB, **1960**, 1093.

[5]. J.J. Berzas, J.R. Flores, M.J.V. Llerena, N.R. Farinas, *Anal. Chim. Acta,* **1999**, *391*, 353.

[6]. T.B. Zanoni, A.A. Cardoso, M.V.B. Zanoni, A.A.P. Ferreira, *Brazilian Journal of Pharmaceutical Sciences*, **2010**, *46*, 723.

[7]. M.D. González, C.F. Sánchez, A.C. García, *Electroanalysis,* **2002**, *14*, 665.

[8]. J.B. He, G. Ma, J.C. Chen, Y. Yao, Y. Wang, *Electrochimica Acta*, **2010**, *55*, 4845.

[9]. C.F. Sanchez, A.C. Garcia, *Electrochemistry Communications*, **2000**, *2*, 776.

[10]. P.F. Bolado, D.H. Santos, P.J.L. Ardisana, A.M. Pernia, A.C. Garcia, *Electrochimica Acta*, **2008**, *53*, 3635.

STUDIA UBB CHEMIA, LVII, 3, 2012 (p. 73 – 80)
(RECOMMENDED CITATION)

INFLUENCE OF TUBULAR TiO_2-ZrO_2 CERAMIC SUPPORT ON THE MORPHO-STRUCTURAL PROPERTIES OF THE UNDOPED AND Cu DOPED CARBON XEROGELS

LIVIU COSMIN COTET[1, *], CARMEN IOANA FORT[1], VIRGINIA DANCIU[1]

ABSTRACT. Undoped and Cu doped carbon xerogels with desired monolithic geometry were synthesized by sol-gel method followed by an ambient drying and a pyrolytic step. Resorcinol and potassium salt of 2,4-dihydroxybenzoic acid were used as precursors in polycondensation with formaldehyde to obtain undoped and Cu doped carbon xerogels, respectively. As reaction catalysts Na_2CO_3 and K_2CO_3, respectively were used. In order to enhance the strength of prepared materials, undoped and Cu doped carbon xerogels were synthesized into porous tubular TiO_2-ZrO_2 walls. The prepared samples were investigated by nitrogen adsorption, SEM, AFM and X-ray diffraction. Micro- and mesoporous carbon structures formed by interconnected carbon nanoparticles were obtained. In the case of Cu doped samples, homogeneous Cu nanoparticles dispersion into carbon xerogel matrix was observed. By synthesis of undoped and Cu doped carbon aerogels into ceramic wall, a decrease from macro- to micropores was observed.

Keywords: *sol-gel process, carbon xerogel, composite.*

INTRODUCTION

In the last decades, the technological development was based more and more on production and using of nanomaterial and nanocomposite with certain properties. In this context, various types of carbon materials are recognized as important materials in the field of catalysis [1,2], electrochemistry [3,4], adsorption [3,5], molecular sieve construction [6], etc.

Carbon xerogels (CX) are materials prepared by sol-gel process which present a high interest in material science [7-9]. Generally, the sol-gel synthesis of this material is based on the polycondensation of resorcinol with formaldehyde using Na_2CO_3 as catalyst [10]. Drying in ambient conditions of resulted RF gels followed by a pyrolysis treatment leads to carbon xerogels. Particular case of this material is metal doped carbon xerogel (Metal-CX)

[1] *Universitatea Babeş-Bolyai, Facultatea de Chimie şi Inginerie Chimică, Str. Kogălniceanu, Nr. 1, RO-400084 Cluj-Napoca, Romania*
[*] ccosmin@chem.ubbcluj.ro

obtained by using the potassium salt of 2,4-dihydroxybenzoic acid as precursor, K_2CO_3 as catalyst and a metal salt aqueous solution as doping solution [11]. The useful characteristic of this synthesis way is morpho-structural controllability of material properties by changing of polycondensation parameters, mainly by ratios between precursors and catalyst or solvent [10-12]. The drying performed in ambient conditions is more economical advantageous than that performed in the supercritical conditions, which are used for aerogel synthesis.

In the case of applications for fluid separation/purification it was observed that is important to have strong molecular sieve membranes with exact geometric size and porosity [6]. Also, Cu based materials are known as catalyst for various chemical reaction such as water-gas shift reaction when H_2 is produced [13,14]. The presence of Cu species (Cu^0, Cu^{2+}) into membrane composition permits to achieve a combination between gas separation and catalytic activities.

The synthesis of CX or Cu-CX into macroporous commercial TiO_2-ZrO_2 ceramic support, stronger composites with both micropore structure and desire geometric dimensions were obtained. These composites, named CX/TiO_2-ZrO_2 and Cu-CX/TiO_2-ZrO_2, respectively present promising characteristics both for simply fluid separation and, in the case of Cu-CX/TiO_2-ZrO_2, for separation-catalytic applications.

In this paper we present the study of the tubular TiO_2-ZrO_2 ceramic support influence on the morpho-structural properties of the undoped and Cu doped carbon xerogels. The morpho-structural properties were investigated by using nitrogen adsorption, SEM, AFM and X-ray diffraction.

RESULTS AND DISCUSSIONS

Synthesis of CX by sol-gel method based on polycondensation of resorcinol or potassium salt of 2,4-dihydroxybenzoic acid and formaldehyde allowed us to obtain various bulk geometry of monolithic samples according to the mould shape where reaction takes place (Figure 1). This property is very important in applications as electrode, supercapacitors or molecular sieve construction [3,4,6].

In the case of the unsupported CX, about 65% and 55% of volume shrinkage is observed during drying and pyrolysis steps, respectively. The volume variation can be adjusted by changing the synthesis parameters, mainly by modifying the ratio between the amount of precursors and catalyst or water used in the polycondensation process [10].

By performing the sol-gel process into porous ceramic supports, CX/ceramic material composite without structural shrinkage is obtained. In figure 2 a blank commercial TiO_2-ZrO_2 ceramic support (a) and a composite obtained by CX synthesized into TiO_2-ZrO_2 ceramic wall (b) are presented.

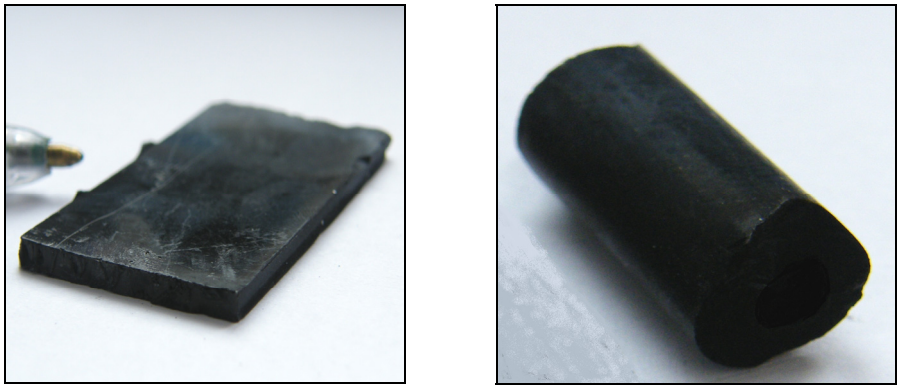

(a) (b)

Figure 1. Plate (a) and tubular (b) geometry of monolithic CX.

This strong composite type can be obtained with desired dimensions and applied, as molecular sieve by tightly placement into a steel reactor, for gas separation [6].

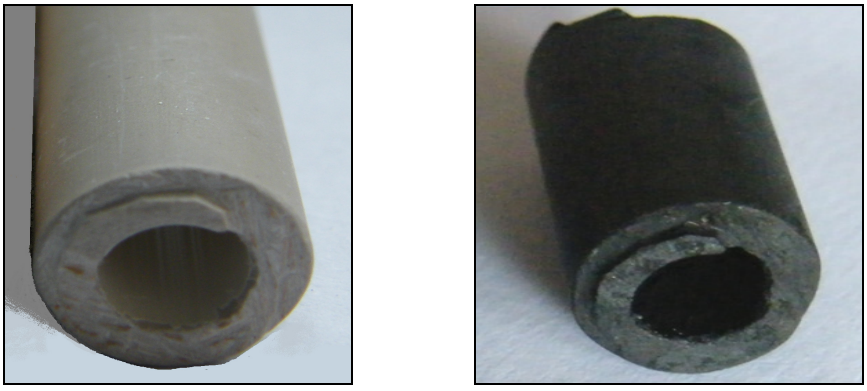

(a) (b)

Figure 2. Blank TiO_2-ZrO_2 (a) and CX/TiO_2-ZrO_2 (b).

A nanoporous structure of CX matrix with interconnected carbon nanoparticles in a size of tens nanometer is visualized by AFM (Figure 3a) and a carbon rough structure in a micrometer scale by SEM investigation (Figure 3b). In the case of Cu-CX the homogeneous dispersion of Cu nanoparticles with diameter around 65 nm into carbon framework is showed by SEM analysis (Figure 4).

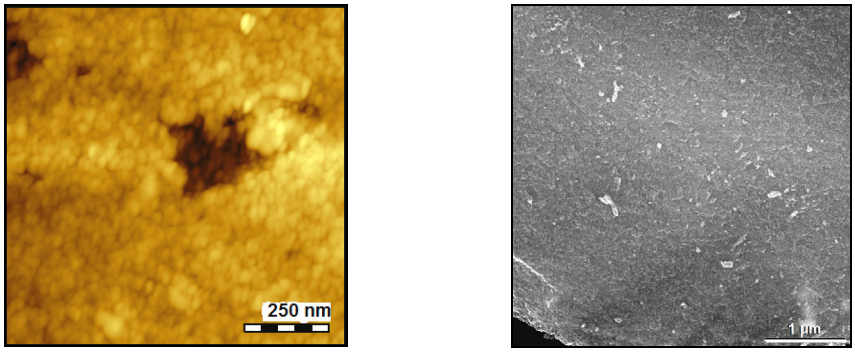

(a) (b)

Figure 3. AFM (a.) and SEM (b.) images of CX.

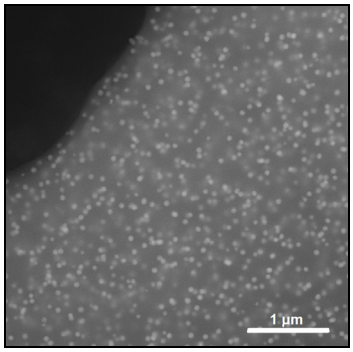

Figure 4. SEM image of Cu-CX.

The X-ray diffraction analysis of CX showed an amorphous structure represented by two large peaks at about $2\theta = 24^{o}$ and 44^{o} (Figure 5). A mixture between an amorphous and crystalline structure is observed for Cu-CX, with the same metal crystalline peak position such as in the case of corresponding Cu doped carbon aerogel [11,12]. A mixture between metallic Cu and Cu oxides is evidenced in metallic nanoparticles (Figure 5).

In case of xerogel/ceramic composite, a nanoporous structure of CX (Figure 6a) or Cu-CX (Figure 6b) which fills the macropore of TiO_2-ZrO_2 ceramic wall is showed by SEM. Also, a homogeneous Cu nanoparticle distribution into CX matrix is visualized for Cu-CX/TiO_2-ZrO_2 composite. A decrease of Cu % for obtained Cu doped composite compared with unsupported Cu-CX is observed (Table 1) by Energy-Dispersive X-Ray Spectroscopy (EDS) applied on the SEM investigated areas (see figures 4 and 6b).

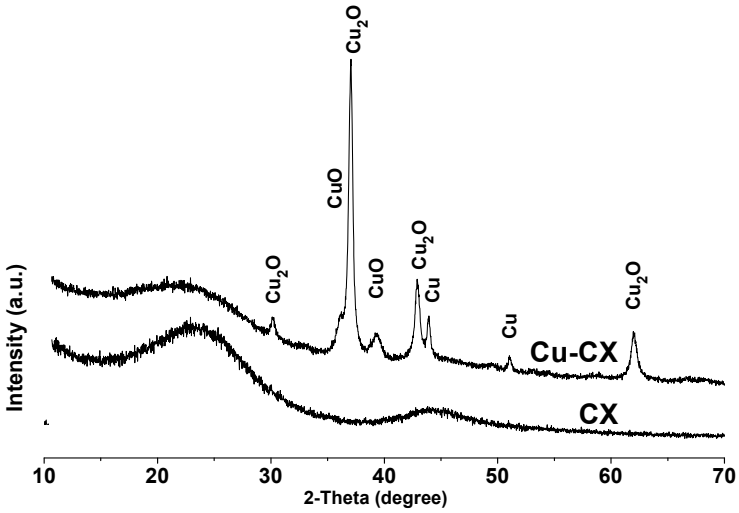

Figure 5. XRD patterns of CX and Cu-CX.

Higher BET surface areas and mesopore volumes are obtained by nitrogen adsorption on the unsupported samples than supported ones (Table 1). In the case of composite preparations, a decrease of the gelation time is observed. This phenomenon could be attributed to the presence of the ceramic support which promotes the increase of the branching of the carbon framework reflected in a decrease of both pore diameter and volume. Thus, the ceramic support can be considered as a second catalyst for the polycondensation reaction.

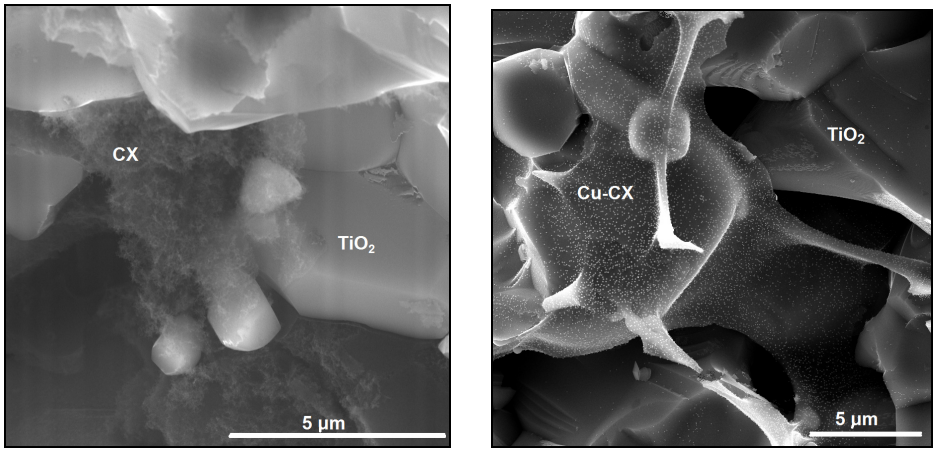

(a) (b)

Figure 6. SEM images of CX/TiO_2-ZrO_2 (a) and Cu-CX/TiO_2-ZrO_2 (b).

Table 1. Structure parameters and Cu concentration of prepared samples.

SAMPLES	S_{BET} [$m^2 g^{-1}$]	V_{meso} [$cm^3 g^{-1}$]	Cu %*
CX	78	1	-
Cu-CX	311	71	5.7
CX/TiO_2-ZrO_2	4	0.85	-
Cu-CX/TiO_2-ZrO_2	17	0.7	2.5

* Cu wt % was determined by EDS for the areas investigated by SEM

EXPERIMENTAL SECTION

Preparation of CX and Cu-CX

Undoped CX synthesis started with a resorcinol-formaldehyde wet gel preparation using resorcinol, *R,* (98 % purity), formaldehyde, *F*, (37 % solution), Na_2CO_3, *C*, (99.9 % purity), all from Aldrich, and bidistilled water, *W* [10]. Resorcinol (0.29 moles) is dissolved in bidistilled water at a *R*/*W* ratio of 0.2 g cm^{-3}. Solution of formaldehyde is added to the resorcinol solution (*R*/*F* = 0.5 molar ratio) under vigorous stirring. Afterwards, 0.1 M Na_2CO_3 aqueous solution is added to the previous prepared mixture (*R*/*C* = 500).

Cu-CX is prepared using as precursor the potassium salt of 2,4-dihydroxybenzoic acid obtained by neutralization of 2,4-dihydroxybenzoic acid, *A,* (99% purity, Aldrich) with K_2CO_3 (99%, Merck) in bidistilled water (*A*/K_2CO_3 = 2, *A*/*W* = 0.03 g cm^{-3}). To the obtained solution, formaldehyde (*A*/*F* = 0.5) and K_2CO_3, *K*, (*A*/*K* = 100) as catalyst are added.

The resulted solutions are placed in tightly closed glass moulds and cured at 70°C for 4 days. Two wet gel types are obtained: an undoped gel and a potassium doped gel. After a day of keeping in distilled water, the potassium doped gel is placed for one day in 0.1 M $Cu(NO_3)_2$ aqueous solution. After a new washing with acetone the next steps are ambient drying and pyrolysis in Ar atmosphere, at 750°C for 2 h. Monolithic undoped and Cu doped carbon xerogels are obtained.

Preparation of CX/TiO_2-ZrO_2 and Cu-CX/TiO_2-ZrO_2 composites

The xerogel/ceramic composite preparations are based on the same reactions and synthesis steps as in the case of unsupported undoped and Cu doped CXs, the difference consisted in the fact that TiO_2-ZrO_2 ceramic is introduced into the starting sol-gel solution. The commercial used TiO_2-ZrO_2 monochannel tube ceramic support (TAMI Industries) had the outer radius of 10 mm and tube wall thickness of 2.4 mm. The tube wall presents external

TiO_2 layer pore size distribution of 5 μm and a thin internal ZrO_2 layer of 3 nm. The sol-gel processes took place into the porous structure of the ceramic wall. The excess wet gel, from outside of ceramic wall, is removed before washing step. Very stable undoped or Cu doped CX/TiO_2-ZrO_2 ceramic composites were obtained after pyrolysis.

Morpho-structural investigations

AFM imagine was obtained with AFM-Agilent 5100. SEM images and EDS analysis were performed with a SEM-Quanta 200F microscope.

Specific surface area, pore size distributions, and pore volume determinations were performed by using Brunauer–Emmett–Teller (BET) and Barrett–Joyner–Halenda (BJH) calculation methods, with a Sorptomatic SO-1990 device. Before measurements the samples were degassed at 120 ^oC for about 12 h.

XRD patterns were recorded in θ - 2θ Bragg-Bretano geometry with a Siemens D5000 powder diffractometer having Cu-Kα incident radiation (λ = 1.5406 Å).

CONCLUSIONS

Very stable monolithic undoped and Cu doped carbon xerogel materials with desired shape but with a strong shrinkage were synthesized previously. The synthesis of CX and Cu-CX into porous TiO_2-ZrO_2 ceramic walls permits to obtain composite materials without shrinkage and interesting properties for molecular sieve construction. In addition, the strong fixation of Cu-CX into ceramic support and Cu nanoparticles into Cu-CX makes Cu-CX/TiO_2-ZrO_2 composite available for reactor-membrane construction.

ACKNOWLEDGEMENTS

This work was possible with the financial support of the Sectorial Operational Programme for Human Resources Development 2007-2013, co-financed by the European Social Fund, under the project number POSDRU 89/1.5/S/60189 with the title "**Postdoctoral Programs for Sustainable Development in a Knowledge Based Society**".

REFERENCES

1. Y. Yang, K. Chiang, N. Burke, *Catalysis Today*, **2011***, 178,* 197.
2. S. Cacchi, C.L. Cotet, G. Fabrizi, G. Forte, A. Goggiamani, L. Martín, S. Martínez, E. Molins, M. Moreno-Mañas, F. Petrucci, A. Roig, A. Vallribera, *Tetrahedron,* **2007**, *63*, 2519.
3. M. Inagaki, *New Carbon Materials*, **2009**, *24*, 193.
4. R. Sanjinés, M.D. Abad, Cr. Vâju, R. Smajda, M. Mionić, A. Magrez, *Surface and Coatings Technology*, **2011**, *206 15,* 727.
5. A. Maicaneanu, L.C. Cotet, V. Danciu, M. Stanca, *Studia UBB Chemia*, **2009**, *54 4*, 33.
6. D. Montané, K. Briceño, R. Garcia-Valls, in: D. Stolten, T. Grube (Eds.), *18th – World Hydrogen Energy Conference*, Essen, **2010**, *78-3*, 466.
7. L. Zubizarreta, A. Arenillas, A. Domínguez, J.A. Menéndez, J.J. Pis, *Journal of Non-Crystalline Solids*, **2008**, *354*, 817.
8. S. Morales-Torres, F.J. Maldonado-Hódar, A.F. Pérez-Cadenas, F. Carrasco-Marín, *Microporous and Mesoporous Materials*, **2012**, *153*, 24.
9. B.S. Girgis, I.Y. El-Sherif, A.A. Attia, N.A. Fathy, *Journal of Non-Crystalline Solids*, **2012**, *358,* 741.
10. L.C. Cotet, A. Roig, I.C. Popescu, V. Cosoveanu, E. Molins, V. Danciu, *Revue Roumaine de Chimie*, **2007**, *52*, 1077.
11. L.C. Cotet, M. Gich, A. Roig, I.C. Popescu, V. Cosoveanu, E. Molins, V. Danciu, *Journal of Non-Crystalline Solids*, **2006**, *352*, 2772.
12. L.C. Cotet, M. Baia, L. Baia, I.C. Popescu, V. Cosoveanu, E. Indrea, J. Papp, V. Danciu, *Jornal of Alloys and Compounds,* **2007**, *434-435*, 854.
13. R.J. Madon, D. Braden, S. Kandoi, P. Nagel, M. Mavrikakis, J.A. Dumesic, *Journal of Catalysis*, **2011**, *281, 1.*
14. K. Sagata, N. Imazu, H. Yahiro, *Catalysis Today*, **2012**, *in press,* http://dx.doi.org/10.1016/j.cattod.2012.03.064.

STUDIA UBB CHEMIA, LVII, 3, 2012 (p. 81 – 90)
(RECOMMENDED CITATION)

NICKEL RECOVERY FROM ELECTRONIC WASTE III. IRON NICKEL SEPARATION

BIANCA ROBOTIN[1], VASILE COMAN[1], PETRU ILEA[1,*]

ABSTRACT. The current study evaluates the separation of Fe from Ni containing solutions. These aqueous solutions are similar to those obtained by the electrochemical dissolution of electron gun (EG) waste. In this context, the effect of temperature and neutralizing agent concentration on the parameters of the separation process was investigated. The results showed that temperature and neutralizing agent concentration have an important impact on the amount of Ni lost in the Fe precipitate. Thus, large amounts of Ni (up to 19%) are incorporated in the precipitate when working at low temperatures (25 and 50 °C) and at a 10% concentration of the neutralizing agent (Na_2CO_3). By this method, 99.9% of Fe was removed from the aqueous solution (Fe residual concentration below 10 mg/L). The Ni losses in the Fe precipitate were below 1% when the experiments were performed at 80 °C, using a 5% Na_2CO_3 concentration.

Keywords: *WEEE, Fe separation, Fe(III) precipitation, Ni losses*

INTRODUCTION

Worldwide attention is focused on environmental protection and especially on developing new technologies which could solve the problems related to the fast accumulation of different types of waste. Of all existing waste, waste electrical and electronic equipment (WEEE) has the highest accumulation rate and this fact raises recycling issues mainly caused by the complexity of their content. [1-6].

The tests evaluating Ni recovery from the metallic components of cathode ray tubes (CRTs), that is the electron gun (EG) and the shadow mask (SM), have showed that the dissolution of these wastes produces aqueous solutions containing large amounts of Ni and Fe, and impurities such as Co and Mn in the case of EG [7]. In order to recover Ni in a pure metallic form from these solutions, it is necessary to remove the Fe content especially. Therefore, Fe separation is an important step to ensure optimal electrowinning parameters for pure Ni. The presence of Fe in the electrolyte solution would lead to a lower purity for the Ni deposits.

[1] *Babes-Bolyai University, Faculty of Chemistry and Chemical Engineering, 11 Arany Janos Street RO-400028, Cluj-Napoca, Romania*
* *pilea@chem.ubbcluj.ro*

Depending on the amount of Fe and Ni in solution, different separation methods can be applied. In the case of dilute solutions (mg/L), these two metals can be separated by using ion exchangers or selective extraction agents [8-12]. When the concentration of the metals in solution is elevated (g/L) Fe can be separated by precipitation, obtaining various oxides forms, such as: goethite (α - FeOOH), hematite (α - Fe_2O_3), and jarosite ($KFe^{3+}{}_3(OH)_6(SO_4)_2$) [8, 13-15].

A statistical analysis and a precipitation model for Fe^{3+}, as well as an estimation of the amount of Ni lost by precipitation were evaluated in a recent study [16]. The authors reached the conclusion that the neutralizing agent type and the stirring rate of the solution have very little effect upon the separation efficiency. The data obtained by Wang *et al.* confirmed the fact that a "high temperature – low pH or low temperature – high pH" neutralizing combination, applied in multiple steps, can be a convenient separation method for Fe [16].

Based on the literature data it can be stated that Fe precipitation can be a simple and very efficient process. In order to have an efficient separation, all the Fe present in the solution has to be in the trivalent form (Fe^{3+}). The literature data shows that Ni^{2+} and Fe^{2+} precipitate at pH values greater than 6 [17, 18]. On the other hand, Fe^{3+} precipitates at pH values lower than 4 [18]. This difference in pH allows for an efficient separation between Fe and Ni from aqueous solutions. The issues raised by this method are related to Ni incorporation in the Fe(III) precipitate.

Most literature studies in this area aim at Fe removal from solution resulting from the leaching of Ni ores. In these solutions, metal concentration does not exceed 1 g/L Fe^{3+} and 0.25 g/L Ni^{2+} [19]. The main concerns are related to the amount of Fe to be removed and the amount of Ni included in the precipitate during Fe precipitation.

The purpose of this study was to find the optimal parameters (temperature, concentration of neutralizing agent) in order to remove the Fe^{3+} ions from the solutions containing Ni^{2+} with a maximum removal efficiency for Fe and minimum losses for Ni.

RESULTS AND DISCUSSION

The proposed technological flow

Scheme 1 illustrates the proposed technological flow for Fe – Ni separation experiments from synthetic solutions similar to those resulting from the dissolution of EG waste. The first step is the heating of the solution at a working temperature (25, 50 or 80 °C). The next step is the controlled increase in pH by adding a neutralizing agent (5 or 10% Na_2CO_3 aqueous solution) with a constant flow rate (0.33 mL/min) under vigorous stirring. The two concentration values for the neutralizing agent were chosen to be sufficiently alkaline to ensure a controlled and relatively rapid increase in pH. It was observed that higher concentrations of the neutralizing agent (>10% Na_2CO_3) generate upon addition a local increase in pH, which leads to the incorporation of large amounts of Ni

in the Fe precipitate. On the other hand, if the concentration of the neutralizing agent is less than 5%, large amounts of neutralizing agent are required to ensure a pH increase from 1.0 to 3.5. The addition of neutralizing agent was stopped when pH reached 3.5 because, according to literature data, above this value the amount of Ni incorporated into the precipitate is increasing significantly [16].

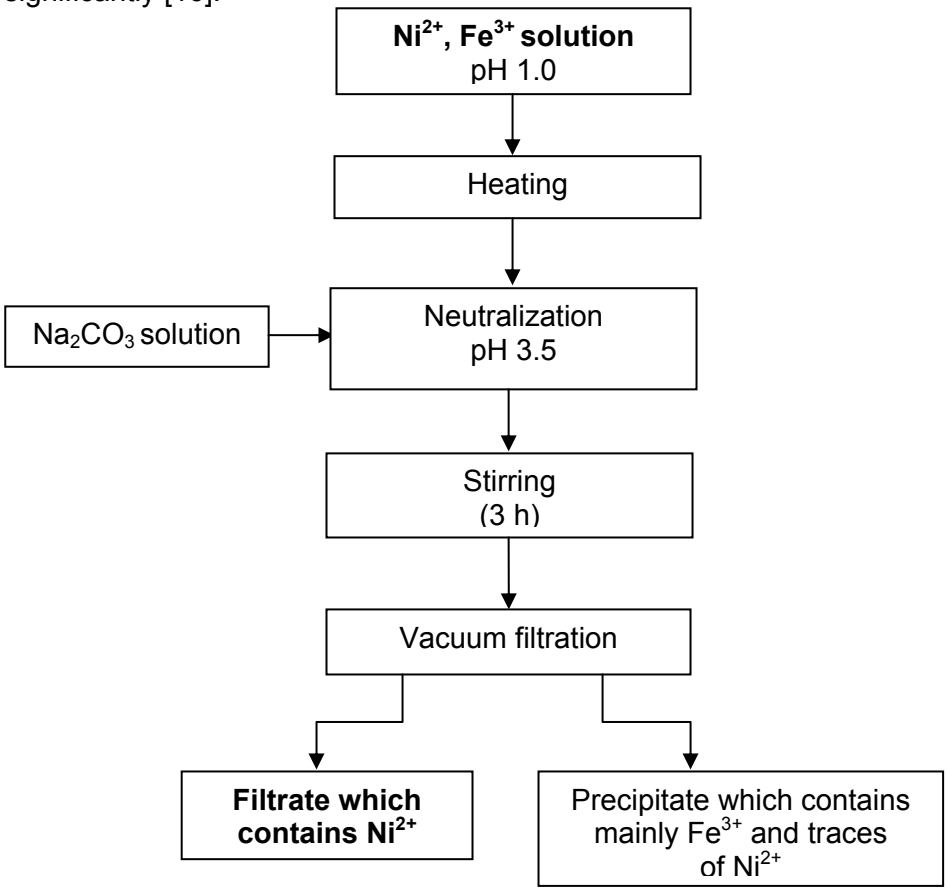

Scheme 1. The proposed technological flow for Fe separation from Ni containing solutions

When the pH reached a value of 3.5, the addition of neutralizing agent was stopped, but the other working conditions (temperature and stirring conditions) were kept constant for another 3 h, in order to bring into solution the amount of Ni incorporated in the Fe precipitate. In the next step, the solution was cooled and vacuum filtered. The precipitate was washed with double distilled water and dried at room temperature. Ni and Fe concentrations in the filtrate and precipitate were determined by Atomic Absorption Spectrometry (AAS) analysis.

pH evolution in time

The solution pH variation with time is depicted in Figure 1 and the evolution of solutions' colour with pH, in Figure 2. In all three cases, three different domains are observed:

(i) a linear increase in pH due to acid neutralization; the solution remains clear, no Fe^{3+} precipitation being observed.

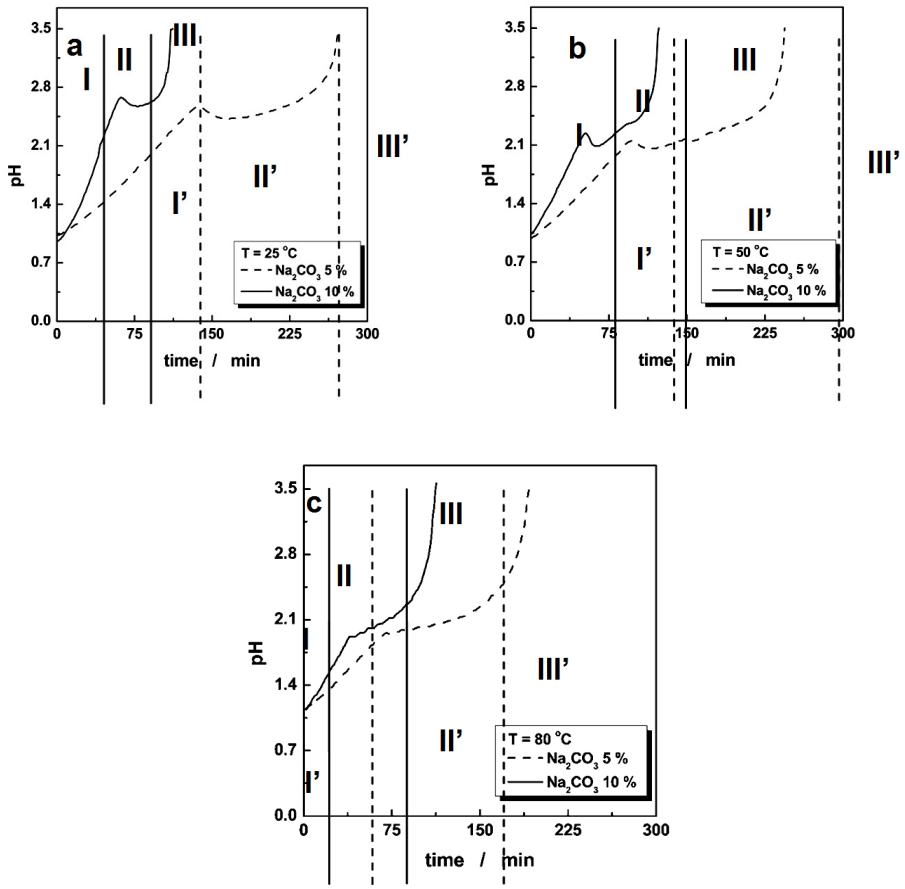

Figure 1. pH evolution with time during the precipitation of Fe^{3+}. Working conditions: a) 25, b) 50, and c) 80 °C; 5 and 10 % Na_2CO_3 as neutralizing agent; flow rate, 0.33 mL/min. I, II and III denote the domains for 10 % Na_2CO_3 (solid line); I', II' and III' denote the domains for 5 % Na_2CO_3 (dashed line)

(ii) a second domain is attributed to the nucleation and growth process of Fe^{3+} precipitation particles [19, 20]. It can be noticed that at 25 and 50 °C a decrease of pH occurs in this domain. Contrarily, at 80 °C a pH plateau is generated,

where the pH increases very slowly from 1.9 to 2.1. Another difference between the three temperatures is that when increasing the temperature the initiation of precipitation of ferric ions starts at lower pH values.

(iii) a third domain, with a steep increase in pH over time. In this region the ratio between the hydroxyl and ferric ions is higher, the precipitation of Fe^{3+} being completed in this area.

The Fe^{3+}precipitation duration decreases when the temperature rises and with the increase of the concentration of the neutralizing agent.

The obtained results for pH evolution in time are similar to those obtained by Wang *et al.*, who investigated the Fe^{3+} precipitation from solutions resulting from leaching of nickel ores [19]. The used concentrations were much smaller than in the current study, and they were 1 g/L Fe^{3+} and between 0 and 0.25 g/L Ni^{2+}, respectively. The authors used as neutralizing agents MgO and $CaCO_3$ and two working temperatures (25 and 85 °C) [19]. When working at low temperature, the authors observe a plateau region in pH evolution with time, not a decrease as in the present case.

During the precipitation experiments, the colour of the solution changed with the pH increase (from 1.0 to 3.5), going from dark green to light brown (see Figure 2). After removing the precipitate, the solution colour returns to light green, due to the presence of Ni ions.

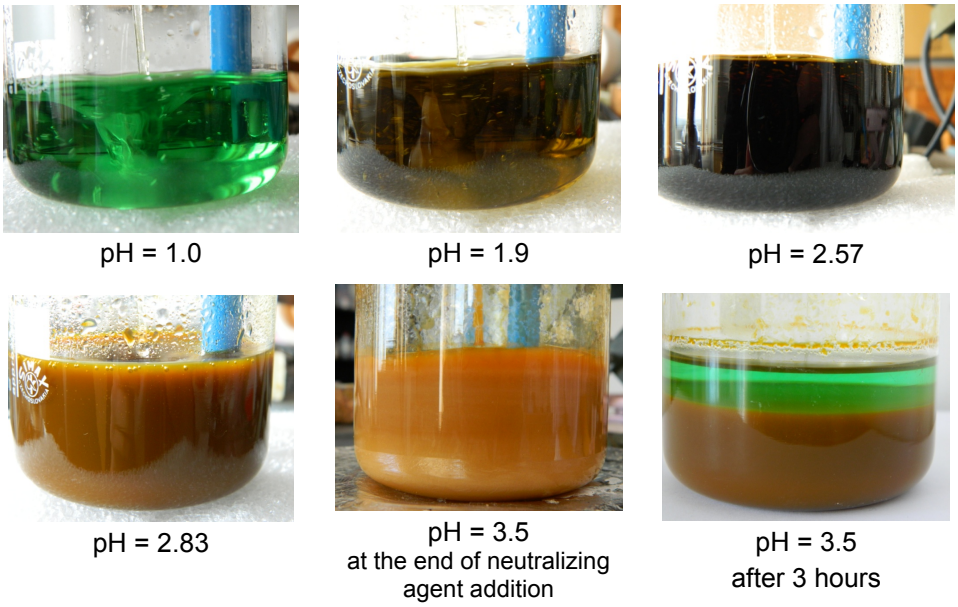

Figure 2. The solution colour change with the increase of pH, for Fe^{3+} - Ni^{2+} separation experiments

Ni losses in the precipitate

The results related to Ni losses in the precipitate during the separation experiments of Fe^{3+} and Ni^{2+}, depending on the temperature and the concentration of the neutralizing agent, are given in Table 1. The results show that the working temperature plays an important role in the separation process, especially on the amount of Ni lost in the precipitate, but it doesn't influence the amount of Fe removed. The minimum amount of Ni incorporated in the precipitate is obtained when working at 80 °C. The percentage of Ni in the precipitate is less than 1% (~ 10 mg/L) for both concentrations of neutralizing agent. On the other hand, the amount of Fe removed by precipitation is greater than 99.5% (corresponding to a residual concentration of 10 mg/L) from the initial quantity for all three temperatures values and for the two concentrations of neutralizing agent, respectively.

Table 1. Ni losses in the precipitate and the Fe removal efficiency from solution

Na_2CO_3 [%]	T [°C]	Ni lost [%]	Fe removal [%]
5	25	5.6	99.8
10		11.3	99.5
5	50	12.5	99.9
10		19.2	99.8
5	**80**	**0.4**	**99.9**
10		**0.9**	**99.8**

According to the mathematical model of Wang *et al.* [16], the highest Ni losses are recorded at pH values higher than 4. At pH 2 (where Ni losses are minimal), an increase in temperature from 25 to 85 °C raises the amount of Ni incorporated into the precipitate from 0.42% to 1.06% [19]. According to the same study, the amount of Fe removed from the solution increases with increasing pH (pH 2 - 40%, pH 3 - 80%, and pH 4 - 100%, respectively). A compromise has to be made for each case with maximum Fe removal rates and minimum Ni losses.

Concerning the initial Ni/Fe ratio in the solution, Chang *et al.* concluded that when increasing the Ni/Fe ratio, the amount of Ni lost in the precipitate increases [15].

The X-Ray Diffraction (XRD) analysis of the precipitate

The XRD analysis of the precipitate confirms the presence of Fe and Ni as various oxides (see Figure 3).

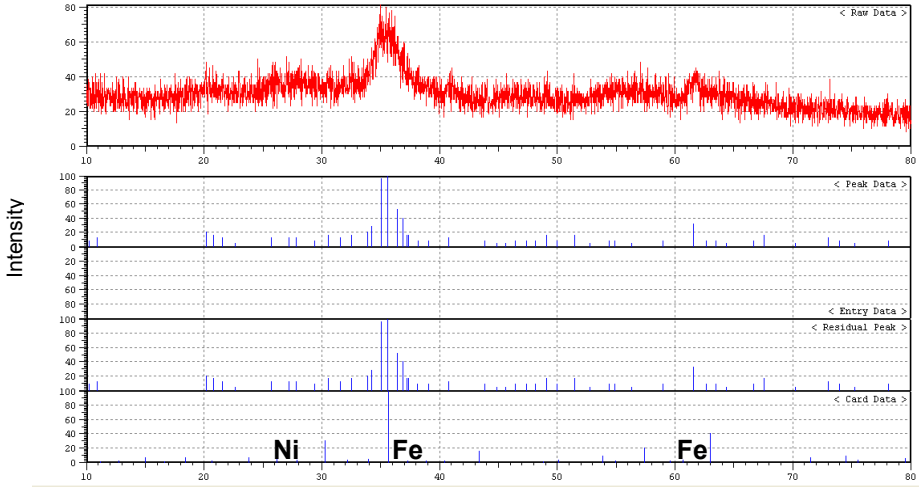

Figure 3. XRD analysis of the precipitate obtained from the Fe – Ni separation experiments

The XRD analysis of the precipitate revealed the presence of trevorite, maghemite, and magnetite. Trevorite is a rare nickeliferous mineral with the chemical formula: $NiFe^{3+}{}_2O_4$. Maghemite and magnetite are ferrimagnetic oxide minerals, having a Fe_2O_3 and Fe_3O_4 structure, respectively.

CONCLUSIONS

In order to remove Fe from the solutions resulted Ni containing CRT waste dissolution, the process was studied on synthetic solutions, with concentrations similar to those of real solutions. The current study evaluated the influence of the temperature and the concentration of a neutralizing agent on the amounts of Fe removed and Ni lost in the precipitate. The addition of the neutralizing agent was stopped when the pH reached a value of 3.5, because Ni losses get higher above this pH [16]. The conclusions derived from this study are:

- The temperature plays a significant role in the Fe – Ni separation, influencing especially the amount of Ni lost in the precipitate.
- The largest amount of Fe removed and the smallest amount of Ni lost were obtained when the working temperature was 80 °C.
- Fe removal efficiency is higher than 99.5% (corresponding to a residual concentration in the solution of 10 mg/L) for all three working temperatures.

- The incorporation of a minimum amount of Ni is influenced by the long-lasting stirring of the solution.
- By using the precipitation of Fe^{3+} as the separation method it was possible to remove 99.9% of the total amount of Fe from the solution, with Ni losses below 1%.
- When the initial Ni concentration is high, the concentration of the neutralizing agent can be elevated (e.g. 10%). In this case the Ni losses are below 1% and the solution is not diluted too much. On the other hand, if the aim is to lose as little Ni as possible, the concentration of the neutralizing agent can be lowered (e.g. 5%), with a corresponding dilution of the target solution. For industrial applications, a succession of the two alternatives can be employed.

EXPERIMENTAL SECTION

Reagents

For the Fe - Ni separation study, the following chemicals were used: $NiSO_4 \cdot 6H_2O$, $Fe_2(SO_4)_3 \cdot 5H_2O$, $Na_2CO_3 \cdot 10H_2O$. All chemicals were of analytical grade and were used as received. All solutions were prepared with double distilled water (Double D Still, JENCONS, England). The Fe – Ni separation tests were performed using 100 mL synthetic solutions containing 10 g/L Ni^{2+}, and 10 g/L Fe^{3+}, respectively.

Experimental setups

The experimental setup used for the separation experiments is given in Scheme 2.

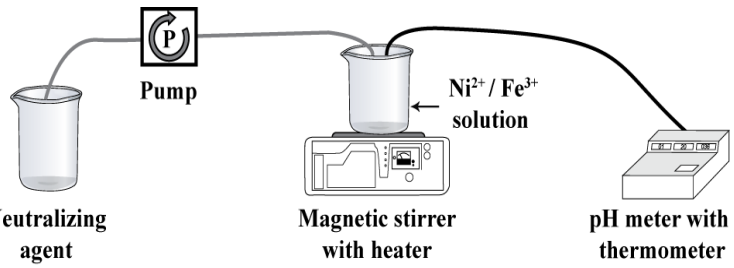

Scheme 2. The experimental setup used during the Fe- Ni separation tests

During the experiments, the pH and temperature were measured with a pH meter with thermometer, pHCond 340i, WTW, Germany.

The neutralizing agent was added using a peristaltic pump, REGLO Analog MS-2/8®, ISMATEC®, Switzerland. The heating and stirring of the solution were performed using a magnetic stirrer with heating, FB15001 Fisher Scientific, Belgium.

The amounts of Ni and Fe in solutions were determined by Atomic Absorbtion Spectrometry (AAS) measurements using an Atomic Absorption Spectrometer (AAS) Avanta 9500 (GBC, Australia).

The composition of the precipitate was established by XRD on a Shimadzu diffractometer XRD-6000 assembled in Bragg-Brentano θ/2θ with a goniometer which operates at atmospheric pressure with Ni filters using CuKα radiation (λ = 1.5418 Å). The standard calibration was made with quartz powder. Data acquisition conditions were: 40 KV operating potential at a 30 mA current. The peaks qualitative identification was realized using the JCPDS (Joint Committee on Powder Diffraction Standards) database.

ACKNOWLEDGMENTS

BR and VC wish to thank for financial support the projects co-financed by the Sectoral Operational Program For Human Resources Development 2007 – 2013 - contract no.: POSDRU/88/1.5/S/60185 – “Innovative doctoral studies in a Knowledge Based Society” and - contract no.: POSDRU/89/1.5/S/ 60189 – “Postdoctoral Programs for Sustainable Development in a Knowledge Based Society”, respectively.

Authors are grateful to Dr. rer. nat. Udo Schmidt (from Technische Universität Ilmenau, Germany) for his help and to Oana Ponta (from Babes-Bolyai University, ICIBNS, Cluj-Napoca) for the XRD measurements.

REFERENCES

1 J. Cui, E. Forssberg, *Jornal of Hazardous Materials,* **2003**, *99*, 243.

2 R. Widmer, H. Oswald-Krapf, D. Sinha-Khetriwal, M. Schnellmann, H. Böni, *Environmental Impact Assesment Review,* **2005**, *25*, 436.

3 J. Cui, L. Zhang, *J. Hazard. Mater.,* **2008**, *158*, 228.

4 A. Das, A. Vidyadhar, S.P. Mehrotra, *Resources, Conservation and Recycling,* **2009**, *53*, 464.

5 B.R. Babu, A.K. Parande, C.A. Basha, *Waste Management and Research,* **2007**, *25*, 307.

6 J.A.S. Williams, *Resources, Conservation and Recycling,* **2006**, *47*, 195.

7 B. Robotin, V. Coman, P. Ilea, *Studia UBB Chemia,* **2011**, *LVI*, 121.

8 A. Agrawal, S. Kumari, K.K. Sahu, *Industrial & Engineering Chemistry Research,* **2009**, *48*, 6145.

9 Hazan, J. Korkisch, *Analytica Chimica Acta,* **1965**, *32*, 46.

10 D. Kogelnig, A. Stojanovic, F. Jirsa, W. Körner, R. Krachler, B.K. Keppler, *Separation and Purification Technology,* **2010**, *72*, 56.

11 J. Korkisch, S.S. Ahluwalia, *Analytica Chimica Acta,* **1966**, *34*, 308.

12 M.-S. Lee, K.-J. Lee, *Hydrometallurgy,* **2005**, *80*, 163.

13 S. Agatzini-Leonardou, P.E. Tsakiridis, P. Oustadakis, T. Karidakis, A. Katsiapi, *Minerals Engineering,* **2009**, *22*, 1181.

14 S. Bhattacharjee, K.K. Gupta, S. Chakravarty, P. Thakur, G. Bhattacharyya, *Separation Science and Technology,* **2004**, *39*, 413.

15 Y. Chang, X. Zhai, B. Li, Y. Fu, *Hydrometallurgy,* **2010**, *101*, 84.

16 K. Wang, J. Li, R.G. McDonald, R.E. Browner, *Hydrometallurgy,* **2011**, *109*, 140.

17 C. Sist, G. Demopoulos, *JOM Journal of the Minerals, Metals and Materials Society,* **2003**, *55*, 42.

18 X. Wei, J. Viadero, K. M. Buzby, *Environmental Engineering Science,* **2005**, *22*, 745.

19 K. Wang, J. Li, R.G. McDonald, R.E. Browner, in *Book Nickel loss during iron precipitation and product characterization*, ed. by Editor, City, **2012**, Vol. 402, Chap. 293.

20 J. Dousma, P. L. De Bruyn, *Journal of Colloid and Interface Science,* **1976**, *56*, 527.

STUDIA UBB CHEMIA, LVII, 3, 2012 (p. 91 – 100)
(RECOMMENDED CITATION)

ECO-FRIENDLY LEACHING OF BASE METALS FROM WASTE PRINTED CIRCUIT BOARDS: EXPERIMENTAL STUDY AND MATHEMATICAL MODELING

SZABOLCS FOGARASI[1], FLORICA IMRE-LUCACI[2], TAMAS VARGA[3], PETRU ILEA[1,*]

ABSTRACT. Our research aims the development of an eco-friendly leaching method for the separation of electronic components with high gold content, from other parts of waste printed circuit boards (WPCBs) without the use of any other separation technique. The base metals were removed in a specially designed leaching reactor using acidic $FeCl_3$ solution. The dependency of the dissolution rate of base metals on the amount of $FeCl_3$ and solid: liquid ratio was determined based on a kinetic model developed in MATLAB. The kinetic parameters identified by the experimental results indicate that the leaching rate of metals is more strongly dependent on the amount of $FeCl_3$ used than on the solid: liquid ratio. The optimal values of the operating parameters were established in order to maximize the amount of dissolved metals and minimize the oxidant consumption.

Keywords: *$FeCl_3$, waste printed circuit boards, metal dissolution, leaching rate.*

INTRODUCTION

The yearly accumulation of waste printed circuit boards (WPCBs) reaches 1.5- 2 million tons, which represents 3 wt. % of the total electronic waste [1-3]. Thanks to the high metal content (~ 40 wt. %), WPCBs are considered an attractive secondary source of metals which can help to preserve the natural resources. It is also important to note that many metals have significantly higher concentration in WPCBs than in mineral resources. For example the gold content in WPCBS can reach 25-250 g/ton compared to only 1-10 g/ton in gold ores. Despite the fact, that the amount of precious metals in WPCBs is less than 1 wt. %, thanks to their high price, they value ~13 €/kg WPCB, which represents more than 80% of the total intrinsic value of WPCBs [4-7]. The importance of metal recovery is also emphasized by the

[1] *Babeş-Bolyai University, Faculty of Chemistry and Chemical Engineering, 11 Arany Janos Street, Cluj-Napoca, RO-400028, Romania, * pilea@chem.ubbcluj.ro*
[2] *Babeş-Bolyai University, Interdisciplinary Research Institute on Bio-Nano-Sciences, 42 Treboniu Laurian Street, Cluj-Napoca, RO-400271, Romania*
[3] *University of Pannonia, Department of Process Engineering,10 Egyetem Street, Veszprém, H-8200, Hungary*

fact that the economically mineable reserves for Au, Ag, Cu and Ni will be depleted in the next fifty years [3-5]. As a result, precious metals are the main targets in WPCBs recycling, followed by Cu, Ni and other base metals [6, 7].

Nevertheless, it is important to consider that together with precious metals and other valuable materials, WPCBs contain various hazardous materials like chlorinated and brominated substances, toxic metals, photoactive and biologically active materials. Therefore many studies have been carried out with the aim of recovering the resources from WPCBs and at the same time preventing environmental contamination [8, 9]. The first industrial methods presented in the literature were based on pyrometallurgical processing; especially open burning, incineration and smelting [10]. These methods are simple but have major disadvantages like non-selectivity, hazardous operating conditions and emission of toxic gases and fumes metals [8-13]. For this reason recently the researches have been focused on hydrometallurgical methods which operate in less dangerous conditions and are more easily controlled [7, 15-17]. Through hydrometallurgical processing it is possible not only to separate the metals from the other main categories of materials but also to realize their selective extraction. This is very important because due to different chemical reactivity, concentration in the WPCBs and economical potential of the metals, diverse leaching agents and experimental conditions are required for their dissolution [18, 19]. For example, the use of a preliminary step in which the base metals are removed from the electronic waste is essential in the recovery of high purity precious metals. However in many situations the pre-concentration of noble metals is preceded or coupled with several separation techniques which can require large investments and increase the complexity of the process [10, 20]. Therefore it is necessary to simplify the recycling technologies by using selective hydrometallurgical methods which can extract the metals efficiently with minimal involvement of other pre-treatment techniques [20, 21].

The current study presents an alternative hydrometallurgical method for the separation of gold rich electronic components from the plastic and metallic parts of WPCBs without the use of any mechanical separation technique. The results show that acidic $FeCl_3$ solutions are efficient leaching agents in the removal of base metals from WPCBs leading to a solid residue containing the gold rich electronic components.

RESULTS AND DISCUSSIONS

Influence of solid: liquid ratio on the leaching process

The influence of solid: liquid (S:L) ratio on the dissolution of metals (Me) was studied in the range of 1:8 – 1:64 (g:mL) using an acidic 0.21 M $FeCl_3$ solution. Figure 1 shows that the amount of dissolved Me (representing the

sum of the total amount of dissolved Cu, Sn, Zn and Pb) increases significantly with the decrease of S:L ratio, reaching a maximum at the value of 1:40. As it can be seen the further decrease of the S:L ratio to 1:64 does not improve the performances of the dissolution process. This can be easily explained considering that the leaching of metals occurs through a diffusion controlled process due to the unstirred solution. Therefore it will be a well defined volume of leaching solution which contains the maximum quantity of $FeCl_3$ which can be transported through diffusion from the bulk to the reaction surface during the experiments. The results shown in Figure 1 indicate that in our experimental conditions this volume is 200 mL which corresponds to a S:L ratio of 1:40. Higher volumes of solutions even if contain more $FeCl_3$ cannot give better performances because only a part of the leaching agent is able to diffuse to the reaction surface during the experiment.

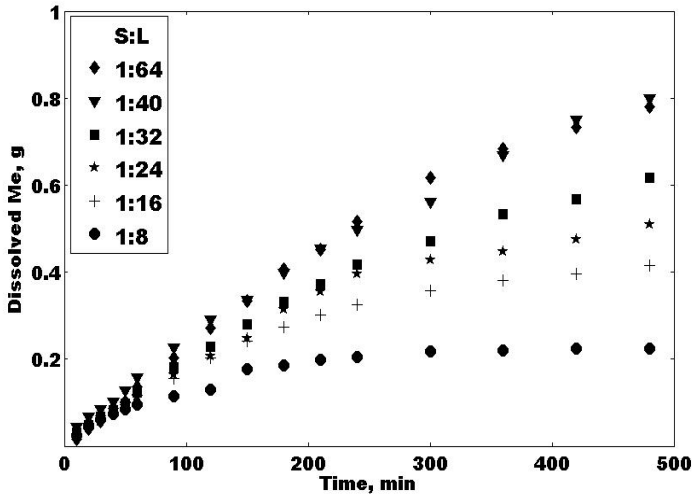

Figure 1. Amount of dissolved Me vs. time at different S:L ratios using 0.21 M $FeCl_3$ in 0.3 M HCl solution

Moreover the use of low S:L ratios is not desired since it can cause difficulties in the further processing of the leaching solutions. Therefore several experiments were carried out in order to determine if it is possible to obtain the same or better performances by using higher S:L ratios than 1:40 and higher oxidant concentrations than 0.21 M. The leaching solutions with different S:L ratios and $FeCl_3$ concentrations were obtained by dissolving the $FeCl_3$ quantities, used in the previous experiments (used to maintain the concentration at 0.21 M), in each volume of solution (Table 2).

Table 2. Oxidant concentrations for different combinations of S:L ratios and $FeCl_3$ quantities

Volume, mL	40	80	120	160	200	320
$FeCl_3$, g	Concentration, M					
1.38	0.21					
2.76	0.42	0.21				
4.15	0.64	0.32	0.21			
5.53	0.85	0.42	0.28	0.21		
6.92	1.06	0.53	0.35	0.26	0.21	
11.07	1.70	0.85	0.56	0.42	0.34	0.21

At constant volume of leaching solutions the use of higher $FeCl_3$ concentrations can improve significantly the dissolution rate of Me. As Figure 2 shows the leaching rate, at the S:L ratio of 1:8, increases almost 10 times by increasing the oxidant concentration 8 times.

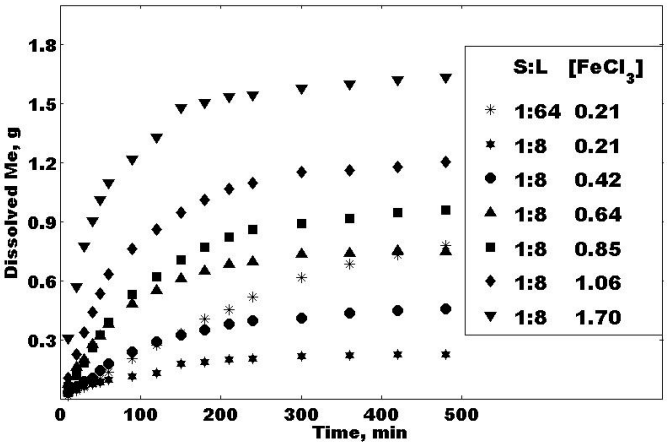

Figure 2. Amount of dissolved Me vs. time at different $FeCl_3$ concentrations and S:L ratios in 0.3 M HCl solution

Furthermore, it can be observed that from the 0.64 M $FeCl_3$ concentration upwards the S:L of 1:8 becomes more efficient than the other ones at 0.21 M $FeCl_3$ concentration. It is also important to note that the higher dissolution rate at the S:L of 1:8 and 0.64 M $FeCl_3$ was achieved using an amount of $FeCl_3$ three times smaller than the one used in the experiment with the S:L of 1:64 and 0.21 M oxidant concentration. It can be concluded that higher S:L ratios can use more efficiently the same amount of oxidant than lower ones. This is also confirmed by comparing the S:L ratios at different concentrations, obtained at a constant amount of $FeCl_3$ (Figure 3).

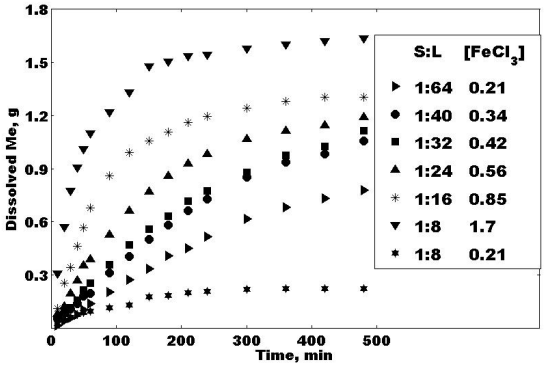

Figure 3. Amount of dissolved Me vs. time at 11.07 g $FeCl_3$ dissolved in different volumes of 0.3 M HCl solution

The results shown in Figure 3 indicate that the highest dissolution rate was achieved by using the highest S:L ratio (1:8) at the highest oxidant concentration (1.7 M).

Mathematical modelling of the leaching process

Since there are many possible combinations of $FeCl_3$ quantities and S:L ratios (Table 2) a mathematical model was developed and implemented in MATLAB in order to determine the dependency of the Me dissolution rate on the operating parameters. The material balance equations for the leaching process were written considering that the dissolution of Me occurs in a batch reactor by the following reaction:

$$2Fe^{3+} + Me \rightarrow Me^{2+} + 2Fe^{2+} \quad (1)$$

Based on the mass balance equations the dependency of the dissolution rate of Me (r) on the concentration of $FeCl_3$ ($C_{Fe^{3+}}$) can be defined by the following rate equation:

$$r = \frac{1}{\nu_{Me}} \cdot \frac{dC_{Fe^{3+}}}{dt} = \frac{1}{2} \cdot k \cdot C^{a}_{Fe^{3+}} \quad (2)$$

Since the volume of the leaching solution can be considered constant during the experiments the rate is expressed in g min^{-1} instead of g min^{-1} L^{-1}:

$$r = \frac{1}{2} \cdot k \cdot m^{a}_{Fe^{3+}} \cdot \frac{M_{Me}}{M_{Fe^{3+}}} \quad (3)$$

Also another term V was introduced in eq. (3) in order to link the dissolution rate of the Me to the S:L ratio:

$$r = \frac{1}{2} \cdot k \cdot \frac{M_{Me}}{M_{Fe^{3+}}} \cdot m_{Fe^{3+}}^{a} \cdot V^{b} \quad (4)$$

By including the constants from eq. (4) into the apparent rate constant (k_{app}):

$$k_{app} = \frac{1}{2} \cdot k \cdot \frac{M_{Me}}{M_{Fe^{3+}}} \quad (5)$$

The following rate equation is obtained:

$$r = k_{app} \cdot m_{Fe^{3+}}^{a} \cdot V^{b} \quad (6)$$

The optimal values for the reaction orders (a, b) and k_{app} were identified by using the least square method and the optimization toolbox provided by MATLAB. The regression method defines the estimate of these parameters as the values which minimize the sum of the squares (hence the name least squares) between the measurements and the model (i.e., the predicted values) [22]. Inserting the best fitting values of the parameters into the objective function the following expression was obtained for the dissolution rate of the Me:

$$r = 1.97 \cdot 10^{-4} \cdot m_{Fe^{3+}}^{3.33} \cdot V^{-0.98} \quad (7)$$

The amount of dissolved Me calculated on the basis of the above equation gives a good fit to the experimental data (Figure 4).

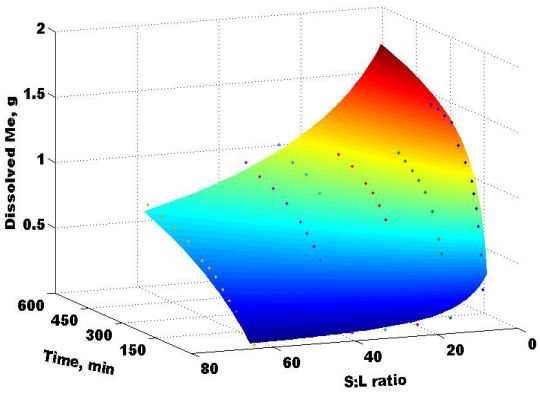

Figure 4. Fitting of the model result to the experimental data

The value of the relative error determined was approximately 8 %. This can be explained by the fact that this model does not include the influence of the reaction surface area modification with time, because it was

not possible to measure it, due to the complex structure of the WPCB samples. However it can be considered that the initial surface area of the Me is identical from one sample to another, because their composition volume and weight is the same in each experiment.

Nevertheless, it is obvious from Figure 4 that the predicted values by the model fit very well with the experimental results. Moreover the values found for a = 3.33 and b = -0.98 sustain the conclusion that the dissolution rate of the Me is more strongly dependent on the amount of $FeCl_3$ used than on the applied S:L ratio. Therefore the amount of dissolved Me will increase with the increase of the amount of $FeCl_3$ and with the increase of the S:L ratio. Moreover the tendency of the dissolution rate suggests that the process can be improved even more by using higher S:L ratio and higher amounts of oxidants than those from the studied range. However, the use of higher S:L ratio is not possible since the uncrushed WPCB samples cannot be covered entirely by smaller volumes of leaching solutions than the one corresponding to the S:L ratio of 1:8.

The efficiency of higher oxidant concentrations than 1.7 M was evaluated by comparing the conclusions drawn from the values of the dissolution rate and a new parameter $f_{met/ox}$. The equation for the efficiency factor ($f_{met/ox}$) was defined as the ratio between the amount of the dissolved Me and total amount of $FeCl_3$ used in the experiment:

$$f_{met/ox} = \frac{\text{Total dissolved metals}}{\text{Amount of } FeCl_3 \text{ used}} \quad \frac{[\text{g Me}]}{[\text{g } FeCl_3]} \tag{8}$$

The values of $f_{met/ox}$, obtained for several experimental conditions (Table 2), show how many grams of Me can be dissolved by using one gram of $FeCl_3$. This parameter reveals which $FeCl_3$ concentration and S:L ratio allows to use more efficiently the existing amount of oxidant. Considering its physical meaning, it is obvious that the efficiency factor is a more important criterion in the identification of the best operating conditions than the dissolution rate. However, in the case of the S:L ratio both parameters give the value of 1:8 as the most suitable for the dissolution of Me. In contrast, for the $FeCl_3$ concentration the two parameters lead to differing conclusions. While the dissolution rate increases with the oxidant concentration, reaching a maximum at 1.7 M $FeCl_3$, the efficiency factor reaches a minimum at the same concentration. The value of $f_{met/ox}$ shows that the dissolution rate is not large enough at the concentrations of 1.7 M, in order to allow for a gram of $FeCl_3$ to dissolve a larger amount of Me than at lower concentrations. In fact, Figure 5 shows that according to $f_{met/ox}$ the most appropriate oxidant concentration for the dissolution of Me is 0.64 M even if the dissolution rate is not the highest at this concentration.

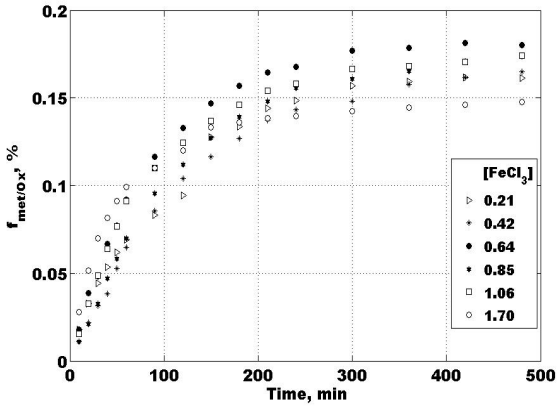

Figure 5. $f_{met/ox}$ vs. time at the S:L ratio of 1:8 using different $FeCl_3$ concentration and 0.3 M HCl solution

CONCLUSIONS

The experimental results proved that acidic $FeCl_3$ solutions are efficient leaching agents for the dissolution of base metals from WPCBs. It was found that the amount of dissolved metals, at constant oxidant concentration, increases significantly with the decrease of S:L ratio reaching a maximum at the value of 1:40. The influence of $FeCl_3$ concentration was also tested at fixed S:L ratio, which revealed that the leaching process is faster if instead of a high volume of leaching solution a lower one is used but at higher oxidant concentration.

Based on the concentration profiles it was also concluded that higher S:L ratios can use more efficiently the same amount of oxidant than lower ones. The mathematical expression for the dependency of the dissolution rate on the S:L ratio and $FeCl_3$ concentration was obtained by using a kinetic model developed in Matlab.

The validated rate equation shows that the Me dissolution rate is approximately minus first order respect to the S:L ratio and 3.3 order respect to the amount of $FeCl_3$. The value of the apparent rate constant at 25 ^oC was determined and found to be $1.97*10^{-4}$ $g^{-2.33} * min^{-1}$, which also confirms the suitability of acidic $FeCl_3$ solutions for the leaching of base metals. The efficiency factor defined in this work along with the dissolution rate lead to the conclusion that the best performances can be obtained at the S:L ratio of 1:8 and 0.64 M $FeCl_3$ concentration.

EXPERIMENTAL SETUP

The leaching tests were carried out in a batch reactor with recirculation which is equipped with a perforated rotating drum instead of an agitator. However, the studies regarding the influence of S:L ratio and oxidant concentration on the

dissolution process presented in this work, were performed in unstirred conditions. All experiments were carried out at room temperature using 5 g of WPCB samples which were inserted in the rotating drum of the reactor. During the experiments the reactor was hermetically sealed in order to prevent the influence of air (O_2) on the oxidation of metals. The leaching solution was prepared by using ferric (III)-chloride (Fluka), 32 % HCl solution and double distilled water. The chemical composition of the WPCB samples (Table 1) was obtained by atomic adsorption spectroscopy after aqua regia mineralization. The same analytical method was used to determine the concentration of metals in the leaching solutions and in the residue at the end of the experiments.

Table 1. Chemical composition of WPCBs

Components	Ag	Au	Cu	Sn	Pb	Zn	Fe	Ni	Solid residue
	wt. %								
WPCB generally	0.02	0.01	20	4	1.9	2	8	2	62.07
WPCBs samples	0.02	0.02	16	6.5	1.9	5.5	-	-	70.06

It is obvious from the data shown in Table 1 that the samples contain only a few of the metals present in the WPCBs and in different concentrations. This limitation was necessary because Cu, Sn and Pb have the most important influence on the recovery of precious metals. It is well known that the extraction of high purity Au or Ag is not possible if the solution contains Cu. Furthermore the dissolution of Sn and Pb (solder) is crucial in the separation of electronic components from the other parts of the WPCBs. Moreover if the leaching of Cu, Sn and Pb occurs efficiently in these experimental conditions than there is no doubt that the more reactive base metals like Ni, Fe will be dissolved with high performances.

ACKNOWLEDGEMENTS

Prof. Chován Tibor, University of Pannonia, Veszprém, Hungary and Prof. Árpád Imre-Lucaci, Babeş-Bolyai University, Cluj-Napoca, Romania, are gratefully acknowledged for discussions which have stimulated the development of the research activity here reported.

The authors also acknowledge the following project for financial support: *Investing in people!* Ph.D. scholarship, Project co-financed by the SECTORAL OPERATIONAL PROGRAM FOR HUMAN RESOURCES DEVELOPMENT 2007 – 2013. Priority Axis 1. "Education and training in support for growth and development of a knowledge based society". Key area of intervention 1.5: Doctoral and post-doctoral programs in support of research. Contract nr.: POSDRU/ 88/1.5/S/60185 – “INNOVATIVE DOCTORAL STUDIES IN A KNOWLEDGE BASED SOCIETY”, Babeş-Bolyai University, Cluj-Napoca, Romania.

REFERENCES

1. J.M. Yoo, J. Jeong, K. Yoo, J.C. Lee, W. Kim, *Waste Management*, **2009**, *29*, 1132.
2. P. Chancerel, S. Rotter, *Waste Management*, **2009**, *29*, 2336.
3. A. Tuncuk, V. Stazi, A. Akcil, E.Y. Yazici, H. Deveci, *Minerals Engineering*, **2012**, *25*, 28.
4. M. Oguchi, H. Sakanakura, A. Terazono, H. Takigami, *Waste Management*, **2012**, *32*, 96.
5. T. Havlik, D. Orac, M. Petranikova, A. Miskufova, F. Kukurugya, Z. Takacova, *Journal of Hazardous Materials*, **2010**, *183*, 866.
6. Y.J. Park, D.J., Fray, *Journal of Hazardous Materials*, **2009**, *164*, 1152.
7. R.U. Ayres, *Resources, Conservation and Recycling*, **1997**, *21*, 145.
8. I. Bereketli, M.E. Genevois, Y.E. Albayrak, M. Ozyol, *Expert Systems with Applications* **2011**, *38*, 71.
9. O. Tsydenova, M. Bengtsson, *Waste Management*, **2011**, *31*, 45.
10. J. Cui, L. Zhang, *Journal of Hazardous Materials*, **2008**, *158*, 228.
11. L. Longa, S. Sun, S. Zhong, W. Dai, J. Liu, W. Song, *Journal of Hazardous Materials*, **2010**, *177*, 626.
12. S. Ilyas, M.A. Anwar, S.B. Niazi, M.A. Ghauri, *Hydrometallurgy*, **2007**, *88*, 180.
13. J. Wang, J. Bai, J. Xu, B. Liang, *Journal of Hazardous Materials*, **2009**, *172*, 1100.
14. A.C. Grosse, G.W. Dicinoski, M.J. Shaw, P.R. Haddad, *Hydrometallurgy*, **2003**, *69*, 1.
15. E.Y. Kim, M.S. Kim, J.C. Lee, J. Jeong, B.D. Pandey, *Hydrometallurgy*, **2011**, *107*, 124.
16. J. Li, M. Safarzadeh, M. Sadegh, S. Michael, J.D. Miller, K.M. LeVier, M. Dietrich, R.Y. Wan, *Hydrometallurgy*, **2011**a. doi: 10.1016/j.hydromet.2011.11.005.
17. K. Huang, J. Guo, Z. Xu, *Journal of Hazardous Materials*, **2009**, *164*, 399.
18. W. Jiang, L. Jia, X. Zhen-Ming, *Journal of Hazardous Materials*, **2009**, *161*, 257.
19. H.Y. Kang, J.M. Schoenung, *Resources, Conservation and Recycling*, **2005**, *45*, 368.
20. R.V. Murugan, S. Bharat, A.P. Deshpande, S. Varughese, P. Haridoss, *Powder Technology*, **2008**, *183*, 169.
21. G. Senanayake, *Minerals Engineering*, **2004**, *17*, 785.
22. E.B. Nauman, *Chemical Reactor Design, Optimization and Scale up*, McGraw-Hill, New York, USA, **2002**, 211.

STUDIA UBB CHEMIA, LVII, 3, 2012 (p. 101 – 108)
(RECOMMENDED CITATION)

INFLUENCE OF ETHYL SILICATE ON THE STRUCTURAL AND MORPHOLOGICAL PROPERTIES OF CALCIUM-PHOSPHATE SOL-GEL DERIVED GLASSES

F. TALOS[1,*], A. VULPOI[1], S. SIMON[1]

ABSTRACT. Structural organization induced by using different concentration of ethyl silicate in the bioactive SiO_2-CaO-P_2O_5 sol-gel glasses, using Fourier transforms infrared spectroscopy (FTIR), X-ray powder diffraction (XRD) and Scanning Electron Microscopy (SEM) was investigated in the present study. Additionally, the incorporation of calcium oxide into glass structure during different heat treatments was also examined. After the thermal treatment at 700°C, XRD patterns evidenced the presence of new calcium phases: calcium pyrophosphate ($Ca_2P_2O_7$) and calcium silicate (Ca_6 (SiO_4) (Si_3O_{10}). FTIR spectra also revealed that after annealing the highest CaO content produces a faster depolymerization of silica network.

Keywords: *sol-gel, FTIR, XRD, SEM, $Ca_2P_2O_7$, Ca_6 (SiO_4) (Si_3O_{10}).*

INTRODUCTION

The rapid development of nanostructure materials presents scientific and technical challenges for the design and fabrication of bioactive materials at low synthesis temperature used for biomedical applications. Hench *et al.* used for the first time the term ''bioactive glasses'' to describe the interfacial bond of silicate-based with calcium and phosphate glasses with the physiological environments [1]. The used synthesis involved in that study provides a high temperature melt-quenching procedure but, twenty years later, the same group showed that the sol–gel process allows the synthesis of high purity, homogeneous materials. Moreover, porous structure can be controlled by modifying the precursor's concentration [2]. In particular, the gel strength of the silica matrix has been modulated, leading to the development of new materials with special properties, such as biosensors, bioreactors [3], encapsulation of bio species [4-6], bioactive glass microspheres [7], drug delivery [8] and hybrid organic-inorganic materials [9]. The tetra-ethyl silicate Si $(OR)_4$, where R= C_2H_5, usually is mixed together with an alcoholic solution in the presence of an acid catalysis and these reactions can be described as

[1] *Institute of Interdisciplinary Research in Bio-Nano-Sciences, 42 Treboniu Laurian, 400271 & Faculty of Physics, Babeş-Bolyai University, 1 Mihail Kogalniceanu, 400084, Cluj-Napoca, Romania*
[*] *florentina.talos@ubbcluj.ro*

an SN_2 nucleophilic substitution. Also, in acidic condition, hydrolysis is relatively faster than condensation, and weakly branched polysiloxane network usually are formed [10]. Thus chemical gels created via sol-gel process provide strong covalent bonding where their cross-links are irreversible [11]. During the ageing stage of the sol-gel process, it was attested that the calcium nitrate is dissolved in the pores, which are generated by the products of the condensation reaction. In addition, during the drying process, calcium nitrate is deposited on the gel surface and further heat treatments provide the diffusion of calcium in the network [12]. Moreover, phosphorus and silicon are considered to be both nucleation agents as well as network formers.

The possible hydrolysis-condensation reactions of sol-gel materials in the presence of salts are presented below:

Hydrolysis

$$Si(OC_2H_5)_4 + H_2O \rightarrow Si(OC_2H_5)_3\text{-}OH + C_2H_5OH \quad (1)$$

$$Si(OC_2H_5)_4 + 4\,H_2O \rightarrow Si(OH)_4 + 4\,C_2H_5OH \quad (2)$$

$$Ca(NO_3)_2 + 2\,H_2O \rightarrow Ca(OH)_2 + 2\,HNO_3 \quad (3)$$

$$(NH_4)_2HPO_4 + 2\,H_2O \rightarrow 2\,NH_4OH + H_3PO_4 \quad (4)$$

Condensation

$$Si(OH)_4 + Si(OH)_4 \rightarrow (HO)_3Si\text{-}O\text{-}Si(OH)_3 + H_2O \quad (5)$$

$$NH_4OH + HNO_3 \rightarrow NH_4NO_3 + H_2O \quad (6)$$

$$H_3PO_4 + Ca(OH)_2 \rightarrow CaHPO_4 + 2\,H_2O \quad (7)$$

The present study aims to synthesize homogeneous polysiloxane gels with inorganic salts at a relatively low pH starting from a non - aqueous solution. To accomplish this purpose, two different concentration of silicon alkoxide (4Si, 2Si) were used in order to obtain materials with controlled morphology, designed for further biomedical applications. Furthermore, structural and morphological modification after drying and annealing were characterized by means of XRD, FTIR, TEM and SEM techniques, respectively.

RESULTS AND DISCUSSION

The structural phases for the dried and 1 hour thermally treated materials at 700°C were characterized by XRD and are shown in Fig.1 (a-b).

The XRD patterns for the 4Si and 2Si samples after being dried at 100˚C exhibit peaks corresponding to un-reacted ammonium nitrate NH_4NO_3 phase. By increasing the temperature at 700˚C the 2Si and 4Si samples revealed peaks

corresponding to calcium pyrophosphate ($Ca_2P_2O_7$) and calcium silicate ($Ca_6(SiO_4)(Si_3O_{10})$) phases, overlapped on the amorphous matrix. The appearance of these phases is inhibited by the higher silicate concentration.

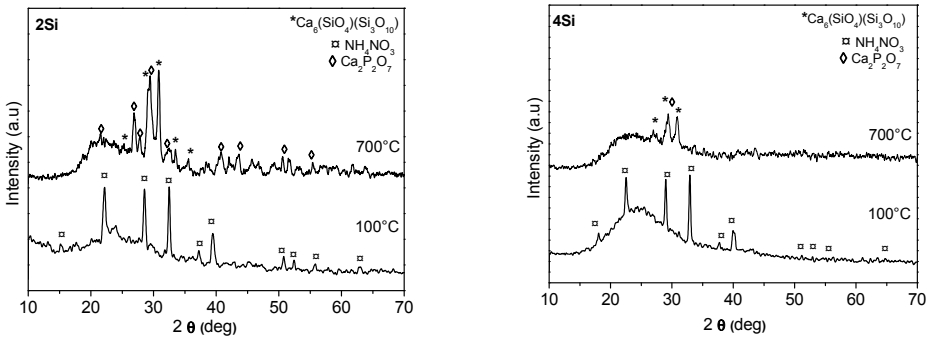

Figure 1. XRD patterns of the glass samples, dried at 100˚C and after thermal treatment at 700˚C: (a) 2Si; (b) 4Si.

In order to obtain more detailed information about the structural changes observed in the XRD patterns, FTIR study has been carried out for these samples. Room-temperature IR spectra of 4Si, 2Si glass samples are presented in Fig. 2.

The 2Si and 4Si dried samples (Fig. 2 (a, b)) present a series of infrared bands located at: 465, 825, 950, 1080, 1129, 1227, 1375, 1637, 2430, 3750 cm^{-1}. The broad absorption band situated between 3750 cm^{-1} and 2910 cm^{-1} becomes larger after thermal treatment. This band is assigned to bending and stretching vibration -OH of molecular water [13]. The peak at 3450 cm^{-1} is associated to silanol groups linked to molecular water through hydrogen bonds. Among 3000-2800 cm^{-1} are located the bands ascribed to the symmetric and asymmetric fundamental stretching vibration of CH_2 and CH_3 groups from the residues of the precursors used in the sol-gel synthesis. The signal recorded at around 1620 cm^{-1} is due to the deformation modes of O-H groups and absorbed water molecules, δ (H-O-H) [13]. The shoulder at 1640 cm^{-1} changes to a smaller one after heating at 700°C.

Moreover, the sharp peak assigned to the nitro group ($-NO_2$) is isoelectric with the carboxylate ion groups ($-CO_2$), both providing very similar spectra for the main functional group and both being located around 1380 cm^{-1}, observed in all dry gels (2Si and 4Si) [14]. This peak disappears in both 2Si and 4Si glasses after annealing at higher temperatures. The small shoulder situated around 1152 cm^{-1} can be ascribed to the longitudinal optical Si-O-Si stretching

vibration [13]. Furthermore, the shoulder situated around 1080 cm^{-1} is attributed to the asymmetric stretching mode of Si-O-Si (asym) bonds in the tetrahedral units, while the shoulder centred at 950 cm^{-1} is attributed to the Si-O-Ca bonds containing non-bridging oxygen [15]. Analysis has revealed also a component at 800 cm^{-1}, assigned to silicon-oxygen symmetric stretching vibration modes. The lower vibrational frequencies may be characteristic to P-O-P linkages in polymeric systems, the ones between 700 cm^{-1} and 770 cm^{-1} corresponds to pyro-phosphates $(P_2O_7)^{4-}$ [16]. Two small peaks at 525 and 630 cm^{-1} are associated to (O-P= (H-O) bending mode of crystalline phosphate formed on the glasses [17]. Also a small absorption signal occurs at 470 cm^{-1}, which can be assigned to the rocking motion of the bridging oxygen atoms perpendicularly to the Si-O-Si plane [18].

An interesting feature observed in the IR spectrum of the 700°C heat treated samples compared with the dried samples, is the increased intensity of the bands located between 1150-950 cm^{-1}. This behaviour is more pronounced for the sample 2Si were the bands attributed to symmetric and asymmetric Si-O-Si respectively to Si-O-NBO presents higher intensity. We assume that lower concentration of ethyl silicate and higher concentration of CaO induces the depolymerisation of the silica matrix. More precisely, the above-mentioned modes have been assigned to different aggregation processes of silica based matrix such as $[SiO_4]^{4-}$ monomers and $[Si_3O_{10}]^{8-}$ trimers, hypothesis supported also by the XRD results. The obtained results reveal thus that CaO leads to depolymerization of silicate network after annealing process.

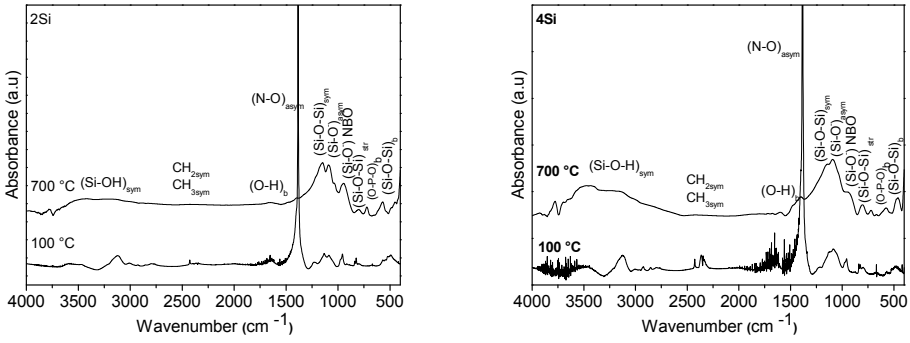

Figure 2. FTIR absorption spectra of the glass samples, dried at 100˚C and after thermal treatment at 700˚C: (a) 2Si; (b) 4Si.

Fig. 3 shows the SEM micrographs realized for 2Si, 4Si glasses dried at 100°C. The surface of the 2Si glasses Fig. 3. (a.I) is composed of larger spherical agglomerates with small crystals while the 4Si material (see Fig. 3. (b.I) displays smaller particles with almost spherical morphology.

After annealing at 700 °C the surfaces of the 2Si glass (Fig. 3.a.II) reveal changes in their morphology, lamellar crystals can be seen on a surface composed by small spherical aggregates. No significant modification was observed for the 4Si samples after heating (Fig. 3.b.II). Based on XRD data (Fig. 1, and SEM images (Fig. 3), it could be concluded that new phases were formed on the materials surface; these changes are more pronounced for the 2Si sample. This outcome is due to a highest resistance at depolymerization of 4Si samples, result showed also by means of FTIR spectroscopy.

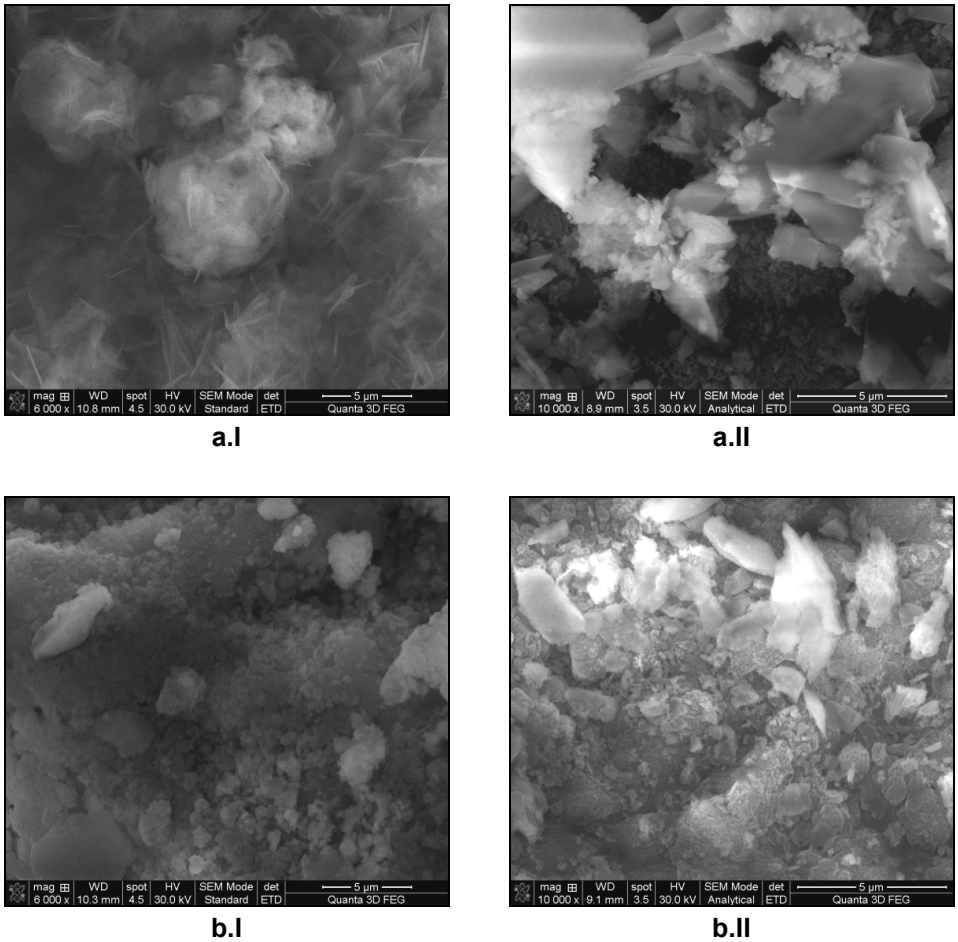

Figure 3. SEM micrographs of the glass samples dried at 100°C (a.I) 2Si, (b.I) 4Si and after heat treatment at 700˚C (a.II) 2Si, (b.II) 4Si.

CONCLUSIONS

Homogeneous 4Si and 2Si samples have been obtained by the sol–gel method. X-ray diffraction analysis for the 4Si, 2Si system reveals crystal phases, associated with calcium pyrophosphate ($Ca_2P_2O_7$) and calcium silicate ($Ca_6(SiO_4)(Si_3O_{10})$) phases, presenting an interesting approach for the material science used in bio-applications. FTIR spectroscopy of the studied samples after their annealing at 700°C indicates the depolymerisation of the local network, resulting mainly in tetrahedral silicate units. This behaviour is more evident for the 2Si sample. The SEM micrographs achieved for the 4Si and 2Si materials prove also the morphological modification after annealing at 700°C.

EXPERIMENTAL SECTION

Two types of glasses with different compositions belonging to the SiO_2-CaO-P_2O_5 system have been obtained by sol–gel method (Table 1). The sol–gel precursors used in this study were tetraethyl orthosilicate (TEOS, (Si $(OC_2H_5)_4$), calcium nitrate tetrahydrate (Ca $(NO_3)_2 \cdot 4H_2O$), di-ammonium hydrogen phosphate $(NH_4)_2HPO_4$. All the gels were prepared at room temperature (nearly 21°C).

Table.1. Nominal compositions (wt. %) of the sol–gel glasses

Glasses Name	SiO_2	CaO	P_2O_5
4Si	70,90	16,54	12,56
2Si	54,91	25,63	19,46

The sol-gel synthesis: The TEOS has been mixed with the solvent (ethanol) and stirred for 30 minutes, in 1:2 molar ratios. The calcium and phosphate salts have been separately dissolved in deionized water, according to the molar ratio 1:2, for 30 minutes. The resulted calcium and phosphorous solutions were firstly mixed together, while the pH was adjusted to 1 using nitric acid (conc. 65%) and then put over the silica solution. The final solution was stirred for 1 hour and introduced in a polyethylene cylindrical recipient at 37°C during 48 hours for aging. After drying at 100ºC for 24 hours, the glass has been annealed at 700ºC for 1 hour and then cooled at room temperature.

The structural changes of the dried and heat treated powders were investigated by X-ray diffraction using a Shimadzu XRD-6000 difractometer with a monochromator of graphite for CuKα (λ=1.54 Å). The diffractograms were performed in a 2θ degree range of 10º–70º with a speed of 2°/min.

For the FTIR measurements, identical amounts of glass powder were mixed with KBr in order to obtain pellets of about 1 mm thickness. The spectra were recorded at room temperature in a 400-4000 cm^{-1} spectral range with a JASCO FT/IR-6200 infrared spectrometer using a maximum resolution of 4 cm^{-1} and 256 scans. Each spectrum was scanned for 32 times to increase the signal-to-noise ratio. The FTIR spectra were performed for the dried and 700°C heat treated samples.

The morphology and microstructure of the prepared composite samples were investigated by scanning electron microscopy (SEM). The SEM imagines were recorded using FEI QUANTA 3D FEG dual beam, which work in high vacuum mode. In order to amplify the secondary electrons signal a cover of 5 nm thickness was performed with Pt-Pd into Agar Automatic Sputter Coater, in Ar atmosphere.

ACKNOWLEDGMENTS

This research was accomplished in the framework PNII IDEI - PCCE 101/2008 PROJECT from the Romanian National University Research Council - CNCSIS. F. Taloş author wishes to thank for the financial support provided from programs co-financed by the Sectoral Operational Programme Human Resources Development POSDRU/88/1.5/S/60185-INNOVATIVE DOCTORAL STUDIES IN A KNOWLEDGE BASED SOCIETY.

REFERENCES

1. L.L. Hench, R.J. Splinter, W.C. Allen, T.K. Greenlee, *Journal of Biomedical Materials Research Part A2*, **1971**, *2*, 117.
2. M.M. Pereira, A.E. Clark and L.L. Hench, *Journal of Biomedical Materials Research Part A2,* **1994**, *28*, 693.
3. M.L. Ferrer, D. Levy, B. Gomez-Lor, M. Iglesias, *Journal of Molecular Catalysis B - Enzymatic*, **2004**, *27*, 107.
4. J.Y. Barreau, J.M. DaCosta, I. Desportes, J. Livage, L. Monjour, M. Gentilini, *Comptes rendus de l'Academie des sciences, Serie III Sciences de la vie*, **1994**, *317*, 653.
5. J. Livage, C. Roux, J.M. Costa, I. Desportes, J.F. Quinson, *Journal of Sol-Gel Science and Technology*, **1996**, *7*, 45.
6. C. Roux, J. Livage, K. Farhati and L. Monjour, *Journal of Sol-Gel Science and Technology*, **1997**, *8*, 663.

7. D. Cacaina, R. Viitala, M. Jokinen, H. Ylänen, M. Hupa, S. Simon, *Key Engineering Materials*, **2005**, *284-286,* 411.
8. M. Goldenberg, R. Langer, X. Jia, *Journal of Biomaterials Science, Polymer Edition*, **2007**, *18*, 241.
9. C. Sanchez, B. Julian, P. Belleville and M. Popall, *Journal of Materials Chemistry*, **2005**, *15*, 3559.
10. C.J. Brinker and G.W. Scherer, "The Physics and Chemistry of Sol-Gel Processing", Academic Press, Inc., San Diego, **1990**.
11. T. Miura, H. Okumoto, H. Ichijo, *Physical Review E*, **1996**, *54*, 6596.
12. S. Lin, C. Ionescu, K.J. Pike, M.E. Smith, J.R. Jones, *Journal of Materials Chemistry*, **2009**, *19*, 1276.
13. G Socrates, "Infrared and Raman Characteristic Group Frequencies, Tables and Charts'', John Wiley and Sons, Ltd., Chichester, UK, **2001**.
14. John Coates, "Interpretation of Infrared Spectra, A Practical Approach. Encyclopedia of Analytical Chemistry'', R.A. Meyers, John Wiley & Sons Ltd, Chichester, **2000**, chapter 3.
15. P. Saravanapavan, L.L. Hench, *Journal of Non-Crystalline Solids*, **2003**, *318*, 1.
16. A. Gozalian, A. Behnamghadera, M. Daliri, A. Moshkforoush, *Scientia Iranica F*, **2011**, *18*, 1614.
17. S. Shahrabi, S. Hesaraki, S. Moemeni, M. Khorami, *Ceramics International*, **2011**, *37*, 2737.
18. A. Chrissanthopoulos, N. Bouropoulos, S.N. Yannopoulos, *Vibrational Spectroscopy*, **2008**, *48*, 118.

STUDIA UBB CHEMIA, LVII, 3, 2012 (p. 109 – 119)
(RECOMMENDED CITATION)

CORRELATING STUDY ON PHISYCO-CHEMICAL AND BIOLOGICAL PROPERTIES OF THIOSEMICARBAZONE AND THIADIAZOLINE DERIVATIVES

IOANA A. IONUŢ[1,*], BRÎNDUŞA TIPERCIUC[1], OVIDIU ONIGA[1], BEATA SZEFLER[2], RALUCA MATIES[3]

ABSTRACT. Thiadiazolines and Thiosemicarbazones represent classes of well-known molecular structures with important biological activities. The set of twenty structures, synthesized in our lab, was characterized about lipophilicity by reverse phase thin layer chromatography (RPTLC) and tested for their antimicrobial activities. These molecular properties were modeled by using topological and quantum descriptors, in the frame of a hypermolecule, with the meaning of a "mean molecule" in the set. A general procedure for developing and validating the models using the above concept is given. Within this frame, a method of data reduction (*i.e.*, selection of relevant descriptors) was exemplified.

Keywords: *thiosemicarbazone, thiadiazoline, hypermolecule, molecular descriptor,QSPR, QSAR*

INTRODUCTION

According to the literature, thiosemicarbazones are reported to possess various biological activities, as antimicrobial, anti-inflammatory, antiviral, antiparasitic, antimalarial, and antituberculosis [1-3].

Also, molecules containing nitrogen- and sulphur-related heterocycles (thiazole, thiazolidine, thiazolidinedione, thiadiazoline) are considered important pharmacophores as they can possess interesting biological activities too. For example, thiadiazolines have antihelmintic, antihypertensive, anticancer, anti-inflammatory, antibacterial, analgesic, and tyrosinase inhibitory activities [4].

Application of QSAR/QSPR techniques in order to elucidate the ways in which the structure can determine physical and/or biological properties has already become an essential tool in the area of medicinal chemistry [5-9]. These techniques combine the ability to predict physico-chemical properties of as yet unmeasured or unknown compounds with the ability to understand just how the structure influences a particular property.

[1] *Department of Pharmaceutical Chemistry, Faculty of Pharmacy, Iuliu Hatieganu University of Medicine and Pharmacy,Cluj-Napoca, Romania*
[2] *Department of Physical Chemistry, Collegium Medicum, Nicolaus Copernicus University, Kurpińskiego 5, 85-950, Bydgoszcz, Poland*
[3] *Faculty of Chemistry and Chemical Engineering, Babeş-Bolyai University, 400028 Cluj, Romania*

The retention chromatographic index, I_{CHR}, is a measure of the interaction between a given compound and two phases: a mobile phase (i.e., the eluent) and a stationary one. This interaction is function of more than one factor, polarity, lipophylicity and the size of the molecule being included. These factors are joined in a "global" molecular property, termed *chromatographic index* [10,11]. It is well known that the values of I_{CHR} vary with the chromatographic systems, pressure and temperature. This is the reason why, in correlating studies, values I_{CHR} from a single experiment are requested. Lipophilicity is related to I_{CHR} and controls the passive transport of a medicinal molecule through the cell membranes (of lipidic nature).

This paper is focused on the development of novel QSPR/QSAR models using quantum molecular and topological descriptors on the ground of available experimental physico-chemical and biological data.

DATA SETS

The molecular structures of thiadiazolines and thiosemicarbazones herein investigated are listed in **Table 1**.

Table 1. Chemical Structures of the Studied Thiadiazolines and Thiosemicarbazones

	Thiadiazolines		**Thiosemicarbazones**
1	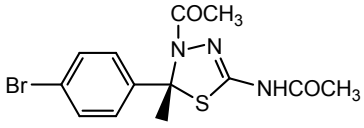	**11**	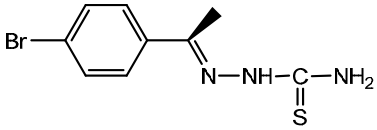
2	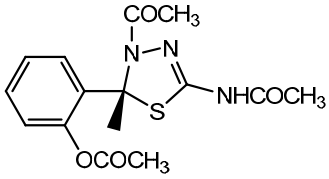	**12**	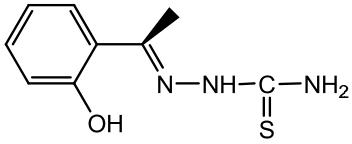
3	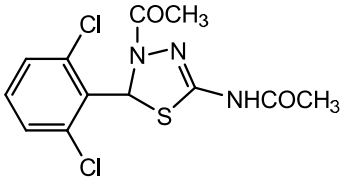	**13**	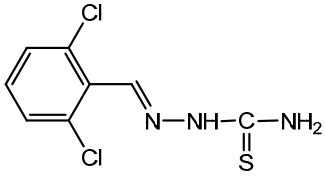

	Thiadiazolines		Thiosemicarbazones
4	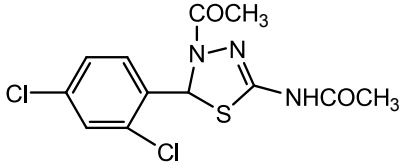	**14**	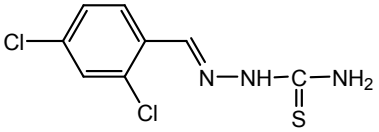
5	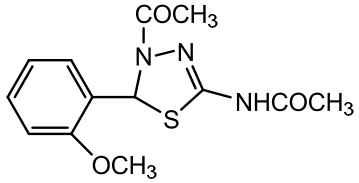	**15**	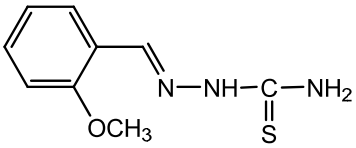
6	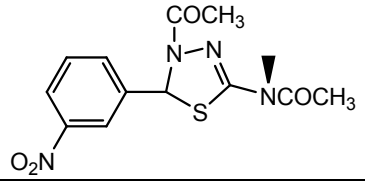	**16**	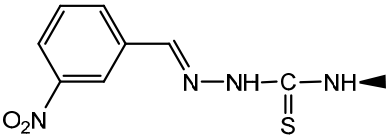
7	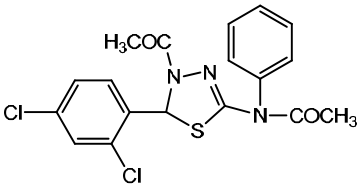	**17**	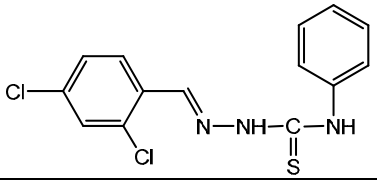
8	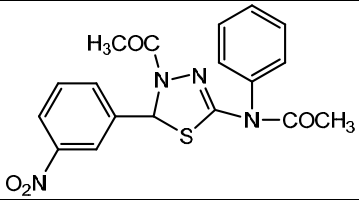	**18**	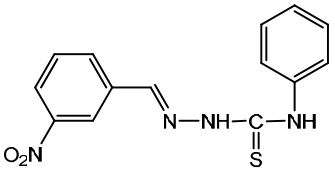
9	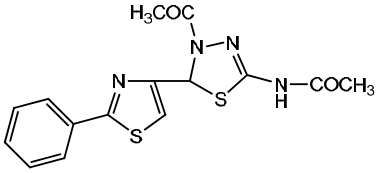	**19**	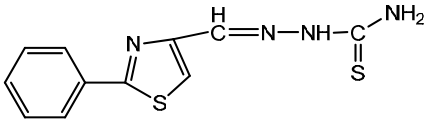
10	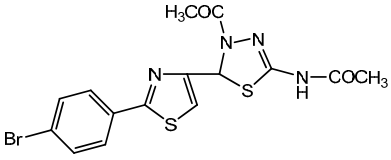	**20**	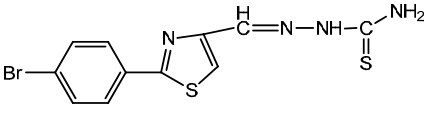

RESULTS AND DISCUSSION

The results of the correlating analysis are presented for both joint and separate sets: thiosemicarbazones (10) and thiadiazolines (10). Before starting the correlating analysis, let us introduce the concept of hypermolecule, as the "mean" molecule [12] within the investigated set of structures.

Hypermolecule Model

The *hypermolecule H* (**Figure 1**) was generated by superimposing all the common features of molecules under study [13,14]. On the already generated hypermolecule, we calculated the mass descriptors **M**, as groups of atoms, *e.g*. CH, Cl, *etc*. for any vertex of H and for all molecules in the set (see the **Appendix**) and used them as independent variables in the correlating study. **Table 2** includes selected mass descriptors along with other descriptors chosen to describe a given position in the hypermolecule, such as partial charges CH, and global descriptors including HOMO level of energy (in au, after Hartree-Fock optimization), HOMO-LUMO gap HL Gap and some global topological indices calculated by TOPO CLUJ program (on distance and detour, respectively).

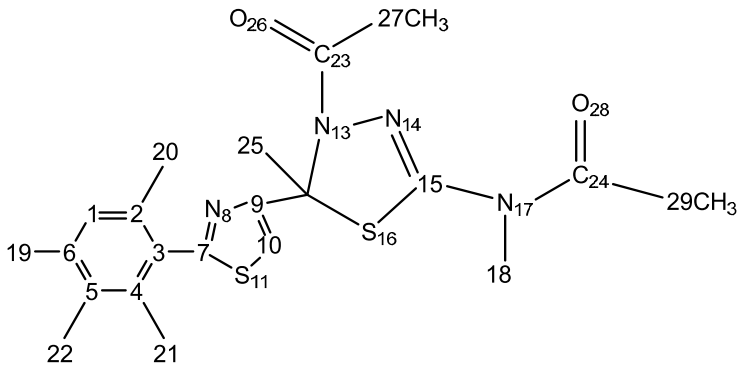

Figure 1. Hypermolecule H

Chromatographic Index I_{chr}.

The reverse phase thin-layer chromatography data, provided by six sets of experiments $\mathbf{P_1}$ to $\mathbf{P_6}$, for the set of 20 molecules in **Table 1** are listed in **Table 3**.

Table 2. Descriptors values for molecules and for relevant positions in the Hypermolecule

Structure	E_{tot} HF	HL Gap	HOMO (eV)	IE CJDE	IE CJDI	14CH	19CH
1	-3780.933	11.627	-8.988	232	526	0.001	-0.069
2	-1438.271	11.991	-9.024	391	723	-0.480	0.146
3	-2090.376	11.605	-9.003	247	515	-0.392	0.187
4	-2090.387	11.828	-9.341	241	539	-0.415	-0.096
5	-1286.481	11.708	-8.566	255	522	-0.468	0.172
6	-1415.089	10.938	-9.464	312	691	-0.437	0.212
7	-2168.147	10.891	-8.141	321	873	-0.369	-0.079
8	-1453.829	9.951	-8.376	367	984	-0.371	0.182
9	-1738.747	10.616	-8.342	337	812	-0.476	0.146
10	-4308.052	10.374	-8.393	374	938	-0.550	-0.054
11	-3477.391	10.815	-8.254	121	230	0.084	-0.042
12	-982.947	11.168	-8.328	124	216	0.229	0.163
13	-1786.829	10.824	-8.359	126	222	0.190	0.190
14	-1786.833	10.386	-8.46	123	234	0.259	-0.062
15	-982.928	10.648	-8.098	132	226	0.369	0.160
16	-1111.539	9.652	-8.526	190	336	0.135	0.200
17	-2016.375	10.262	-8.314	353	669	0.103	-0.062
18	-1302.051	9.522	-8.416	405	765	0.191	0.204
19	-1435.190	9.984	-8.3	188	397	0.034	0.149
20	-4004.494	9.809	-8.386	214	476	0.114	-0.036

Table 3. Chromatographic index I_{chr} values for the molecules in Table 1

Structure	P_1	P_2	P_3	P_4	P_5	P_6
1	0.317	0.376	0.470	0.588	0.635	0.682
2	0.576	0.588	0.658	0.747	0.770	0.817
3	0.364	0.423	0.505	0.623	0.670	0.717
4	0.305	0.364	0.458	0.582	0.635	0.682
5	0.476	0.541	0.611	0.717	0.753	0.788
6	0.388	0.458	0.541	0.647	0.694	0.729
7	0.070	0.105	0.164	0.270	0.341	0.388
8	0.264	0.352	0.447	0.576	0.641	0.682
9	0.352	0.447	0.529	0.647	0.694	0.741
10	0.235	0.341	0.429	0.552	0.623	0.670
11	0.282	0.376	0.447	0.576	0.635	0.682
12	0.470	0.558	0.594	0.705	0.752	0.788
13	0.300	0.140	0.441	0.588	0.647	0.688
14	0.223	0.305	0.352	0.517	0.564	0.605
15	0.400	0.482	0.535	0.623	0.705	0.752
16	0.352	0.429	0.488	0.623	0.670	0.694
17	0.210	0.294	0.337	0.498	0.531	0.586

Structure	P_1	P_2	P_3	P_4	P_5	P_6
18	0.164	0.247	0.311	0.470	0.535	0.576
19	0.247	0.341	0.417	0.552	0.611	0.652
20	0.270	0.235	0.411	0.558	0.623	0.658

Looking at the I_{chr} values in Table 3, one can see that these are inter-correlated, as shown in the matrix below (the highly correlated ones in bold characters):

Intercorrelating matrix for the Chromatographic index I_{chr}

	P_1	P_2	P_3	P_4	P_5	P_6
P_1	1	0.88168	**0.96396**	0.90565	0.87199	0.85756
P_2		1	0.89156	0.85531	0.8393	0.84362
P_3			1	**0.97806**	**0.96257**	0.95364
P_4				1	**0.99451**	**0.99071**
P_5					1	**0.99855**
P_6						1

It comes out that some statistical data will be very close for the highly inter-correlated chromatographic parameters P_n.

Data Reduction and Models

Data reduction was made in view of eliminating the irrelevant descriptors and/or inactive positions in the hypermolecule, either in chromatography or biological activity terms. The procedure implies the calculation of a first regression with as many as possible invariant descriptors followed by the stepwise elimination of the irrelevant ones.

The quality of statistics was monitored by Pearson correlation coefficient R, by Fischer ratio F (as higher value, as better quality regression) and also by the percentage variance CV%, expressing the accuracy of the prediction (particularly the non-explained part of the data variation). The correlating equations are listed in **Tables 4** to **6**.

As an example, data reduction dropped the initial 18 descriptors to only 4 ones (see **Table 4)**, with statistical relevance in the description of the chromatographic index. One can see that a same set of descriptors correlates differently with the different dependent variables.

Note that, among many, the mass descriptors **M** and partial charges **CH** have been successfully used. The best models also included the global molecular parameters such as HOMO-LUMO Gap **HL Gap** (**Table 5**), HOMO energy (**Table 6**) and topological descriptors, e.g., the **Cluj index** IECJDE (**Table 4, 6**) [15,16].

Table 4. Chromatographic index I_{chr} values P_1 to P_5 correlated by the same set of descriptors

Descriptors	Coeff	Const	R	CV%	F
P_1		-0.012	0.861	25.127	11.506
18M	-0.003				
19M	-0.002				
2M	0.027				
IECJDE	0.0003				
P_2		-1.186	0.786	24.13	6.068
18M	-0.003				
19M	-0.002				
2M	0.123				
IECJDE	0.0003				
P_3		-0.013	0.921	14.828	22.461
18M	-0.003				
19M	-0.002				
2M	0.038				
IECJDE	0.0003				
P_4		-0.009	0.945	10.624	33.465
18M	-0.003				
19M	-0.001				
2M	0.048				
IECJDE	0.0002				
P_5		-0.008	0.958	0.053	8.821
18M	-0.002				
19M	-0.001				
2M	0.053				
IECJDE	0.0002				

Table 5. High quality QSPRs for the P_6 set of I_{chr} data

Descriptors	Coeff	Const	R	CV%	F
P_6		-0.007	0.960	8.177	66.578
18(20)M	-0.002				
19(20)CH	-0.001				
2(20)M	0.058				
P_6		-0.011	0.970	7.303	63.947
18(20)M	-0.002				
19(20)CH	0.350				
2(20)M	0.037				
HL GAP	0.021				
P_6		-0.004	0.968	7.587	58.951
14(20)CH	-0.042				
18(20)M	-0.002				
19(20)CH	0.321				
2(20)M	0.054				

Model Validation

Despite the small number of experimental data concerning the antimicrobial activity (10 data), we could find that the prediction by QSAR was not "by chance": changing the order of data in the column "*B. cereus*" (**Table 7**), by "*B. cereus**" we could observe a large drop in R and F and an increase in the explained variance (**Table 7**, the bolded and underlined rows, respectively).

We could not split the data set in "training set" and "prediction set" in order to calculate the predictive power of the model. Our intention was only to give a methodology, rather than to offer the best model for a given property/activity.

Table 6. QSARs for the activity against *B.cereus*

Descriptors	Coeff	Const	R	CV%	F	*B.cereus*	*B. cereus**
B. cereus		18.633	0.879	3.005	11.859	**18**	18
14(10)CH	-4.660					**18**	18
18(10)M	-0.025					**18**	16
B. cereus		**10.659**	**0.951**	**2.105**	**18.877**	**18**	18
14(10)CH	**-5.407**					**16**	16
18(10)M	**-0.018**					**18**	18
HOMO	**-0.912**					**16**	16
*B. cereus**		11.388	0.529	5.771	0.776	**16**	18
14(10)CH	-4.458					**18**	18
18(10)M	-0.002					**18**	18
HOMO	-0.777						
B. cereus		8.512	0.968	1.884	18.299		
14(10)CH	-5.084						
18(10)M	-0.019						
HOMO	-1.039						
IECJDE	0.003						
B. cereus		8.124	0.968	2.100	11.784		
14(10)CH	-5.185						
18(10)M	-0.019						
HOMO	-1.022						
HL Gap	0.045						
IECJDE	0.003						
B. cereus		8.103	0.969	2.060	12.280		
14(10)CH	-4.837						
18(10)M	-0.019						
19(19)M	0.002						
HOMO	-1.066						
IECJDE	0.004						

CONCLUSIONS

In the present paper, we used (local) molecular descriptors for encoding a hypermolecule, as the "mean molecule" in the set. Next, we have calculated quantum molecular and topological indices/descriptors to model the chromatographic retention index $\mathbf{I_{chr}}$ in reversed phase, having the meaning of molecular lipophilicity and being involved in the transport of drugs through membranes to the biological receptors. The biological activity against *Bacillus cereus* was also modeled. Even the work didn't provide the best predictive model, it has a methodological value.

EXPERIMENTAL

Computational

The QSPR study was performed on a series of 20 structures, 10 thiadiazolines and 10 thiosemicarbazones, vs the chomathographic retention index $I_{CHR,}$ while the QSAR study was realized only on the 10 thiadiazolines.

The molecular graphs have been optimized by the Molecular Mechanics MM+ procedure and next at the Hartree-Fock HF level of theory. From the outputs, the HOMO energy, HOMO_LUMO Gap, and the partial charges of all the atoms have been collected. The calculations have been done on Gaussian G09 [17].

Thin-layer chromatography

The reverse phase thin-layer chromatography of the set of 20 molecules, listed in Table 1, was performed using a mixture of *i*-propanol-water as mobile phase, in six different ratios. This experiment provided data, with the meaning of molecular lipophilicity, for multi-linear regression. The chromatographic experimental data were listed in **Table 3**.

Appendix

Mass descriptors **M**, according to the hypermolecule H

	Positions in the Hypermolecule H																							
Structure	**1**	**2**	**3**	**4**	**5**	**6**	**7**	**8**	**9**	**10**	**11**	**12**	**13**	**14**	**15**	**16**	**17**	**18**	**19**	**20**	**21**	**22**	**23**	**24**	**25**
1	13	13	12	13	13	12	0	0	0	0	0	12	14	14	12	32	14	1	0	0	0	0	43	43	15
2	13	13	12	12	13	13	0	0	0	0	0	12	14	14	12	32	14	1	0	0	59	0	43	43	15
3	13	12	12	12	13	13	0	0	0	0	0	13	14	14	12	32	14	1	0	35.5	35.5	0	43	43	0
4	13	12	12	12	13	13	0	0	0	0	0	13	14	14	12	32	14	1	35.5	0	35.5	0	43	43	0
5	13	13	12	12	13	13	0	0	0	0	0	13	14	14	12	32	14	1	0	0	31	0	43	43	0
6	13	13	12	13	12	13	0	0	0	0	0	13	14	14	12	32	14	15	0	0	0	46	43	43	0
7	13	12	12	13	13	12	0	0	0	0	0	13	14	14	12	32	14	77	35.5	35.5	0	0	43	43	0

	Positions in the Hypermolecule H																								
Structure	**1**	**2**	**3**	**4**	**5**	**6**	**7**	**8**	**9**	**10**	**11**	**12**	**13**	**14**	**15**	**16**	**17**	**18**	**19**	**20**	**21**	**22**	**23**	**24**	**25**
8	13	13	12	13	12	13	0	0	0	0	0	13	14	14	12	32	14	77	0	0	0	46	43	43	0
9	13	13	12	13	13	13	12	14	12	13	32	13	14	14	12	32	14	1	0	0	0	0	43	43	0
10	13	13	12	13	13	12	12	14	12	13	32	13	14	14	12	32	14	1	80	0	0	0	43	43	0
11	13	13	12	13	13	12	0	0	0	0	0	12	14	15	12	32	14	1	80	0	0	0	0	1	15
12	13	13	12	12	13	13	0	0	0	0	0	12	14	15	12	32	14	1	0	0	17	0	0	1	15
13	13	12	12	12	13	13	0	0	0	0	0	13	14	15	12	32	14	1	0	35.5	35.5	0	0	1	0
14	13	12	12	13	13	12	0	0	0	0	0	13	14	15	12	32	14	1	35.5	35.5	0	0	0	1	0
15	13	13	12	12	13	13	0	0	0	0	0	13	14	15	12	32	14	1	0	0	31	0	0	1	0
16	13	13	12	12	12	13	0	0	0	0	0	13	14	15	12	32	14	15	0	0	0	46	0	1	0
17	13	13	12	12	13	12	0	0	0	0	0	13	14	15	12	32	14	77	35.5	0	35.5	0	0	1	0
18	13	13	12	13	12	13	0	0	0	0	0	13	14	15	12	32	14	77	0	0	0	46	0	1	0
19	13	13	12	13	13	13	12	14	12	13	32	13	14	15	12	32	14	1	0	0	0	0	0	1	0
20	13	13	12	13	13	12	12	14	12	13	32	13	14	15	12	32	14	1	80	0	0	0	0	1	0

AKNOWLEDGEMENTS

I.A.I. acknowledges the support by POS DRU/107/1.5/S/78702 European project; B.S. thanks to Computational Grant No. 133, PCSS (Poznań, Poland).

REFERENCES

1. T.M. de Aquino, A.P. Liesen, R.E.A. da Silva, V.T. Lima, C.S. Carvalho, A.R. de Faria, J.M. de Araujo, J.G. de Lima, A.J. Alves, E.J.T. de Melo, A.J.S. Goes, *Bioorg. Med. Chem.,* **2007**, *16,* 446-456.
2. S.A. Khan, P. Kumar, R. Joshi, P.F. Iqbal, K. Saleem, *Eur. J. Med. Chem.*, **2008**, *43*, 2029-2034.
3. R.B. Oliveira, E.M. de Souza-Fagundez, R.P.P. Soares, A.A. Andrade, A.U. Krettli, C.L. Zani, *Eur. J. Med. Chem.*, **2008**, *43*, 1983-1988.
4. M. Yusuf, P. Jain, *Arab. J. Chem.*, **2011**: in press.
5. H. Kubinyi, *Quant. Struct.-Act. Relat.*, **1994**, *13*, 285-294.
6. G.G. Oakley, U. Devanaboyina, L.W. Robertson, R.C. Gupta, *Chem. Res. Toxicol.,* **1996**, *9*, 1285-1292.
7. E.M. Silberhorn, H.P. Glauert, L.W. Robertson, *CRC Crit. Rev. Toxicol.,* **1990**, *20*, 439-496.

8. S.C. Basak, G.D. Grunwald, B.D. Gute, K. Balasubramanian, D. Opitz, *J. Chem. Inf. Comput. Sci.,* **2000**, *40*, 885-890.
9. M.V. Diudea, Ed., *QSPR/QSAR Studies by Molecular Descriptors*, Nova Science Publishers, Inc., **2001**.
10. L. Jantschi, S.D. Bolboaca, M.V. Diudea, *Int. J. Mol. Sci.*, **2007**, *8*, 1125-1157.
11. L. Jantschi, S. Mureşan, and M.V. Diudea, *Studia UBB Chemia*, **2001**, *45*, 313-318.
12. R.P. Sheridan, *J. Chem. Inf. Comput. Sci.,* **2000**, *40*, 1456-1469.
13. O.M. Minailiuc, and M.V. Diudea, TI-MTD Model. Applications in Molecular Design, in: *QSPR/QSAR Studies by Molecular Descriptors*, Nova Science Publishers, Inc., **2001**, 363-388.
14. A.T. Balaban, A. Chiriac, I. Motoc and Z. Simon, in: *Lectures Notes in Chemistry*, Vol. 15, Springer, Berlin, **1980**, Chap. 6.
15. M.V. Diudea, *J. Chem. Inf. Comput. Sci.* **1997**, *37*, 300-305
16. M.V. Diudea, *MATCH*, *Commun. Math. Comput. Chem.,* **1997**, *35*, 169-183.
17. Gaussian 09, Revision A.1, Frisch MJ, Trucks GW, Schlegel HB, Scuseria GE, Robb MA, Cheeseman JR, Scalmani G, Barone V, Mennucci B, Petersson GA, Nakatsuji H, Caricato M, Li X, Hratchian HP, Izmaylov AF, Bloino J, Zheng G, Sonnenberg JL, Hada M, Ehara M, Toyota K, Fukuda R, Hasegawa J, Ishida M, Nakajima T, Honda Y, Kitao O, Nakai H, Vreven T, Montgomery JA, Peralta JE, Ogliaro F, Bearpark M, Heyd JJ, Brothers E, Kudin KN, Staroverov VN, Kobayashi R, Normand J, Raghavachari K, Rendell A, Burant JC, Iyengar SS, Tomasi J, Cossi M, Rega N, Millam NJ, Klene M, Knox JE, Cross JB, Bakken V, Adamo C, Jaramillo J, Gomperts R, Stratmann RE, Yazyev O, Austin AJ, Cammi R, Pomelli C, Ochterski JW, Martin RL, Morokuma K, Zakrzewski VG, Voth GA, Salvador P, Dannenberg JJ, Dapprich S, Daniels AD, Farkas Ö, Foresman JB, Ortiz JV, Cioslowski J, Fox DJ (2009) Gaussian Inc Wallingford CT.

STUDIA UBB CHEMIA, LVII, 3, 2012 (p. 121 – 126)
(RECOMMENDED CITATION)

OMEGA POLYNOMIAL IN *AST*-CRYSTAL STRUCTURE

MAHBOUBEH SAHELI[1,*], MOHAMMAD MEHTARI ARANI[1], BEATA SZEFLER[2]

ABSTRACT. Graphs associated to crystal networks can be designed by operations on maps. A repeating unit, made by such an operation, is used to build up the translational network. The topology of the *ast* crystal network is described here in terms of Omega counting polynomial. Close formulas for calculating the polynomial and the Cluj-Ilmenau index derived from it are given for two embeddings of this network.

Keywords: *Omega polynomial, CI index, ast-crystal lattice.*

INTRODUCTION

Several new carbon allotropes have been discovered and studied for applications in nano-technology, in the last twenty years, which can be assigned as the “Nano-era”. The impact of the Nano-Science resulted in reduction of dimensions of electronic devices and increasing their performances, al a lower cost of energy and money. Among the carbon new structures, fullerenes (zero-dimensional), nanotubes (one dimensional), graphene (two dimensional) and spongy carbon (three dimensional) are the most studied [1,2]. The attention of scientists was also focused to inorganic compounds, a realm where almost any metal atom can form clusters, tubules or crystal networks, very ordered structures at the nano-level. Recent articles in crystallography promoted the idea of topological description and classification of crystal structures [3-8]. They present data on real, but also hypothetical lattices, designed by computer.

The present study deals with the design and topological description, in terms of Omega polynomial, of the ast/octadecasil crystal network, presented here in two embeddings.

OMEGA POLYNOMIAL

Let $G(V,E)$ be a connected graph, with the vertex set $V(G)$ and edge set $E(G)$. Two edges $e = uv$ and $f = xy$ of G are called *codistant e co f* if they obey the following relation [9]:

[1] *Payame Noor University, Tehran, 3697-19395, I. R. Iran*
[2] *Department of Physical Chemistry, Collegium Medicum, Nicolaus Copernicus University, Kurpińskiego 5, 85-950, Bydgoszcz, Poland*

$$d(v,x) = d(v,y) + 1 = d(u,x) + 1 = d(u,y) \quad (1)$$

which is reflexive, that is, *e co e* holds for any edge *e* of *G*, and symmetric, if *e co f* then *f co e*. In general, relation *co* is not transitive; an example showing this fact is the complete bipartite graph $K_{2,n}$. If "*co*" is also transitive, thus an equivalence relation, then *G* is called a *co-graph* and the set of edges $C(e) := \{f \in E(G);\ f\ co\ e\}$ is called an *orthogonal cut oc* of *G*, *E*(*G*) being the union of disjoint orthogonal cuts: $E(G) = C_1 \cup C_2 \cup ... \cup C_k,\ C_i \cap C_j = \varnothing, i \neq j$. Klavžar [10] has shown that relation *co* is a theta Djoković-Winkler relation [11,12].

We say that edges *e* and *f* of a plane graph *G* are in relation *opposite, e op f,* if they are opposite edges of an inner face of *G*. Note that the relation *co* is defined in the whole graph while *op* is defined only in faces. Using the relation *op* we can partition the edge set of *G* into *opposite* edge *strips, ops.* An *ops* is a quasi-orthogonal cut *qoc*, since *ops* is not transitive.

Let *G* be a connected graph and S_1, S_2, ..., S_k be the *ops* strips of *G*. Then the *ops* strips form a partition of *E(G)*. The length of *ops* is taken as maximum. It depends on the size of the maximum fold face/ring F_{max}/R_{max} considered, so that any result on Omega polynomial will have this specification.

Denote by *m*(*G*,*s*) the number of *ops* of length *s*. The Omega polynomial [13-15] is defined as:

$$\Omega(G,x) = \sum_s m(G,s) \cdot x^s \quad (2)$$

Its first derivative (in *x*=1) equals the number of edges in the graph:

$$\Omega'(G,1) = \sum_s m(G,s) \cdot s = e = |E(G)| \quad (3)$$

On Omega polynomial, the Cluj-Ilmenau index [9], *CI*=*CI*(*G*), was defined:

$$CI(G) = \{[\Omega'(G,1)]^2 - [\Omega'(G,1) + \Omega''(G,1)]\} \quad (4)$$

LATTICE BUILDING

The crystal network named ast/octadecasil/sqc3869 is a 2-nodal net that belongs to the group Fm-3m [16]. It has the point symbol for net $(4^3.6^3)4(6^6)$ and stoichio-metry (4-c)4(4-c). Figure 1, left presents the unit CQ_32, designed by the quadrupling *Q*-map operation performed on the cube C and having 32 atoms; in the right part of this figure the unit cell of the net is illustrated.

The net is constructed by identifying the hexagonal faces of the units and is denoted CQ6. Figure 2 presents two different embeddings of this crystal network, on which we performed the calculations.

Figure 1. Repeating unit of ast/sqc3869 network: CQ_32; $(4.6^2)(6^3)$ (left) and CQ6_unit cell (right)

Figure 2. Two embeddings of ast network: CQ6_DP-series ((3,3,3)_492, left) and CQ6_TP-series ((3,3,3)_484, right)

MAIN RESULTS

Within this paper, the Omega polynomial and derived Cluj-Ilmenau CI index refer to $F_{max}(6)$. Data were calculated by software program Nano Studio [17], developed at the TOPO Group Cluj. Formulas for the infinite networks of the two series were derived by numerical analysis, function of *k* that is the number of repeating units in a row of a cubic domain (*k*,*k*,*k*), and are listed in Tables 1 and 2; examples are given at the bottom of these tables. Formulas for the number of vertices and number of various rings are given in Tables 3 and 4, respectively.

Table 1. Omega polynomials in **CQ6_DP**

Formulas
$\Omega(G,x) = 2\left[\sum_{i=1}^{k-1} x^{(2k-2)+(4k+4)i} + \sum_{i=1}^{k} x^{2i^2+6i} + 2\sum_{i=1}^{k-1} x^{2k+(2k+2)i} + \sum_{i=1}^{\frac{2k-7-(-1)^k}{4}} x^{(2k^2+6k)+4(k-1-i)i}\right]$
$+ (2k+2)\, x^{2k(k+2)} + k\, x^{4k(k+1)} + \frac{3+(-1)^k}{2}\, x^{(3k^2+4k+\frac{1-(-1)^k}{2})} + 1\, x^{4k^2+6k-2}$
$CI(G) = 400k^6 + \frac{7756}{5}k^5 + \frac{2648}{3}k^4 - \frac{3532}{3}k^3 + \frac{2384}{6}k^2 - \frac{1408}{15}k + 8$
$\lvert E(G)\rvert = 20k^3 + 40k^2 - 14k + 2$

k	Omega polynomial: examples	*e*(*G*)	*CI*(*G*)
2	$2x^{8}+4x^{10}+2x^{14}+6x^{16}+2x^{20}+2x^{24}+1x^{26}$	294	81352
3	$2x^{8}+4x^{14}+4x^{20}+4x^{22}+8x^{30}+4x^{36}+1x^{40}+3x^{48}+1x^{52}$	860	711552
4	$2x^{8}+4x^{18}+2x^{20}+2x^{26}+4x^{28}+2x^{36}+4x^{38}+2x^{46}+10x^{48}+2x^{56}+2x^{64}+2x^{66}+4x^{80}+1x^{86}$	1866	3383432
5	$2x^{8}+2x^{20}+4x^{22}+2x^{32}+4x^{34}+2x^{36}+4x^{46}+4x^{56}+4x^{58}+12x^{70}+4x^{80}+2x^{92}+1x^{96}+2x^{104}+5x^{120}+1x^{128}$	3432	11511472
6	$2x^{8}+2x^{20}+4x^{26}+2x^{36}+2x^{38}+4x^{40}+4x^{54}+2x^{56}+2x^{66}+4x^{68}+2x^{80}+4x^{82}+2x^{94}+14x^{96}+2x^{108}+2x^{122}+2x^{124}+2x^{132}+2x^{150}+6x^{168}+1x^{178}$	5678	31627912

Table 2. Omega polynomials in **CQ6_TP**

Formulas

$$\Omega(G,x)=2\left[\sum_{i=1}^{k}x^{i^2+4i+1}+3\sum_{i=1}^{k-1}x^{2k+(4k+2)i}+\sum_{i=1}^{\frac{2k-7-(-1)^k}{4}}x^{k^2+4k+1+2(k-1)i-2i^2}\right]$$

$$+\frac{3+(-1)^k}{2}\,x^{\frac{6k^2+12k+5-(-1)^k}{4}}+3k\;x^{2k(k+2)}+3\;x^{4k(k+1)}$$

$$CI(G)=400k^6+\frac{6969}{5}k^5+917k^4-650k^3-116k^2+\frac{86}{5}k+6$$

$$\left|E(G)\right|=20k^3+36k^2-6k-2$$

k	Omega polynomial: examples	*e*(*G*)	*CI*(*G*)
2	$2x^{6}+2x^{13}+6x^{14}+6x^{16}+3x^{24}$	290	79250
3	$2x^{6}+2x^{13}+6x^{20}+2x^{22}+1x^{24}+9x^{30}+6x^{34}+3x^{48}$	844	686034
4	$2x^{6}+2x^{13}+2x^{22}+6x^{26}+2x^{33}+2x^{37}+6x^{44}+12x^{48}+6x^{62}+3x^{80}$	1830	3257022
5	$2x^{6}+2x^{13}+2x^{22}+6x^{32}+2x^{33}+2x^{46}+2x^{52}+7x^{54}+15x^{70}+6x^{76}+6x^{98}+3x^{120}$	3368	11094692
6	$2x^{6}+2x^{13}+2x^{22}+2x^{33}+6x^{38}+2x^{46}+2x^{61}+6x^{64}+2x^{69}+2x^{73}+6x^{90}+18x^{96}+6x^{116}+6x^{142}+3x^{168}$	5578	30544554

Table 3. Number of atoms $v = |V(G)|$

$\|V(CQ6\_DP)\| = 10k^3 + 26k^2 - 4k,$ $\|V(CQ6\_TP)\| = 10k^3 + 24k^2 - 2$		
k	CQ6_DP	CQ6_TP
2	176	174
3	492	484
4	1040	1022
5	1880	1848
6	3072	3022

Table 4. Number of rings

$CQ6\_DP \Rightarrow |R[4]| = 6k^3 + 20k^2 + 18k + 6, \quad |R[6]| = 10k^3 + 36k^2 + 33k + 12$

$CQ6\_TP \Rightarrow |R[4]| = 6k^3, \quad R[6]| = 10k^3 + 3k^2 - 3k + 2$

	CQ6_DP		CQ6_TP	
k	R[4]	R[6]	R[4]	R[6]
2	50	91	48	88
3	170	302	162	290
4	402	705	384	678
5	782	1360	750	1312
6	1346	2327	1296	2252

CONCLUSIONS

Crystal networks can be represented by graphs of which design can be performed by operations on maps. The repeating unit, made by Quadrupling operation applied on the cube, was used to build up the *ast*-network. The topology of this crystal network was described in terms of Omega counting polynomial. Close formulas for calculating the polynomial and the Cluj-Ilmenau index were given for two embeddings of the net.

ACKNOWLEDGMENTS

Authors are indebted to Prof. Davide Proserpio, University of Milan, Italy, for the crystallographic data.

REFERENCES

1. M.V. Diudea, Ed., “Nanostructures, novel architecture”, NOVA, **2005**.
2. M.V. Diudea and Cs.L. Nagy, “Periodic Nanostructures”, Springer, **2007**.
3. L. Carlucci, G. Ciani and D. Proserpio, *Coord. Chem. Rev.*, **2003**, *246*, 247.
4. L. Carlucci, G. Ciani and D. Proserpio, *Cryst. Eng. Comm.*, **2003**, *5*, 269.
5. V.A. Blatov, L. Carlucci, G. Ciani and D. Proserpio, *Acta Cryst. Eng. Comm*., **2004**, *6*, 377.
6. I.A. Baburin, V.A. Blatov, L. Carlucci, G. Ciani and D. Proserpio*, J. Solid State Chem.*, **2005**, *178*, 2452.
7. O. Delgado-Friedrichs and M. O’Keeffe, *J. Solid State Chem.*, **2005**, *178*, 2480.
8. V.A. Blatov, O. Delgado-Friedrichs, M. O’Keeffe, and D. Proserpio, *Acta Cryst. Eng. Comm.*, **2007**, A63, 418.
9. P.E. John, A.E., Vizitiu, S. Cigher, M.V. Diudea, *MATCH Commun. Math. Comput. Chem.*, **2007**, *57*, 479.
10. S. Klavžar, *MATCH Commun. Math. Comput. Chem.*, **2008**, *59*, 217.
11. D.Ž. Djoković, *J. Combin. Theory Ser. B*, **1973**, *14*, 263.
12. P.M. Winkler, *Discrete Appl. Math.,***1984**, *8*, 209.
13. M.V. Diudea, *Carpath. J. Math.*, **2006**, *22*, 43.
14. M.V. Diudea, S. Cigher and P.E. John, *MATCH Commun. Math. Comput. Chem*., **2008**, *60*, 237.
15. M.V. Diudea, S. Cigher, A.E. Vizitiu, M.S. Florescu and P.E. John, *J. Math. Chem*., **2009**, *45*, 316.
16. http://www.topos.ssu.samara.ru/index.html
17. Cs.L. Nagy, M.V. Diudea, “Nano Studio software“, Babes-Bolyai Univ., **2009**.

STUDIA UBB CHEMIA, LVII, 3, 2012 (p. 127 – 136)
(RECOMMENDED CITATION)

CLUJ, OMEGA AND RELATED POLYNOMIALS IN TORI T(4,4)R[*c*,*n*]

FARZANEH GHOLAMI-NEZHAAD[1], BEATA SZEFLER[2], MONICA STEFU[3]

ABSTRACT. Cluj and Omega polynomials were designed to describe the graphs associated to polyhedral nanostructures: their exponents express the extent of partitions of a graph property while the coefficients count the partitions of a given extent. Basic definitions and properties of these and some other related counting polynomials are given, as derived from the cutting procedure of their calculation. Formulas to calculate these polynomials in T(4,4)R[*c*,*n*] tori are given and exemplified.

Keywords: *Cluj polynomial, Omega polynomial, nanotori*

POLYNOMIALS IN CHEMISTRY

One of the most used representations of a molecular graph is that of a polynomial. In Quantum Chemistry, the early Hückel theory made use of the *characteristic polynomial* in calculating the levels of π-electron energy of the molecular orbitals, in conjugated hydrocarbons [1-4]:

$$Ch(x) = \det[x\mathbf{I} - \mathbf{A}] \quad (1)$$

In the above, **I** is the unit matrix of a pertinent order and **A** the adjacency matrix of the graph *G*. The characteristic polynomial is involved in the evaluation of topological resonance energy TRE, the topological effect on molecular orbitals TEMO, the aromatic sextet theory, the Kekulé structure count, *etc*. [4-8]

A general form of a counting polynomial is the following:

$$P(\mathbf{M}, x) = \sum_k m(k) \cdot x^k \quad (2)$$

where the exponents represent the extent of partitions *p*(*G*), $\cup\, p(G) = P(G)$ of a graph property *P*(*G*) while the coefficients $m(k)$ are related to the number of

[1] *Department of Nanocomputing, Institute of Nanoscience and Nanotechnology, University of Kashan, Kashan 87317-51167, I. R. Iran*
[2] *Department of Physical Chemistry, Collegium Medicum, Nicolaus Copernicus University, Kurpińskiego 5, 85-950, Bydgoszcz, Poland*
[3] *Faculty of Chemistry and Chemical Engineering, Babes-Bolyai University, 400028 Cluj, Romania, diudea@gmail.com*

partitions of extent *k*. In relation (2), the coefficients $m(k)$ are calculable from the graph *G* by a method making use of the *Sachs graphs*, which are subgraphs of *G*. Some numeric methods of linear algebra, can eventually be more efficient in large graphs [9,10]. More about the characteristic polynomial, the reader can find in ref [1].

In the Mathematical Chemistry literature, the counting polynomials have been introduced by Hosoya [11,12] and later by other scientists [12,21].

POLYNOMIALS OF VERTEX PROXIMITY

Cluj polynomials are defined [22-25] on the basis of vertex proximities p_i,

$$P(\mathbf{UCJ}, x) = \sum_k m(k) \cdot x^k \tag{3}$$

where summation runs over all $k = |\{p\}|$ in *G* with *p* being the proximity of the vertex *i* with respect to any vertex *j* in *G*, joined to *i* by an edge $\{p_{e,i}\}$ (the Cluj-edge polynomials) or by a path $\{p_{p,i}\}$ (the Cluj-path polynomials), taken as the shortest (*i.e.*, distance DI) or the longest (*i.e.*, detour DE) paths.

In (3), the coefficients *m*(*k*) can be calculated from the entries in the non-symmetric Cluj matrices (as provided by the TOPOCLUJ software program) [26] which represent vertex proximities. To define these, we need some theoretical background, as follows.

A graph *G* is a *partial cube* if it is embeddable in the *n*-cube Q_n, which is the regular graph whose vertices are all binary strings of length *n*, two strings being adjacent if they differ in exactly one position [27]. The distance function in the *n*-cube is the Hamming distance. A hypercube can also be expressed as the Cartesian product: $Q_n = \square_{i=1}^{n} K_2$. A subgraph $H \subseteq G$ is called *isometric*, if $d_H(u,v) = d_G(u,v)$, for any $(u,v) \in H$; it is *convex* if any shortest path in *G* between vertices of *H* belongs to *H*.

For any edge *e*=(*u*,*v*) of a connected graph *G* let n_{uv} denote the set of vertices lying closer to *u* than to *v*: $n_{uv} = \{w \in V(G) \mid d(w,u) < d(w,v)\}$. It follows that $n_{uv} = \{w \in V(G) \mid d(w,v) = d(w,u) + 1\}$. The sets (and subgraphs) induced by these vertices, n_{uv} and n_{vu}, are called *semicubes* of *G*; the semicubes are called *opposite semicubes* and are disjoint [28].

A graph *G* is bipartite if and only if, for any edge of *G*, the opposite semicubes define a partition of *G*: $n_{uv} + n_{vu} = v = |V(G)|$. These semicubes are just the vertex proximities of (the endpoints of) edge *e*=(*u*,*v*), which *CJ* polynomial counts. In partial cubes, the semicubes can be estimated by an orthogonal edge-cutting procedure.

The orthogonal cuts form a partition of the edges in *G*:

$$E(G) = c_1 \cup c_2 \cup ... \cup c_k,\ c_i \cap c_j = \varnothing, i \neq j\ .$$

To perform an orthogonal edge-cutting [25,29-32] take a straight line segment, orthogonal to the edge *e*, and intersect *e* and all its parallel edges (in a polygonal plane graph). The set of these intersections is called an *orthogonal cut* c_k, k=1,2,..,k_{max} of *G*, with respect to the edge *e* (Figure 1). To any orthogonal cut c_k, two numbers are associated: first one represents the *number of edges* e_k "cut-off", or the cutting cardinality | c_k | while the second (in round brackets, in Figure 1) is v_k or the number of points lying to the left hand with respect to c_k.

Cluj and some related polynomials are calculable from the semicubes in *G* (see the polynomial exponents, Figure 1), they differing only in the mathematical operation used in composing the edge contributions to the global graph property. Because, in a bipartite graph, the opposite semicubes define a partition of vertices, it is easily to identify the two semicubes: $n_{uv} = v_k$ and $n_{vu} = v\text{-}v_k$ or vice-versa.

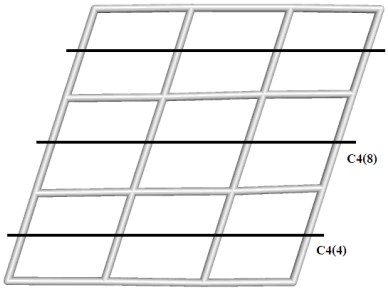

CJ S(x) = 2·2·4(x^4+x^{12})+ 2·1·4(x^8+x^8)
= 16x^4+16x^8+16x^{12}
CJ S'(1) = 384;
PI$_v$(x) = 2·2·4(x^{4+12})+ 2·1·4(x^{8+8})
=16x^{16} +8x^{16} = 24x^{16};
PI$_v$'(1) = 384;

CJ P(x) = 2·2·4($x^{4.12}$)+ ·1·4($x^{8.8}$)
= 16x^{48}+ 8x^{64} =SZ(x)
CJ P'(1) = 1280=SZ'(1);

$\Omega(x)$ = (2·3)x^4
$\Omega'(1)$ =24=*e*=|*E*(*G*)|
$CI(G) = 480$;
$\Theta(x)$ = 4(2·3)x^4
$\Theta'(1) = 96$;
$\Pi(x)$ = 4(2·3)x^{20}
$\Pi'(1)$ =480=PI'(1)

Figure 1. Calculating of several topological descriptors by the Cutting procedure

The coefficients of these descriptors are calculated (with some exceptions) as the product of three numbers (in the front of brackets - right hand part of Figure 1) with the meaning: (i) symmetry of *G*; (ii) occurrence of c_k (in the whole structure) and (iii) e_k.

According to the mathematical operation used in composing the graph semicubes, four polynomials can be defined:

(i) *Summation*, and the polynomial is called *Cluj-Sum*, by Diudea *et al*. [22-25,31-33] (and symbolized CJ_eS):

$$CJ_eS(x) = \sum_e \left(x^{v_k} + x^{v-v_k} \right) \tag{4}$$

(ii) *Pair-wise summation*, with the polynomial called (vertex) Padmakar-Ivan [34] by Ashrafi [35-38] (and symbolized PI_v):

$$PI_v(x) = \sum_e x^{v_k + (v-v_k)} \tag{5}$$

(iii) *Pair-wise product*, while the polynomial is called *Cluj-Product* (and symbolized CJ_eP) [25,31,39-43] or also *Szeged* polynomial (and symbolyzed *SZ*) [36-38]:

$$CJ_eP(x) = SZ(x) = \sum_e x^{v_k (v-v_k)} \tag{6}$$

The first derivative (in x=1) of a (graph) counting polynomial provides single numbers, often called topological indices.

It is not difficult to see that the first derivative (in x=1) of the first two polynomials gives one and the same value; however, their second derivative is different and the following relations hold in any graph [24]:

$$CJ_eS'(1) = PI_v'(1)\ ;\ CJ_eS''(1) \neq PI_v''(1) \tag{7}$$

The number of terms is given by the value of the polynomial in x=1: it is $CJ_eS(1)=2e$ and $PI_v(1)=e$, respectively, because in the last case the two endpoint contributions are pair-wise summed for any edge in a bipartite graph.

Observe the first derivative (in x=1) of $PI_v(x)$ takes the maximal value in bipartite graphs:

$$PI_v'(1) = e \cdot v = |E(G)| \cdot |V(G)| \tag{8}$$

It can also be seen by considering the definition of the corresponding index [44]:

$$PI_v(G) = PI_v'(1) = \sum_{e=uv} n_{u,v} + n_{v,u} = |V| \cdot |E| - \sum_{e=uv} m_{u,v} \tag{9}$$

where $n_{u,v}$, $n_{v,u}$ count the non-equidistant vertices with respect to the endpoints of the edge $e=(u,v)$ while $m(u,v)$ is the number of equidistant vertices *vs*. u and v. However, it is known that, in bipartite graphs, there are no equidistant vertices *vs*. any edge, so that the last term in (9) is null. The value of $PI_v(G)$ is thus maximal in bipartite graphs, among all graphs on the same number of vertices; the result of (8) can be used as a criterion for checking the "bipatity" of a graph.

The third polynomial uses the pair-wise product; notice that Cluj-Product $CJ_eP(x)$ is precisely the (vertex) Szeged polynomial $SZ_v(x)$, defined by Ashrafi *et al*. [36-38].This comes out from the relations between the basic Cluj (Diudea [39-41,45,46]) and Szeged (Gutman [46,47]) indices:

$$CJ_eP'(1) = CJ_eDI(G) = SZ(G) = SZ_v'(1) \tag{10}$$

These polynomials (and their derived indices) do not count the equidistant vertices, an idea introduced in Chemical Graph Theory by Gutman [47]. When subscript letter is missing, $SZ(x)$ is $SZ_v(x)$.

POLYNOMIALS OF VERTEX PROXIMITY IN RHOMB-TILED TORI

The covering (4,4)S, embedded in the torus, can be changed to the rhombic (4,4)R pattern by the Medial *Med* operation on maps [48].

$$Med(\mathrm{T}(4,4)\mathrm{S}[c,n]) \longrightarrow (\mathrm{T}(4,4)\mathrm{R}[2c,n]) \tag{11}$$

Since the *Med* operation will double the number of points in the original object (*i.e.*, the vertex multiplicity m =2), it is clear that these graphs are bipartite.

The cutting procedure can be applied in case of rhomb-tiled tori T(4,4)R[*c*,*n*]; each cutting provides halves, as illustrated in Figure 2. Table 1 includes both formulas and pertinent examples in this series.

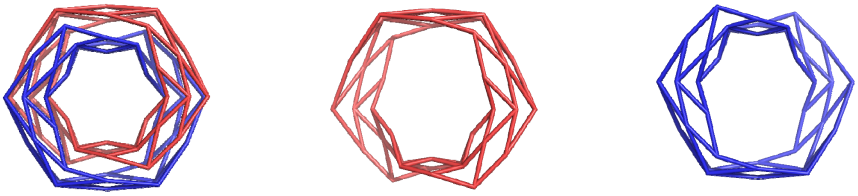

Figure 2. Cutting procedure in rhomb-tiled tori T(4,4)R[*c*,*n*]; the two halves are red/blue colored.

The rhomb-tiled tori are not partial cubes, then the cutting procedure cannot be applied in calculating the Wiener index $W(G)$ [30].

POLYNOMIALS OF EDGE PROXIMITY

Let $G=(V(G),E(G))$ be a connected graph, with the vertex set $V(G)$ and edge set $E(G)$. Two edges $e = (u,v)$ and $f = (x,y)$ of G are called *co-distant* (briefly: *e co f*) if the notation can be selected such that [28,49]:

$$e\ co\ f \Leftrightarrow d(v,x) = d(v,y)+1 = d(u,x)+1 = d(u,y) \tag{12}$$

where d is the usual shortest-path distance function. Relation *co* is reflexive, that is, *e co e* holds for any edge *e* of G and it is also symmetric: if *e co f* then also *f co e*. In general, *co* is not transitive. A graph is called a *co-graph* if the relation *co* is transitive and thus an equivalence relation.

Table 1. Polynomials of vertex proximity in tori T(4,4)R[*c*,*n*] designed by Med(T(4,4)S[*c*,*n*]); vertex multiplicity *m*=2.

Formulas	
$CJS(x) = e(x^{v/2} + x^{v/2})$	$CJP(x) = SZ(x) = e(x^{v/2 \cdot v/2})$
$CJS'(1) = e(v/2 + v/2) = e \cdot v = 2(cn)^2$	$CJP'(1) = e(v/2 \cdot v/2) = e(v/2)^2$
$PI_v(x) = e(x^{v/2+v/2}) = e \cdot x^v$	$= (1/2)v^3 = (1/2)(cn)^3$
$PI_v'(1) = e \cdot v = CJ_eS'(1)$	$v = cn;\ \ e = 2c \cdot 2n$

Examples

Med(T(4,4)S[5,10]): CJS(x)=400x^{50}; P`(1)=20000; PI$_v$(x)=200x$^{100}$; P`(1)=20000
Med(T(4,4)S[5,15]): CJS(x)=600x^{75}; P`(1)=45000; PI$_v$(x)=300x$^{150}$; P`(1)=45000
Med(T(4,4)S[5,20]): CJS(x)=800x^{100}; P`(1)=80000; PI$_v$(x)=400x$^{200}$; P`(1)=80000
Med(T(4,4)S[5,10]): CJP(x)=200x^{2500}; P`(1)=500000; *v*=100; *e*= 200.
Med(T(4,4)S[5,15]): CJP(x)=300x^{5625}; P`(1)= 1687500; *v*=150; *e*= 300.
Med(T(4,4)S[5,20]): CJP(x)=400x^{10000}; P`(1)= 4000000; *v*=200; *e*= 400.

For an edge $e \in E(G)$, let $c(e) := \{f \in E(G);\ f\ co\ e\}$ be the set of edges codistant to *e* in *G*. The set *c*(*e*) can be obtained by an *orthogonal cut oc* of *G*, with respect to *e*. If *G* is a *co-graph* then its orthogonal cuts form a partition in *G* (see above). A bipartite graph *G* is a *co-graph* if and only if it is a *partial cube*, and all its semicubes are convex. However, a *co*-graph can also be non-bipartite [32] (*e.g.*, it shows a transitive *co*-relation but has at least one odd cycle, thus being no more a partial cube). It was proven that relation *co* is a *theta* (Djoković [50]) and Winkler [51]) relation.

Two edges *e* and *f* of a plane graph *G* are in relation *opposite, e op f,* if they are opposite edges of an inner face of *G*. Then *e co f* holds by assuming the faces are isometric. Note that relation *co* involves distances in the whole graph while *op* is defined only locally (it relates face-opposite edges). If *G* is a *co*-graph, then its opposite edge strips *ops* {s_k} superimpose over the orthogonal cut sets *ocs* {c_k} and $|c_k|=|s_k|$.

Using the relation *op* we can partition the edge set of *G* into *opposite* edge *strips, ops*: any two subsequent edges of an *ops* are in *op* relation and any three subsequent edges of such a strip belong to adjacent faces. Note that John *et al*. [49] implicitly used the "*op*" relation in defining the Cluj-Ilmenau index *CI* (see below).

Let us denote by *m*(*s*) or simply *m* the number of *ops* of length $s=|s_k|$ and define the Omega polynomial as [52-55]:

$$\Omega(x) = \sum_s m \cdot x^s \tag{13}$$

The exponents count just the intersected edges by the cut-line (in a cutting procedure), which does not need to be orthogonal on all the edges of an *ops.*

In *co*-graphs/partial cubes, other two related polynomials [48] can be calculated:

$$\Theta(x) = \sum_s ms \cdot x^s \tag{14}$$

$$\Pi(x) = \sum_s ms \cdot x^{e-s} \tag{15}$$

The above polynomials count codistant and non-codistant edges, respectively. Thus, non-co-distance is related to edge-proximity, and the name of these polynomials is immediate.

The first derivative (computed at x=1) of these counting polynomials provide interesting topological indices [48]:

$$\Omega'(1) = \sum_s ms = e = |E(G)| \tag{16}$$

$$\Theta'(1) = \sum_s ms^2 = \Theta(G) \tag{17}$$

$$\Pi'(1) = \sum_s ms(e-s) = \Pi(G) \tag{18}$$

On $\Omega(x)$ an index, called Cluj-Ilmenau [49] *CI*(*G*), was defined

$$CI(G) = \left\{[\Omega'(1)]^2 - [\Omega'(1) + \Omega''(1)]\right\} \tag{19}$$

In *co*-graphs, there is the equality [48]: $CI(G) = \Pi(G)$. This result can be obtained applying the definition (19):

$$CI(G) = \left(\sum_s ms\right)^2 - \left[\sum_s ms + \sum_s ms(s-1)\right] = e^2 - \sum_s ms^2 = \Pi(G) \tag{20}$$

Relation (20) is just the formula proposed by John *et al*. [56] to calculate the Khadikar's *PI* index [34]. According to Ashrafi's notations [57], PI_e (to difer from PI_v) can be written as:

$$PI_e(G) = \sum_{e \in E(G)} \left[n(e,u) + n(e,v)\right] - m(u,v) \tag{21}$$

where $n(e,u)$ is the number of edges lying closer to the vertex u than to the v vertex while $m(u,v)$ is the number of edges equidistant from u and v.

This index can be calculated as the first derivative, in x=1, of the polynomial defined by Ashrafi [57] as:

$$PI_e(x) = \sum_{e \in E(G)} x^{n(e,u)+n(e,v)} \tag{22}$$

In bipartite graphs, either *co*-graphs or not, the equality: $\Pi(G) = PI_e(G)$ is true, but not in general graphs. In partial cubes, since they are also bipartite, the previous equality can be expanded to

$$CI(G) = \Pi(G) = PI_e(G) \tag{23}$$

a relation precisely true in partial cubes but not in all *co*-graphs (e.g., in non-bipartite co-graphs). As the rhomb-tiled tori are not *co*-graphs, then $CI(G) \neq \Pi(G)$.

Formulas for the above three polynomials in rhomb-tiled tori T(4,4)R[*c*,*n*] are given in Table 2, along with some examples.

Table 2. Polynomials of Edge Proximity in tori T(4,4)R[*c*,*n*] designed by Med(T(4,4)S[*c*,*n*]); vertex multiplicity *m*=2.

Formulas	
$\Omega(x) = 2c \cdot x^{2n}$	$\Pi(x) = e \cdot x^{e-(6c-2)}$
$CI = 16c^2n^2 - 8cn^2$	$\Pi'(1) = e[e-(6c-2)]$
$\Theta(x) = 2c \cdot 2n \cdot x^{6c-2} = e \cdot x^{6c-2}$	$v = cn\,;\ \ e = 2c \cdot 2n$
$\Theta'(1) = e \cdot (6c-2)$	
Examples	
T[**10**,30]; $\Omega(x)$ =20x^{60}; CI=1368000;	$\Theta(x)$ =1200x^{58}; $\Theta'(1)$ = 69600;
	$\Pi(x)$ =1200x^{1142}; $\Pi'(1)$ =1370400
T[**15**,30]; $\Omega(x)$ =30x^{60}; CI=3132000;	$\Theta(x)$ =1800x^{88}; $\Theta'(1)$ =158400;
	$\Pi(x)$ =1800x^{1712}; $\Pi'(1)$ =3081600
T[**10**,40]; $\Omega(x)$ =20x^{80}; CI=2432000;	$\Theta(x)$ =1600x^{58}; $\Theta'(1)$ =92800;
	$\Pi(x)$ =1600x^{1542}; $\Pi'(1)$ =2467200

CONCLUSIONS

Cluj and Omega polynomials can be defined on the ground of an orthogonal cutting procedure. Some other related counting polynomials were derived by the cutting procedure. Formulas to calculate these polynomials in T(4,4)R[*c*,*n*] tori were given and exemplified.

REFERENCES

1. M.V. Diudea, I. Gutman, L. Jäntschi, *Molecular Topology*, NOVA, New York, **2002**.
2. F. Harary, *SIAM Rev*., **1962**, *4*, 202.
3. H. Sachs, *Publ. Math. (Debrecen),* **1964**, *11*, 119.
4. N. Trinajstić, *Chemical Graph Theory*, II[nd] Ed. CRC Press, **1992**.
5. I. Gutman, M. Milun, N. Trinajstić, *MATCH Commun. Math. Comput. Chem.*, **1975**, *1*, 171.
6. J. Aihara, *J. Am. Chem. Soc.*, **1976**, *98*, 2750.
7. I. Gutman, M. Milun, N. Trinajstić, *J. Am. Chem. Soc*., **1977**, *99*, 1692.
8. A. Tang, Y. Kiang, G. Yan, S. Tai, *Graph Theoretical Molecular Orbitals*; Science Press, Beijing, **1986**.
9. P. S. Dwyes, *Linear Computations*, Wiley, N.Y., **1951**.
10. D.K. Fadeev, I.S. Sominskii, *Problems in Higher Algebra*, Freeman, San Francisco, **1965**.
11. H. Hosoya, *Bull. Chem. Soc. Japan*, **1971**, *44*, 2332.
12. H. Hosoya, *Discrete Appl. Math*., **1988**, *19*, 239.
13. E.V. Konstantinova, M.V. Diudea, *Croat. Chem. Acta*, **2000**, *73*, 383.
14. I. Gutman, S. Klavžar, M. Petkovšek, P. Žigert, *MATCH Commun. Math. Chem.*, **2001**, *43*, 49.
15. H. Hosoya, T. Yamaguchi, *Tetrahedron Lett*., **1975**, 4659.
16. N. Ohkami, H. Hosoya, *Theoret. Chim. Acta*, **1983**, *64*, 153.
17. N. Ohkami, A. Motoyama, T. Yamaguchi, H. Hosoya, *Tetrahedron*, **1981**, *37*, 1113.
18. H. Hosoya, *Topics Curr. Chem*., **1990**, *153*, 255.
19. E. Clar, *Polycyclic Hydrocarbons*, Acad. Press, London, **1964**.
20. E. Clar, *The Aromatic Sextet*, Wiley, New York, **1972**.
21. I. Gutman, H. Hosoya, *Z. Naturforsch*., **1990**, *45a*, 645.
22. M.V. Diudea, *J. Math. Chem*., **2009**, *45*, 295.
23. M.V. Diudea, A.E. Vizitiu, D. Janežič, *J. Chem. Inf. Model*., **2007**, *47*, 864.
24. M.V. Diudea, A. Ilić, M. Ghorbani, A.R. Ashrafi, *Croat. Chem. Acta*, **2010**, *83*, 283.
25. M.V. Diudea, N. Dorosti, A. Iranmanesh, *Studia UBB Chemia*, **2010**, *55* (*4*), 247.
26. O. Ursu, M.V. Diudea, TOPOCLUJ software program, Babes-Bolyai University, Cluj, 2005.
27. F. Harary, *Graph theory*, Addison-Wesley, Reading, MA, 1969.
28. M.V. Diudea, S. Klavžar, *Acta Chem. Sloven.*, **2010**, *57*, 565.

29. I. Gutman, S. Klavžar, *J. Chem. Inf. Comput. Sci*., **1995**, *35*, 1011.
30. S. Klavžar, *MATCH Commun. Math. Comput. Chem.,* **2008**, *60*, 2554.
31. M.V. Diudea, in I. Gutman, B. Furtula (Eds.), New Molecular Structure Descriptors - Theory and Applications I, Univ. Kragujevac, Kragujevac Kragujevac, **2010**, p. 191.
32. M.V. Diudea, *MATCH Commun. Math. Comput. Chem.,* **2010**, *64*, 569.
33. A.E. Vizitiu, M.V. Diudea, *Studia UBB Chemia*, **2009**, *54*(1), 173.
34. P.V. Khadikar, *Nat. Acad. Sci. Lett*., **2000**, *23*, 113.
35. M.H. Khalifeh, H. Yousefi-Azari, A.R. Ashrafi, *Discrete Appl. Math.,* **2008**, *156*, 1780.
36. M.H. Khalifeh, H. Yousefi-Azari, A.R. Ashrafi, *Linear Algebra Appl*., **2008**, *429*, 2702.
37. A.R. Ashrafi, M. Ghorbani, M. Jalali, *J. Theor. Comput. Chem.,* **2008**, *7*, 221.
38. T. Mansour, M. Schork, *Discr. Appl. Math*., **2009**, *157*, 1600.
39. M.V. Diudea, *J. Chem. Inf. Comput. Sci.,* **1997**, *37*, 300.
40. M.V. Diudea, *MATCH Commun. Math. Comput. Chem.,* **1997**, *35*, 169.
41. M.V. Diudea, B. Parv, I. Gutman, *J. Chem. Inf. Comput. Sci.,* **1997**, *37*, 1101.
42. I. Gutman, M.V. Diudea, *J. Serb. Chem. Soc*., **1998**, *63*, 497.
43. M.V. Diudea, G. Katona, I. Lukovits, N. Trinajstić, *Croat. Chem. Acta*, **1998**, *71*, 459.
44. A. Ilić, *Appl. Math. Lett.*, **2010**, *23*(*10*), 1213.
45. M.V. Diudea, *Croat*. *Chem*. *Acta,* **1999**, *72*, 835.
46. M.V. Diudea, I. Gutman, L. Jäntschi, *Molecular Topology*. NOVA, New York, **2002**.
47. I. Gutman, *Graph Theory Notes New York*, **1994**, *27*, 9.
48. M.V. Diudea, Nanomolecules and Nanostructures, Polynomials and Indices, MCM, No. 10, Univ. Kragujevac, Serbia, **2010**.
49. P.E. John, A.E. Vizitiu, S. Cigher, M.V. Diudea, *MATCH Commun. Math. Comput. Chem.*, **2007**, *57*, 479.
50. D.Ž. Djoković, *J. Combin. Theory Ser. B*, **1973**, *14*, 263.
51. P.M. Winkler, *Discrete Appl. Math*., **1984**, *8*, 209.
52. M.V. Diudea, *Carpath. J. Math*., **2006**, *22*, 43.
53. M.V. Diudea, A. Ilić, *Carpath. J. Math*., **2009**, *25*, 177.
54. M.V. Diudea, *J. Math. Chem*., **2009**, *45*, 309.
55. M.V. Diudea, A.E. Vizitiu, F. Gholaminezhad, A.R. Ashrafi, *MATCH Commun. Math. Comput. Chem.,* **2008**, *60*, 945.
56. P.E. John, P.V. Khadikar, J.A. Singh, *J. Math. Chem*., **2007**, *42*, 37.
57. A.R. Ashrafi, B. Manoochehrian, H. Yousefi-Azari, *Util. Math*., **2006**, *71*, 97.

STUDIA UBB CHEMIA, LVII, 3, 2012 (p. 137 – 141)
(RECOMMENDED CITATION)

ESTIMATING THE ENERGY OF NANOHORNS

ALI REZA ASHRAFI[1], FATEMEH NASSAJ[1], MORTEZA FAGHANI[1], PADMAKAR V. KHADIKAR[2]

ABSTRACT. Let E(NH[n]) denotes the energy of a five pentagons nanohorn, where n is the number of layers of NH[n]. In this paper, some calculations are given in view of estimating the energy of nanohorns.

Keywords: *Energy, nanohorn.*

INTRODUCTION

Fullerenes, carbon nanotubes and carbon nanohorns are three major materials produced by the nanotechnology. Fullerenes are a near spherical cage form of carbon molecule that is neither graphite nor diamond. It was discovered at Rice University in 1985 by R.F. Curl, R.E. Smalley and H.W. Kroto [1]. Carbon Nanotubes (CNTs) were discovered in 1991 by Sumio Iijima [2]. The carbon nanohorns (CNHs) are nanotubes capped by halves of fullerenes. CNHs can serve as vehicles for intracellular delivery and also found interest in photo-voltaic elements because of to their ability to accept electrons and readily diffuse them along the cone. Carbon Nanohorns were first prepared by Harris et al. [3] in 1994. (without this part you loose refs [1] [2] and [3]

Let G be a molecular graph with vertex and edge-sets V(G) and E(G), respectively. The entries in the square matrix A(G) = [a_{ij}] equal 1 if vertices v_i and v_j are neighbors and zero if they are not neighbors or belong to the diagonal. The characteristic polynomial $\chi(G, k)$ is the polynomial of degree n, defined as $\det[\lambda I_n - A(G)]$, where I_n is the unit matrix of order n [4].

Let A be an n × n matrix. The scalars λ and vectors x satisfying Ax = λx are called eigenvalues and eigenvectors of A, respectively. The spectrum of A is the multi-set of all eigenvalues of A. The eigenvalues and spectrum of a graph is the eigenvalues and spectrum of its adjacency matrix. All the eigenvalues of a graph are real numbers, and their sum is equal to zero.

[1] *Department of Nanocomputing, Institute of Nanoscience and Nanotechnology, University of Kashan, Kashan 87317-51167, I. R. Iran*
[2] *Research Division, Laxmi Fumigation & Pest Control, PVT Ltd., 3 Khatipura, Indore 452007 India*

A molecular graph G is called bipartite if there exists a coloring of V(G) by two colors. Here, a coloring of G is a coloring of its vertices such that two adjacent vertices have different colors. (why do you need bipartite graph IF nanohorn IS NOT bipartite !!!)

In the Hückel theory, the total π-electron energy of a bipartite molecular graph G is defined as the sum $E_\pi(G) = \sum_{i=1}^{n} |\lambda_i|$ of the absolute values of the eigenvalues $\lambda_1 \le \lambda_2 \le \ldots \le \lambda_n$ of the adjacency matrix A(G). This energy is in good linear correlation with the observed heats of formation of the corresponding conjugated hydrocarbons and it is related to other relevant chemical invariants [5-10].

In a mechanical system, the stable equilibrium positions minimize the potential energy. In data analysis, the most fundamental method for fitting a function to a set of sampled data points is to minimize the least squares error, which serves as a measurement of the overall deviation between the sample data and the function.

The aim of this paper is to investigate the energy of CNH[n] nanohorns, see Figure 1. Notice that the carbon atoms in CNH are entirely sp^+ hybrids, and so our calculations give an approximation of the whole energy of CNH. We encourage the reader to consult papers [11-14] for background material as well as basic computational techniques. Our notation is standard and taken mainly from [4,15].

RESULTS AND DISCUSSION

In this section, the eigenvalues of CNH[n] nanohorn, $1 \le n \le 14$, are computed by the matrix package MATLAB. To do this, we first drawn the molecule by HyperChem [16] and then the adjacency matrix of the molecular graphs of nanohorns is computed by TopoCluj software program [17]. In Table 1, we give the energy of these nanohorns for $1 \le n \le 14$, according to the Figure 1. Our aim is to apply curve fitting method to find a polynomial of the best degree for approximating the energy of nanohorns.

Suppose F(n) = |V(CNH[n])| and G(n) = |E(CNH[n])|. By solving a simple recursive equation, one can see that $F(n) = n^2 + 20n + 40$ and $G(n) = 3/2\ n^2 + 59/2n + 55$.

Define A[r] = E(CNH[r]), $1 \le r \le 14$. We first consider the basic set {A[1], …, A[9]} and apply the least squares method to fit these data by a polynomial F1(x). We have:

$$F(x) = 1.5763\ x^2 + 27.9351\ x + 29.5637. \quad (1)$$

The error of Eq. (1) is E_1 = 3.5219e-004. If we choose the basic set {A[1], …, A[5], A[11], …, A[14]} and apply the least square method then we obtain the following polynomial:

$$G_1(x) = 1.5755\ x^2 + 1.5755\ x + 29.5528. \quad (2)$$

Again the error of Eq. (2) is E_2 = 6.3105e-004. Finally, if we choose the set {A[6],…,A[14]} then we obtain the polynomial $H_1(x) = 1.5746\ x^2 + 27.9574\ x + 29.4968$ with maximum error E_3 = 9.0818e-008.

By using the same data sets for computing polynomials of degree 3, we have:

$$F_2(X) = -0.0004\ x^3 + 1.5829\ x^2 + 27.9073\ x + 29.5927, \quad (3)$$

$$G_2(x) = -0.0001\ x^3 + 1.5783\ x^2 + 27.9256\ x + 29.5751, \quad (4)$$

$$H_2(x) = -0.0000\ x^3 + 1.5748\ x^2 + 27.9553\ x + 29.5031, \quad (5)$$

Then the errors are E_4 = 7.7013e-005, E_5 = 1.9304e-004 and E_6 = 1.7253e-008 for equations (3-5), respectively. Also, it is possible to find four degree polynomials for these data sets, Eqs. (6-8), as follows:

$$F_3(x) = 0.0001\ x^4 - 0.0024\ x^3 + 1.5963\ x^2 + 27.8736\ x + 29.6173, \quad (6)$$

$$G_3(x) = 0.0000\ x^4 - 0.0011\ x^3 + 1.5879\ x^2 + 27.8937 + 29.6031, \quad (7)$$

$$H_3(x) = 0.0000x^4 - 0.0001\ x^3 + 1.5757\ x^2 + 27.9500\ x + 29.5154. \quad (8)$$

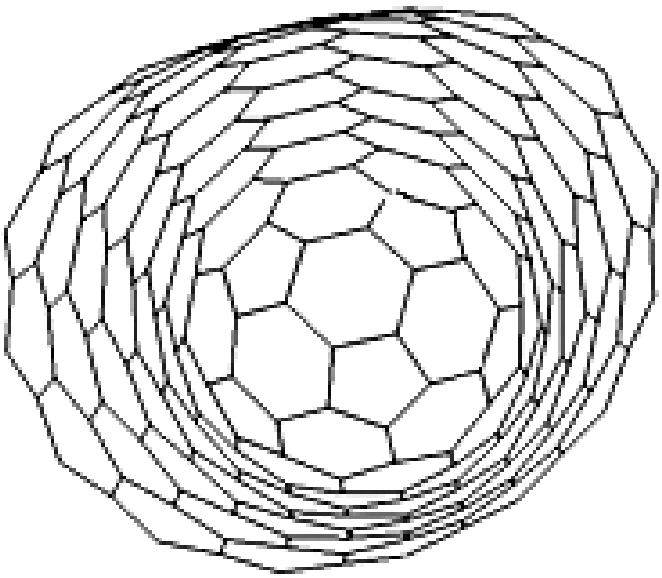

Figure 1. The 3D-Molecular Shape of a Carbon Nanohorn CNH[7].

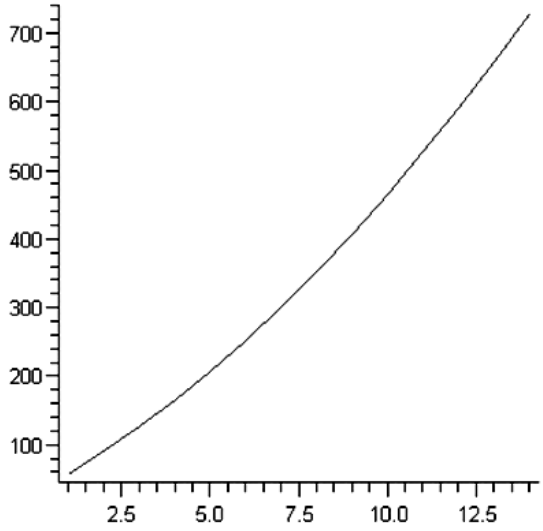

Figure 2. The Diagram of the Energy of Carbon Nanohorn

Table 1. The Energy of CNH[N], 1 ≤ N ≤ 14.

n	E(CNH[n])	n	E(CNH[n])
1	59.08575641	**8**	353.9302518
2	91.72904077	**9**	408.6559100
3	127.5493480	**10**	466.5308048
4	166.5226908	**11**	527.5548855
5	208.6496781	**12**	591.7280919
6	253.9269078	**13**	659.0504641
7	302.3537837	**14**	729.5219742

CONCLUSIONS

Suppose A = {A[1], …, A[14]}. If we compute the functions F_1, F_2, F_3, G_1, G_2, G_3, H_1, H_2 and H_3 on the set A and compare them with values of Table 1, then we can see that our functions calculate the energy of nanohorn with almost one digit accuracy. So, it seems that if we want to estimate energy of this nanohorn by polynomials then polynomials of degree 2 is enough exact.

ACKNOWLEDGEMENT

The authors are indebted to the referee for some comments and helpful remarks. The research of the first author has been supported by the research affair of the University of Kashan, I R Iran under grant number 159020/5.

REFERENCES

1. H.W. Kroto, J.R. Heath, S.C. O'Brien, R.F. Curl, R.E. Smalley, *Nature,* **1985**, *318*, 162–163.
2. S. Iijima, *Nature*, **1991**, *354*, 56–58.
3. P.J.F. Harris, "Carbon nanotube and related structures, new materials for the twenty – first century", Cambridge University Press, Cambridge, **1999**.
4. D. Cvetković, M. Doob, H. Sachs, "Spectra of Graphs-Theory and Application", third ed., Johann Ambrosius Barth Verlag, Heidelberg, Leipzig, **1995**.
5. I. Gutman, *Ber Math. Statist, Sek. Forsch-ungszentram Graz,* **1978**, *103*, 1–22.
6. I. Gutman, „The energy of a graph: Old and new results", in: A. Betten, A. Kohnert, R. Loue, A. Wassermann (Eds.), Algebraic Combinatorics and Applications, Springer-Verlag, Berlin 196–211, **2001**.
7. I. Gutman, *Theoret. Chim. Acta,* **1977***, 45*, 79–87.
8. I. Gutman, *J. Math. Chem*., **1987**, *1*, 123–143.
9. I. Gutman, Y. Hou, *MATCH Commun. Math. Comput. Chem.,* **2001**, *43*, 17–28.
10. Y. Hou, I. Gutman, C.-W. Wou, *Linear Algebra Appl.,* **2002**, *356*, 27–36.
11. A.R. Ashrafi, P. Nikzad, *Dig. J. Nanomat. Bios.,* **2009**, *4*, 383–388.
12. A.R. Ashrafi, M. Sadati, *Optoelectron. Adv. Mater.-Rapid Comm.,* **2009**, *3*, 821–822.
13. A.R. Ashrafi, B. Bazigaran, M. Sadati, *Optoelectron. Adv. Mater.-Rapid Comm.,* **2009**, *3*, 1080–1082.
14. A.R. Ashrafi, M. Faghani, S. M. Seyedaliakbar, *Dig. J. Nanomat. Bios.,* **2009**, *4*, 59–61.
15. N. Trinajstić, Chemical Graph Theory, CRC Press, Boca Raton, FL, **1992**.
16. HyperChem package Release 7.5 for Windows, Hypercube Inc., 1115 NW 4th Street, Gainesville, Florida 32601, USA, **2002**.
17. M.V. Diudea, O. Ursu, Cs.L. Nagy, TopoCluj, Babes-Bolyai University, Cluj, **2002**.

STUDIA UBB CHEMIA, LVII, 3, 2012 (p. 143 – 150)
(RECOMMENDED CITATION)

PREPARATION AND CHARACTERIZATION OF DIAMOND-LIKE CARBON FILMS ON VARIOUS SUBSTRATES BY PECVD SYSTEM

ELNAZ VAGHRI[1], ZAHRA KHALAJ[1], MAHMOOD GHORANNEVISS[1,*]

ABSTRACT. Diamond–like carbon (DLC), a form of amorphous carbon (a-C) or hydrogenated amorphous carbon (a-C: H) has been actively studied due to its interesting properties in many fields of industry. In this work, Diamond-like carbon films were deposited on silicon, glass and quartz substrates via DC plasma enhanced chemical vapor deposition (DC-PECVD) system at the substrate temperature of 180°C from gaseous mixtures of C_2H_2/H_2. The deposited films were characterized by Atomic Force Microscopy (AFM), Fourier Transform Infrared (FTIR) and Raman spectroscopy. FTIR measurements depict the C-H and C-C vibration mode assignments in DLC structures in all of the samples. The Raman spectra confirm the formation of DLC structures due to the existence of the D and G peaks. The surface morphology of the grown films was investigated by AFM analysis.

Keywords: *DLC, FTIR, Plasma Enhanced CVD.*

INTRODUCTION

Diamond-Like Carbon film is an amorphous phase of carbon and atomically, it is consist of sp^2-bonded clusters interconnected by a random network of sp^3-bonded atomic sites [1-2]. These films are classified into two main groups: amorphous carbon (a-C) with approximately no hydrogen and hydrogenated amorphous carbon (a-C: H) with some hydrogen. During the last decades, DLC films have been intensively studied and also utilized in many fields of industry, owing to their outstanding properties like high hardness, low friction coefficient, chemical inertness, and etc [3-5]. DLC films used as protective coatings for magnetic recordings [6] antireflective layers for silicon solar cell [7], solid lubricant coatings for vacuum applications [8] and, so on. Also they can be used as gate dielectrics, intermetal dielectrics and passivation layers for microelectronic purposes [9-10].

A wide range of various deposition techniques have been devised to deposit DLC films such as sputtering [11], ion beam deposition (IBD)[12], cathodic vacuum arc [13], microwave electron cyclotron resonance (ECR) plasma

[1] *Plasma Physics Research Center, Science and Research Branch, Islamic Azad University, Tehran, Iran. P.O .Box: 14665/678*
* *Correspondent: Ghoranneviss@gmail.com*

CVD[14], plasma enhanced chemical vapor deposition (PECVD) [15-17], because deposition of DLC films requires their surfaces to be continuously bombarded by high energetic ions [18]. The most common deposition methods, suitable for depositing DLCs are DC and RF Plasma Enhanced Chemical Vapor deposition.DLC films deposited by DC-PECVD technique exhibit smaller stress values in comparison with RF-PECVD technique [3, 18]. The possibility of the deposition on a large area and at low temperature is the main advantage of the PECVD technique [15].In this paper, DLC films were coated on quartz, glass and silicon substrates by DC-PECVD system in a mixture of acetylene (C_2H_2) and hydrogen (H_2) in total flow ratio of 200 sccm (C_2H_2/H_2:25 vol. %). The topography of samples was carried out by AFM analysis (Park Scientific instruments, Auto probe cp) in contact mode. Raman measurements were performed using an Almega Thermo Nicolet Dispersive Raman Spectrometer with 532 nm of an Nd: YLF laser. The bonding structures of the DLC films were characterized by Fourier transform infrared (FTIR).

RESULTS AND DISCUSSION

Morphology of the films

Atomic Force Microscopy (AFM) images provide more detailed information involving the surface morphology of the films. Figure 1 show the 3D AFM images of the DLC films produced on S_1, S_2, S_3 and S_4 substrates. The root mean square (RMS) surface roughness is one of the most important parameters to characterize of surface structures. The RMS surface roughness of all samples is less than 5nm over the area of 3μmx3μm. It shows that the DLC films grown on various substrates have a smooth surface. Fig.1 (a) shows the 3D AFM image of the as-deposited DLC on the surface. It can be seen that the surface of the film has tightly packed configuration and smooth surface morphology. The homogeneity and packed configuration of the films were reduced in S_2 and S_3 (see Fig.1 (b, c)). Whereas, The RMS surface roughness of the films deposited on S_4 is increased to 4.68nm, as shown in Fig.1 (d).

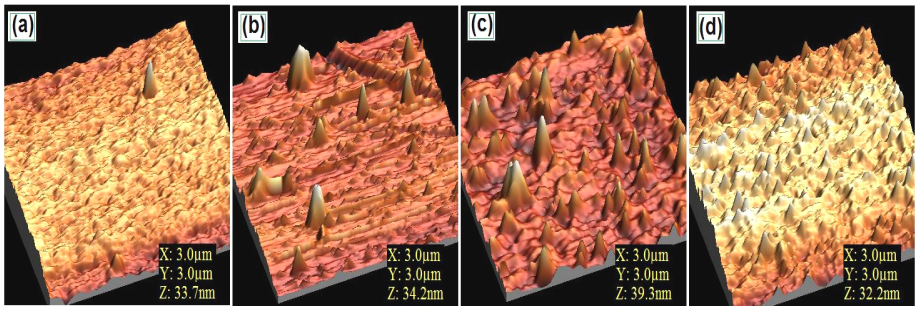

Figure 1. Three dimensional AFM images of the DLC films deposited on different substrates

Figure 2 shows kinds of height changes in a segment AFM images. Existence of valleys in the Figure is related to DLC homogeneity of the surface. As we can see in figure 2(a, b), the peak and valley intensities are near to each other which result in a more homogeneous film deposition on the surface. However, this homogeneity reduces for S_3 and S_4 (see Fig. 2(c, d)). The results of the AFM studies are listed in Table 1.

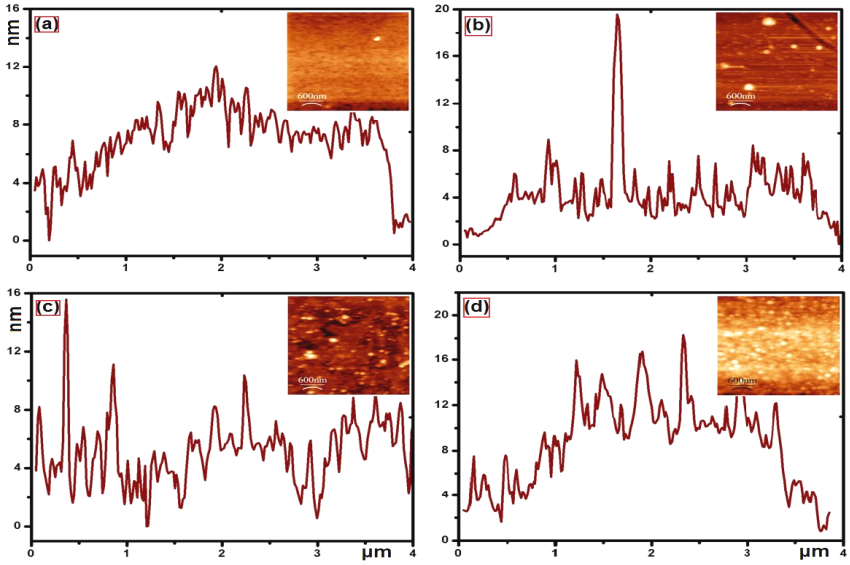

Figure 2. Height changes of the as-deposited DLC on samples (a) S_1, (b) S_2, (c) S_3, (d) S_4

Table 1. AFM studies of the as-deposited DLC on various substrates.

No.	Sample	Etching gas	RMS. rough. (nm)	Ave.Rough (nm)
S_1	glass-Au	H_2	3.29	2.57
S_2	glass	H_2	2.76	1.70
S_3	quartz-Au	H_2	3.90	2.62
S_4	Si -Au	H_2	4.68	3.86

Raman spectroscopy

Raman spectroscopy is a powerful tool for investigating the detailed bonding structure of the DLC films [19]. Fig.3 shows the Raman spectra of the DLC samples, which were measured by Nd: LYF laser at 532nm excitation wave length. The DLC coatings usually have two main features in their Raman

spectra which are commonly well-known as the D and G peaks. The G peak corresponds to the zone center phonons of E_{2g} symmetry while the D peak attributed to the breathing mode of A_{1g} symmetry that contains phonons near the K zone boundary [20]. As shown in Fig. 3, there are two major peaks in these spectra; the peak which is located at a wave number of 1392.80 cm^{-1} is related to the D (labeled 'D' for disorder) bond and another peak at around 1527.72 cm^{-1} is attributed to the G(labeled 'G' for graphite) bond, whereas the D peak for the DLCs deposited on S_2 sample are observed approximately at 1392.47 cm^{-1} and the G peak shifted toward higher wave number at about 1533.6 cm^{-1}[21]. In principle, in the Raman spectra of carbon based materials the G-peak positions move to higher wave number due to two processes: the high sp^2 content or cluster size and due to higher compressive stress [26]. Also we observed the D peak for the DLC samples deposited on S_3, S_4 substrates appeared at around 1395.55 cm^{-1}, 1392.37 cm^{-1}, and the G peak at about 1527.14 cm^{-1} and 1529.30 cm^{-1} [22], respectively. The intensity ratio of the D and G peaks, I_D/I_G and the position of the G peak, Pos (G), have been widely used for qualitative estimation of sp^3 content in DLC [23]. S. Zhang et. al. display that the sp^3 fraction is inversely proportional to the band ratio I_D/I_G [24, 25]. Spectra of the samples show that the intensity ratio, I_D/I_G, is decreased from 1.80 to 1.44, 1.40 and finally 0.95 (See Fig. 4). Therefore, the DLCs deposited on S_1 substrate have more SP^3 bonded carbon atoms and it has a better quality in comparison with samples.

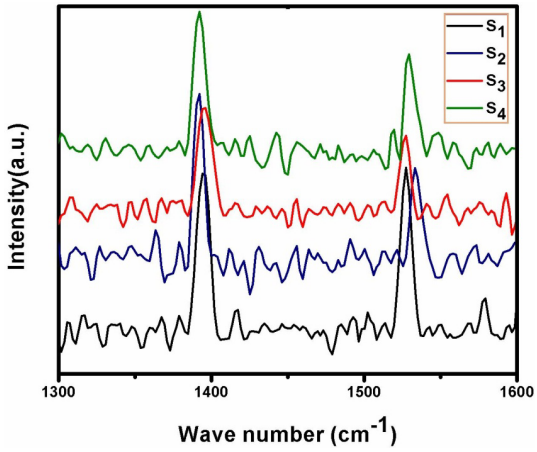

Figure 3. Raman spectra of the DLC films deposited on:
(a) S_1, (b) S_2, (c) S_3 and (d) S_4

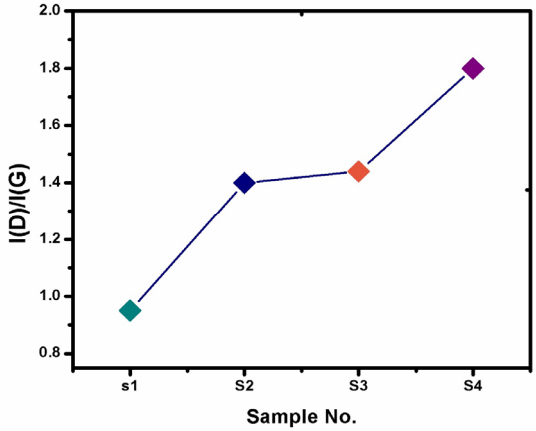

Figure 4. Intensity ratio versus different type of samples

Fourier transform infrared spectroscopy

Fourier Transform Infrared (FTIR) spectroscopy is such a spectroscopic technique to characterize the chemical bonds, molecular structures and C-H_n (n=1, 2, 3) bonding configurations, in DLC films and another carbon material. The infrared spectra of the DLCs deposited on S_1, S_2, S_3, S_4 substrates in the range of 600-3500 cm^{-1} are shown in Fig.5. It is composed of bending vibration (1300-1700 cm^{-1}) and stretching vibration (2700-3100 cm^{-1}) regions of C-H groups. The FTIR spectrum of carbon films grown on samples indicates the major peaks (See Fig. 5). The peak at around 913.85 cm^{-1} can be attributed to CH_2 (olefinic) bond in sp^2 type carbon. The absorption peak at around 1373.05 cm^{-1} may arise due to sp^3 CH_3 configuration and the band at approximately 1449.94cm^{-1} is due to C-H_2 vibration mode. The other absorption peak appeared at about 1596.92 cm^{-1} could be related to sp^2 C-C vibration mode. The peaks near 2861.54 cm^{-1} and 2864.61 cm^{-1} [27], assigned to stretching vibrations of sp^3 CH_3 groups in S_3, S_4 and S_1, S_2 samples, respectively. In addition, the peak which is located around 2969.33 cm^{-1} can be associated with sp^3 CH_3 configuration. IR vibrational mode assignments of the samples are summarized in Table 2.

Table 2. FTIR results for DLC deposited on samples

Samples	Wave numbers (cm^{-1})	*Assignment*
S_1 S_2 S_3 S_4	913.85	Olefinic sp^2 C-H_2
	1373.05	sp^3 C-H_3
	1449.94	sp^3 C-H_2, Olefinic sp^2 C-H_2
	1596.92	Olefinic sp^2 C-C
	2864.61, 2861.54	sp^3 C-H_3
	2969.33	sp^3 C-H_3

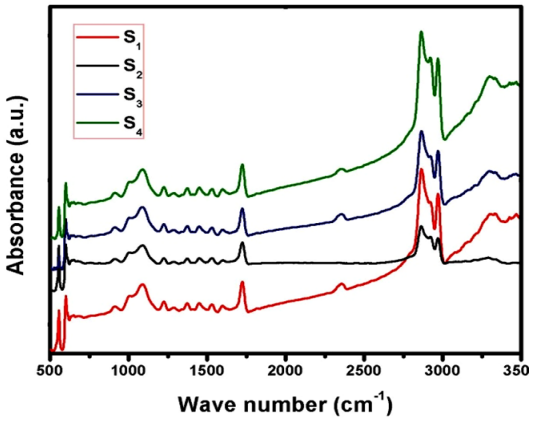

Figure 5. FTIR absorbance spectra of the DLC films grown on S_1, S_2, and $S_3$and S_4 substrates

CONCLUSIONS

In this paper, growth of DLC films on glass-Au, glass, quartz-Au and Si-Au, substrates were investigated by DC-PECVD method. The morphology and the root mean square roughness (R_{rms}) of the DLC films on various substrates were investigated by AFM. The results of the AFM show three-dimensional morphological images of the DLC films. It presents detailed data on the variation of R_{rms} of the diamond-like carbon films. In all cases, the roughness of the films remained low between 2.76 nm and 4.68 nm. However, DLC films maintain their smooth surface and the FTIR spectra indicative of the formation of sp^2 and sp^3 hybridized bonds in all samples. It was observed that the intensity ratio, I_D/I_G, in Raman spectra decreased from S_4 to S_1. Consequently, the DLCs grown on S_1 substrate have better quality compared with the other samples.

EXPERIMENTAL DETAILS AND METHODOLOGY

Substrate treatments and Film synthesis

Diamonds like carbon (DLC) films were prepared using DC-Plasma Enhanced Chemical Vapor Deposition (PECVD) system. The characteristic of the system were discussed in our previous works [15]. Glass, quartz and P type silicon (100) wafers were used as substrate and pre-cleaned with acetone, ethanol, and de ionized water for 15 minutes in an ultrasonic bath. The samples were coated by gold using DC magnetron sputtering system. The DLC films were deposited on glass-Au, glass, quartz-Au and Si-Au after in situ

etching treated with hydrogen ion for 15 minutes. Deposition was carried out at a fixed pressure of C_2H_2 and H_2 mixture gas (C_2H_2/H_2 25 vol. %), with flux rates of 200 sccm. The chamber pressure was adjusted at 15 Torr, and the stage temperature was set at 180°C during deposition. The applied current and voltage in this experiment were 50 mA and 400 V respectively.

ACKNOWLEDGEMENTS

The authours would like to thank the Iran National Science Foundation (INSF) for supporting this project and Miss Somayeh Shams for the technical supports in the PECVD system.

REFERENCES

1. J. Robertson, E.P. O'Reilly, *Phys. Rev. B,* **1987**, *35* (6), 2946–2957.

2. Paul K. Chu, Liuhe Li, *Mater Chem*, **2006**, *96*, 253–277.

3. J.C. Damasceno, S.S. Camargo Jr., F.L. Freire Jr., R. Carius, *Surf. Coat. Technol.,* **2000**, *247*,133–134

4. K.H. Lee, H. Sugimura, Y. Inoue, O. Takai, *Thin Solid Films*, **2003**, *435*, 150.

5. N.V. Novikov, A.G. Gontar, S.I. Khandozhko, A.M. Kutsay, V.N. Tkach, V.Yu. Gorokhov, G.M. Belitsky, A.V. Vasin, *Diamond Relat. Mater.*, **2000***, 9*, 792.

6. S.T. Patton, B. Bhushan, *IEEE Trans. Magn.,* **1998**, *34*, 575–587.

7. M. Alaluf, J. Appelbaum, L. Klibanov, D. Brinker, D. Scheiman, N. Crotoru, *Thin Solid Films*, **1995**, *256*, 1–2.

8. R. Maboudian, *Surf. Sci. Rep.,* **1998**, *30*, 207–269.

9. A. Grill, V. Patel, C. Jahnes, *J. Electrochem. Soc.,* **1998**, *145* (5), 1649–1653.

10. W.I. Urruchi, M. Massi, H.S. Maciel, C. Otani, L.N. Nishioka, *Diamond Relat. Mater.,* **2000**, *9*, 685–688.

11. K. Bewilogua, R. Wittorf, H. Thomsen, M. Weber, *Thin Solid Films,* **2008**, *447*,142.

12. D.-J. Jan, C.-F. Ai, C.C. Lee, *Vacuum*, **2004**, *74*, 531.

13. J.-B. Wu, J.-J. Chang, M.-Y. Li, M.-S. Leu, A.-K. Li, *Thin Solid Films*, **2007**, *516*, 243.

14. S.B. Singh, M. Pandey, N. Chand, A. Biswas, D. Bhattacharya, S. Dash, A.K. Tyagi, R. M. Dey, S.K. Kulkarni, D.S. Patil, *Bull. Mater. Sci.,* **2008**, *31*, 813.

15. E. Vaghri, Z. Khalaj, M. Ghoranneviss, M. Borghei, *Fusion. Energy*, **2011**, *30*, 447-452.

16.D. Caschera, F. Federici, S. Kaciulis, L. Pandolfi, A. Cusmà, G. Padeletti, *Mater. Sci. Eng. C,* **2007**, *27*,1328.

17. R. Paul, S. Hussain, S. Majumder, S. Varma, A.K. Pal, *Mat. Sci. Eng. B,* **2009**, *164,* 156.

18. S.S. Tinchev, Y. Dyulgerska, P. Nikolova, D. Grambole, U. Kreissig, Tz. Babeva, *J. Optoelectron Adv. M.,* **2006**, *8*, 308-311.

19. A.C. Ferrari, J. Robertson, *Phil. Trans. R. Soc. London A,* **2004**, *362*, 2477.

20. S.I. Hosseini, B. Shokri, M. Abbasi Firouzjah, S. Kooshki, M. Sharifian, *Thin Solid Films,* **2011**, *519*, 3090-3094.

21. E. Tomasella, L. Thomas, M. Dubois, C. Meunier, *Diamond & Relat. Mater.,* **2004**, *13*, 1618–1624.

22. Elidiane C. Rangel, Nilson C. da Cruz,1 Milton E. Kayama, Rita C. C. Rangel, Nazir Marins and Steven F. Durrant, *Plasmas and Polymers*, **2004**, *9*, no. 1.

23. W.G. Cui, Q.B. Lai, L. Zhang, F.M. Wang, *Surf. Coat. Technol.,* **2010**, *205*, 1995–1999.

24. S. Zhang, X.T. Zeng, H. Xie, P. Hing, *Surf. Coat. Technol.,* **2000**, *123*, 256.

25. A. Zeng, E. Liu, P. Hing, S. Zhang, S.N. Tan, I.F. Annergren, J. Gao, *Int. J. Mod. Phys. B,* **2002**, *16*, 1024.

26. J.K. Shin, C.S. Lee, K.R. Lee, K.Y. Eun, *Appl. Phys. Lett.,* **2011**, *78*, 631.

27. G.E. Stan, D.A. Marcov, A.C. Popa, M.A. Husanu, *Nanomaterials and Biostructures*, **2010**, *5*, 705–718.

STUDIA UBB CHEMIA, LVII, 3, 2012 (p. 151 – 156)
(RECOMMENDED CITATION)

SOME TOPOLOGICAL INDICES OF AN INFINITE 1,3-ADAMANTANE ARRAY

ALI ASGHAR BEHROOZPOOR[1], GHOLAM HOSSEIN FATH-TABAR[2], FARZANEH GHOLAMINEZHAAD[2]

ABSTRACT. A topological index is a real number related to a molecular graph, which is a graph invariant. In this paper, formulas for calculating the Szeged index, Wiener index and edge Wiener index of an infinite array of 1,3-adamantane are presented.

Keywords: *Szeged index, Wiener index, edge Wiener index, 1,3-adamantane.*

1. INTRODUCTION

Let G = (V, E) be a simple molecular graph. The sets of vertices $V(G)$ and edges $E(G)$ of G represent atoms and bonds, respectively [1]. The graph G is said to be connected if for every vertex x and y in $V(G)$ there exists a path connecting them. The distance $d(u,v)$ between vertices u and v of a connected graph G is the number of edges in a minimum path from u to v.

A topological index is a real number related to a molecular graph, which is a graph invariant. There are several topological indices already defined. The Wiener index (W) is the first topological index that was introduced in 1947 by Harold Wiener [2]. It is defined as the sum of distances between all pairs of vertices in the graph. The Szeged index (Sz) is another topological index, introduced by Ivan Gutman [3]. To define the Szeged index of a graph G, we assume that $e = uv$ is an edge connecting the vertices u and v. Suppose $n_u(e)$ is the number of vertices of G lying closer to u and $n_v(e)$ is the number of vertices of G lying closer to v, then the Szeged index of the graph G is defined as $Sz(G) = \sum_{e=uv\in E(G)}[n_u(e)n_v(e)]$; notice that vertices equidistant to u and v are not taken into account. For details and other related topological indices, the reader is invited to consult refs. [4-17].

[1] *Department of Science, Bushehr Branch, Islamic Azad University, Bushehr, Iran*
[2] *Department of Statistics and Computer Science, Faculty of science, University of Kashan, Kashan 87317-51167, I. R. Iran*

In this paper, formulas for calculating the Szeged index, Wiener index and edge Wiener index of an infinite array of 1,3-adamantane (see Figure 1) are presented.

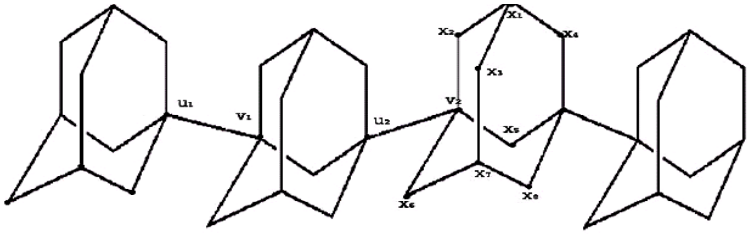

Figure 1. Tetrameric 1, 3-adamantane.

2. MAIN RESULTS

In this section, we will derive the formulas for calculating Sz index, Wiener index and edge Wiener index of an infinite array of 1,3-adamantane.

2.1. Szeged index of adamantane array A[n]

In the following we compute the index *Sz(A[n])* for an infinite array of 1, 3-adamantane.

We partition the edge set in two parts: first part is the set of edges which link all the adamantane units together, and second part is the set of edges which belong to adamantane units.

We name the edges in the first part the *linked edges* and consider $e = u_i v_i$ as a member of that part. *A[n]* has *n - 1* linked edges. Let $e = u_i v_i$ be a *linked edge* then we see that $n_{u_i}(e) = 10i$ and $n_{v_i}(e) = 10(n - i)$. Each adamantane unit has 12 edges, Figure 1. We consider the k[th] adamantane. For the edges $e = uv$ of that adamantane unit we have:

If $e = uv = x_1x_2, u_kx_5, x_6x_7$

then $n_u(e) = 10(n - k) + 6$ and $n_v(e) = 10(k - 1) + 4$.

If $e = uv = x_1x_4, v_{k-1}x_5, x_7x_8$

then $n_u(e) = 10(n - k) + 4$ and $n_v(e) = 10(k - 1) + 6$.

If $e = x_1x_3, x_2v_{k-1}, v_{k-1}x_6, x_4u_k, u_kx_8, x_3x_7$

then $n_u(e) = 10(n - 1) + 6$ and $n_v(e) = 4$.

Theorem 1. The Szeged index of an infinite array of 1,3-adamantane is calculated by formula:

$$Sz(A[n]) = \frac{350}{3}n^3 + 240n^2 - \frac{206}{3}n$$

Proof. $Sz(A[n]) = \sum_{e=uv}(n_u(e)n_v(e))$

$$= 100\sum_{i=1}^{n-1} i(n-1) + 3\sum_{k=1}^{n}(10(n-k)+6)(10(k-1)+4)$$
$$+ 3\sum_{k=1}^{n}(10(n-k)+4)(10(k-1)+6) + 6\sum_{k=1}^{n}4(6+10(n-1))$$
$$= \frac{50}{3}(n^3 - n) + 100n^3 + 240n^2 - 52n$$
$$= \frac{350}{3}n^3 + 240n^2 - \frac{206}{3}n.$$

2.2. Wiener index of A[n]

In the following we obtain the wiener index of *A[n]*:

For this we first divide the graph to two parts: consider the first adamantane unit as part one A1, and A_{m-1} for the rest of the graph. By this way we can prove that $W(A_m) = W(A_1) + W(A_{m-1}) + d(A_1, A_{m-1})$; we have:

$$\sum_{m=2}^{n}(W(A_m) - W(A_{m-1})) = \sum_{m=2}^{n}(W(A_1) + d(A_1, A_{m-1}))W(A_n)W(A_n)$$
$$= nW(A_1) + \sum_{m=2}^{n} d(A_1, A_{m-1}). \qquad (I)$$

Theorem 2. $W(A_n) = 50n^3 + 80n^2 - 34n$.

Proof. In Graph theory it has been defined that $d(G, u) = \sum_{x \in V(G)} d(u, x)$; thus

$$d(A_1, x_1) = d(A_1, x_7) = d(A_1, u) = d(A_1, v) = 18,$$

$$d(A_1, x_2) = d(A_1, x_3) = d(A_1, x_4) = d(A_1, x_5) = d(A_1, x_6) = d(A_1, x_8) = 20$$

$$\Rightarrow W(A_1) = \frac{1}{2}\sum_{u,v \in V(A_1)} d(u, v) = 96.$$

As in the following $d(A_1, A_{m-1})$ based on m is:

$$d(A_1, A_{m-1}) = 360(m-1) + 100(1 + 4 + 7 + \cdots)$$

in which the number of sentences in the second parenthesis is m-1. Finally by constituting $W(A_1)$ and $d(A_1, A_{m-1})$ in relation (I) the polynomial of $W(A_n)$ based on n will obtain:

$$W(A_n) = n\,W(A_1) + \sum_{m=2}^{n} d(A_1, A_{m-1}) = 96n + \sum_{m=2}^{n} (150m^2 + 10m - 160)$$
$$= 50n^3 + 80n^2 - 34n$$

2.3. Edge Wiener index of A[n]

In the following we obtain the edge Wiener index of *A[n]* , denoted by $W_e(A[n])$.

We consider the k[th] adamantane and then compute the summation of all distances of each edge, from all other edges of the graph. Then one can see that $d(G,e) = \sum_{e' \in E(G)} d(e,e')$. Then we compute the following polynomials:

$$d(G, x_1x_2) = d(G, x_6x_7) = \frac{39}{2}n^2 + 39k^2 - 39nk + \frac{67}{2}n - 52k + 11,$$
$$d(G, x_1x_3) = d(G, x_3x_7) = \frac{39}{2}n^2 + 39k^2 - 39nk + \frac{67}{2}n - 39k - 2,$$
$$d(G, x_1x_4) = d(G, x_7x_8) = \frac{39}{2}n^2 + 39k^2 - 39nk + \frac{41}{2}n - 26k - 2,$$
$$d(G, x_4u_k) = d(G, x_8u_k) = \frac{39}{2}n^2 + 39k^2 - 39nk + \frac{15}{2}n - 13k - 2,$$
$$d(G, v_{k-1}x_2) = d(G, x_6v_{k-1}) = \frac{39}{2}n^2 + 39k^2 - 39nk + \frac{67}{2}n - 65k + 24,$$
$$d(G, x_5u_k) = \frac{39}{2}n^2 + 39k^2 - 39nk + \frac{15}{2}n - 26k + 11,$$
$$d(G, x_5v_{k-1}) = \frac{39}{2}n^2 + 39k^2 - 39nk + \frac{41}{2}n - 52k + 24.$$

Now we consider the *linked edge* u_kv_k and find the distance of u_kv_k from all other edges of graph:

$d(G, u_kv_k) = \frac{39}{2}n^2 + 39k^2 - 39nk - \frac{11}{2}n + 2$. Thus:

Theorem 3. $W_e(A[n]) = \frac{169}{2}n^3 + 13n^2 - \frac{49}{2}n - 1.$

Proof 1. $W_e(G) = \frac{1}{2}\sum_{e,e' \in E(G)} d(e,e') =$

$$\frac{1}{2}\left(\sum_{k=1}^{n}(234n^2 + 468k^2 - 468nk + 285n - 468k + 93) + \sum_{k=1}^{n-1}\left(\frac{39}{2}n^2 + 39k^2 - 39nk - \frac{11}{2}n + 2\right)\right)$$

$$\Rightarrow \quad W_e(TA[n]) = \frac{169}{2}n^3 + 13n^2 - \frac{49}{2}n - 1.$$

Proof 2. Consider the first adamantane unit and edge u_1v_1 as A_1, and the other remained parts of graph A_2. Then we the edge Wiener index of A_n is as follows:

$$W_e(A_n) = n\,W_e(A_1) + \sum_{m=2}^{n} d(A_1, A_{m-1}).$$

Now we obtain $W_e(A_1)$: it can be seen that the sum of all distances between each edge of adamantane array, and all other edges of adamantane is equal to 12 and the summation of all distances between u_1v_1 and all other edges of adamantane equals 15. According to these we obtain: $W_e(A_1) = \frac{1}{2}(12)(12) + 15 = 87$. To find the formula of $W_e(A_n)$ it is enough to obtain (A_1, A_{m-1}):

$d(A_1, A_{m-1})$ = (the summation of all distances of adamantane A_1 from the adamantanes of A_{m-1})

+ (the summation of all distances of adamantane A_1 from the linked edges of A_{m-1})

+ (the distances of u_1v_1 from the adamantanes of A_{m-1})

+ (the distances of u_1v_1 from all linked edges of A_{m-1}).

Then we conclude that:

$$d(A_1, A_{m-1}) - 360(m-1) + 144\,(1+4+7+\cdots) + 15(m-2) + 12(3+6+9+\cdots) + 15(m-1) + 12(3+6+9+\cdots) + (2+5+8+\cdots).$$

In this polynomial the number of sentences in the second parenthesis is m-1 and in other sequences is m-2. Thus $d(A_1, A_{m-1}) = \frac{507}{2}m^2 - \frac{455}{2}m - 40$.

By constituting $W_e(A_1)$ and $d(A_1, A_{m-1})$ in relation I the final result would is as follows:

$$W_e(A_n) = n\,W_e(A_1) + \sum_{m=2}^{n} d(A_1, A_{m-1}) = 87\,n + \sum_{m=2}^{n}\left(\frac{507}{2}m^2 - \frac{455}{2}m - 40\right)$$

$$\Rightarrow W_e(TA[n]) = \frac{169}{2}n^3 + 13\,n^2 - \frac{49}{2}n + 14$$

ACKNOWLEDGMENT

The first author has been financially supported by the office of vice chancellor for research of Islamic Azad University, Bushehr Branch. The second author has been financially supported by University of Kashan (Grant No. 159021/2).

REFERENCES

1. M.V. Diudea, I. Gutman and L. Jantschi, *Molecular Topology*, Huntington, NY, **2001**.
2. H. Wiener, *J. Amer. Chem. Soc.*, **1947**, *69*, 17.
3. I. Gutman, *Graph Theory Notes of New York*, **1994**, *27*, 9.
4. A.R. Ashrafi, M. Ghorbani and M. Jalali, *J. Theor. Comput. Chem.*, **2008**, *2*, 221.
5. G.H. Fath-Tabar, T. Doslic and A.R. Ashrafi, *Linear Algebra Appl.,* **2010**, *433*, 662.
6. G.H. Fath-Tabar, M.J. Nadjafi-Arani, M. Mogharrab and A.R. Ashrafi, *MATCH Commun. Math. Comput. Chem*., **2010**, *63*, 145.
7. M. Mogharrab and G.H. Fath-Tabar, *MATCH Commun. Math. Comput. Chem*., **2011**, *65*, 33.
8. I. Gutman, P.V. Khadikar, T. Khaddar, *MATCH Commun. Math. Comput. Chem.*, **1997**, *35*, 105.
9. M.H. Khalifeh, H. Yousefi-Azari and A.R. Ashrafi, *Discrete Appl. Math.*, **2008**, *156*, 1780.
10. M.H. Khalifeh, H. Yousefi-Azari, A.R. Ashrafi, *Discrete Appl. Math.*, **2008**, *10*, 1780.
11. S. Klavžar, A. Rajapakse and I. Gutman, *Appl. Math. Lett.*, **1996**, *9*, 45.
12. H. Yousefi-Azari, B. Manoochehrian and A.R. Ashrafi, *Curr. Appl. Phys.*, **2008**, *8*, 713.
13. Z. Yarahmadi, G.H. Fath-Tabar, *MATCH Commun. Math. Comput. Chem.,* **2011**, *65*, 201.
14. G.H. Fath-Tabar, B. Furtula and I. Gutman, *J. Math. Chem.,* **2010**, *47*, 477.
15. M. Mogharrab, G.H. Fath-Tabar, *MATCH Commun. Math. Comput. Chem.,* **2011**, *65*, 33.
16. G.H. Fath-Tabar, S. Moradi and Z. Yarahmadi, *MATCH Commun. Math. Comput. Chem*., **2012**, *67*, 495.
17. G.H. Fath-Tabar, B. Vaez-Zadeh, A.R. Ashrafi and A. Graovac, *Discrete Appl. Math*., **2011**, *159*, 1323.

STUDIA UBB CHEMIA, LVII, 3, 2012 (p. 157 – 166)
(RECOMMENDED CITATION)

THE EDGE WIENER INDEX OF ROOTED PRODUCT OF GRAPHS

ESMAEIL BABAEI[1], ALI IRANMANESH[1,*]

ABSTRACT. In a connected graph *G*, the sum of distances between all its vertex pairs is known as the Wiener index. The edge-Wiener index is conceived in an analogous manner as the sum of distances between all pairs of edges of the connected graph. In this paper, we compute the edge-Wiener index of the rooted product of graphs and some types of dendrimers.

Keywords: *graph, distance sum, edge-Wiener index*

INTRODUCTION

Let G be a connected graph with the vertex and edge sets $V(G)$ and $E(G)$, respectively. Throughout this paper, we suppose that G is connected. The Wiener index is defined as $W(G)=\sum_{\{u,v\}\subseteq V(G)} d(u,v\,|\,G)$, where $d(u,v\,|\,G)$ denotes the distance between vertices u and v.

This index was introduced by the chemist Harold Wiener [1] within the study of relations between the structure of organic compounds and their thermodynamic properties. It found many applications in chemistry, pharmaceutics etc [2- 9].

The edge-Wiener index version was defined in ref [10] as $W_{ei}(G)=\sum_{\{e,f\}\subseteq E(G)} d_i(e,f\,|\,G), 0\le i\le 4.$ For $i=0$, $d_0(e,f\,|\,G)=d(e,f\,|\,L(G))$, where, $L(G)$ is the line graph of G, i.e. a graph of which vertices are the edges of G, with two vertices connected in $L(G)$ whenever the corresponding edges of G are adjacent.

Also $d_3(e,f\,|\,G)=\begin{cases} d_1(e,f\,|\,G) & e\neq f \\ 0 & e=f \end{cases}$,

where $d_1(e,f\,|\,G)=\min\{d(x,u),d(x,v),d(y,u),d(y,v)\}$, such that $e=xy$ and $f=uv$. Similarly, $d_4(e,f\,|\,G)=\begin{cases} d_2(e,f\,|\,G) & e\neq f \\ 0 & e=f \end{cases}$,

[1] *Department of Mathematics, Tarbiat Modares University, P.O. Box: 14115-137, Tehran, Iran*
** iranmanesh@modares.ac.ir*

where, $d_2(e,f\,|\,G)=\max\{d(x,u),d(x,v),d(y,u),d(y,v)\}$, such that $e=xy$ and $f=uv$. Next, d_1,d_2 are not distances and $d_0(e,f\,|\,G)=d_3(e,f\,|\,G)$ for all $\{e,f\}\subseteq E(G)$ [10]. Thus for the first edge-Wiener index we have

$$W_{e0}(G)=W_{e3}(G)=\sum_{\{e,f\}\subseteq E(G)}d_0(e,f\,|\,G)=\sum_{\{e,f\}\subseteq E(G)}d_3(e,f\,|\,G).$$

And for the second edge-Wiener index: $W_{e4}(G)=\sum_{\{e,f\}\subseteq E(G)}d_4(e,f\,|\,G)$.

The rooted product of graph G and rooted graph H, GoH, is obtained by taking one copy of G and $|V(G)|$ copies of H, and by joining the root vertex of the i[th] copy of H to the i[th] vertex of G for $i=1,2,...,|V(G)|$.

Let H be a labeled graph on n vertices, G be a sequence of n rooted graphs $G_1,...,G_n$, then $H(G)$ denotes the graph obtained by identifying the root of G_i with the i[th] vertex of H, which is called the rooted product of H by G. Thus, $GoH=G(\underbrace{H,...,H}_{|V(G)|})$ [11].

In this paper, we compute the edge-Wiener index of the rooted product of graphs and also obtain this index for some dendrimers.

Computation of the edge Wiener index of rooted product of graphs

Lemma 1 [10]**.** Let m be the number of edges of the graph G, then $W_{e0}(G)=W_{e1}(G)+\frac{m(m-1)}{2}$ and $W_{e4}(G)=W_{e2}(G)-m$.

Now, let H be a labeled graph on n vertices and m edges, G be a sequence of n rooted graphs; $G_1,...,G_n$ such that G_i has n_i vertices and m_i edges and $H(G)$ be the rooted product of H by G, then $H(G)$ will have $M=m+\sum_{i=1}^{n}m_i$ edges. We define

$$d_{ki}(G_i)=\sum_{e\in E(G_i)}d_k(e,x_i)\text{ and }d_{ki}(H)=\sum_{e\in E(H)}d_k(e,x_i),k=1,2,$$

where x_i is the root of G_i, also we define

$$d_1(e,x)=\min\{d(x,u),d(x,v)\},d_2(e,x)=\max\{d(x,u),d(x,v)\}$$

such that $x\in V(G)$, $u\in E(G)$ and $e=uv$.

Proposition 1. Let H be a labeled graph on n vertices and m edges, G be a sequence of n rooted graphs: $G_1,...,G_n$ such that G_i has n_i vertices and m_i edges. Let $H(G)$ be the rooted product of H by G, then

$$W_{ek}(H(G)) = \sum_{i=1}^{n} W_{ek}(G_i) + W_{ek}(H) + m\sum_{i=1}^{n} d_{ki}(G_i) + \sum_{i=1}^{n} m_i d_{ki}(H)$$
$$+\sum_{i=1}^{n}\sum_{j=1,j\neq i}^{n} m_j d_{ki}(H) + \frac{1}{2}\sum_{i=1}^{n}\sum_{j=1,j\neq i}^{n} m_i m_j d_H(x_i,x_j), k = 1,2$$

Proof. Let $e_\lambda;\lambda = 1,...,m_i$, be an edge of G_i, $e_\gamma;\gamma = 1,...,m_j$ be an edge of G_j, $i \neq j$, then,

$$d_k(e_\lambda,e_\gamma) = d_k(e_\lambda,x_i) + d_H(x_i,x_j) + d_k(e_\gamma,x_j), k = 1,2.$$

Hence

$$d_k(e_\lambda,G_j) = \sum_{\gamma=1}^{m_j} d_k(e_\lambda,e_\gamma) = \sum_{\gamma=1}^{m_j}[d_k(e_\lambda,x_i) + d_H(x_i,x_j) + d_k(e_\gamma,x_j)]$$
$$= m_j d_k(e_\lambda,x_i) + m_j d_H(x_i,x_j) + d_{kj}(G_j),$$

$$d_k(G_i,G_j) = \sum_{\lambda=1}^{m_i} d_k(e_\lambda,G_j) = \sum_{\lambda=1}^{m_i}[m_j d_k(e_\lambda,x_i) + m_j d_H(x_i,x_j) + d_{kj}(G_j)]$$
$$= m_j d_{ki}(G_i) + m_i m_j d_H(x_i,x_j) + m_i d_{kj}(G_j),$$

$$\sum_{j=1,j\neq i}^{n} d_k(G_i,G_j) = \sum_{j=1,j\neq i}^{n}[m_j d_{ki}(G_i) + m_i m_j d_H(x_i,x_j) + m_i d_{kj}(G_j)],$$

$$\sum_{i=1}^{n}\sum_{j=1,j\neq i}^{n} d_k(G_i,G_j) = \sum_{i=1}^{n}\sum_{j=1,j\neq i}^{n}[m_j d_{ki}(G_i) + m_i m_j d_H(x_i,x_j) + m_i d_{kj}(G_j)]$$
$$= 2\sum_{i=1}^{n}\sum_{j=1,j\neq i}^{n} m_j d_{ki}(G_i) + \sum_{i=1}^{n}\sum_{j=1,j\neq i}^{n} m_i m_j d_H(x_i,x_j)$$

Now, let e be an edge of H, then,

$$d_k(e,G_j) = \sum_{\gamma=1}^{m_j} d_k(e,e_\gamma) = \sum_{\gamma=1}^{m_j}[d_k(e,x_j) + d_k(x_j,e_\gamma)] = m_j d_k(e,x_j) + d_{kj}(G_j)$$

$$d_k(H,G_j) = \sum_{i=1}^{m} d_k(e_i,G_j) = \sum_{i=1}^{m}[m_j d_k(e_i,x_j) + d_{kj}(G_j)] = m_j d_{kj}(H) + m d_{kj}(G_j)$$

$$\sum_{j=1}^{n} d_k(H,G_j) = \sum_{j=1}^{n}[m_j d_{kj}(H) + m d_{kj}(G_j)] = \sum_{j=1}^{n} m_j d_{kj}(H) + m\sum_{j=1}^{n} d_{kj}(G_j)$$

Therefore,

$$W_{ek}(H(G)) = \sum_{\{e,f\}\subseteq E(H(G))} d_k(e,f \mid H(G))$$

$$= \sum_{i=1}^{n} \sum_{\{e,f\}\subseteq E(G_i)} d_k(e,f \mid G_i) = \frac{1}{2}\sum_{i=1}^{n}\sum_{j=1,j\neq i}^{n} d_k(G_i,G_j)$$

$$+ \sum_{i=1}^{n} d_k(H,G_i) + \sum_{\{e,f\}\subseteq E(H)} d_k(e,f \mid H)$$

Thus,

$$W_{ek}(H(G)) = \sum_{i=1}^{n} W_{ek}(G_i) + W_{ek}(H) + m\sum_{i=1}^{n} d_{ki}(G_i) + \sum_{i=1}^{n} m_i d_{ki}(H)$$

$$+ \sum_{i=1}^{n}\sum_{j=1,j\neq i}^{n} m_j d_{ki}(H) + \frac{1}{2}\sum_{i=1}^{n}\sum_{j=1,j\neq i}^{n} m_i m_j d_H(x_i,x_j), k = 1,2.$$

Corollary 1. By the above assumption, we have

$$W_{e0}(H(G)) = W_{e1}(H(G)) + \frac{M(M-1)}{2}$$

and $W_{e4}(G) = W_{e2}(H(G)) - M$.

where $M = m + \sum_{i=1}^{n} m_i$.

Proof. This follows from Lemma 1.

Corollary 2. Let G be a connected graph with n_1 vertices and m_1 edges, H be a rooted graph with n_2 vertices and m_1 edges, then,

$$W_{ek}(GoH) = n_1 W_{ek}(H) + W_{ek}(G) + m_1 n_1^2 d_{k1}(H)$$

$$+ m_2 \sum_{j=1}^{n_1} d_{kj}(G) + \frac{1}{2}\sum_{i=1}^{n_1}\sum_{j=1,j\neq i}^{n_1} m_2^2 d_G(i,j), k = 1,2.$$

Proof. Hence, $GoH = G(\underbrace{H,...,H}_{n_1})$. Therefore, the result follows from proposition 1.

Lemma 2. Let K_n, P_n, C_n and S_n denote the complete graph, path, cycle and star on n vertices, respectively. Also let $K_{a,b}$ be the complete bipartite graph on the parts A and B of the sizes $|A|=a$ and $|B|=b$. Put $d_{ki}(G)=\sum_{e\in E(H)} d_k(e,i), k=1,2.$ where i is i[th] vertex of G. Then,

(i) $d_{1i}(K_{a,b})=\begin{cases} ab-b & i\in A \\ ab-a & i\in B \end{cases}$, $d_{2i}(K_{a,b})=\begin{cases} 2ab-b & i\in A \\ 2ab-a & i\in B \end{cases}$,

(ii) $d_{1i}(S_n)=d_{1i}(K_{1,n-1})=\begin{cases} 0 & i\in A \\ n-2 & i\in B \end{cases}$,

(iii) $d_{2i}(S_n)=d_{2i}(K_{1,n-1})=\begin{cases} n-1 & i\in A \\ 2n-3 & i\in B \end{cases}$,

(iv) $d_{1i}(K_n)=\frac{(n-1)(n-2)}{2}$, $d_{2i}(K_n)=(n-1)^2$

(v) $d_{1i}(C_n)=\begin{cases} \sum_{j=1}^{k-1} 2j & n=2k \\ \sum_{j=1}^{k-1} 2j+k & n=2k+1 \end{cases}$,

(vi) $d_{2i}(C_n)=\begin{cases} \sum_{j=1}^{k-1} 2j & n=2k \\ \sum_{j=1}^{k-1} 2j+k+1 & n=2k+1 \end{cases}$,

(vii) $d_{1i}(P_n)=\sum_{j=1}^{n-1-i} j+\sum_{j=1}^{i-1}(j-1)$, $d_{2i}(P_n)=\sum_{j=1}^{n-i} j+\sum_{j=1}^{i-1} j$.

Proof. Straight forward.

Computation of the edge Wiener index of some dendrimers

Definition 1 (Generalized Bethe Tree)**.** Let B_k be a generalized Bethe tree of k levels (k>1) or a rooted tree in which vertices at the same level/ generation have the same degree [12]. For $j=1,2,...,k$, denote by d_{k-j+1} and

n_{k-j+1}, the degree of the vertices at the level j and their numbers, respectively. Thus, $d_1 = 1$ is the degree of the vertices at the level k and d_k is the degree of the rooted vertex. On the other hand, $n_k = 1$, pertaining to the single vertex at the first level, the root vertex. For example, B_4 is given in Figure 1.

Proposition 2. Let B_k be a generalized Bethe tree. Then we have

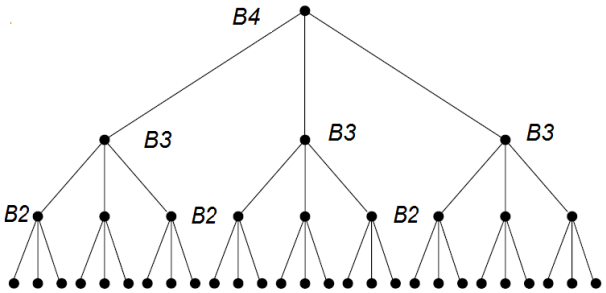

Figure 1. Generalaized Beth tree of 4 levels

$$W_{e1}(B_k) = d_k W_{e1}(B_{k-1}) + d_k{}^2(d_{1i}(B_{k-1}) + m_{k-1}d_{1i}(B_{k-1}) + m_{k-1}{}^2) - d_k(m_{k-1}d_{1i}(B_{k-1}) + m_{k-1}{}^2),$$
$$W_{e2}(B_k) = d_k W_{e2}(B_{k-1}) + d_k{}^2(1 + m_{k-1} + d_{2i}(B_{k-1}) + m_{k-1}d_{2i}(B_{k-1}) + m_{k-1}{}^2) - d_k(m_{k-1}d_{2i}(B_{k-1}) + m_{k-1}{}^2),$$

where, m_k is the number of edges of B_k. Therefore,

$$W_{e0}(B_k) = W_{e1}(B_k) + \frac{m_k(m_k - 1)}{2} \text{ and } W_{e4}(B_k) = W_{e2}(B_k) - m_k .$$

Proof: Suppose that B_k is a generalized Bethe tree with k levels, then a subtree B_{k-j+1} of B_k corresponding to j th level, is a tree with its root at level j. Now, we can define B_k by the rooted product of trees. Let B_i be a subtree corresponding to $k-i+1$-th level of B_k; in this case, B_i will be defined as

$$B_i = S_{d_{k-i+1}+1}(P_1, B_{i-1}, B_{i-1}, ..., B_{i-1})$$

where, S_{d+1} is a star on the $d+1$ vertices. Accordingly, B_k will be defined as

$$B_k = S_{d_k+1}(P_1, B_{k-1}, B_{k-1}, ..., B_{k-1})$$

The number of edges of B_k is obtained by

$$m_k = d_k + d_k d_{k-1} + d_k d_{k-1} ... d_2$$

Also we have

$$d_{1i}(B_k) = \sum_{e \in E(B_k)} d_1(e,i) = d_k d_{k-1} + 2 d_k d_{k-1} d_{k-2} + ... + (k-1) d_k d_{k-1} ... d_2$$

$$d_{2i}(B_k) = \sum_{e \in E(B_k)} d_2(e,i) = d_k + 2 d_k d_{k-1} + ... + k d_k d_{k-1} ... d_2$$

where, i is the root of B_k.

Therefore, by Proposition 1, we have:

$$W_{el}(B_k) = W_{el}(S_{d_k+1}(P_1, B_{k-1}, B_{k-1}, ..., B_{k-1}))$$

$$= \sum_{i=2}^{d_k+1} W_{el}(B_{k-1}) + W_{el}(S_{d_k+1}) + d_k \sum_{i=2}^{d_k+1} d_{li}(B_{k-1}) + \sum_{i=2}^{d_k+1} m_{k-1} d_{li}(S_{d_k+1})$$

$$+ \sum_{i=2}^{d_k+1} \sum_{j=2, j \neq i}^{d_k+1} m_{k-1} d_{li}(B_{k-1}) + \frac{1}{2} \sum_{i=2}^{d_k+1} \sum_{j=2, j \neq i}^{d_k+1} {m_{k-1}}^2 d_H(i_1, i_2), l = 1, 2,$$

where, i_1 and i_2 are the roots of two B_{k-1} in the level 2. We have $d_{S_{d_k+1}}(i_1, i_2) = 2$ and $W_{e1}(S_{d_k+1}) = 0; W_{e2}(S_{d_k+1}) = {d_k}^2$. Also by Lemma 2, we have $d_{1i}(S_{d_k+1}) = 0; d_{2i}(S_{d_k+1}) = d_k$. Therefore, the results are obtained.

Definition 2 (Dendrimer Graph)**.** A highly branched tree, $T_{k,d}$, is called a regular dendrimer graph, for $k \geq 0$ and $d \geq 3$, in particular, $T_{k,d}$ stands for the k[th] regular dendrimer graph of degree d [8,13]. Dendrimer graph is a kind of generalized Bethe tree for any $d \geq 3$. $T_{0,d}$ is the one-vertex graph and $T_{1,d}$ is the star with $d+1$ vertices. Then for $k = 2, 3, ...$ and $d \geq 3$ the tree is obtained by attaching $d-1$ new vertices of degree one to the vertices of degree one of $T_{k-1,d}$. Figure 2 presents the first four regular dendrimer graphs of degree four. An auxiliary tree $B_{k,d}$ is introduced below.

Each of the d branches attached to the central vertex of $T_{k,d}$ is isomorphic to $B_{k-1,d}$. It is immediately seen that $B_{0,d}$ is the one-vertex graph

and $B_{1,d}$ is the star with d vertices. Further, for $k = 2,3,...$ and $d \geq 3$, the tree $B_{k,d}$, is obtained by attaching $d-1$ new vertices of degree one to the vertices of degree one of $B_{k-1,d}$. The tree of the type $B_{3,4}$ is given in Figure 3.

Proposition 3. Let $T_{k,d}$ be a dendrimer graph for which $k \geq 0$ and $d \geq 3$, then we have

$$W_{e1}(T_{k,d}) = dW_{e1}(B_{k,d}) + d^2(d_{1i}(B_{k,d}) + m_{k,d}d_{1i}(B_{k,d}) + m_{k,d}{}^2) - d(m_{k,d}d_{1i}(B_{k,d}) + m_{k,d}{}^2),$$

$$W_{e2}(T_{k,d}) = dW_{e2}(B_{k,d}) + d^2(1 + m_{k,d} + d_{2i}(B_{k,d}) + m_{k,d}d_{2i}(B_{k,d}) + m_{k,d}{}^2) - d(m_{k,d}d_{2i}(B_{k,d}) + m_{k,d}{}^2),$$

Therefore,

$$W_{e0}(T_{k,d}) = W_{e1}(T_{k,d}) + \frac{m(m-1)}{2} \text{ and } W_{e4}(T_{k,d}) = W_{e2}(T_{k,d}) - m$$

where m is the number of edges of $T_{k,d}$.

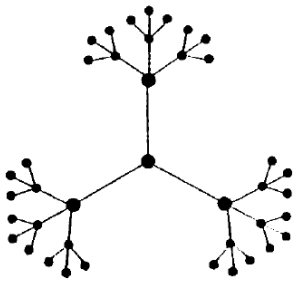

Figure 2. Example of regular dendrimer graphs

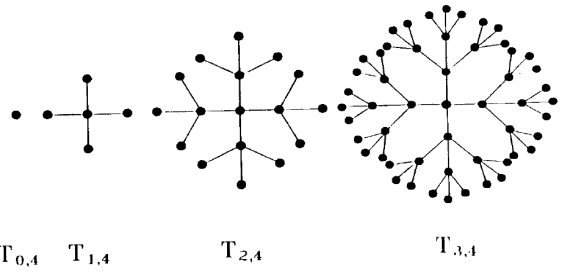

Figure 3. Tree of the type $B_{3,4}$

Proof. The number of edges of $T_{k,d}$ is obtained as:

$$m = |E(T_{k,d})| = d + d(d-1) + d(d-1)^2 + ... + d(d-1)^{k-1}$$

Also the number of edges of $B_{k,d}$ is obtained as:

$$m_{k,d} = |E(B_{k,d})| = (d-1) + (d-1)^2 + ... + (d-1)^k$$

Now we can define $B_{k,d}$ and $T_{k,d}$ by the rooted product of trees similar to Proposition 2

$$B_{k,d} = S_d(P_1, B_{k-1,d}, B_{k-1,d}, ..., B_{k-1,d})$$
$$T_{k,d} = S_{d+1}(P_1, B_{k,d}, B_{k,d}, ..., B_{k,d})$$

Also, we have

$$d_{1i}(B_k) = \sum_{e \in E(B_k)} d_1(e,i) = (d-1)^2 + 2(d-1)^3 + ... + (k-1)(d-1)^k,$$
$$d_{2i}(B_k) = \sum_{e \in E(B_k)} d_2(e,i) = (d-1) + 2(d-1)^2 + ... + k(d-1)^k.$$

where i is the root of $B_{k,d}$. Then the result is obtained by Proposition 2.

As examples, we calculated the first and second type of edge-Wiener index of $T_{3,4}$. The results are listed in Tables 1 and 2.

Table 1. Edge-Wiener index of $T_{k,4}$.

k	1	2	3
$m_{k,4}$	3	12	39
$d_{1i}(B_{k,4})$	0	9	63
$d_{2i}(B_{k,4})$	3	21	102
$W_{e1}(B_{k,4})$	54	1755	29700
$W_{e1}(B_{k,4})$	171	3195	43857

Table 2. Edge-Wiener index of $T_{3,4}$.

$m = \| E(T_{3,4}) \|$	52
$W_{e1}(T_{3,4})$	167544
$W_{e0}(T_{3,4})$	168870
$W_{e2}(T_{3,4})$	243688
$W_{e4}(T_{3,4})$	243636

ACKNOWLEDGEMENTS

The authors would like to thank the referee for his careful reading and useful suggestions.

REFERENCES

[1] H. Wiener, *J. Am. Chem. Soc*., **1947**, *69*, 17.

[2] F. Buckley, F. Harary, *Distance in Graphs*, Addison-Wesley, Redwood, CA, **1990**.

[3] F. Buckley, *Congr. Number*, **1981**, *32*, 153.

[4] A.A. Dobrynin, R. Entringer, I. Gutman, *Acta Apppl. Math*., **2001**, *66*, 211.

[5] A.A. Dobrynin, I. Gutman, S. Klavzar, P. Zigert, *Acta Appl. Math*., **2002**, *72*, 247.

[6] A.A. Dobrynin, L.S. Mel'nikov, *MATCH Commun. Math. Comput. Chem*., **2005**, *53*, 209.

[7] I. Gutman, O. Polansky, *Mathematical Concepts in Organic Chemistry*, Springer-Verlag, Berlin, Germany, 1986.

[8] I. Gutman, Yeong-Nan Yeh, Shyi-Long Lee, Jiang-Cherng Chen, *MATCH Commun. Math. Comput. Chem*., **1994**, *30*, 103.

[9] A. Gravac, T. Pisaski, *J. Math. Chem*., **1991**, *8*, 53.

[10] A. Iranmanesh, I. Gutman, O. Khormali, A. Mahmiani, *MATCH Commun. Math. Comput. Chem*., **2009**, *61*, 663.

[11] C.D. Godsil, B.D. Mckay, *Bull. Austral. Math. Soc*., **1978**, *18*, 21.

[12] O. Rojo, *Lin. Algebra Appl*., **2007**, *420*, 490.

[13] A. Heydari, On the topological indices of graph of nanotubes, Ph.D. Thesis, Isfahan University of Technology, Isfahan, Iran, **2008**.

STUDIA UBB CHEMIA, LVII, 3, 2012 (p. 167 – 176)
(RECOMMENDED CITATION)

HOW PLASMA SPECIES AFFECT THE STRUCTURAL AND MORPHOLOGICAL PROPERTIES OF MWCNTS

SOMAYEH SHAMS[1, *], ZAHRA KHALAJ[1], MAHMOOD GHORANNEVISS[1]

ABSTRACT. Multi wall carbon nanotubes have been synthesized by DC-Plasma Enhanced Chemical Vapor Deposition with different plasma species. N_2 and Ar were added individually to the mixture of C_2H_2/H_2 plasma in the growth step of CNTs synthesis. The effect of plasma on pretreatment of catalyst film was studied as well as its effects on the CNTs diameter, structural quality and growth density, as given by Raman spectroscopy and Scanning Electron Microscopy. Special feature of this work is the use of gold as catalyst over Ni substrate. The results indicate that using $N_2/C_2H_2/H_2$ plasma, the diameter size of the CNTs in comparison with C_2H_2/H_2 plasma was increased whereas structural quality of these samples is the same. Conversely, using $Ar/C_2H_2/H_2$ plasma, a considerable decrease in the diameter size and quality of the CNTs was observed.

Keywords: *Plasma CVD, nanotubes, Hydrogen etching, Gold catalyst.*

INTRODUCTION

Carbon nanotubes (CNTs) synthesis based on CVD methods involves the catalytic decomposition of a carbon precursor on the substrate [1]. Transition metals such as Fe, Co, Ni, Mo, etc. [2-6] have been used as catalyst for CNTs growth in most of the researches and synthesis parameters for CNTs growth over these catalysts have been widely studied [7-15]. Studies have shown gold (Au) in nanometer scale with catalytic properties, in addition to photo catalytic properties; it has attracted considerable researches in biomedical [16-23] and imaging filed [24, 25]. On the other hand, applications of CNTs in technologies such as field-emission devices, nanolithography, ballistic transistors, X-ray generators, gas sensors [26-31] are well known nowadays. Due to the scale, structure and biocompatibility of CNTs, considerable attention was paid in biomedical applications, such as drug delivery, cancer therapy, imaging and diagnostics [32,33]. It is expected that, in the CNTs tip-growth mode [34, 35] over the Au catalyst, CNT tops be ended by Au nanoparticles. This combination CNT/Au would be attractive for biomedical applications.

[1] *Plasma Physics Research Center, Science and Research Branch, Islamic Azad University, Tehran, Iran*
[*] *Correspondent: somayehshamss@gmail.com*

After discovery of CNTs, by Iijima in 1991 [36] by arc discharge in the helium atmosphere, several methods have been developed for CNTs synthesis. The main methods are: arc discharge, laser ablation and several types of CVD. Among these last methods, Plasma CVD is applied widely for synthesizing carbon nanotubes and other carbon nanostructures [37,38]. Electrical field of plasma makes the grown structures well aligned, with high quality, in lower temperature comparison to other methods; plasma enhanced PECVD is a controllable and predefined method in this respect. Therefore, we used a home made PECVD apparatus (see below) for CNTs growth. The quality of carbon nanotube deposits on the gold catalyst were analyzed by using Atomic Force Microscopy (AFM), Scanning Electron Microscopy (SEM) and Raman spectroscopy.

RESULTS AND DISCUSSION

Various plasma mixtures have been applied for CNTs growth up to date: Okita et al. have used a mixture of H_2/CH_4 [9], Gulas et al. have investigated gas phase kinetics of the CNT synthesis, by using different ratios of $NH_3/C_2H_2/H_2$ [3]. In the present study, three different mixtures of plasma C_2H_2/H_2, $N_2/C_2H_2/H_2$, $Ar/C_2H_2/H_2$ were used and the effects of each of them on the CNTs structure and morphological properties were comparatively analyzed.

The experimental results of this study have shown remarkable changes in diameter size, length, growth density and structural quality of the MWCNTs. In addition, the effect of plasma etching over the catalyst layer was investigated. The noticeable point is the growth temperature which was set on 550 ˚C, lower in comparison to the growth temperature reported by others [39].

The XRD spectrum, Figure 1, indicates the structural details of the substrate used within this work. The three peaks, representing the structure of nickel, hcp (002) at 2Θ=42°, fcc (111) at 44.63° and fcc (200) at 2Θ=52.09° with the intensity of 1066.63, 333.69 and 9068.81, respectively, are evidenced. Therefore, according to this XRD pattern, the substrate is made of pure Ni, with more fcc structure.

Atomic force microscopy (AFM, XE-NSOM) was performed on the nickel substrate before and after the catalyst deposition, in contact mode on 3μm x 3μm area. Figure 2 shows 3D images and histograms of the topography versus the number of events for both types of the samples. The 3D images of the both samples show different topography, speaking about different average roughness for each sample. Therefore, as can be seen in Figure 2(a) and (c), the surface roughness for the pure nickel is much higher than for nickel coated by gold.

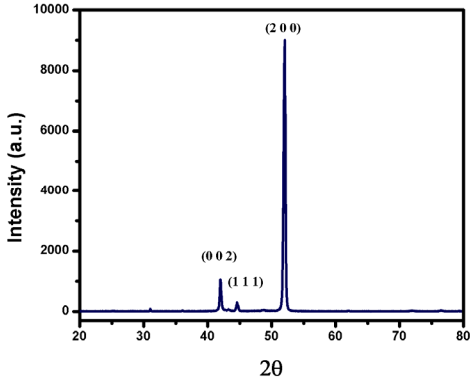

Figure 1. XRD pattern for the high purity nickel substrate

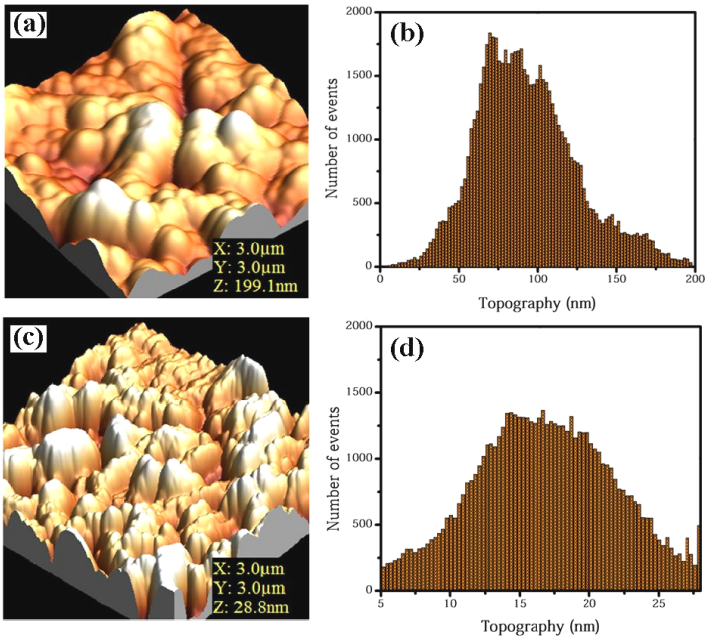

Figure 2. Three dimensional AFM images and histograms of the surface topography of: (a,b) pure nickel and (c,d) gold coated nickel substrate

The average roughness was found around 27.980 nm for the Ni substrate with no coatings. After gold coating, the morphology of the Ni surface was changed and the average roughness was reduced to 5.376 nm. As the Gaussian diagrams show, the homogeneity is lower for the pure nickel (Figure 2 (b)) than for the gold coated nickel substrate (Figure 2(d)).

The thickness of the gold nanolayer deposited on the nickel substrate as a catalyst by sputtering system was about 28.77 nm. Film thickness was measured using Rutherford back scattering (RBS) technique, using He^+ ion beam of 10μm in diameter, at 2.0 MeV. A typical RBS spectrum of Au thin film is given in Figure 3. The red line is obtained from exprimental data while the blue one is related to simulated data. The peak in the channel range of 310 to 340 indicated Au in the sample.

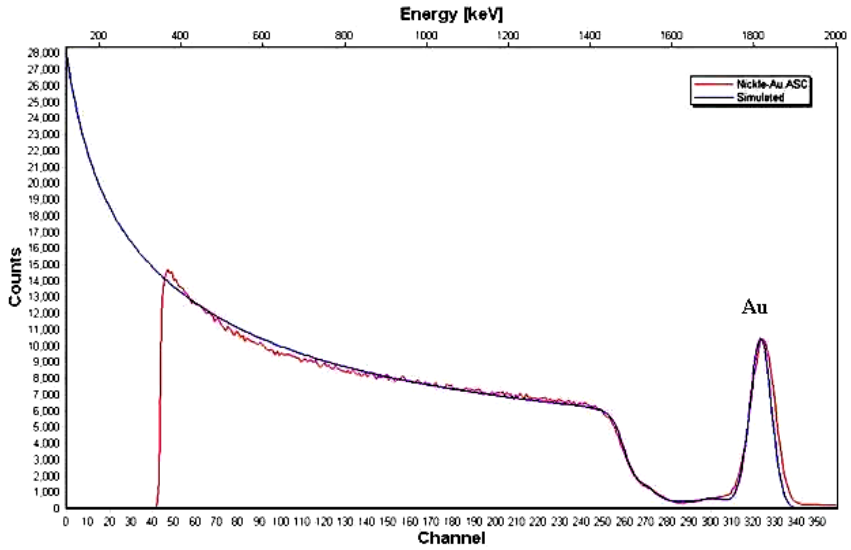

Figure 3. RBS curve shows the thicknesses of Au thin film deposited on nickel substrate

The SEM micrographs for the CNTs of the samples grown at different gase mixtures are shown in Figure 4. The range of CNTs diameter size, observesed in SEM images were analyzed statisticaly. The results are shown as a bar graphs in Figure 5. The red rectangular marks on the bars indicate the average diameter. Therefore, according to the bar graphs, the most disperse diameter size belongs to the samples S_1 and S_2, with the averege of 53 and 85 nm, respectively.

Adding N_2 gas to the plasma in the growth step resulted in new walls added to CNTs instead of growth in axial direction and length, so it has the maximum average among the other samples. The smalest bar graph belongs to the sample S_3. It means that adding Ar gas to the plasma in the growth phase, the diameter of CNTs and diversity in the size were dropped. The average in the sample S_3 is 23 nm although it had the lowest growth density on the surface, according to Figure 4. The last bar graph is referred

to S_4, of which size diversity is less than that of S_1 while the averege diameter decreased from 53 nm to 43.5 nm, more probably due to the lack of the etching step.

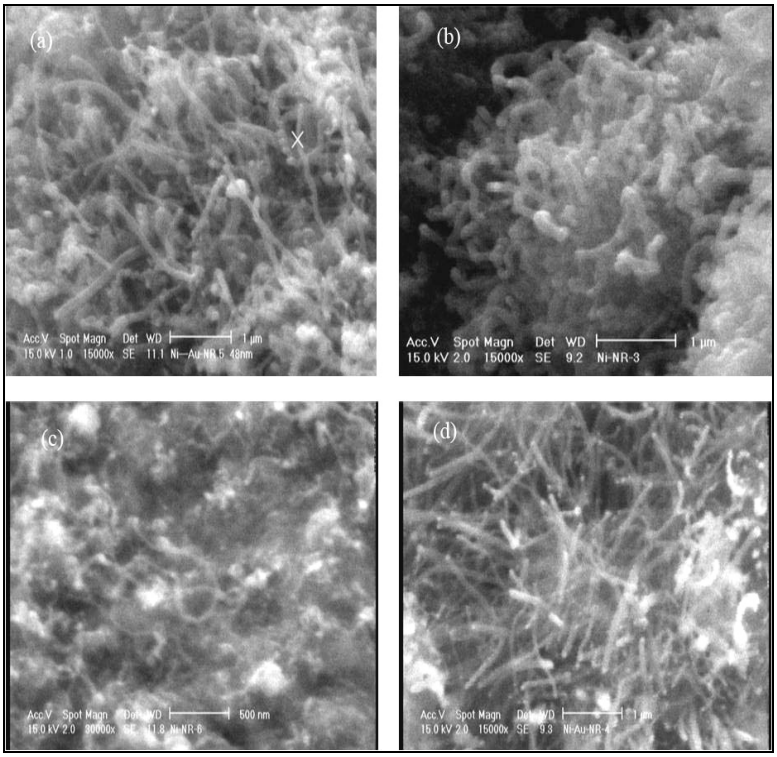

Figure 4. SEM micrographs show the effect of the dilution gases on CNTs growth: (a) S_1: H_2 ,(b) S_2: H_2/ N_2, (c) S_3: H_2/ Ar, (d) S_4: H_2 without plasma etching process

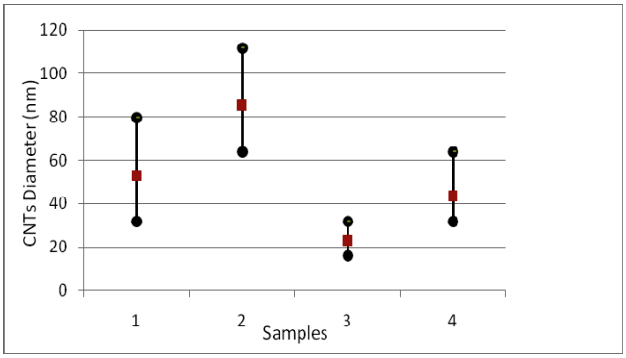

Figure 5. The bar graphs show the range of CNTs diameter size on the samples, the red rectangular marks indicating the average diameter.

Raman spectroscopy is widely used for the characterization of CNTs and the origins of the Raman bands seem to be well understood [40, 41]. The Raman spectra of the four samples are shown in the Figure 6; they are recorded on samples without purification. The peak around 1600 cm^{-1} is related to the stretching mode in the graphite plane, in the CNTs axial direction, which is called the G-band. The other wide peak, related to the D-band longitudinal optical phonon, is around 1350 cm^{-1} that is attributed to the pores or other defects in the sp^2 carbon structure. The G and D bands of samples S_1 and S_2 were observed at 1597 cm^{-1} and 1354 cm^{-1}, respectively. These values were shifted to 1586 cm^{-1} and 1342 cm^{-1} in the sample S_2. The related peaks for S_3 were observed at 1600 cm^{-1} and 1357 cm^{-1}. Therefore, the results show the plasma species in the growth step have influence on peaks position.

The ratio of D-band to G-band intensities I_D/I_G is an important factor to analyze the quality of CNTs structure, whatever this value is less than one the non-defect graphene structure is much than the disorder structure and amorphus carbon in the sample. The lower I_D/I_G values, of 0.967 and 0.968 are related to the sample S_1 and S_2, respectively. Although the CNT deposit appearance of the two above samples differs in diameter size, length and growth density, they have quite the same structural quality. For the sample S_3 the ratio was incresed to 0.976 but the difference is just 0.01. Finaly, the maximum ratio value, of 1.026, belongs to the sample S_4 so the effects of plasma etching process on the Au catalyst layer is obvious in the quality of CNTs structure.

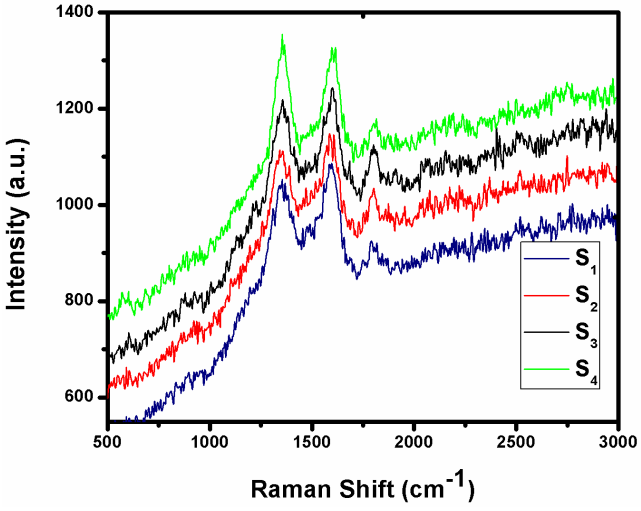

Figure 6. Raman spectra of the carbon nanotubes synthesized on gold coated nickel substrate: S_1 to S_4

We calculated the ratio $L_a=44/(I_D/I_G)$ to evaluate the CNTs quality. The results are 45.501, 45.454 and 45.082, for the samples S_1, S_2 and S_3 respectively. The value for S_4 is decreased to 42.885, therefore the effect of H_2 plasma etching treatment is clear here.

CONCLUSIONS

In this paper, the effects of hydrogen etching gas and different gas mixtures were investigated. Using the gold nanolayer catalyst, enabled the carbon nanotube growth at relatively low temperature (550 ˚C) and with a high quality. Using the hydrogen etching gas favored the Au thin film reductions and created suitable sites for nanotubes tip growth. The SEM and Raman spectroscopy have shown that the CNTs grown by H_2 /C_2H_2 plasma S_1 have the highest quality, with lower I_D/I_G= 0.967 and the average diameter size about 53 nm. The next one is S_2 with I_D/I_G= 0.968, however this mixture of plasma increased the diameter size to 85 nm. In S_3 the average diameter size decreased to 23 nm. In addition, the ratio of I_D/I_G increased to 0.976 and the density growth on the surface was remarkably decreased. In conclusion, by using suitable etching gas, good catalyst layer and relevant gas mixture, resulted in production of high quality carbon nanotubes.

EXPERIMENTAL DETAILS

Pure wafer of nickel (Ni) with 1 mm thickness was used as substrate in 5×5 mm^2 surface dimension. The substrate was cleaned with acetone, ethanol and deionized water in an ultrasonic bath 15 min for each step and then was dried in air. Structure characterization of the substrate was performed by X-ray diffraction instrument (Siemens -D500 XRD). Atomic Force Microscopy (AFM-Park Scientific Instruments Auto Probe CP) was used to determine the substrate morphology in this step.

The cleaned substrate was transferred to a DC-sputtering system for catalyst coating. A thin film of gold (Au) with 28.77 nm thickness was coated on the Ni substrate in Ar plasma. In this step, AFM was used to compare the surface topography of the pure one and the other after catalyst layer deposition. Rutherford back scattering (RBS) analysis was applied to measure the layer thickness.

Plasma Enhanced Chemical Vapor Deposition system, manufactured by our group in Plasma Physics Research Center (PPRC), was applied for CNT growth (Figure 7). The coated substrate was put in the DC-PECVD reactor. The chamber was evacuated to 10^{-5} Torr and then, in the presence of H_2, the substrate was heated up to 550°C. The temperature was kept fix during the etching and growth processes. Etching processes performed by H_2 plasma. A mixture of C_2H_2/H_2 was used as carbon source and dilution gas. We investigated the gas mixture effects on CNTs growth by adding Ar and N_2 to the reactor in the growth process step. The experimental conditions are listed in Table 1.

Table 1. Experimental conditions for the carbon nanotubes growth on gold coated Ni substrate

Sample No.	Etching gas	$P_{etching}$ (Torr)	Gas Mixture	Flow ratio	P_{growth} (Torr)	t_{growth} (min)
S_1	H_2	2.5	C_2H_2 / H_2	35/140	5	20
S_2	H_2	2.5	C_2H_2 / H_2 / N_2	35/70/70	5	20
S_3	H_2	2.5	C_2H_2 /H_2/ Ar	35/70/70	5	20
S_4	-	-	C_2H_2 / H_2	35/140	5	20

Second harmonic of a Nd:YLF laser with 532 nm wavelength was used for Raman spectroscopy. SEM (XL30, Phillips, Holland) was used to determine the morphology and diameter estimates of the carbon nanotube deposits.

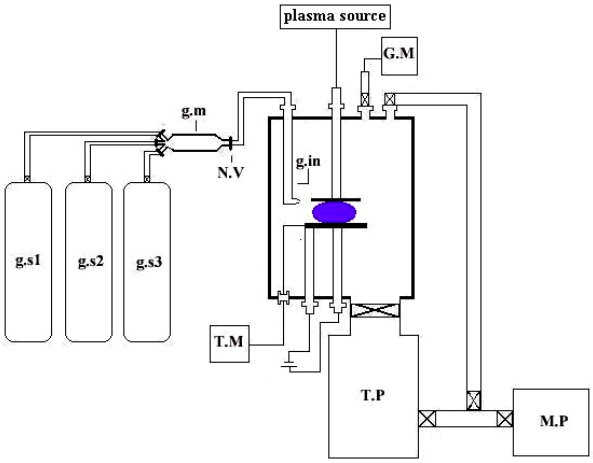

Figure 7. Schematic of the PECVD system manufactured by Plasma Physics Research Center.

REFERENCES

1. Yong Seob Park, Eun Chang Choi, Byungyou Hong, *Applied Surface Science*, **2009**, *255*, 6028.
2. H. Sato et al., *Vacuum*, **2009**, *83*, 515.
3. M. Gulas, F. Le Normand, P. Veis, *Applied Surface Science*, **2009**, *255*, 5177.
4. H. Yoshida et al., *Nano Lett.*, **2009**, *9*, 3810.
5. J.K. Radhakrishnan et al., *Applied Surface Science*, **2009**, *255*, 6325.

6. Yeau-Ren Jeng, Hua-Chiang Wen, Ping-Chi Tsai, *Diamond & Relat. Mater.,* **2009**, *18*, 528.
7. M.R. Maschmann et al., *Carbon*, **2007**, *45*, 2290.
8. Duck-Hyun Lee et al., *Nanosci. Nanotechnol.,* **2008**, *8*, 5571.
9. A. Okita et al., *Carbon*, **2007**, *45*, 1518.
10. Y. Abdi et al., *Carbon*, **2008**, *46*, 1611.
11. F. Javier del Campo et al., *Electrochem. Commun*., **2008**, *10*, 1242.
12. I. Jang et al., *Carbon*, **2007**, *45*, 3015.
13. A. Chandrashekar et al., *Thin Solid Films*, **2008**, *517*, 525.
14. Ting Xu et al., *Materials Lett.*, **2009**, *63*, 867.
15. H. Ohno, *Surface Sci. Nanotechnol*., **2009**, *7*, 904.
16. Wei Fu et al., *Materials Res. Soc. Bull.,* **2004**, *845*, 223.
17. H.K. Patra et al., *Nanomedicine*, **2007**, *3*, 111.
18. G. F Paciotti et al., *Drug Delivery*, **2004**, *11*, 169.
19. S. Dhar et al., *Chem. Eur. J.,* **2008**, *12*, 10244.
20. J. Nam et al., *J. Am. Chem. Soc.*, **2009**, *131*, 13639.
21. N.P. Praetorius, T.K. Mandal, *Rec. Pat Drug Deliv. Formul*., **2007**, *1*, 37.
22. P. Chandra et al., *Digest J. Nanomater. Biostruct.*, **2010**, *5*, 363.
23. Z. Krpetic et al., *Gold Bull*., **2006**, *39*, 66.
24. In-Cheol Sun et al., *Chem. Eur. J*., **2009**, *15*, 13334.
25. Xiangyang Shi et al., *Small*, **2007**, *3*, 1245.
26. Seong Chu Lim et al., *NANO*, **2007**, *2*, 69.
27. Won Bong Choi et al., *Jpn. J. Appl. Phys*, **2000**, *39*, 2560.
28. A. Okazaki et al., *Jpn. J. Appl. Phys*, **2000**, *39*, 7067.
29. A. Javey et al., *Nature*, **2003**, *424*, 654.
30. O.E. Alon, *Phys. Rev. Lett*., **2000**, *85*, 5218.
31. A. Modi et al., *Nature*, **2003**, *424*, 171.
32. A.R. Harutyunyan et al., *Eur. Cells Mater*., **2002**, *3*, 84.
33. Zhuang Liu, Kai Chen, C. Davis et al., *Cancer Res.*, **2008**, *68*, 6652.
34. V.I. Merkulov et al., *Appl. Phys. Lett*., **2001**, *79*, 2970.
35. A. Gohier et al., *Carbon*, **2008**, *46*, 1331.
36. S. Iijima, *Nature*, **1991**, *354*, 56.
37. E. Vaghri, Z. Khalaj, M. Ghoranneviss, M. Borghei, *J. Fusion Energ*., **2011**, *30*, 447.

38. Z. Khalaj, M. Ghoranneviss, E. Vaghri, A. Saghaleini, M.V. Diudea, *Acta Chim. Slo*., **2012**, *59*, 338.

39. Ch. Taschner et al., *Surf. Coat. Technol*., **2003**, *81*, 174–175.

40. J.-Ph. Tessonnier et al., *Carbon*, **2009**, *47*, 1779.

41. J. Maultzsch, S. Reich, C. Thomsen, *Phys. Rev. B*, **2002**, *65*, 115.

STUDIA UBB CHEMIA, LVII, 3, 2012 (p. 177 – 182)
(RECOMMENDED CITATION)

OMEGA POLYNOMIALS AND CLUJ-ILMENAU INDEX OF CIRCUMCORONENE SERIES OF BENZENOID

MOHAMMAD REZA FARAHANI[1,*], KATALIN KATO[2], MIRANDA P. VLAD[3]

ABSTRACT. The "Omega" Ω(G,x) polynomial was defined by Diudea on the ground of quasi-orthogonal cut "qoc" edge strips. Two topological indices CI(G) (Cluj-Ilmenau index) and Omega index I_Ω are defined on the above polynomial. The goal of this paper is to compute the Omega polynomial and the corresponding indices in the circumcoronene series of benzenoids.

Keywords: *Omega polynomial, Cluj-Ilmenau index, Circumcoronene.*

INTRODUCTION

Let *G*=(*V*,*E*) be a molecular graph, with the vertex set *V*=*V*(*G*) and edge set *E*=*E*(*G*). Two edges *e*=*uv* and *f*=*xy* of G are called co-distant, "e co f", if and only if they obey the following relation [1]

$$d(v,x)=d(v,y)+1=d(u,x)+1=d(u,y)$$

where the distance d(x,y) between x and y is defined as the length of a shortest path between x and y. For some edges of *G* the following relations are satisfied [1,2]

$$e \ co \ e$$
$$e \ co \ f \Leftrightarrow f \ co \ e$$
$$e \ co \ f \ \& \ f \ co \ h \Rightarrow e \ co \ h$$

though the last relation is not always valid. In other words, relation *co* is not transitive, in general and if *co* is also transitive, the above relations represent an equivalence; then *G* is called a *co-graph* and $C(e)=\{f \in E(G);\ f \ co \ e\}$, denoting the set of edges in *G*, co-distant to the edge $e \in E(G)$, is called an *orthogonal cut* (denoted by oc) of *G*, *E*(*G*) being the union of disjoint orthogonal cuts

[1] *Department of Mathematics of Iran University of Science and Technology (IUST), Narmak, Tehran 16844, Iran.* [*] *Mr_Farahani@Mathdep.iust.ac.ir*
[2] *Faculty of Chemistry and Chemical Engineering, Babes-Bolyai University, 400028, Aranj Janos 11, Cluj, Romania*
[3] *Faculty of Economic Sciences Cluj, Dimitrie Cantemir University, Bucharest*

$$\mathrm{E}(\mathrm{G}) = \mathcal{C}_1 \cup \mathcal{C}_2 \cup ... \cup \mathcal{C}_{k-1} \cup \mathcal{C}_k \text{ and } \mathcal{C}_i \cap \mathcal{C}_j = \varnothing,$$
$$\text{for } i \neq j \quad \text{and} \quad i, j = 1, 2, .., k .$$

If any two consecutive edges *e* and *f* of a plane graph *G* of an edge-cut sequence are topologically parallel within the same face of the covering, such a sequence is called a quasi-orthogonal cut qoc strip. Obviously, any orthogonal cut strip is a qoc strip but the reverse is not always true. This means the transitivity relation of the *co* relation is not necessarily obeyed [1, 3-5].

The *Omega Polynomial Ω(G,x)* for counting qoc strips in G was defined by *M.V. Diudea* [6] as

$$\Omega(\mathrm{G}, \mathrm{x}) = \sum_c \mathrm{m}(\mathrm{G}, c)\, \mathrm{x}^c$$

where m(G,c) denote the number of qoc strips of length c. The summation runs up to the maximum length of qoc strips in G.

Also, first derivative of Omega polynomial (in *x*=1) equals the number of edges in the graph G (see also [1-4, 6-9])

$$\Omega'(\mathrm{G}, 1) = \sum_c \mathrm{m}(\mathrm{G}, c) \times c = |E(G)|$$

An index, called *CI* (Cluj-Ilmenau), is derived from and its first and second derivatives, in *x*=1, as [5]

$$CI(G) = \left[\Omega'(\mathrm{G}, \mathrm{x})\right]^2 - \left[\Omega'(\mathrm{G}, \mathrm{x}) + \Omega''(\mathrm{G}, \mathrm{x})\right]_{x=1}$$

CI index is eventually equal to the well-known *Padmakar-Ivan index* (PI) [1, 10], in polycyclic graphs embedded in the plane. *PI* index of G is an important topological descriptor in chemical graph theory and is defined as

$$PI(G) = \sum_{e \in E(G)} \left(m_u(e \mid G) + m_v(e \mid G)\right)$$

where $m_u(e \mid G)$ is the number of edges of G lying closer to u than to v and $m_v(e \mid G)$ is the number of edges of G lying closer to v than to u.

Another single number descriptor is calculable from the Ω(*G,x*) derivatives *d*, in *x*=1, and normalized to the first polynomial derivative. The Omega index is equal to

$$I_\Omega(G) = \frac{1}{\Omega'(G, \mathrm{x})} \sum_d \sqrt[d]{\Omega^d(G, \mathrm{x})}\Big|_{x=1}$$

In fact, d is up to the maximum length of qoc strips in G.

The aim of this study is to compute the Omega polynomial, Omega and Cluj-Ilmenau index of Circumcoronene series of benzenoidd H_k, with *k* being a positive integer number. A general representation of circumcoronene family is shown in Figure 1.

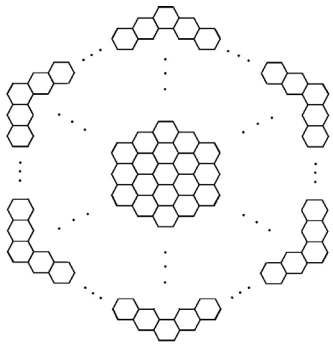

Figure 1. A view of circumcoronene series of benzenoids $H_k, k \geq 1$.

RESULTS AND DISCUSSION

The aim of this paper is to compute the Omega polynomial and Omega and Cluj-Ilmenau indices of Circumcoronene series of benzenoids. We know that the general case of this molecular graph has $6k^2$ vertices and $9k^2-3k$ edges (Figure 1).

Theorem 1. Consider the molecular graph of Circumcoronene series of benzenoids $H_k, \forall k \in \square$, then

- The Omega polynomial of H_k is as follows

$$\Omega(H_k, x) = 6\sum_{i=1}^{k-1} x^{k+i} + 3x^{2k}$$

- The Cluj-Ilmenau index of H_k is equal to

$$CI(H_k) = k(81k^3 - 68k^2 + 12k - 1)$$

- The Omega index of H_k is

$$I_\Omega(H_k) = \left(\frac{1}{9k^2-3k}\right)\sum_{d=1}^{2k} d\sqrt{6\sum_{i=1}^{k-1}\left(\prod_{j=0}^{d-1}(k+i-j)\right)+3\left(\prod_{j=0}^{d-1}(2k-j)\right)}$$

Proof. Let $G = H_k$ be the Circumcoronene series of benzenoids. This graph has $6k^2$ vertices. *Cut Method* and its general form was studied by *S. Klavzar* [11] and others [5, 12]. Now, by using this method and Figure 1, there are k distinct cases of qoc strips. Obviously, Circumcoronene series of benzenoids is a co-graph, thus the size of a qoc strip C_i for every $(i = 1,...,k-1)$

is equal to $k+i=c_i$ since $\forall e \in \mathcal{C}_i$ there are k+i-1 co-distant edges with e (see Figure 2.) and the number of repetitions of these quasi-orthogonal cuts $\mathcal{C}_i$ $\forall i=1,...,k-1$ is six times $\left(m(H_k,c_i)=6\right)$. The number of repetitions of qoc $\mathcal{C}_k$ is three times $\left(m(H_k,c_k)=3\right)$, respectively. This implies that

$$3|\mathcal{C}_k|+6|\mathcal{C}_{k-1}|+...+6|\mathcal{C}_1|=6\sum_{i=1}^{k}[k+i]-6k=9k^2-3k=\left|E(H_k)\right|.$$

So, we have

$$\begin{aligned}\Omega(H_k,x)&=\sum\nolimits_c m(H_k,c)x^c\\&=\sum_{\substack{i=1\\c_i=k+i}}^{k} m(H_k,c_i)x^{c_i}\\&=\sum_{i=1}^{k-1}\left(m(H_k,c_i)x^{c_i}\right)+m(H_k,c_k)x^{c_k}\\&=\sum_{i=1}^{k-1}\left(6x^{k+i}\right)+3x^{2k}\end{aligned}$$

Now, we can calculate the Cluj-Ilmenau index of H_k as

$$\begin{aligned}CI(H_k)&=\left[\Omega'(H_k,x)\right]^2-\left[\Omega'(H_k,x)+\Omega''(H_k,x)\right]_{x=1}\\&=\left[\left(\sum_{i=1}^{k-1}\left(6x^{k+i}\right)+3x^{2k}\right)'\right]^2-\left[\left(\sum_{i=1}^{k-1}\left(6x^{k+i}\right)+3x^{2k}\right)'+\left(\sum_{i=1}^{k-1}\left(6x^{k+i}\right)+3x^{2k}\right)''\right]_{x=1}\\&=\left[6\sum_{i=1}^{k-1}(k+i)x^{(k+i-1)}+6kx^{2k-1}\right]^2-\\&-\left[6\sum_{i=1}^{k-1}(k+i)x^{(k+i-1)}+6kx^{2k-1}+6\sum_{i=1}^{k-1}(k+i)(k+i-1)x^{(k+i-2)}+6k(2k-1)x^{2k-2}\right]_{x=1}\\&=\left[6\sum_{i=1}^{k-1}(k+i)+6k\right]^2-\left[6\sum_{i=1}^{k-1}(k+i)+6k+6\sum_{i=1}^{k-1}(k+i)(k+i-1)+6k(2k-1)\right]\\&=k(81k^3-68k^2+12k-1)\end{aligned}$$

Now, we compute the Omega index of Circumcoronene series of benzenoids as

$$I_\Omega(H_k)=\frac{1}{\Omega'(H_k,x)}\sum_d \sqrt[d]{\Omega^d(H_k,x)}\Big|_{x=1}$$

since $$\Omega^d\left(H_k,\mathrm{x}\right)=6\sum_{i=1}^{k-1}\left(\prod_{j=0}^{d-1}\left(k+i-j\right)\right)\mathrm{x}^{(k+i-d)}+3\left(\prod_{j=0}^{d-1}\left(2k-j\right)\right)x^{2k-d}$$

In final, for every integer k, $I_\Omega\left(H_k\right)$ will be

$$I_\Omega(H_k)=\left(\frac{1}{9k^2-3k}\right)\sum_{d=1}^{2k}\sqrt[d]{6\sum_{i=1}^{k-1}\left(\prod_{j=0}^{d-1}\left(k+i-j\right)\right)+3\left(\prod_{j=0}^{d-1}\left(2k-j\right)\right)}$$

Thus completing the demonstration.

Lemma 2. By refering to the definition of I_Ω it is easy to see that $I_\Omega(G)\geq 1.$

Since $$I_\Omega(G)=\underbrace{\frac{1}{\Omega'(G,\mathrm{x})}\sqrt[1]{\Omega'(G,\mathrm{x})}\Big|_{x=1}}_{=1}+\underbrace{\frac{1}{\Omega'(G,\mathrm{x})}\sum_{d\in\mathbb{N}-\{1\}}\sqrt[d]{\Omega^d\left(G,\mathrm{x}\right)}\Big|_{x=1}}_{\geq 0}$$

The second part of the above equation is positive, because polynomial $\Omega(\mathrm{G},\mathrm{x})=\sum_c \mathrm{m}(\mathrm{G},c)\,\mathrm{x}^c$ and its all derived of order d have positive integer coefficients. Of course, if s is the maximum length of qoc strips in G, then $\Omega^d\left(G,\mathrm{x}\right)=0,\forall d\geq s.$

Obviously, this lower bound of $I_\Omega(G)$ holds if and only if G is the complete graph K_2 or path P_2.

Conjecture 1. For every molecular graph G, the upper bound of $I_\Omega(G)$ is two. Thus, we have

$$\frac{1}{\Omega'(G,\mathrm{x})}\sum_{d\in\mathbb{N}-\{1\}}\sqrt[d]{\Omega^d\left(G,\mathrm{x}\right)}\Big|_{x=1}<2$$

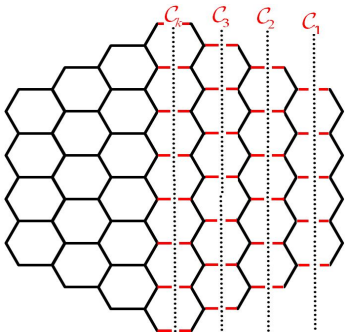

Figure 2. The presentation of quasi-orthogonal cuts qoc strips of H_4.

Example 1. By Figure 2, it is obvious that the Omega polynomial of H_4 is as follows:

$$\Omega\left(H_4, \mathrm{x}\right) = 6\mathrm{x}^5 + 6\mathrm{x}^6 + 6\mathrm{x}^7 + 3x^8$$

Also, the CI and I_Ω indices of H_4 are equal to $CI\left(H_4\right) = 16572$ and $I_\Omega(H_4) =$ 1.586

CONCLUSIONS

In this paper, we obtained the Omega polynomial, Omega and Cluj-Ilmenau indices of molecular graph Circumcoronene series of benzenoids $H_k \ (k \geq 1)$ and for the first time and we conjectured the lower and upper bounds for I_Ω of any molecular graph G, as $1 \leq I_\Omega(G) < 2.$

REFERENCES

1. P.E. John, A.E. Vizitiu, S. Cigher, M.V. Diudea, *MATCH Commun. Math. Comput. Chem.*, **2007**, *57*, 479.
2. M.V. Diudea, S. Cigher, P.E. John, *MATCH Commun. Math. Comput. Chem.*, **2008**, *60,* 237.
3. M.V. Diudea, S. Cigher, A.E. Vizitiu, O. Ursu, P.E. John, *Croat. Chem. Acta*, **2006**, *79*, 445.
4. A.E. Vizitiu, S. Cigher, M.V. Diudea and M.S. Florescu, *MATCH Commun. Math. Comput. Chem.*, **2007**, *57*, 457.
5. M.V. Diudea, *MATCH Commun. Math. Comput. Chem.,* **2010,** *64*, 569.
6. M.V. Diudea, *Carpath. J. Math.,* **2006**, *22*, 43.
7. M.V. Diudea, S. Cigher, A.E. Vizitiu, M.S. Florescu, P.E. John, *J. Math. Chem.,* **2009**, *45,* 316.
8. A.E. Vizitiu, S. Cigher, M.V. Diudea, M.S. Florescu, *MATCH Commun. Math. Comput. Chem.,* **2007**, *57*, 457.
9. M. Saheli, M. Neamati, A. Ilić, M.V. Diudea, *Croat. Chem. Acta,* **2010**, *83*, 395.
10. P.V. Khadikar, P.P. Kale, N.V. Despande, S. Karmarkar, V.K. Agrawal, *J. Math. Chem.*, **2001**, *29*, 143.
11. S. Klavzar. *MATCH Commun. Math. Comput. Chem.,* **2008**, *60,* 255.
12. P.E. John, P.V. Khadikar, J. Singh, *J. Math. Chem.*, **2007**, *42*, 27.

STUDIA UBB CHEMIA, LVII, 3, 2012 (p. 183 – 190)
(RECOMMENDED CITATION)

SOME TOPOLOGICAL INDICES OF C_{12n+4} FULLERENES

HAMID DARABI[1,*], SAMANEH MIRZAIE[2], YASER ALIZADEH[2]

ABSTRACT. A method for computing some topological descriptors based on distance in a graph, such as the molecular topological index (MTI), Schultz, Modified Schultz, Szeged and vertex PI_v indices in simple connected graphs and in the family of C_{12n+4} fullerenes is presented.

Keywords: *Molecular topological index (MTI), Schultz index, Modified Schultz index, Szeged index, vertex Padmakar-Ivan index (PI_v), C_{12n+4} fullerenes.*

INTRODUCTION

A topological index is real number mathematically derived from the structural graph of a molecule. Hundreds of different topological indices have been investigated so far and used in the Quantitative Structure Property Relationship (QSPR) studies, with various degrees of success. These invariants belong to one of two broad classes: distance-based indices or bond-additive ones. The first class includes indices defined on topological distances between pairs of vertices while the indices of the second class are defined as the sums of contributions over all edges. Topological indices based on the distances in graph are widely used to establish relationships between the structure of a molecular graph and their physicochemical properties. Let G be a simple connected graph, the vertex and edge sets of G being denoted by V(G) and E(G), respectively. The distance between two vertices u and v of G is denoted by d(u,v) and it is defined as the number of edges in a shortest path connecting u and v. Diameter of G is denoted by d(G).

The molecular topological index MTI of G was introduced by Schultz in 1989 [1]. It is defined as:

[*] *Author to whom correspondence should be addressed*
[1] *Department of Mathematics, Esfarayen Branch, Islamic Azad University, Esfarayen, Iran, darabi@iauesf.ac.ir*
[2] *Department of Mathematics, Tarbiat Modares University, Tehran, Iran s.mirzaie@modares.ac.ir, yalizadeh@modares.ac.ir*

$$MTI(G) = \sum_{i \in V(G)} \sum_{j \in V(G)} (a_{ij} + d_{ij})\delta_i \quad (1)$$

where δ_i is the degree of vertex *i* in *G* and a_{ij} and d_{ij} are elements of the adjacency matrix and distance matrix of G, respectively.

The molecular topological index has found interesting chemical application [2-10]. Mathematical properties of MTI are also described in several articles [11-13]. Let G be a simple connected graph, then MTI can also be expressed as [14]:

$$MTI(G) = \sum_{u \in V(G)} D_u \delta_u + \sum_{u \in V(G)} \delta_u^{\,2} \quad (2)$$

where $D_u = \sum_{v \in V(G)} d(u,v)$ is the sum of distances between vertex i and all other vertices of G. The Schultz index was introduced by Harry Schultz [3]. The non-trivial part of MTI is called the Schultz index and is defined as:

$$S(G) = \sum_{\{u,v\} \subseteq V(G)} (\delta_u + \delta_v) d(u,v) \quad (3)$$

where δ_u is the degree of vertex *u* and *d(u,v)* denote the distance between vertices *u* and *v*.

The main chemical applications and mathematical properties of this index were established in a series of studies [6,11,15]. Also a comparative study of molecular descriptors showed that the Schultz index and Wiener index are mutually related [14,16].

Klavzar and Gutman in [17] defined the modified Schultz index as:

$$MS(G) = \sum_{\{u,v\} \subseteq V(G)} (\delta_u \delta_v) d(u,v) \quad (4)$$

The Szeged index [18,19] is another such topological index and is closely related to the Wiener index; in particular, the Wiener and the Szeged index coincide in trees. The Wiener index also attracted considerable attention [20, 21].

The Szeged index is a vertex-multiplicative index. Let e=uv be an edge in G. The number of vertices in G lying closer to vertex u than to vertex v is denoted by $n_u(e)$. Analogously, $n_v(e)$ is the number of vertices in G lying closer to vertex v than vertex u. The Szeged index is defined as:

$$Sz(G) = \sum_{e=uv \in E(G)} n_u(e) \times n_v(e) \tag{5}$$

Khadikar et al. [22, 23] have defined a new topological index and named it Padmakar-Ivan PI index:

$$PI(G) = \sum_{e=uv \in E(G)} m_u(e) \times m_v(e) \tag{6}$$

where $m_u(e)$ is the number of edges of G lying closer to vertex *u* than vertex v. Applications of PI index to QSRP/QSAR were studied in [24]. The index was mostly compared to the Wiener and Szeged indices.

The vertex version of PI index was also considered [25]

$$PI_v(G) = \sum_{e=uv \in E(G)} n_u(e) + n_v(e) \tag{7}$$

In this paper we give a method for computing the MTI, Schultz, Modified Schultz, Szeged and PI_v indices for the family of fullerenes C_{12n+4}. In a series of papers, these indices have been computed for various molecular graphs [26-31].

Computing the MTI, Schultz, Modified Schultz, Szeged and PIv indices in fullerenes C12n+4

Carbon exists in the nature in three allotropic forms: diamond, graphite and fullerenes. Fullerene C_{60} has been discovered by Kroto *et al* in 1985 [32]. Fullerenes are large carbon cage molecules. A fullerene is associated to a planar, 3-regular and 3-connected graph and is tessellated by pentagons and hexagons. The molecular graph of C_{12n+4} fullerenes is illustrated in Figure 1, where *n* is the number of layers of 12 vertices.

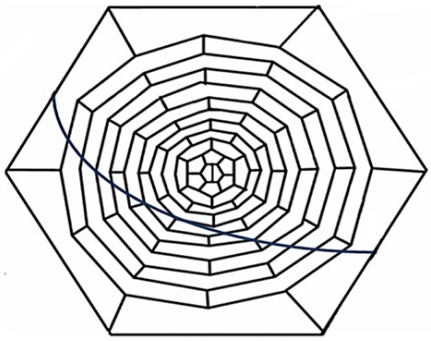

Figure 1. Fullerene C_{12n+4}; n=11

In this section, we give a GAP program for computing the MTI, Schultz, Modified Schultz, Szeged and vertex PI indices in simple connected graphs but also in C_{12n+4} fullerenes.

We denote the set of vertices of which distance to the vertex u is t, by $D_{u,t}$ and $D_{u,o} = \{u\}$. Eccentricity of the vertex u in G is the path length from the vertex u to the vertex υ that is farthest from u:

$$\varepsilon(u) = Max\{d(u,v) | v \in V(G)\} \tag{8}$$

For computing the topological indices based on distance, it is sufficient to obtain the sets $D_{u,t}$ for each vertex u and $1 \le t \le \varepsilon(u)$. In a series of papers, an algorithm for computing the sets $D_{u,t}$ and some topological indices in molecular graphs was presented [28, 30]. Let $e = u\upsilon$ be an edge of G. By obtaining the sets $D_{u,t}$ and following the definition relations, the topological indices such as the MTI, Schultz, Modified Schultz, Szeged and PI_v, could be computed:

$$\varepsilon(u) = Max\{t | D_{u,t} \neq \emptyset\},$$
$$\delta_u = |D_{u,1}|,$$
$$n_u(e) = \sum_{t=1}^{\varepsilon(u)} |D_{u,t} \setminus (D_{v,t} \cup D_{v,t-1})|,$$
$$D_u = \sum_{t=1}^{\varepsilon(u)} t \times |D_{u,t}|,$$
$$S(G) = \sum_{u \in V(G)} \sum_{t=1}^{\varepsilon(u)} \sum_{v \in D_{u,t}} (\delta_u + \delta_v) \times t,$$
$$MS(G) = \sum_{u \in V(G)} \sum_{t=1}^{\varepsilon(u)} \sum_{v \in D_{u,t}} (\delta_u \delta_v) \times t.$$

The following GAP program computes the sets $D_{u,t}$ for any simple connected graph. The input of the program is the adjacent vertices set of each vertex.

```
D:=[];
for i in [1..n] do
D[i]:=[];D[i][1]:=N[i];u:=Union(u,D[i][1]);r:=1;
t:=1; u:=[i];
while r<>0 do   D[i][t+1]:=[];
for j in D[i][t] do
for m in Difference (N[j],u) do
AddSet(D[i][t+1],m);
od;
od;
u:=Union(u,D[i][t+1]);
if  D[i][t+1]=[]  then  r:=0;
fi;
t:=t+1;
od;
od;
D; # D[i][t] is the set D_{i,t}
```

We computed the MTI, Schultz, Modified Schultz, Szeged and PI_v indices of C_{12n+4} for various values of n and some results are shown in Table 1.

Table 1. Some Topological Indices of C_{12n+4}

n	MTI	Schultz index	Modified Schultz index	PI index	Szeged index
3	14628	7188	10782	924	5072
4	36408	18024	27036	1984	16404
5	71196	35364	53046	3492	38168
6	121680	60552	90828	5440	72958
7	190788	95052	142578	7804	122686
8	281856	140532	210798	190966	190966
9	398268	198684	298026	13900	278834
10	543480	271236	406854	17596	388582
11	720948	359916	539874	21724	522642
12	934128	466452	699678	26284	683526
13	1186476	592572	888858	31276	873798

It is easy to see that the diameter of the molecular graph of C_{12n+4} is $2n-1$ for $n \geq 7$. By interpolation of our data, we conjecture the following formula for MTI (C_{12n+4}).

$$\mathrm{MTI}(C_{12n+4}) = 576n^3 - 1152n^2 + 11004n - 27360, \; n \geq 7 \tag{9}$$

In the following, a mathematical method is presented to demonstrate the above conjecture.

Since C_{12n+4} is a 3-regular graph we have the following relation:

$$\begin{aligned} MTI(C_{12n+4}) &= 3 \sum_{u \in V(G)}{}' D_u + 9(12n+4) \\ &< 3\binom{12n+4}{2}(2n-1) + 108n + 36 \\ &= 432n^3 + 36n^2 + 18n + 36. \end{aligned} \tag{10}$$

Hence $MTI(C_{12n+4})$ is a polynomial with degree at most 3.

Proposition 1: If $p(x)$ and $q(x)$ are two polynomials of degrees m and n, respectively $(m \leq n)$ and have more than n points in common, then $p(x) = q(x)$.

Proof: $q(x) - p(x)$ is a polynomial with degree at most n and more than n roots. Since a nonzero polynomial of degree n has at most n real roots, hence $q(x) - p(x)$ must be 0 and the proof is completed.

Theorem 1. For $n \geq 7$ we have:

$$MTI(C_{12n+4}) = 576n^3 - 1152n^2 + 11004n - 27360.$$

Proof: Let $P(n) = MTI(C_{12n+4})$ and $q(n) = 576n^3 - 1152n^2 + 11004n - 27360, n \geq 7$. $p(n)$ and $q(n)$ are two polynomial with degrees at most 3 and by Table1, have more than 3 points in common, hence by Proposition 1, we have:

$$MTI(C_{12n+4}) = P(n) = q(n) = 576n^3 - 1152n^2 + 11004n - 27360, n \geq 7.$$

By a similar method, the other topological indices of C_{12n+4} fullerenes can be computed. In the next theorem, the explicit formulas for the Schultz, Modified Schultz, Szeged and PI_v indices of C_{12n+4} fullerenes is presented.

Theorem 2.

$$S(C_{12n+4}) = 288n^3 - 576n^2 + 5448n - 13644, \quad n \geq 7,$$
$$MS(C_{12n+4}) = 432n^3 - 864n^2 + 8172n - 20466, \quad n \geq 7,$$
$$PI_v(C_{12n+4}) = 216n^2 - 408n + 76, \quad n \geq 7,$$
$$Sz(C_{12n+4}) = 432n^3 - 864n^2 + 9264n - 49722, \quad n \geq 12.$$

CONCLUSIONS

It takes a long time to compute the topological indices based on distances in a graph. In this paper, a method is presented for computing some topological indices such as the MTI, Schultz, Modified Schultz, Szeged and PI_v indices. By the presented method, we can compute the above topological indices for the family of fullerenes C_{12n+4} by the GAP program and present explicit formulas for them.

ACKNOWLEDGMENT

This research is supported by Esfarayen branch, Islamic Azad University.

REFERENCES

1. H.P. Schultz, *J. Chem. Inf. Comput. Sci,* **1989**, *29*, 227.
2. H.P. Schultz, E.B. Schultz and T.P. Schultz, *J. Chem. Inf. Comput. Sci*, **1990**, *30*, 27.
3. H.P. Schultz and T.P. Schultz, J. *Chem. Inf. Comput. Sci,* **1991**, *31*, 144.
4. H.P. Schultz, E.B. Schultz and T.P. Schultz, *J. Chem. Inf. Comput. Sci,* **1992**, *32*, 69.
5. H.P. Schultz and T.P. Schultz, *J. Chem. Inf. Comput. Sci,* **1992**, *32*, 364.
6. H.P. Schultz, T.P. Schultz, *J. Chem. Inf. Comput. Sci*, **1993**, *33*, 240.
7. H.P. Schultz, E.B. Schultz and T.P. Schultz, *J. Chem. Inf. Comput. Sci,* **1993**, *33*, 863.
8. H.P. Schultz, E.B. Schultz and T.P. Schultz, *J. Chem. Inf. Comput. Sci,* **1994**, *34*, 1151.
9. H.P. Schultz, E.B. Schultz and T.P. Schultz, *J. Chem. Inf. Comput. Sci,* **1995**, *35*, 864.
10. H.P. Schultz, E.B. Schultz and T.P. Schultz, *J. Chem. Inf. Comput. Sci,* **1996**, *36*, 994.
11. W.R. Muller, K. Szymanski, J.V. Knop, N. Trinajstic, *J. Chem. Inf. Comput. Sci,* **1990**, *30*, 160.
12. D. Klein, Z. Mihalic, D. Plavsic and N. Trinajstic, *J. Chem. Inf. Comput. Sci,* **1992**, *32*, 304.
13. D. Plavsic, S. Nikolic, N. Trinajstic and D. Klein, *Croat. Chem. Acta*, **1993**, *66*, 345.
14. I. Gutman, S. Klavzar, *J. Chem. Inf. Comput. Sci*, **1996**, *36*, 1001.
15. Z. Mihalic, S. Nikolic, N. Trinajstic, *J. Chem. Inf. Comput. Sci,* **1992**, *32*, 28.
16. I. Gutman, S. Klavzar, *J. Chem. Inf. Comput. Sci*, **1997**, *37*, 741.
17. S. Klavzar, I. Gutman, *Disc. Appl. Math*, **1997**, *80*, 73.
18. I. Gutman, *Graph Theory Notes of New York*, **1994**, *27*, 9.
19. P.V. Khadikar, N.V. Deshpande, P.P. Kale, A. Dobrynin and I. Gutman, *J. Chem. Inf. Comput. Sci,* **1995**, *35*, 547.
20. V. Chepoi and S. Klavzar, *J. Chem. Inf. Comput. Sci,* **1997**, *37*, 752.
21. A. Graovac, M. Juvan, M. Petkovsek, A. Vesel, J. Zerovnik, *MATCH Commun. Math. Comput. Chem*., **2003**, *49*, 47.
22. P.V. Khadikar, *Nat. Acad. Sci. Lett,* **2000**, *23*, 113.
23. P.V. Khadikar, S. Karmarkar, V.K. Agrawal, *Nat. Acad. Sci. Lett,* **2000**, *23*, 165.

24. P.V. Khadikar, S. Karmarkar, V.K. Agrawal, *J. Chem. Inf. Comput. Sci*, **2001**, *41*, 934.

25. H. Yousefi-Azari, A.R. Ashrafi and M.H. Khalifeh*, Digest Journal of Nanomaterials and Biostructures,* **2008**, *3*, 315-318.

26. A. Iranmanesh, B. Soleimani, *MATCH Commun. Math. Comput. Chem,* **2007**, *57*, 251.

27. A. Iranmanesh, B. Soleimani, A. Ahmadi, *J. Comput. Theor.* Nanosci, **2004**, *4*, 147.

28. A. Iranmanesh, Y. Alizadeh and B. Taherkhani, *Int. J. Mol. Sci*, **2008**, *9*, 131.

29. Mehdi Eliasi and Nafiseh Salehi, *Int. J. Mol. Sci.,* **2008**, *9*, 2016.

30. A. Irnmanesh, Y. Alizadeh, S. Mirzaie, *Studia UBB Chemia*, **2010**, *4*, 269.

31. Y. Alizadeh, A. Iranmanesh, S. Mirzaie, *Digest Journal of Nanomaterials and Biostructures*, **2009**, 4, 7.

32. H.W. Kroto, J.R. Heath, S.C. O'Brien, R.F. Curl and R.E. Smalley, *Nature*, **1995**, *318*, 162.

STUDIA UBB CHEMIA, LVII, 3, 2012 (p. 191 – 198)
(RECOMMENDED CITATION)

CORRELATING METAL IONIC CHARACTERISTICS WITH BIOLOGICAL ACTIVITY USING QSAR MODEL. ELECTRONIC PROPERTIES

ZOLTAN SAITOS[1], MARIUS LAZEA[1], ADRIAN CHIRIAC[1]

ABSTRACT. Quantitative structure activity relationships (QSARs) were developed to predict toxicity of metal ions (from the aquatic environment and soil) by correlating the biological activity, $A=\log(1/EC_{50})$, values with four ion descriptors, chosen to represent the binding tendencies of metals to ligands, electronic and electrical effects: the electronegativity coefficient (χ), enthalpy of hydration (ΔH_{hyd}), the first hydrolysis constant (K_{OH}) and the $\log(Z^2/r\Delta E_0)$, where Z^2/r reflects the energy of an ion when interacting electrostatically with a ligand and ΔE_0 reflects the effects of atomic ionization potential. Most QSARs are developed for organic toxicants, with inorganic toxicants (metals) being under-represented. Successful predictive models for relative toxicity of metal ions (monovalent and divalent ones) using ion characteristics have been developed. Relative metal toxicity (Li^+, Na^+, K^+, Ca^{2+}, Ba^{2+}, Cd^{2+}, Co^{2+}, Cu^{2+}, Sr^{2+}, Hg^{2+}, Mg^{2+}, Mn^{2+}, Ni^{2+}, Pb^{2+} and Zn^{2+}) was predicted by least squares linear regression and several ion characteristics. Toxicity was most effectively predicted (R=0.84) with $\log K_{OH}$ (where K_{OH} is the first hydrolysis constant) and electronegativity, which reflects a metal ion tendency to bind to intermediate ligands such as biochemical functional groups with oxygen atom donors. These QSAR correlations could be useful in ecological risk assessment.

Keywords: *QSAR, binding tendency, correlation, biological activity, hydrolysis*

INTRODUCTION

Quantitative Structure-Activity Relationships (QSARs) are empirical models that relate experimental properties/activities of compounds with their molecular structures. The rapid development of quantum theory and ab initio computational methods made possible the prediction of molecular properties of small isolated molecules within experimental error. QSARs have been widely applied to predict the bioactivity (toxicity or bioavailability) of organic compounds in pharmacology and toxicology. In contrast, models

[1] *Laboratory of Computational and Structural and Physical Chemistry, Chemistry Departament, West University of Timişoara, Pestalozzi Street no. 16, Romania, Correspondence author e-mail: laz_marius2@yahoo.com*

correlating metal ionic characteristics with their bioactivity remain poorly explored. During the last one and a half century, many scientific researchers have tried correlations between physical and chemical properties of metal cations and their toxicity [1-5]. However, the majority of industrially and environmentally important chemical processes, and biochemical transformations in living organisms take place in heterogeneous condensed media and hence the use of QSARs that proceed directly from the endpoint of interest is an attractive and fast alternative to predict molecular properties in complex environments [6,7].

The direct prediction of properties is in general not feasible either due to the lack of computing resources or lack of knowledge about the relationship between the structure and property. QSAR predictions for inorganic toxicity (especially for the toxicity of metal ions) are, however, less developed. In 2000, a paper entitled, “QSARs for metals - fact or fiction?”, authored by Walker and Hickey [8] raised a number of issues.

Newman and co-workers [1,2,5,9,10] developed a novel quantitative ion character–activity relationship (QICAR) to predict the relative toxicity of metal ions, based on metal–ligand binding tendency. The metal-biological system interaction, in terms of the nature of reacting species and the types of formed products, needs to be characterized. Tatara et al. (1997) argued [11] that the first hydrolysis constant reflects the metal ion’s tendency to bind to intermediate ligands. McKinney et al. (2000) also analysed the biological activity of metal ions [12]. Ownby and Newman further demonstrated that the QICAR approach is also suitable for prediction of toxicity in binary metal mixtures [5].

Metal toxicity is largely determined by the functional ionic selectivity of proteins (e.g., complexation, coordination, chelation, ion exchange, adsorption, etc.). The QSAR methods offer a new way to explore the interaction between the absorbed metal ions and the functional groups on the biomass [4,13-16]. Metals can cause toxicity at the cellular level [15-17] in plants by affecting the membrane permeability, by inhibiting, inducing or increasing the activity of enzymes and by activating the defending mechanisms against the increased metal phytotoxicity.

RESULTS AND DISCUSSION

The objective of this study was to establish a QSAR model between the metal ionic properties and their biological activity (EC_{50}).

Ion characteristics used in modelling (Table 1) were obtained from a variety of sources: Ionic radii (r) are from Shannon and Prewitt [18,19] and *CRC Handbook of Chemistry and Physics* [20], the first hydrolysis constants ($\log K_{OH}$) are from Baes and Mesmer [21] and Brown and Allison [22], the ΔE_0 values were obtained from Kaiser [23], and average electronegativity values (χ) were taken from Allred [24]. The mean effect concentration values (EC_{50}) were taken from John T. Mccloskey [9].

Table 1. Metal ion characteristics and biological activity (A^{obs}) used in regressions

No.	*Ion*	EC_{50} *(μM/L)*	A^{obs}= $\lvert log(EC_{50})\rvert$	χ	pKa= $\lvert logK_{OH}\rvert$	ΔH_{hyd} *(kJ/mol)*	SI= Z^2/r	ΔE_0 *(V)*	$log(SI/\Delta E_0)$
1.	Mn^{2+}	1.571	0.196176	1.55	10.6	–1845.6	4.82	1.03	-0.68305
2.	Cd^{2+}	27.000	1.431364	1.69	11.7	–2384.9	4.21	0.40	-0.62428
3.	Ca^{2+}	94.702	1.976359	1.00	12.7	–1592.4	4.00	2.76	-0.60206
4.	Li^{+}	294.13	2.468547	0.98	13.8	–514.1	1.35	3.05	-0.13033
5.	K^{+}	625.24	2.796047	0.82	11.6	–320.9	0.72	2.92	0.142668
6.	Sr^{2+}	235.52	2.372041	0.95	13.18	–1444.7	3.54	2.89	-0.549
7.	Ba^{2+}	95.455	1.979799	0.89	13.82	–1303.7	2.94	2.90	-0.46835
8.	Zn^{2+}	35.000	1.544068	1.65	9.60	–2044.3	5.33	0.76	-0.72673
9.	Cu^{2+}	1.620	0.209515	1.90	8.96	–2100.4	5.48	0.16	-0.73878
10.	Hg^{2+}	0.919	0.03668	2.00	3.40	–1853.5	3.92	0.91	-0.59329
11.	Na^{+}	401.00	2.603144	0.93	14.48	–405.4	0.98	2.71	0.008774
12.	Co^{2+}	874.00	2.941511	1.88	9.65	–2054.3	5.33	0.28	-0.72673
13.	Ni^{2+}	566.00	2.752816	1.91	9.86	–2105.8	5.8	0.23	-0.76343
14.	Mg^{2+}	87.242	1.940726	1.31	11.42	–1922.1	5.56	2.38	-0.74507
15.	Pb^{2+}	1.150	0.060698	2.33	7.80	–1479.9	3.39	0.13	-0.5302

Some data in Table 1 were calculated from the literature data, e.g., the biological activity $\boldsymbol{A^{obs}} = |\log_{10}(EC_{50})|$, the *polarizing power*, Z^2/r (where Z is the ion charge and ***r*** the ionic radius), the absolute difference in electrochemical potential between an ion and its first stable reduced state (ΔE_0), *electronegativity* (χ), the *acidity of metal ions pKa* like $|\log K_{OH}|$ and the *enthalpy of hydration* ΔH_{hyd} (kJ/mol).

Since the usual statistic analysis demands the *trial* and *test* stages in validation, the ions metal of Table 1 were classified accordingly based on the best fit of the normal distribution of input data (EC_{50}), as evidenced in Figure 1, such that each category of metal ions to be represented in both "trial" and "test" sets of toxicants.

We obtained structure activity relationships for all the possible correlation models considered for the data in Table I together with the corresponding statistics (simple correlation factor, standard error of estimation SEE). The results are given in Table 2. Data for the test set are given in Table 3.

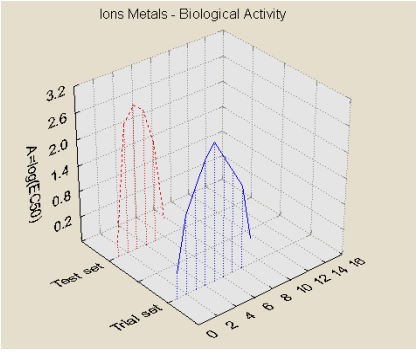

Figure 1. The plot of metal ions EC_{50} toxicities of Table 1.

Table 2. Structure activity relationships for the "Trial set" (9 ions metal) of Table 1 (No. 1, 2, 3, 4, 5, 6, 7, 8, 9)

No. Eq.	*Model*	*R*	*SEE*
1.	$A^{obs} = -2.7577 + 0.3755\ pK_a$	0.7140	0.6983
2.	$A^{obs} = 4.6933 - 0.9319\ \chi + 0.3923\ \chi^2$	0.8407	0.5731
3.	$A^{obs} = 2.7737 + 2.2807\ \log(SI/\Delta E_0)$	0.7328	0.6787
4.	$A^{obs} = -11.7454 + 0.4123\ pK_a + 0.0823\ \Delta H_{hyd}$	0.7505	0.7112
5.	$A^{obs} = 2.8364 + 0.0046\ pK_a - 0.6942\ \chi^2$	0.8467	0.5833
6.	$A^{obs} = -0.8472 + 1.0689 pK_a - 0.0432 pK_a^2 - 4.7761\chi + 1.1913\chi^2$	0.8531	0.6884

Table 3. Observed and predicted activity for the "Test set" metal ions of Table 1 (No. 10, 11, 12, 13, 14, 15) using model equations (1 to 6) from Table 2.

Metal Ion	*A observed*	*A predicted*					
		Model 1	**Model 2**	**Model 3**	**Model 4**	**Model 5**	**Model 6**
Hg^{2+}	0.03668	-1.481	4.3987	1.420583	-162.887	0.07524	-2.49933
Na^{+}	2.603144	2.67954	4.165933	2.793711	-39.1397	2.302594	2.161293
Co^{2+}	2.941511	0.86587	4.327873	1.116247	-176.836	0.42721	0.676256
Ni^{2+}	2.752816	0.94473	4.344521	1.032545	-180.987	0.349245	0.715898
Mg^{2+}	1.940726	1.53051	4.145737	1.074419	-165.226	1.697615	1.513348
Pb^{2+}	0.060698	0.1712	4.65173	1.564473	-130.325	-0.89646	0.201068
	R	0.7436	0.6684	0.0276	0.0519	0.5990	0.7121
	SEE	1.0014	1.1140	1.4972	1.4958	1.1993	1.0515

As can be seen in Table 2, we obtained useful information about the structure parameters in correlation with electronegativity, acidity, heat of hydration, the size of ions (SI) and biological activity. For the metal ion series, the maximum of R (0.8467) is given by the two-variable model using pK_a and χ^2 , A=f(pK_a, χ^2), (eq. 5, Table 2) this being the most reliable correlation across the A models of Table 2. This also shows the second lowest SEE (0.5833) value. The best one-variable model is that using the electronegativity like χ and χ^2 (R=0.8407; SEE=0.5731, eq. 2, Table 2) and next was the model using the size of ion (SI) and the absolute difference in electrochemical potential between an ion and its first stable reduced state (ΔE_0) with R=0.7328 (eq. 3, Table 2).

The significant relationships, above presented, indicates that the toxicity of all series of metal ions can be best described in terms of pK_a, pK_a^2, χ, and χ^2, by a regression model. The toxicity (EC_{50}) of the metal ion series could be also described by a multilinear regression model including the acidity and the electronegativity (eq. 6, Table 2) but the corresponding SEE is rather high. The best predictive ability (R=0,7437), is shown by the model 1, followed by the model 6 (R=0.7121).

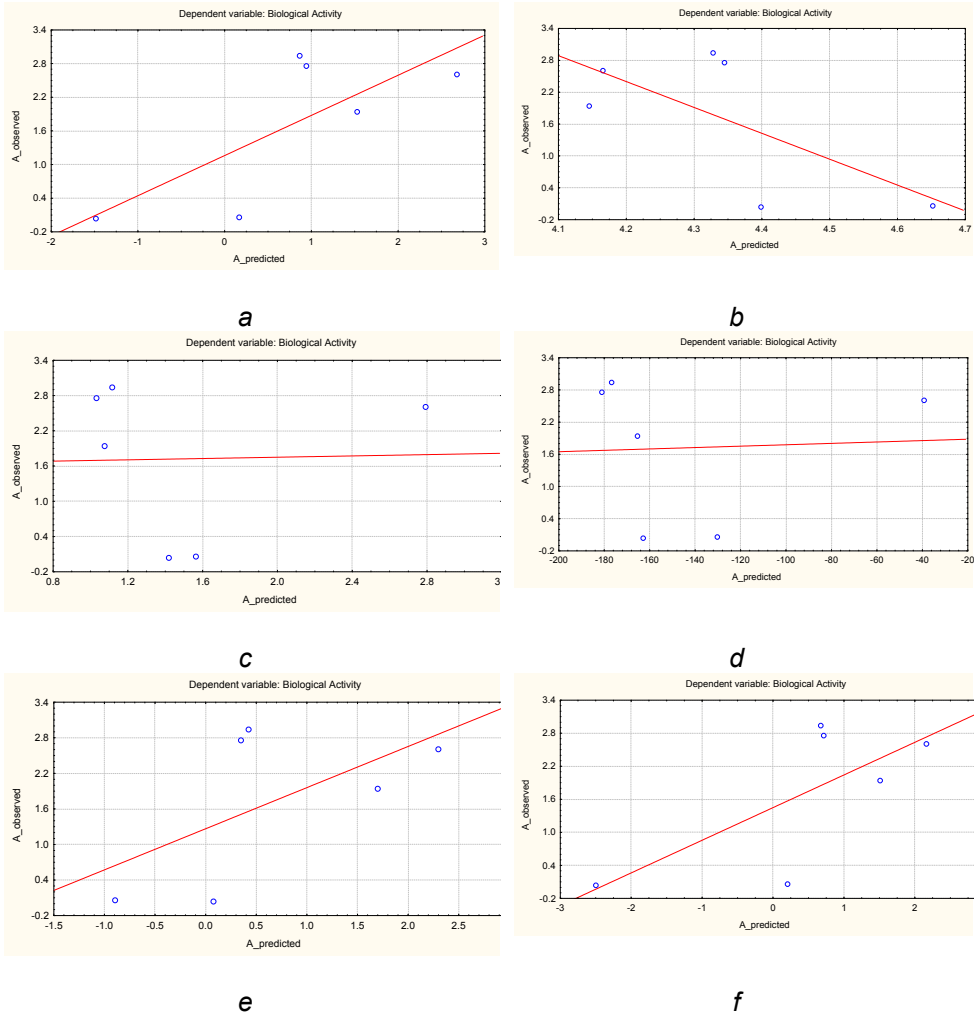

Figure 2. Correlation between observed and calculated activity for the test compounds (NonGaussian) of Table1, cf. data in Table 2 for:
a) model (I) of Eq. (1); b) model (II) of Eq. (2); c) model (III) of Eq. (3).
d) model (IV) of Eq. (4); e) model (V) of Eq. (5); f) model (VI) of Eq. (6).

These predictive models, if developed, could be very useful in areas where data on metal toxicity or sublethal effects are lacking or incomplete. Once a model has been developed with representative metals for a particular organism under certain environmental conditions, the relative effect of additional metals could be predicted.

The present analysis showed the parabolic dependence of activity on the acidity and electronegativity, as the most reliable model (the model 5) on a collection of QSAR trial equation.

Relatively high correlation coefficients were obtained in the present study between ion characteristics and biological activity. These types of information could be extremely useful in ecological risk assessment.

CONCLUSIONS

Our results (models of metal ion toxicity using ion characteristics) agree with the theory on toxicants interaction with the living organisms. Actually, for a group of metal ions (monovalent and divalent), the trial set of compounds provided a good parabolic dependency of the activity by means of the chemical transport index of electronegativity and first constant of hydrolysis, even the predictive ability did not support the trial test (due, maybe, of a limited data set). Such a behaviour is susceptible for further generalization in the future studies and will be reported in the subsequent communications.

METHODS

In predictive toxicology, we exploit the toxicological knowledge about a set of chemical compounds in order to predict the activity of other compounds [25].

Ion characteristics of inorganic species can be used to predict the relative toxicity or sublethal effects of metal ions. Many of these characteristics reflect the binding tendency of metals to ligands. For example, *polarizing power*, Z^2/r (where Z is the ion charge and $\boldsymbol{r}$ is the ionic radius), is a measure of strength of the electrostatic interaction between a metal ion and a ligand; the ΔE_0 (where ΔE_0 is the absolute difference in electrochemical potential between an ion and its first stable reduced state) reflects the ability of an ion to change its electronic state; *electronegativity* (χ) is correlated with the energy of an empty valence orbital and reflects the ability of a metal to accept electrons, combining electronegativity with the ionic radius yields an index that quantifies the importance of covalent interactions relative to ionic interactions [14]; the *acidity of metal ions pKa* like $|\log K_{OH}|$, where K_{OH} is the first hydrolysis constant: $[M(H_2O)_n]^{x+} + HOH \rightarrow [M(H_2O)_{n-1}OH]^{(x-1)+} + H_3O^+$ (metal ions in aqueous solution behave as Lewis acids); the *enthalpy of hydration* ΔH_{hyd} of an ion is the amount of energy released when a mole of the ion dissolves in a large amount of water forming an infinite dilute solution in the process.

Multilinear models have been in use since a long time. As linear equations, they are easy to use and relatively straightforward to interpret. For n instances they are defined as the coefficients that minimize the error on a system of n linear equations [26, 27, 28]:

$$y_i = b_1 x_{i1} + b_2 x_{i2} + ... + b_m x_{im} + d \qquad i \in \{1, ..., n\},$$

or in a more compact notation, $y = (\langle X, b \rangle + d)$ where $\langle ..., ... \rangle$ denotes the normal dot product and b and d are the coefficients to learn. Multilinear models assume linear relationships between features and activities [26]. The prediction $f(x_q)$ is obtained by [25]:

$$f(x_q) = (\langle x_q, b \rangle + d).$$

ACKNOWLEDGMENTS

This article is supported by the project "Creşterea calităţii şi a competitivităţii cercetării doctorale prin acordarea de burse". This project is co-funded by the European Social Fund through The Sectorial Operational Programme for Human Resources Development 2007-2013, coordinated by the West University of Timisoara in partnership with the University of Craiova and Fraunhofer Institute for Integrated Systems and Device Technology - Fraunhofer IISB.

REFERENCES

1. M.C. Newman, J.T. McCloskey, *Environ. Toxicol. Chem.,* **1996**, *15*, 275.
2. M.C. Newman, J.T. McCloskey, C.P. Tatara, *Environ. Health Persp.*, **1998**, *106,* 1419.
3. H.T. Wolterbeek, T.G.Verburg, *Sci. Total Environ.*, **2001**, *279*, 87.
4. K.L.E. Kaiser, *QSAR Comb. Sci.*, **2003**, *22*, 185.
5. D.R. Ownby, M.C. Newman, *QSAR Comb. Sci.*, **2003**, *22*, 241.
6. J.D. Walker, M. Enache, J.C. Dearden, *Environ. Toxicol. Chem.*, **2003**, *22*, 1916.
7. J.F. Capitani, D.M. Di Toro, "Quantitative structure activity relationships for toxicity and fate parameters of metals and metal compounds", University of Delaware, **2004**, 84.
8. J.D. Walker, J.P. Hickey, "QSARs for metals - fact or fiction?" in: J.A. Centeno, P. Colleery, G. Vernet, R.B. Finkelman, H. Gibb, J.C. Etienne (Eds.), "Metal Ions in Biology and Medicine", John Libbey Eurotext Limited, Montrouge France, **2000**, 401.
9. J.T. McCloskey, M.C. Newman, S.B. Clark, *Environ. Toxicol. Chem.*, **1996**, *15*, 1730.
10. C.P. Tatara, M.C. Newman, J.T. McCloskey, P.L. Williams, *Aquat. Toxicol.*, **1998**, *42*, 255.
11. C.P. Tatara, M.C. Newman, J.T. McCloskey, P.L. Williams, *Aquat. Toxicol.*, **1997**, *39*, 279.

12. J.D. McKinney, A. Richard, C. Waller, M.C. Newman, F. Gerberick, *Toxicol. Sci*., **2000**, *56*, 8.
13. R.G. Pearson, *J. Am. Chem. Soc*., **1963**, *85*, 3533.
14. E. Nieboer, D.H.S. Richardson, *Environ. Pollut. Ser. B*., **1980**, *1*, 3.
15. M. Badea, M. Moga, N. Taus, N. Bigiu, S.C. Conzac, *J. Environ. Protect. Ecol.*, **2009**, *10(4)*, 1005.
16. M. Dragomir, S. Masu, C. Bogatu, B. Lixandru, M. Lazarovici, C. Cristea, *J. Environ. Protect. Ecol.*, **2009**, *10(1)*, 42.
17. J. Vangronsveld, H. Clijsters, "Toxic effects of metals", in: M.E. Farago. (Ed.), "Plants and the Chemical Elements Biochemistry Uptake, Tolerance and Toxicity", *VCH*, Weinheim (Germany), **1994**, 149.
18. R.D. Shannon, C.T. Prewitt, *Acta Crystallogr. Sect. B Struct. Sci.*, **1969**, *25*, 925.
19. R.D. Shannon, C.T. Prewitt, *Acta Crystallogr. Sect. B Struct. Sci. B*., **1970**, *26*, 1046.
20. D.R. Lide, "*CRC Handbook of Chemistry and Physics",* 73rd ed. CRC, Boca Raton, FL, USA, **1992**.
21. C.F. Baes, R.E. Mesmer, "*The Hydrolysis of Cations",* John Wiley & Sons, New York, NY, USA, **1976**.
22. D.S. Brown and J.D. Allison: "MINTEQA1, an equilibrium metal speciation model: User's manual", EPA/600/23-87/012. U.S. Environ. Protect. Agency, Athens, GA, **1987**.
23. K.L. Kaiser, *Can. J. Fish. Aquat. Sci.*, **1980**, *37*, 211.
24. A.L. Allred, *J. Inorg. Nucl. Chem.*, **1961**, *17*, 215.
25. C. Hansch, T. Fujita, *J Am. Chem Soc*., **1964**, *86*, 1616.
26. M. Pavan, T. Netzeva, A. Worth, "Validation of a QSAR model for acute toxicity. SAR and QSAR in Environmental Research"*,* **2006**, 147.
27. M.V. Putz, A.M. Putz, M. Lazea and A. Chiriac, *J. Theoret. Comput. Chem.*, **2009**, *8(6)*, 1235.
28. M.V. Putz, A.M. Putz, M. Lazea, L. Ienciu and A. Chiriac, *Int. J. Molec. Sci.*, **2009**, *10*, 1193.

STUDIA UBB CHEMIA, LVII, 3, 2012 (p. 199 – 211)
(RECOMMENDED CITATION)

POTENTIAL BACTERIAL SOIL INOCULANT MADE UP BY *RHODOCOCCUS* SP. AND *PSEUDOMONAS* SP. FOR REMEDIATION *IN SITU* OF HYDROCARBON – AND HEAVY METAL POLLUTED SOILS

TIBOR BENEDEK[1], ISTVÁN MÁTHÉ[2], ROZÁLIA SALAMON[2], SZABOLCS RÁKOS[2], ZOLTÁN PÁSZTOHY[3], KÁROLY MÁRIALIGETI[4], SZABOLCS LÁNYI[2]

ABSTRACT. Since bioremediation is an environmentally friendly, cost effective approach to treat hydrocarbon-contaminated soils, in this study our aim was to develop a bacterial soil inoculant applicable in elimination of aliphatic, simple- and polyaromatic hydrocarbons from soils. To reach our goal two bacterial strains, *Pseudomonas fluorescens* BBN1 and *Rhodococcus qingshengii* BBG1, were selected to investigate their hydrocarbon-degrading abilities at DNA level and in microcosm experiments followed by GC-FID, as well as their ability to tolerate heavy-metal concentrations. Our results revealed that the proposed bacterial soil inoculant is suitable for elimination of aliphatic, monoaromatic and polycyclic aromatic hydrocarbons from soil samples, reaching degradation rates of 95% (n-dodecane), 66% (toluene), 70% (naphthalene) and 67% (phenanthrene) of initial pollutant concentrations within 42 days.

Keywords: *bioaugmentation, in situ bioremediation, PAHs, catA, C23O, alkB, GC-FID*

INTRODUCTION

In recent years microorganisms (bacteria, fungi) have increasingly gained interest in different industrial, biotechnological settings, since they can synthesize compounds (surfactants, amides, polymers etc.), or even they can transform a wide range of chemicals (aliphatic-, mono- and polycyclic aromatic hydrocarbons; chlorinated hydrocarbons; biphenyls etc.) into harmless

[1] *Polytehnical University of Bucharest, Department of Analytical Chemistry and Environmental Engineering, Splaiul Independenţei, Nr. 313, RO-060042 Bucharest, Romania, benedektibor@sapientia.siculorum.ro*
[2] *Sapientia Hungarian University of Transylvania, Bioengineering Department, Piaţa Libertăţii, Nr. 1, RO-530104 Miercurea Ciuc, Romania*
[3] *Pedological and Agrochemical Research Institute, Str. Progresului, Nr. 22, Miercurea Ciuc, Romania*
[4] *Eötvös Loránd University, Department of Microbiology, Pázmány Péter sétány, Nr. 1/C, H-1117 Budapest, Hungary*

substances. Taking advantage of these beneficial properties, several studies have reported successful use of microorganisms in elimination of organic contaminants from different environments (soil, aquatic ecosystems, sediments etc.). For instance, Ueno et al. (2006) by introduction of *Pseudomonas aeruginosa* strain WatG into diesel-oil-contaminated soil microcosms achieved a higher degradation rate (64% ± 4.2%) of pollutants during the first two weeks, than in only Luria-Bertani medium amended microcosms (49.5% ± 12%) [1]. In addition, Franzetti et al. (2009) reported a surface active compounds (extracellular bioemulsans and cell-bound biosurfactants) producing *Gordonia* sp. strain BS29 which effectively contributed to the removal of crude oil and PAH (polycyclic aromatic hydrocarbon) from soil. Beside bioaugmentation (introduction of microbial strains into contaminated environments in order to enhance the bioremediation process) with single strains, the use of microbial consortia of many hydrocarbon-degrading microorganisms proved to be more effective in remediation approaches, by the fact that intermediates of a catabolic pathway of one strain may be further degraded by other strains [3]. For example, Jacques et al. (2008) studied the capacity of a microbial consortium (*Mycobacterium fortuitum*, *Bacillus cereus*, *Microbacterium* sp., *Gordonia polyisoprenivorans*, *Microbacteriaceae* bacterium and *Fusarium oxysporum*) to degrade and mineralize PAH compounds. They found that the consortium degraded 96-99% of the PAHs in the soil, in 70 days, although the autochthonous soil microbial population showed no remarkable mineralization of these pollutants [4]. Another beneficial effect of the use of microbial consortia would be the observation that the presence of one strain in a mixed-contaminated environment (e.g. heavy-metals and hydrocarbons) may promote the expression of beneficial properties of another strain by e.g. sequestration of heavy-metals. In this context, Roane et al. (2001) used dual-bioaugmentation technique to decontaminate both 2,4-dichlorophenoxyactetic acid (2,4-D) and cadmium (Cd) impacted soil using a bacterial consortium made up by *Pseudomonas* sp. strain H1 and *Ralstonia eutropha* JMP134. The Cd tolerant *Pseudomonas* sp. H1, by intracellular sequestration, was able to decrease the level of soluble toxic Cd ions enhancing thus the degradation of 2,4-D by the less heavy-metal resistant *R. eutropha* [5].

Forasmuch, throughout Romania the number and extension of hydrocarbon polluted zones is increased (50 000 ha in 1999, according to Research Institute for Soil Science and Agro-chemistry) [6] the need of an innovative, efficient remediation technology is indispensable. Taking into account the aforementioned successful use of microorganisms in degradation processes of hydrocarbon pollutants, and the fact that bioremediation is a cheaper and more environmentally friendly approach than the conventional methods (physical and chemical approaches), we are committed to develop a microbial soil inoculant which can be used in decontamination of petroleum hydrocarbon polluted sites even in presence of heavy-metals.

RESULTS AND DISCUSSIONS

The isolation source of the investigated bacterial strains is discussed in detail in our previous work [7]. Seen from that preliminary results this highly hydrocarbon and heavy-metal impacted environment contributed to the evolution of several distinctive species with increased ability to degrade hydrocarbons or/and to resist in presence of heavy-metals. Therefore, to prepare a bacterial soil inoculant which might be applicable in bioremediation of hydrocarbon/ heavy-metal contaminated soils we selected two bacterial strains *R. qingshengii* BBG1 and *P. fluorescens* BBN1 isolated from contaminated soil samples collected from Bălan (Harghita County, Romania).

Testing hydrocarbon-degrading ability of strains revealed that *R. qingshengii* strain BBG1 is able to proliferate in presence of all tested hydrocarbons and shows a remarkable higher degradation activity in test solutions, indicated by the reduced absorbance of the resazurin amended test solution at 610 nm. The highest biodegradation activity of strain BBG1 was observed in test solution amended with n-dodecane, where formation of a biofilm also occurred. Strain BBN1 showed a lowest degradation capability supported by the weak discoloration of the resazurin and hydrocarbon amended test solution (Figure 1), compared to the blank samples.

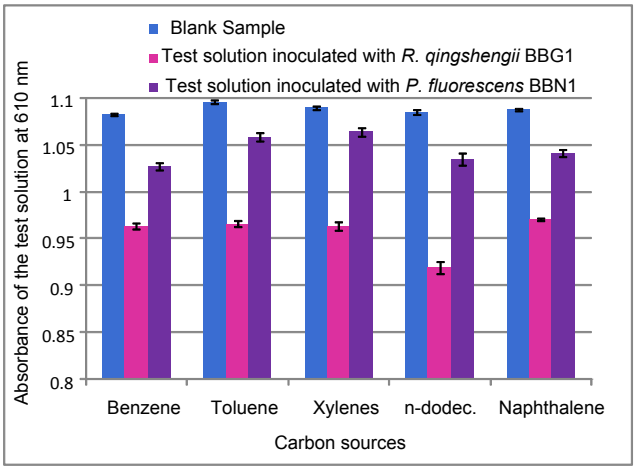

Figure 1. Hydrocarbon degradation potential of investigated strains.

The aliphatic and aromatic hydrocarbon degradation ability of *R. qingshengii* strain BBG1 was also demonstrated by the detection of biodegradative functional *catA* and *alkB* genes. By using RHO-F/R and RalkB-F/R primer pairs polymerase chain reaction yielded amplicons of 530 bp and 595 bp, respectively.

The presence of *C23O* gene, responsible for extradiol cleavage of the aromatic ring, was demonstrated by obtaining a 250 bp sized amplicon in *P. fluorescens* strain BBN1, although in test solution, supplemented with aromatic hydrocarbons, the activity of strain BBN1 was not remarkable (data not shown).

Regarding heavy-metal tolerance, we found that *R. qingshengii* BBG1 and *P. fluorescens* BBN1 have similar resistance against the tested heavy-metals, and are able to tolerate high heavy-metal levels. Since the tolerated Pb^{2+} and Zn^{2+} levels by the two strains are the same, the highest Cu^{2+} resistance was observed at strain BBG1 (Table 4). In the most increased manner the Zn^{2+} was tolerated by both strains.

Table 4. Heavy-metal tolerance of the selected strains

Tested bacterial strains	Maximum Tolerable Concentrations (mM)		
	$Pb(NO_3)_2$	$ZnSO_4 \cdot 7H_2O$	$CuSO_4 \cdot 5H_2O$
P. fluorescens BBN1	3.5	4	2
R. qingshengii BBG1	3.5	4	3

Optimal culturing conditions (pH and temperature) determination revealed that in case of *P. fluorescens* BBN1 different pH values did not play a decisive role in proliferation of bacteria, within the investigated pH interval. The highest cell density was observed after 12 hour of incubation, when the optical density of the inoculated nutrient solution exceeded the value of 0.7 (Figure 2.B.). As it is observable from Figure 2.A. *R. qingshengii* strain BBG1 had a longer adaptation period (*lag* phase), the exponential phase peaked after 18 hour of incubation, when a cell density of almost 0.8 was reached. A pH value of 7.5 seemed to extend the adaptation phase of bacteria.

The influence of different temperatures on the multiplication of investigated strains is presented on Figure 3. (A; B). As it is evident from Figure 3. A. the highest cell densities (absorbance of the inoculated solution at 590 nm ~ 0.8) of *R. qingshengii* BBG1 after 30 hour of incubation were reached in nutrient solutions maintained at 26ºC and 30ºC, respectively. A temperature of 20ºC delayed (~ 8 hours) the exponential phase of the bacterial growth. No or slight proliferation was observed in case of both investigated strains at 10ºC. As in the previous case, the largest increase in cell densities of *P. fluorescens* BBN1 inoculated nutrient solutions were obtained at 26ºC and 30ºC, although a temperature of 20ºC did not remarkably delayed (4 hours) the exponential phase of bacterial growth as in case of strain BBG1.

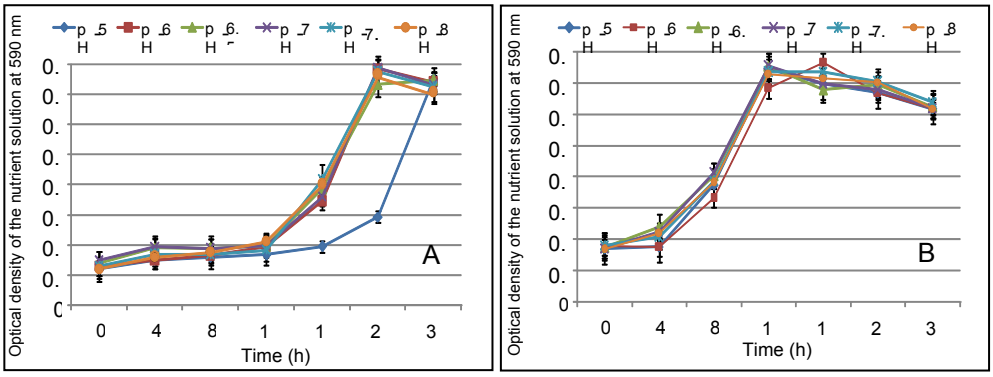

Figure 2. Influence of pH variation on proliferation of (A) *R. qingshengii* BBG1 and (B) *P. fluorescens* BBN1.

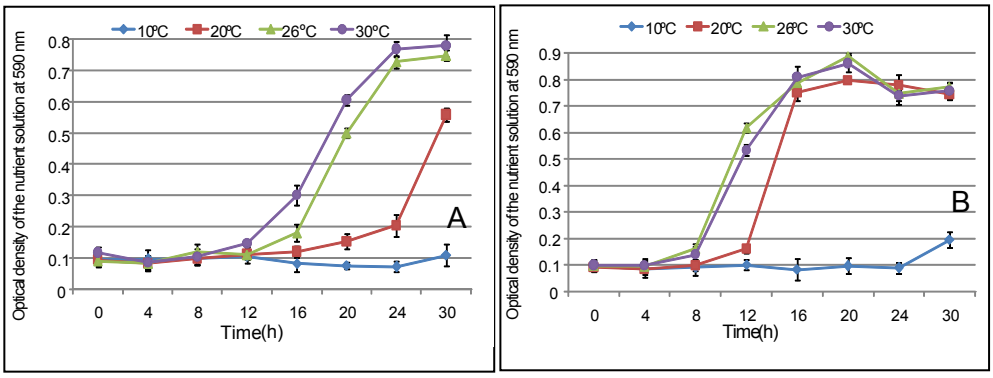

Figure 3. Influence of different temperature values on proliferation of (A) *R. qingshengii* BBG1 and (B) *P. fluorescens* BBN1.

Microcosm experiments revealed that the inoculated bacterial strains were suitable to improve the bioremediation potential of the investigated soil. Developed soil inoculant was able to degrade aliphatic, simple aromatic, as well as polycyclic aromatic hydrocarbons, proven by the results of the gas chromatography measurements. The highest biodegradation rate was observed in case of n-dodecane, when the bioaugmentation contributed to the almost complete elimination of the pollutant from soil (~95% of the initial n-dodecane was degraded). Compared to the degradation activity of indigenous microorganisms the inoculated microcosms showed a remarkably higher degradation potential (B1 and B2 samples degraded only 56%, respectively 40% of the initial n-dodecane concentration) (Figure 4).

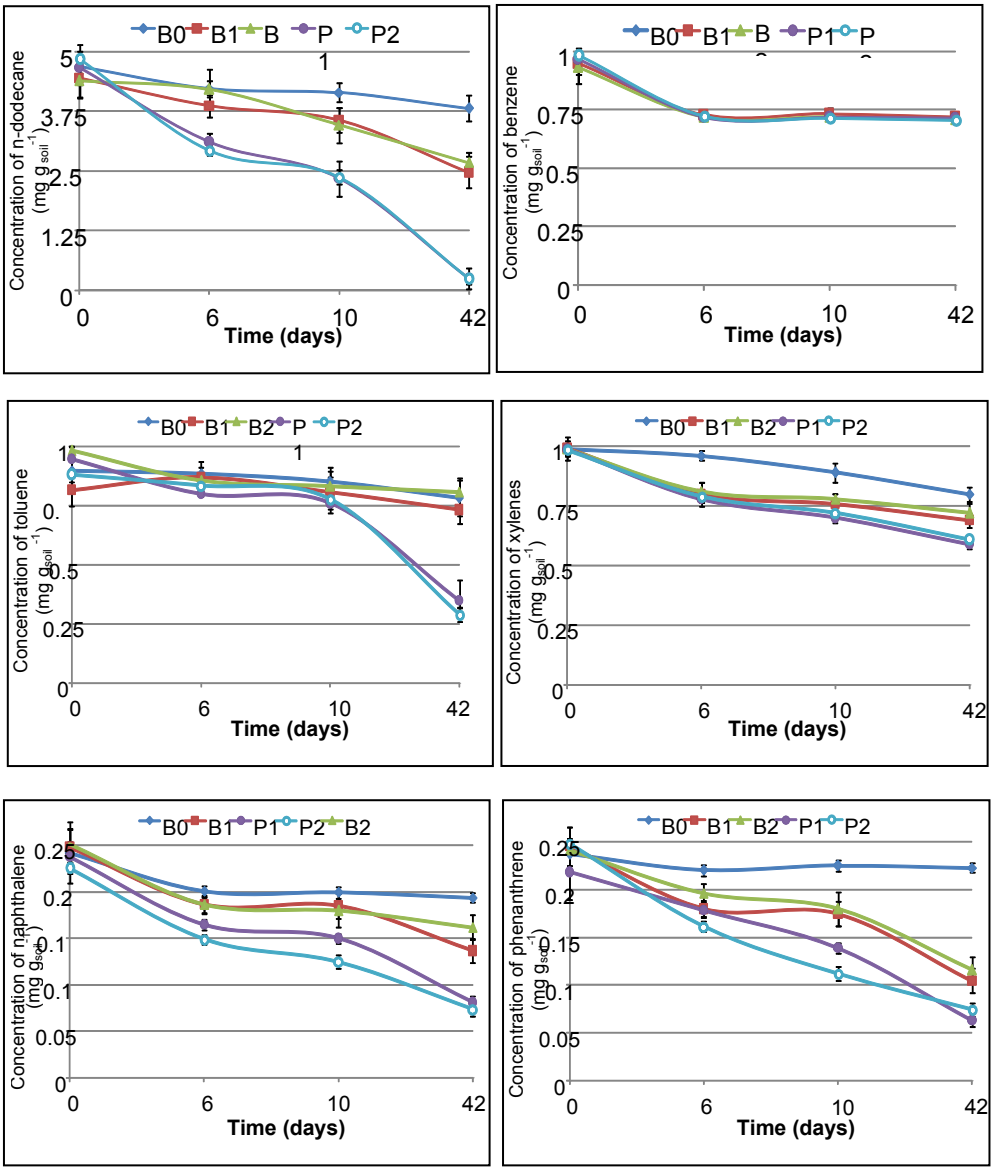

Figure 4. Biodegradation of aliphatic (n-dodecane), simple aromatic (benzene, toluene, xylenes) and polycyclic aromatic hydrocarbons (naphthalene, phenanthrene).

Benzene was the sole hydrocarbon pollutant whose degradation was not observed in none of the microcosms. A slight decrease might be observable among the first two samplings for chemical analysis, but to our opinion this decrease is due to the volatilization of benzene (Figure 4). After 42 days of

incubation a significantly higher toluene degradation was observed in bacterial inoculated soil microcosms compared to other samples. In bioaugmented soil almost 66% of the initial toluene concentration was degraded, in contrast with toluene degradation activity of indigenous microorganisms (soil microcosms without inoculum) where the efficiency of the pollutant degradation was only 35% (B1) and 29% (B2), respectively. Compared to abiotic control slight, unremarkable xylenes degradation was observed in un-sterilized and inoculated soil microcosms, although soil samples with *P. fluorescens* BBN1 and *R. qingshengii* BGG1 bacterial inoculum showed a higher toluene degradation, but the difference is not remarkable (Figure 4). Interestingly, a higher degradation of recalcitrant, hard-biodegradable polycyclic aromatic hydrocarbons (naphthalene, phenanthrene) by the used microbial consortia was also observed. The initial concentration (0.25 g kg^{-1}) of naphthalene was decreased to 0.081 g kg^{-1} in heavy-metal free inoculated soil sample, as well as to 0.074 g kg^{-1} in heavy-metal impacted soil representing a degradation rate of almost 67%. The degradation rate of phenanthrene in inoculum treated and heavy-metal contaminated sample, as well as in heavy-metal free sample was 70% and 68%, respectively. The degradation rate of naphthalene and phenanthrene in un-inoculated soil samples by indigenous bacterial population was 42%, respectively 60% in heavy-metal free samples, and 36%, respectively 65% in heavy-metal amended soils.

Since introduced heavy-metals Cu^{2+}, Pb^{2+}, Zn^{2+} did not influenced negatively the degradation rate of hydrocarbon pollutants, neither in inoculum free soil samples we may assume that the applied concentration of heavy-metals did not affected negatively the bacterial growth and the biodegradation activity.

CONCLUSIONS

A bacterial consortium made up by *Rhodococcus qingshengii* BBG1 and *Pseudomonas fluorescens* BBN1 was developed in order to eliminate hydrocarbon pollutants from contaminated soils.

Due to the wide pH tolerance this bacterial inoculum might be applicable in various soils with different pH.

Since selected strains possess also a remarkable heavy-metal tolerance the developed bacterial inoculant might be used for elimination of hydrocarbons from soil even in presence of heavy-metals.

By using this soil bacterial inoculant 95% of the initial n-dodecane, 66% of toluene, 67% of naphthalene and almost 70% of phenanthrene concentration was degraded within 42 days of microcosm experiment.

EXPERIMENTAL SECTION

Isolation source of hydrocarbonoclastic bacteria

The used hydrocarbon-degrading bacterial species, namely *Rhodococcus qingshengii* strain BBG1 and *Pseudomonas fluorescens* strain BBN1, in this study were obtained after enrichment from hydrocarbon and heavy-metal

contaminated soil collected from Bălan. As described previously, during the enrichment 1 g of contaminated soil sample was added to 99 ml BBH mineral broth medium supplemented with 1% (v/v) diesel fuel. After 2 weeks of incubation (23ºC), as a second selection, the obtained cultures were serially diluted and inoculated onto BBH agar plates. The lid of the Petri-dishes contained 250 µl of sterile diesel-fuel as sole source of carbon and energy [7]. Since this soil contains remarkable amounts of total petroleum hydrocarbons (TPHs – 16 400 mg kg^{-1}), PAHs (73.8 mg kg^{-1}), as well as heavy-metals (Pb^{2+} – 67 mg kg^{-1}, Cu^{2+} – 441 mg kg^{-1}, Zn^{2+} – 298 mg kg^{-1}) we assumed that this ecosystem contributed to the evolution of bacterial species, with increased ability to degrade hydrocarbons and to tolerate the presence of heavy-metals at the same time. The used bacterial strains in this study are deposited in the National Collection of Agricultural and Industrial Microorganisms under the following accession number: NCAIM(P)B001401 for *R. qingshengii* BBG1 and NCAIM(P)001400 for *P. fluorescens* BBN1.

Screening hydrocarbon-degradation capability of strains

Selected bacterial strains *R. qingshengii* BBG1 and *P. fluorescens* BBN1 were tested in order to determine their ability to degrade different hydrocarbons. Tests were done in 50 ml BBH (Bacto-Bushnell-Haas) [8] mineral salts solution supplemented with resazurin indicator (10 mg l^{-1}), and one of the following filter sterilized (0.2 µm) hydrocarbons (1 g l^{-1}) as sole carbon source: n-dodecane, benzene, toluene, xylenes and naphthalene (Sigma-Aldrich, Germany). The obtained test solutions were inoculated with 250 µl strain culture suspensions (OD_{600}=0.5). Degradation ability of strains was determined spectrophotometrically, by measuring the absorbance of the solution at 610 nm (absorbance of the redox indicator resazurin) compared to the absorbance of blank (un-inoculated, negative control) samples. A lower absorbance of the solution at 610 nm represents a higher activity of tested bacteria, and an increased degradation rate of the tested hydrocarbons.

Functional *catA, C23O* and *alkB* gene detection

Functional *catA* and *C23O* genes encode for intradiol *"ortho"* cleavage enzyme catechol 1,2-dioxygenase and extradiol "*meta*" cleavage enzyme catechol 2,3-dioxygenase, respectively. These key enzymes are known to accomplish the first step of catalysis of the aromatic ring fission, the most time consuming process in biodegradation of aromatic compounds [9]. Since *catA* and *C23O* genes catalyze the aromatic ring fission, *alkB* genes are responsible for expression of alkane-1-monooxygenase enzyme, involved in the initial attack of the aliphatic hydrocarbon chain by microbial mono-oxygenation.

To demonstrate the hydrocarbon-degradation potential of selected bacterial isolates at DNA level as well, *catA* and *alkB* functional genes were detected in *R. qingshengii* strain BBG1, as well as *C23O* genes in *P. fluorescens* strain BBN1 by using polymerase chain reaction (PCR) method.

PCR reaction mixture (50 µl) contained 1X DreamTaq^{TM} buffer with $MgCl_2$ (2 mM), 0.2 mM of each of the four dNTPs, 0.3 µM of each primer, 1 U *DreamTaq^{TM} DNA Polymerase* (Fermentas, Lithuania), 1 µl DNA template and molecular-grade water up to 50 µl. The used temperature profile for primer sets presented in Table 1 was the following: initial denaturation for 3 min at 95°C, followed by 32 cycles of denaturation for 0.5 min at 94°C, annealing for 0.5 min at the annealing temperature reported in Table 1, and elongation for 1 min at 72°C. The last step was a final extension for 10 min at 72°C. All amplifications were performed using ABI GeneAmp 2700 thermo cycler system (Applied Biosystems, USA).

Detection of genes was realized under UV light, after electroforetic migration (80V, 40 min) of PCR amplified gene fragments in 1% agarose gel.

Table 1. Used primer pairs for detection of *catA*, *C23O* and *alkB* genes

Primer pair	Primer sequence	Gene	Targeted organism	Annealing temperature (ºC)	Ref.
XYLE1-F XYLE1-R	5'-CCGCCGACCTGATCWSCATG-3' 5'-TCAGGTCAKCACGGTCAKGA-3'	*C23O*	*Pseudomonas* sp.	61.5	[10]
RHO-F RHO-R	5'-GCCGCCACCGACAAGTT-3' 5'-CACCATGAGGTGCAGGTG-3'	*catA*	*Rhodococcus* sp.	56	[11]
RalkB-F RalkB-R	5'-TACTACCGGTACTGCACCTAC-3' 5'-CCGTARTGYTCGAGGTAGTT-3'	*alkB*	*Rhodococcus* sp.	54	[12]

Testing heavy-metal tolerance of strains

Heavy-metal tolerance of strains was tested by using casamino-acid agar plates (casamino-acid 5 g l^{-1}; agar 17 g l^{-1}) containing different concentrations (0.2, 0.4, 0.6, 0.8, 1.0, 1.5, 2.0, 2.5, 3.0, 3.5, 4.0 mM) of $Pb(NO_3)_2$, $CuSO_4 \cdot 5H_2O$ and $ZnSO_4 \cdot 7H_2O$ (Merck, Germany). Heavy-metal amended plates were spot inoculated with bacterial cell suspensions (5 µl, OD_{600}=1) and incubated at 30ºC for 2 days [7]. All tests were done in triplicates and the results were evaluated visually for growth against heavy-metal free control cultures.

Determination of the optimal culturing conditions (pH and temperature)

For determining the optimal values of pH for meso-scale cultivation of *R. qingshengii* BBG1 and *P. fluorescens* BBN1 Nutrient Broth liquid media were used with different values of pH (5; 6; 6.5; 7; 7.5; 8). Initial bacterial suspension (OD_{590}=0.5) was obtained in physiological solution (0.9% NaCl) using a bacterial culture of 24 h. Liquid nutrient solutions (20 ml) with different pH values after sterilization were inoculated with 250 µl of previously made bacterial solution. Inoculated mediums were incubated at 28°C and shaken

at 145 rpm for 34 hours. Growing curves of the investigated strains at different pH levels were obtained after measuring (time intervals 0, 4, 8, 12, 16, 20 and 34 h) the optical density of the inoculated nutrient solutions at 590 nm by using a microplate reader type FLUOstar Optima (BGM Labtech).

In order to determine the optimal temperature for cultivation of investigated bacterial strains, bacterial isolates were incubated at the following temperatures: 10, 20, 26 and 30°C. Bacterial inoculated Nutrient Broth solutions were prepared as described in the earliest paragraph, and maintained at different temperatures by shaking at 145 rpm. Evaluation of the results was carried out on basis of the growth curves, obtained after measuring the cell densities of nutrient solutions at 590 nm at different time intervals (0, 4, 8, 12, 16, 20, 24, 30 h).

Microcosm experiment

For determining the beneficial effect of bacterial soil inoculation on the degradation of hydrocarbon-pollutants soil, microcosm experiments were set up (maintained at 26ºC), using argillic brown soil with known pedological characteristics (Table 2) collected from Cozmeni (Harghita County).

Soil samples serving as abiotic controls (sample label B0, negative control), as well as inoculated soil samples (sample labels P1, P2) prior bacterial strain inoculation were first time sterilized at 101ºC for 60 min for three times. As a second sterilization round the aforementioned microcosms were flooded with water and autoclaved again at 101ºC for 60 min. As a final sterilization soil samples were air dried and autoclaved again at 120ºC for 20 min.

Table 2. Pedological characterization of the utilized soil (data provided by Pedological and Agrochemical Research Institute, Harghita County, Romania)

Pedological characteristics								
Gravel (%)	Sand (%)	Silt (%)	Clay (%)	N_T (%)	Humus (%)	pH	C:N	Humidity (%)
24.7	46.1	18.5	10.7	0.108	1.6	6.2	11.6	16.6

The artificially hydrocarbon contaminated soil microcosms contained: n-dodecane (5 g kg^{-1}); benzene, toluene and xylenes (1 g kg^{-1}); naphthalene and phenanthrene (0.25 g kg-1) as hydrocarbon pollutants. In order to investigate the biodegradation potential of strains even in the presence of heavy-metals heavy-metal and hydrocarbon contaminated microcosms were also set up, where the concentration of artificially introduced heavy-metals were as follows: Cu^{2+} (2 mM), Pb^{2+} (3 mM), Zn^{2+} (4 mM).

Table 3. Designation of the soil microcosms

Sample designation	Sample description	Type of contaminants
B0	Abiotic control	n-dodecane, BTEX, PAHs and heavy-metals (Cu^{2+}, Zn^{2+} and Pb^{2+})
B1	Non sterilized, un-inoculated soil sample	n-dodecane, BTEX and PAHs
B2	Non sterilized, un-inoculated soil sample	n-dodecane, BTEX, PAHs and heavy-metals (Cu^{2+}, Zn^{2+} and Pb^{2+})
P1	Sterilized soil inoculated with *R. qingshengii* BBG1 and *P. fluorescens* BBN1	n-dodecane, BTEX and PAHs
P2	Sterilized soil inoculated with *R. qingshengii* BBG1 and *P. fluorescens* BBN1	n-dodecane, BTEX, PAHs and heavy-metals (Cu^{2+}, Zn^{2+} and Pb^{2+})

Soil microcosms were set up in triplicates using 500 ml vials with screw cap containing 100 g soil with known soil characteristics (Table 2). Multi-sterilized abiotic control sample (B0) was contaminated with both heavy-metals and hydrocarbons. To determine the effect of the indigenous microorganisms on biodegradation non-sterilized, un-inoculated soil samples (positive control) were polluted with hydrocarbons (B1) and hydrocarbons/heavy-metals (B2) as well. P1 and P2 soil microcosms were contaminated with hydrocarbons or hydrocarbons/heavy-metals and were inoculated with *R. qingshengii* BBG1 and *P. fluorescens* BBN1.

To prepare the inoculum *R. qingshengii* BBG1 and *P. fluorescens* BBN1 were grown to the late exponential phase on Nutrient Broth solid mediums. Cells were collected with sterile inoculation loop and placed to sterile physiological solution to obtain a bacterial cell suspension OD_{590}=0.5 (approx. 10^8 bacterial cells ml^{-1}). The bacterial suspensions (1-1 ml) were applied in droplets to the soil surface to reach a cell concentration of 10^6 cell g_{soil}^{-1}, and then the soil was thoroughly mixed with sterile spatula

In order to insure the oxygen supply for bacterial activity, microcosms were aerated in every 2 days by mixing in sterile environment. The water content of all microcosms was adjusted to 50% of the maximum water holding capacity of soil using sterile water.

Analysis of hydrocarbons in soil microcosms

To follow the biodegradation rate of hydrocarbons at various intervals, 2 g (dry wt) of soil sample from each microcosm was transferred to 35 ml vials and mixed with 10 ml hexane (Merck, Germany), followed by sonication (50 Hz)

for 50 min in a water bath. 1 µl of extract was analyzed using gas chromatograph (Varian CP 3380; Varian, USA) equipped with flame ionization detector (FID) and CP SIL-5CB WCOT Fused Silica column (25 m x 0.25 mm internal diameter). During the analysis the injector and detector temperatures were maintained at 140ºC and 290ºC, respectively. The temperature program was set to 40ºC for 1 min, increasing at a rate of 25ºC min^{-1} to 140ºC, and finally hold at 140ºC for 10 min.

ACKNOWLEDGMENTS

The authors are grateful to the Sectoral Operational Programme Human Resources Development 2007-2013 of the Romanian Ministry of Labour, Family and Social Protection through the Financial Agreement POSDRU/88/1.5/S/60203. Tibor Benedek also wishes to express his thanks to the Foundation of Domus Hungarica Scientiarum et Artium.

REFERENCES

1. A. Ueno, M. Hasanuzzaman, I. Yumoyo, H. Okuyama, *Current Opinion in Microbiology*, **2006**, *52*, 182.
2. A. Franzetti, P. Caredda, C. Ruggeri, L. la Colla, E. Tamburini, M. Papacchini, G. Bestetti, *Chemosphere*, **2009**, *75*, 801.
3. A. Mrozik, Z. Piotrowska-Seget, *Microbiological Research,* **2010**, *165*, 363.
4. R.J.S. Jacques, B.C. Okeke, F.M. Bento, A.S. Teixeira, M.C.R. Peralba, F.A.O. Camargo, *Bioresource Technology*, **2008**, *99*, 2637.
5. T.M. Roane, K.L. Josephson, I.L. Pepper, *Applied Environmental Microbiology,* **2001**, *67*, 3208.
6. G. Pavelescu, C. Roman, E. Pfeiffer, E.A. Levei, M. Miclean, D. Savastru, E. Cordos, "Evaluation of petroleum contaminants in soils in Suplacu de Barcău area, Romania", 4th Bio Remediation Conference, **2008**, Greece.
7. I. Máthé, T. Benedek, A. Táncsics, M. Palatinszky, Sz. Lányi, K. Márialigeti, *International Biodeterioration and Biodegradation*, **2012**, *73*, 41.
8. U. George-Okafor, F. Tasie, F. Muotoe-Okafor, *Journal of Physical and Natural Sciences*, **2009**, *3*, 1.
9. F.T. Shen, J.L. Lin, C.C. Huang, Y.H. Ho, A.B. Arun, L.S. Young, C.C. Young, *Systematic and Applied Microbiology*, **2009**, *32*, 291.
10. B. Hendrickx, H. Junca, J. Vosahlova et al., *Journal of Microbiological Methods*, **2006**, *64*, 250.

11. A. Táncsics, S. Szoboszlay, B. Kriszt, J. Kukolya, E. Baka, K. Márialigeti, S. Révész, *Journal of Applied Microbiology*, **2008**, *105*, 1026.
12. T. Benedek, I. Máthé, A. Táncsics, K. Márialigeti, B. Albert, Sz. Lányi, *U.P.B. Scientific Bulletin*, **2011**, *73*, 51.

STUDIA UBB CHEMIA, LVII, 3, 2012 (p. 213 – 222)
(RECOMMENDED CITATION)

A COMPUTATIONAL STUDY OF THE SURFACE PROPERTIES OF THE HUMAN AND BACTERIAL CHITOTRIOSIDASE

ALECU-AUREL CIORSAC[1], VASILE OSTAFE[2, 3], ADRIANA ISVORAN[2, 3]

ABSTRACT. Mapping of physicochemical properties of surfaces of the human, bacterial and fungal chitotriosidases reveals that the three enzymes present distinct local surface properties, suggesting the possibility of specific inhibition of the human chitotriosidase. The results obtained for the volumes of the largest cavity differ qualitatively and quantitatively between the two employed tools (CASTp and Fpocket). Nevertheless, both algorithms concur in indicating that the human, bacterial and fungal chitotriosidase pockets are different.

Keywords: *chitotriosidase, fractal surface dimension, surface properties, ligand binding, specific inhibition.*

INTRODUCTION

Chitinases belong to the glycosyl hydrolase 18 family that cleave the glycosidic bond in chitin, and are found in bacteria, fungi, insects, plants and mammals [1]. Although it was thought for many years that humans do not possess and process chitin, it was more recently discovered that humans have a chitinase activity associated to conditions such as allergies, asthma, fungal infections and cancer [2]. Among the human chitinases, chitotriosidase (CHT) and acidic mammalian chitinase (AMCase) hydrolise the chitin [3] contained in fungal cell walls and exoskeletons of numerous parasitic worms [4]. Even if the biological function of CHT is not yet fully established, it is already known that it plays an important role as a pathogen-defence protein. Chitotriosidase is a specific marker for lysozomal storage disorders and it was also proposed to be a possible target for the design of chemotherapeutics against human pathogens [1, 5] [7]. Most chitotriosidase inhibitors show no selectivity and competitively inhibit family 18 chitinases [8, 9]. It becomes important to identify common inhibitors of human CHT, family 18 chitinases and chitinases in the pathogenic organisms and to design new specific inhibitors for CHT.

[1] *Politehnica University of Timisoara, Department of Physical Education and Sport, 2 P-ta Victoriei, RO-300006, Timisoara, Romania*
[2] *West University of Timisoara, Department of Chemistry, 16 Pestallozi, RO-300115, Timisoara, Romania, aisvoran@cbg.uvt.ro*
[3] *Laboratory of Advanced Researches in Environmental Protection, 4 Oituz, Timisoara, RO-300086, Romania*

Here, we analyze the surface properties of the human bacterial and fungal chitotriosidases in correlation with those of their known ligands, in order to obtained clues useful for the design of new possible therapeutic molecules selectively blocking the human CHT enzymatic activity.

RESULTS AND DISCUSSION

The sequences of the human, fungal (*Aspergillus fumigatus*) and bacterial (*Serratia marcescens*) chitotriosidases, retrieved from UniProtKB databases (codes entry Q13213, Q54276 and Q873X9 respectively), reveal only 48% sequence identity (data not shown).

Figure 1 illustrates the determination of the surface fractal dimension for the free human chitotriosidase. The computed fractal dimension is 2.24±0.01 and it reflects the complexity of the surface shape of the protein in good agreement with other published data concerning fractal aspects of protein surfaces [10-12].

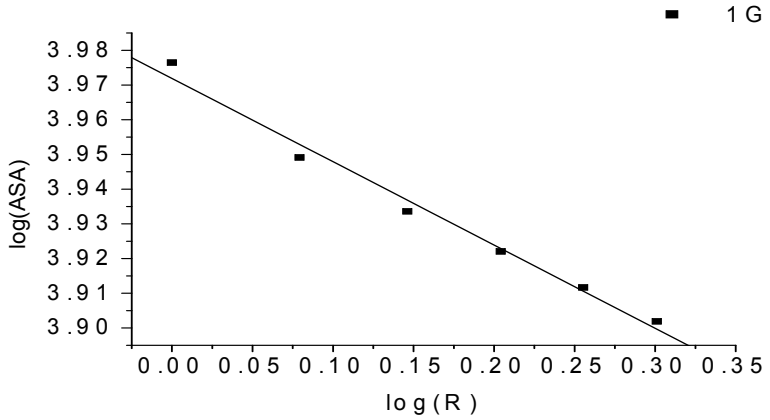

Figure 1. Determination of the global fractal dimension of human chitotriosidase (pdb entry 1GUV)

The surface fractal dimensions for the surfaces corresponding to all the considered chitotrisidases determined using this algorithm are presented in Table I, alongside the root mean square deviation (RMSD) obtained by superimpositions of the structure of human chitotriosidase and the other considered structures.

The superimposition of structural files indicates that globally the structural properties of the investigated CHTs are relatively similar. Thus, between the bacterial and fungalCHTs the RMSD values are situated around 0.828 Å. Between the human CHT and its complexes there are only small differences, and this is also true for *Serratia marcescens* (RMSD between 0.345 Å and 0.398 Å) and *Aspergillus fumigatus* (RMSD between 0.346 Å and 0.562 Å). The

accessible surface area is higher for the free CHT in comparison to that of its complexes, and the surface fractal dimension is smaller for the free CHT. These results emphasise the high complexity of the protein surface and its sensitive conformational changes when the protein interacts with ligands.

Table I. Global surface properties for considered chitotriosidases and their complexes (ASA – accessible surface area; Df – fractal dimension, electrostatics-based 'contact potential'). The ligand was removed from the structural file when computing the surface properties of the complexed proteins.

Chitotriosidase	PDB code	RMSD (Å)	ASA (Å^2)	D_f	Contact potential
Human CHT free	1GUV	-	8894.94	2.24±0.01	-57.68 +57.68
Human CHT in complex with chitobiose	1LG1	0.439	8405.06	2.30±0.02	-58.02 +58.02
Human CHT in complex with ethylene glycol	1LG2	0.495	8120.77	2.31±0.01	-57.64 +57.64
Human CHT in complex with glucoallosamidin B	1HKI	0.361	8366.75	2.28±0.02	-57.90 +57.90
Human CHT in complex with methylallosamidin	1HKJ	0.370	8322.26	2.34±0.02	-56.41 +56.41
Human CHT in complex with allosamidin	1HKK	0.413	8230.84	2.28±0.02	-58.07 +58.07
Human CHT in complex with demethylallosamidin	1HKM	0.373	8249.76	2.27±0.03	-57.24 +57.24
Human CHT in complex with argadin	1WAW	0.528	8282.47	2.30±0.01	-56.98 +56.98
Human CHT in complex with argifin	1WB0	0.429	8373.07	2.27±0.02	-57.09 +57.09
Serratia marcescens CHT	1E15	1.108	7785.90	2.20±0.02	-48.41 +48.41
D142N mutant of serratia marcescens CHT in complex with allosamidin	1OGG	1.014	7725.90	2.11±0.02	-47.81 +47.81
Aspergillus fumigatus CHT	1W9P	1.129	8893.97	2.26±0.03	-55.03 +55.03
Aspergillus fumigatus CHT in complex with argadin	1W9U	1.116	9029.36	2.25±0.02	-55.01 +55.01
Aspergillus fumigatus CHT in complex with argifin	1W9V	1.112	8956.74	2.24±0.03	-55.06 +55.06
Aspergillus fumigatus CHT in complex with theofillin	2A3A	1.102	9168.12	2.24±0.02	-55.02 +55.02
Aspergillus fumigatus CHT in complex with caffeine	2A3B	1.117	9171.72	2.25±0.02	-55.12 +55.12
Aspergillus fumigatus CHT in complex with pentoxifillin	2A3C	1.111	9169.94	2.24±0.01	-55.09 +55.09
Aspergillus fumigatus CHT in complex with alosamidin	2A3E	0.996	9156,89	2.22±0.02	-55.27 +55.27

Table I also shows differences between the structures and surfaces of bacterial, fungal and human chitotriosidases, which are in line with the sequence dissimilarities. Contact potential calculations reveal that local charge density is different for the three CHTs. This property, in addition to other determined surface properties of the investigated proteins and the structural features of ligands, allows us to predict possible regions for charged ligands binding. Also, the solvent accessible surface is higher for fungal CHTs in comparison with human and bacterial CHTs. We must underline that human CHT is a monomer and bacterial and fungal CHTs form dimers.

The dimensional properties of the largest cavity identified for the chitotrisidases using the CASTp [13] software are presented in Table II, and help to assess the accessibility of this cavity to various ligands and substrates. Additionally, the Fpocket [14] data in Table II also reveal that the largest identified pockets for all considered chitotriosidases usually have hydrophobic character and present local regions of high hydrophobic density.

The volumes of the pockets are different when identified by CASTp and Fpocket. Disturbingly, the differences are on the order of 100-200%, and no trends are conserved. Whereas CASTp claims that the bacterial enzyme has the largest pocket (almost three times larger than human and fungi CHTs), Fpocket claims that the bacterial enzyme has smaller pocket, almost half of one of the pockets seen in one of the human enzymes. Nevertheless, both algorithms concur in saying that the human, fungal and bacterial pockets are different. Unavoidably, the scoring functions are strongly dependent on the quality of the pocket identification and delimitation and they are sensitive to conformational changes. All these reflect that both of two servers give the probable but not exact binding pockets and makes comparison between methods difficult and only qualitative in nature. It has been also proved that the pocket volume computed by Fpocket is only approximated [14]. On the other hand the advantage of Fpocket is that it also specifies the global and local hydrophobicity, important for ligand binding. The values presented in Table II also emphasise that the structural changes that occur when CHT interacts with its ligands strongly affect the surface properties. These changes may be understood easier if we take into account also the properties of the ligands (as computed using the chimera software [15]), cf. Table III. The volumes and surface areas of known CHT ligands are smaller in comparison to those identified for the cavities by the CASTp software.

Figure 2 illustrates the largest pocket identified for CHT using the Fpocket tool. The pocket is presented as grey small spheres and the protein is presented as cartoon.

Table II. Geometrical properties of the biggest cavity identified by CASTp and Fpocket respectively into the investigated structures

Chitotrisodase/ Chitotriosidase complex	PDB code entry	CASTp		Fpocket		
		Area (Å^2)	Volume (Å^3)	Hydrophobicity score	Local hydrophobic density	Pocket volume (Å3)
Human CHT free	1GUV	823.6	1518.5	31.28	53.49	2207.92
Human CHT in complex with chitobiose	1LG1	821.1	1371.4	30.66	45.92	2634.06
Human CHT in complex with ethylene glycol	1LG2	749.0	1264.2	28.46	45.44	1869.06
Human CHT in complex with glucoallosamidin B	1HKI	829.1	1353.6	27.02	47.98	1832.71
Human CHT in complex with methylallosamidin	1HKJ	821.8	1397.6	35.28	48.98	2530.02
Human CHT in complex with allosamidin	1HKK	749.1	1305.0	32.51	54.45	2461.55
Human CHT in complex with demethylallosamidin	1HKM	842.5	1406.5	34.71	52.68	1863.28
Human CHT in complex with argadin	1WAW	894.8	1630.1	31.07	57.98	3107.77
Human CHT in complex with argifin	1WB0	782.1	1322.9	18.77	33.05	1144.65
Serratia marcescens CHT	1E15	1929.0	3506.1	24.38	57.52	1716.32
D142N mutant of Serratia marcescens CHT in complex with allosamidin	1OGG	1848.6	3686.1	27.76	54.39	1842.65
Aspergillus fumigatus CHT	1W9P	686.7	981.1	26.90	47.25	1931.73
Aspergillus fumigatus CHT in complex with argadin	1W9U	826.6	1402.4	26.63	46.74	1811.49
Aspergillus fumigatus CHT in complex with argifin	1W9V	817.6	1384.8	30.22	37.25	1481.11
Aspergillus fumigatus CHT in complex with theofillin	2A3A	768.7	1271.4	27.00	45.37	1484.51
Aspergillus fumigatus CHT in complex with caffeine	2A3B	851.7	1315.2	22.09	39.18	1100.90
Aspergillus fumigatus CHT in complex with pentoxifillin	2A3C	1165.2	1854.9	18.99	58.68	690.32
Aspergillus fumigatus CHT in complex with alosamidin	2A3E	856.8	1350.6	22.87	37.29	724.44

Table III. Geometrical properties of known ligands

Ligand	Surface area (Å^2)	Volume (Å^3)
chitobiose	322.8	339.5
ethylene glycol	341.2	281.3
glucoallosamidin B	484.1	533.2
methylallosamidin	498.1	556.8
allosamidin	933.4	1106
demethylallosamidin	462.7	505.1
argadin	904.5	954.1
argifin	976.3	919.0

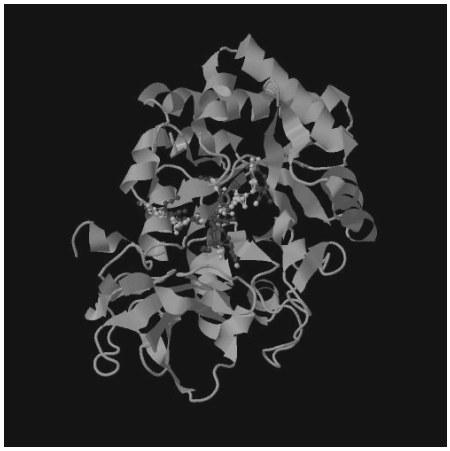

Figure 2. The largest pocket (grey spheres) for the human chitotriosidase (code entry 1GUV) detected using Fpocket

CONCLUSIONS

Mapping of physicochemical characteristics onto the surface of a protein can be used in the characterization and identification of similarities within protein surface regions. We have used this mapping to compare the surface properties of human, bacterial and fungal chitotriosidases. Our study reveals distinct surface properties for human, bacterial and fungi CHTs and also underlines that interactions of protein with its ligands affect the surface properties, such as solvent accessible area and surface roughness.

There are a few determined three dimensional structures of the human chitotriosidase in complex with inhibitors such as chitooligossacharide [1], allosamin and its derivatives, demethylallosamidin, methylallosamidin, and glucoallosamidin B [17] and two natural peptide products, argifin and argadin [18]. These structures show that the effect of inhibition is the alteration of the hydrophobic interactions and hydrogen binding [1, 17, 18]. Our data, predicting a large hydrophobic binding pocket in the structures of investigated CHTs, are in good agreement with these findings revealing an elongated active site cleft compatible with the binding of chitinopolymers. Also, our data suggest that the active site has an open architecture and a potential selective inhibitor of CHT must be a hydrophobic molecule.

The sequence differences and structural dissimilarities of the bacterial, fungal and human chitotriosidases reflected in their distinct surface properties allow us to speculate that there is the possibility of designing specific inhibitors for human chitotriosidases.

EXPERIMENTAL SECTION

For the human and bacterial chitotriosidase (CHT) the surface properties examined within this study are: the solvent accessible area (ASA) of the protein, the surface roughness, the dimensional and physicochemical properties of its identified cavities and/or pockets and its electric potential respectively. The three dimensional structures of free CHT and of its complexes with small drug molecules are retrieved from the Protein Data Bank [19] and their entry codes are presented in Table 1. When more than one chain is present in the structural file (as in the case of bacterial CHT), only one monomer (chain A) is considered.

The protein surface area can be computed starting from various models[20]. For example, in order to identify the protein surface cavities the CASTp [13] or Fpocket [15] tools may be used, and in order to compute the accessible surface area the GETAREA [21] tool may be used. CASTp provides identification and measurements of surface accessible pockets as well as interior inaccessible cavities using the weighted Delaunay triangulation and the alpha complex for shape measurements [13]. It computes a triangulation of the protein's surface atoms using alpha shapes and these triangles are then grouped by letting small triangles flow toward neighbouring larger triangles, which act as sinks. The pocket is defined as the collection of empty triangles. The Fpocket detection algorithm is based on Voronoi tessellation and also allows to extract pocket descriptors and a druggability prediction score [14]. This tool is based on the geometric approach of an alpha sphere contacting four atoms on its boundary (all the four atoms are at an equal distance, sphere

radius, to the alpha sphere centre) and containing no internal atom. Alpha sphere identification is based on Voronoi decomposition of space: the centre of alpha spheres correspond to Voronoi vertices, i.e. points at which Voronoi regions intersect. Next step consists in identifying clusters of spheres close together, to identify pockets, and to remove clusters of poor interest. For proteins, small spheres are located within the protein, clefts and cavities correspond to spheres of intermediate radii and large spheres are located at the protein surface. It is then possible to filter the ensemble of alpha spheres according to some minimal and maximal radii values in order to address pocket detection. After that the properties of the atoms of the pocket are considered in order to score each pocket.

In our study we have considered only the largest identified pocket as such a pocket tends to frequently correspond to the observed ligand binding site [21].

Another property that we investigate is the surface roughness quantitatively expressed by the surface fractal dimension. In order to determine this quantity we compute the surface area SA of each protein for different radii of the rolling probe using the on-line tool GETAREA [22] . The surface fractal dimension is determined using the scaling law between the surface area *(SA)* of the protein and the radius of the rolling probe molecule *(R)*

$$SA \sim R^{2-D_s} \tag{1}$$

from the slope of the double logarithmical plot of *SA* versus *R* [23]. The surface area of the protein has been calculated using the probe radii of 1, 1.2, 1.4, 1.6, 1.8 and 2 Å respectively.

The qualitative electrostatic properties of the surfaces of investigated structures, expressed by the contact potential, are computed using the PyMol software [16]. This software can provide information on the local charge density (within 10 angstroms), regarding how positive, negative or neutral a region of the protein surface is relative to the rest of the protein.

ACKNOWLEDGMENTS

This study benefited by the financial support of projects POSDDRU 21/1.5/G/38347, IPA-464 ROSNET and POSDRU 21/1.5/13798.

REFERENCES

1. F. Fusetti, H. von Moeller, D. Houston, H.J. Rozeboom, B.W. Dijkstra, R.G. Boot, J.M.F.G. Aerts, D.M.F. van Aalten, *Journal of Biological Chemistry,* **2002**, *27,* 25537.
2. J. Kzhyshkowska, A. Gratcev, S. Goerdt, *Biomarker Insights*, **2007**, *2*, 128.
3. G.H. Renkema, R.G. Boot, F.L. Au, *European Journal of Biochemistry*, **1998**, *251*, 504.
4. R.N. Tharanathan, F.S. Kittur, *Critical Reviews of Food and Scientific Nutrition*, **2003**, *43*, 61.
5. K.B. Eide, A.L. Norberg, E.B. Heggset, A.R. Lindbom, K.M. Vaarum, V.G.H. Eijsink, M. Sorlie, *Biochemistry*, **2012**, *51*, 487.
6. I.M.A. Nooren, J.M. Thornton, *EMBO Journal*, **2003**, *22*, 3486.
7. M. Kuepper, K. Bratke, J.C. Virchow, *Journal of Medicine,* **2008**, *358*, 1073.
8. C.L. Rush, A.W. Schuttelkopf, A.W. Hurtado-Guerrero, D.E. Blair, A.F.M. Ibrahim, D.S. Desvergnes, I.M. Eggleston, D.M. van Aalten, *Chemistry & Biology,* **2010**, *17*, 1275.
9. T.E. Sutherland, O.A. Andersen, M. Betou, I.M. Eggleston, R.M. Maizels, D.M. van Aalten, J.E. Allen, *Chemistry & Biology,* **2011**, *18*, 569.
10. A. Isvoran, *Chaos Solitons & Fractals*, **2004**, *19*, 141.
11. L. Pitulice, A. Isvoran, A. Chiriac, *Journal of the Serbian Chemical Society*, **2008**, *73,* 805.
12. A. Isvoran, L. Pitulice, C.T. Craescu, A. Chiriac, *Chaos Solitons & Fractals*, **2008**, *35*, 960.
13. J. Dundas, Z. Quyang, J. Tseng, A. Binkowski, Y. Turpaz, J. Liang, *Nucleic Acids Research,* **2006**, *34*, W116.
14. V. le Guilloux, P. Schmidtke, P. Tuffery, *BMC Bioinformatics,* **2009***, 10*, 168.
15. E.F. Pettersen, T.D. Goddard, C.C. Huang, G.S. Couch, D.M. Greenblatt, E.C. Meng, T.E. Ferrin, *Journal of Computational Chemistry*, **2004**, *25*, 1605.
16. W.L. DeLano, "The PyMOL Molecular Graphics System", DeLano Scientific, San Carlos, **2002**.
17. F.V. Rao, D.R. Houston, R.G. Boot, J.M. Aerts, S. Sakuda, D.M. van Aalten, *Journal of Biological Chem*istry, **2003**, *278*, 20110.
18. F.V. Rao, D.R. Houston, R.G. Boot, J.M. Aerts, M. Hodgkinson, D.J. Adams, S. Omura, D.M. van Aalten, *Chemical Biol*ogy, **2005**, *12*, 65.
19. H.M. Berman, J. Westbrook, Z. Feng, G. Gilliland, T.N. Bhat, H. Weissig, I.N. Shindyalov, P.E. Bourne, *Nucleic Acids Research,* **2000**, *28,* 235.

20. D. Crăciun, L. Pitulice, A. Isvoran, *International Journal of Chemical Modeling,* **2009**, *2*, 34.

21. M. Nayal, B. Honig, *Proteins: Structure, Function and Bioinformatics*, **2006**, *6,* 892.

21. R. Franczkiewicz, W. Braun, *Journal of Computational Chem*istry, **1998**, *19*, 319.

22. B.B. Mandelbrot, "Fractals and chaos. The Mandelbrot set and beyond", Springer Verlag, New York, **2004**, chapter 5.

STUDIA UBB CHEMIA, LVII, 3, 2012 (p. 223 – 236)
(RECOMMENDED CITATION)

ANODIC DISSOLUTION OF SOME ELECTRODE MATERIALS INVOLVED IN ELECTROCHEMICALLY ASSISTED COAGULATION

MARIUS SEBASTIAN SECULA[1], GHEORGHE NEMTOI[2], IGOR CRETESCU

ABSTRACT. A study approaching the anodic dissolution of iron and aluminum based electrodes in aqueous solutions containing sulfate or chloride ions is presented in this paper. Beside the influence of the supporting electrolyte, it is experimentally established the influence of the solution pH on the anodic dissolution of the two anodic materials considered. As the anodic dissolution of the anode surface is the first step of electrocoagulation processes, the results obtained are important in order to achieve a better understanding of these processes. The anodic dissolution process depends mainly on the specific electrical charge passed. Current density at null potential, heterogeneous constant rate in mixed regime and dissolution rate are determined. The influence of mass transport over the global rate of the dissolution rate of aluminum and iron respectively is established.

Keywords: *electrocoagulation, anodic dissolution, iron, aluminum, corrosion parameters*

INTRODUCTION

In the last decades, electrochemical technologies of wastewater treatment have been undergoing intensive development. Among these technologies, one of the most promising is electrochemically assisted coagulation that can compete with the conventional chemical coagulation process in the treatment of wastewaters [1,2].

In electrocoagulation, an electrochemical cell is used to provide aluminum or iron ions into the wastewater. Depending on the pH conditions and wastewater chemistry, these ions destabilize the colloidal pollutants, similarly to the case of conventional coagulation process. The turbulence

[1] *TUIASI - "Gheorghe Asachi" Technical University, Faculty of Chemical Engineering and Environmental Protection, 73 Prof. Dr. docent D. Mangeron, 700050, Iasi, Romania, mariussecula@ch.tuiasi.ro*
[2] *"Al. I. Cuza" University, Faculty of Chemistry, 11 Carol I, 700506, Iasi, Romania*

generated by the oxygen and the hydrogen evolution generates a soft mix that helps the destabilized colloids to flocculate (to link together and to generate bigger particles). Finally, the pollutants are removed from the wastewater by sedimentation, filtration or flotation [3].

Although, electrocoagulation is a rather old technology, it has received very little scientific attention. Only in the last few years, some works focused on the study of electrocoagulation technology and especially on the fundamental principles lying at its basis [4,5]. Nevertheless, to make this technology competitive, a better understanding of the involved processes has to be achieved. Canizares et al. [5-7], in case of aluminum anode, and Noubactep and Schoner [8], in case of iron anode, investigated the mechanisms of electrocoagulation with a special regard to the speciation of the dissolved metals. Recently, Mouedhen et al. [9] reported several results on the corrosion of aluminum in the presence of NaCl, in the range of 0-1.7 mM. However, according to our knowledge mass transport phenomena taking place at the anode surface under the condition specific to electrocoagulation systems have not been addressed yet. In spite of numerous studies reported on the corrosion of both aluminum and iron in the presence of the two considered background electrolytes, there is no systematic approach of these systems with regard to the electrocoagulation technique.

The main purpose of this work is to study the anodic dissolution of iron and aluminum into diluted aqueous solutions. The characterization of the first step of electrocoagulation is of very high importance in order to achieve a thorough understanding of the whole process. Linear sweep voltammetry was employed to characterize the dissolution process of aluminum and iron in diluted aqueous solutions of sodium chloride or sodium sulfate. By using the potentiodynamic polarization curves on a wide potential range, the limiting rates of the investigated anodic dissolution processes were established. The method of linear polarization resistance, Evans diagrams and Stern's second method were used to estimate the values of corrosion currents that define the specific dissolution process. Also, values of dissolution rate of the anodic dissolution processes taking place under kinetic and mixed regimes at various potential values were calculated.

THEORY

It is well known that in order to generate coagulant into an electrocoagulation reactor, it is necessary to apply a potential difference between electrodes. Occurring electrode reactions depend on the operating pH and species present in the electrochemical system. The electrode material generates the type of coagulant cation and thus, the electrochemical reactions.

Electrocoagulation literature describes the following reactions taking place at the anode and cathode [3]:

At the anode:

$$M_{(s)} \rightarrow M_{(aq)}^{n+} + ne^- \quad (1)$$

$$2H_2O_{(l)} \rightarrow O_{2(g)} + 4H_{(aq)}^{+} + 4e^- \quad (2)$$

At the cathode:

$$2H_2O_{(l)} + 2e^- \rightarrow H_{2(g)} + 2OH^-_{(aq)} \quad (3)$$

These reactions explain the appearance of bubbles near the cathodes and anodes during the process and can also explain the consequent increase of pH (dependent on the solution alkalinity and electrochemical process rate, i.e., the intensity of the electric current and operation time).

When iron or aluminum electrodes are involved, the generated $Fe_{(aq)}^{2+}$ or $Al_{(aq)}^{3+}$ ions will immediately undergo further spontaneous reactions to produce the corresponding hydroxides and/or polyhydroxides [6,10].

Throughout the anodic range of the polarization curves there might be identified several energetic areas (potential ranges) where electrode materials emphasize certain behaviors. Thus, in certain potential ranges the metal material is strongly corroded, while, in others, the electrode becomes passivated.

Based on the linear polarization curves, important parameters of anodic dissolution process such as corrosion and passivation potentials and their corresponding current densities can be determined [11].

Cyclic potentiodynamic curves might present a hysteresis that describes the material tendency toward a certain type of corrosion (intergranular, pitting, crevice etc.) [12].

Steady-state polarization consists in applying of a potential difference between reference electrode and working electrode. When the steady-state is reached, the current response is recorded.

The process kinetics is strongly influenced by the electrode potential and is described by the Butler-Volmer equation that can be simplified for two extreme cases [12].

For a high value of the overpotential, the reaction becomes irreversible and consequently one of the exponential terms becomes insignificant. Therefore, Butler-Volmer equation can be simplified to [11]:

$$\ln|i| = \ln i_0 + \frac{\alpha \cdot n \cdot F}{R \cdot T}\eta \quad (4)$$

According to Stern's first method [13,14], Tafel slope leads to the value of charge transfer coefficient, α, while the intercept leads to the value of exchange current, i_0.

However, at high values of polarization potential, the corresponding current can dissolve the metal or might reduce some superficial films on the electrode. These might influence the interphase state and the values of corrosion rates [15].

Stern's second method avoids these deficiencies due to the determination of corrosion current takes also into account the polarization resistance [16]. For a low variation of the potential, Butler-Volmer equation becomes [16]:

$$i = i_0 \frac{n \cdot F}{R \cdot T} \eta \tag{5}$$

where is overpotential, i_0 – the exchange current, R – gas constant, T – temperature, F – Faraday's constant and n – number of electrons.

Current-overpotential relationships allow one to determine the exchange current density, i_0, also named the corrosion current density, when the corrosion process takes place.

Corrosion potential can be determined from the polarization curves by means of Evans plots (logarithm of current density vs. overpotential) [17].

Resistance to exchange transfer was calculated using the following equation:

$$R_p = \frac{R \cdot T}{n \cdot F \cdot I_0} \tag{6}$$

The rate of an anodic dissolution process is defined by the relationship [18]:

$$v_D = \frac{dm_O}{S \cdot dt} \tag{7}$$

where m is the quantity of species O, kg; S – cross section area normal to the ax of mass flow, m^2. Taking into account Farraday's laws, eq. (7) becomes:

$$v_D = \frac{M_O \cdot i}{n \cdot F} \tag{8}$$

RESULTS AND DISCUSSION

Aluminum dissolution in diluted aqueous solution containing NaCl

Fig. 1a shows several sweep linear voltammograms obtained at aluminum dissolution into sodium chloride of different pH. These voltammograms were used to determine the polarization resistance, according to eq. (6), corrosion currents, by means eq. (5), and Tafel corrosion currents, based on eq. (4). Considering current values at different relative electrode potentials, aluminum dissolution rates were calculated with eq. (8) in order to point out the intensity of the dissolution process taking place at various values of pH.

Fig. 1a pinpoints that the slopes of current-potential dependences present no significant change throughout a relative wide potential range. This means the current is not limited by mass transfer. Therefore, the electrochemical reaction is the limiting rate.

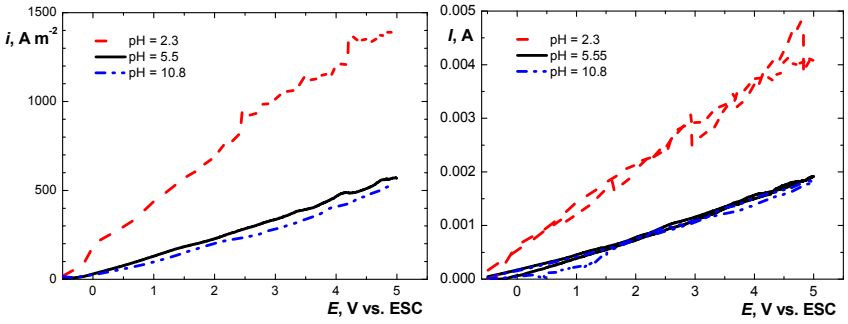

(a) (b)

Figure 1. Linear sweep (a) and cyclic (b) voltammograms of aluminum anode – 3.42 mM NaCl system at three values of pH. Potential ranges: -0.5 – 5 V/ESC and -0.5 – 5 -0.5 V/ESC; sweep rate 50 mV·s^{-1}; Resolution time 0.8 s, T = 298 K, anode diameter 2.07 mm

Cyclic voltammograms (Fig. 1b) present a small hysteresis. However, it is obvious that on these ranges of the potential the corrosion phenomena occur at all three values of pH. In case of acid medium, several bounces of the current can be noticed. These may be explained by the detachment of oxygen bubbles formed onto the electrode surface. The competition between aluminum dissolution and oxygen evolution leads to a decrease in aluminum generation efficiency [4].

According to the studies performed by Macdonald [19], the corrosion current increases with the potential sweep rate. As listed in Table 1, in case of aluminum dissolution in diluted aqueous solution of NaCl with a pH of 5.5, the increase of corrosion current with sweep rate is valid for both calculation methods of corrosion current. In Fig. 2 are shown Evans plots for aluminum dissolution in sodium chloride solution at various values of pH (Fig. 2a), and sweep rates of potential (Fig. 2b). Then, the values of corrosion current were determined according to the second method of Stern.

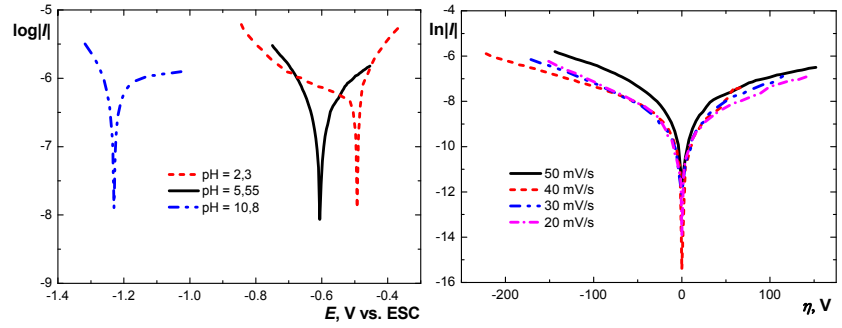

(a) (b)

Figure 2. Semi logarithmic I-η plot of aluminum dissolution in sodium chloride solution (a) at various pH values and (b) at various sweep rates of potential, pH = 5.5

Table 1. Corrosion parameters of Al÷3.42 mM NaCl system at various sweep rates and different values of pH

Run No.	pH	Potential range	Sweep rate	E_{cor}	$I_{O,\ init}$	R_p	$I_{O,\ Tafel}$	$i_{O,\ Tafel}$
		V vs. ESC	$mV \cdot s^{-1}$	V	A	$\Omega \cdot m^2$	A	$A \cdot m^{-2}$
1	5.5	−0.15 ÷ 0.15	50	-0.514	$2.641 \cdot 10^{-07}$	0.108	$2.392 \cdot 10^{-07}$	0.071
2	5.5	−0.15 ÷ 0.15	40	-0.525	$4.818 \cdot 10^{-08}$	0.590	$8.378 \cdot 10^{-08}$	0.025
3	5.5	−0.15 ÷ 0.15	30	-0.525	$4.643 \cdot 10^{-08}$	0.612	$7.421 \cdot 10^{-08}$	0.022
4	5.5	−0.15 ÷ 0.15	20	-0.587	$4.362 \cdot 10^{-08}$	0.652	$6.919 \cdot 10^{-08}$	0.021
5	2.3	−0.5 ÷ 5	50	-0.595	$2.52 \cdot 10^{-08}$	1.127	$1.296 \cdot 10^{-06}$	0.385
6	5.5	−0.5 ÷ 5	50	-0.601	$8.41 \cdot 10^{-08}$	0.338	$2.040 \cdot 10^{-07}$	0.061
7	10.8	−0.5 ÷ 5	50	-1.170	$5.11 \cdot 10^{-08}$	0.556	$1.684 \cdot 10^{-07}$	0.050

As can be noticed, in strong acid medium aluminum dissolution is more pronounced, and Tafel corrosion current is one order of magnitude higher than the corrosion currents obtained for this system in alkaline medium as emphasized in Fig. 1a. The obtained results are in agreement with those reported by Mouedhen et al. [9]. In the presence of chloride ion enhances the pitting corrosion phenomena onto the metal surface [20].

Fig. 3 shows the variation of dissolution rate of aluminum in solution containing chloride ion at different values of electrode potential and pH.

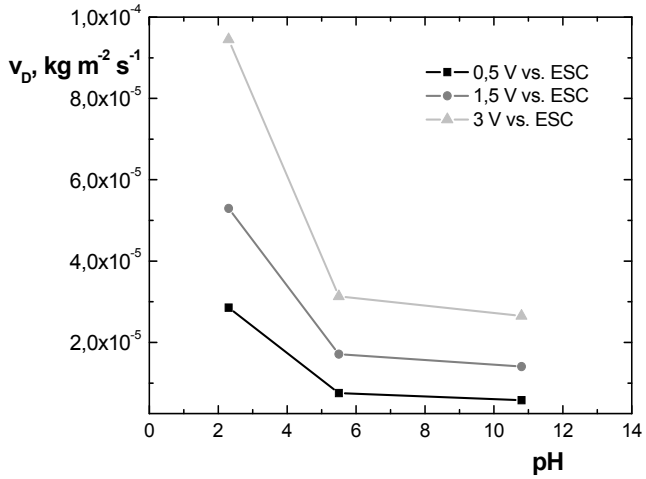

Figure 3. Dependence of aluminum dissolution rate on the solution pH

The acid pH favors the dissolution process, and the dissolution rate of aluminum increases proportionally with the potential for all pH values.

Aluminum dissolution in diluted aqueous solution containing Na_2SO_4

In Fig. 4 are shown the linear sweep and cyclic voltammograms obtained for Al-100mM Na_2SO_4 system. Table 2 presents the corrosion parameters calculated by means of potentiodynamic polarization curves recorded at aluminum dissolution in diluted aqueous solutions of 0.1 M Na_2SO_4.

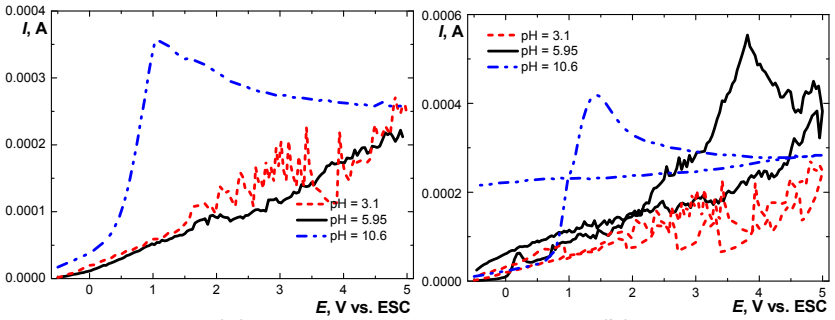

Figure 4. Linear sweep (a) and cyclic (b) voltammograms obtained at different values of pH. Potential ranges: -0.5 – 5 V/ESC and -0.5 – 5.5 -0.5 V/ESC; sweep rate 50 $mV \cdot s^{-1}$; Resolution time 0.8 s, T = 298 K, anode diameter 2.07 mm

Table 2. Corrosion parameters of Al÷100 mM Na_2SO_4 system at different values of pH

Run No.	pH	Potential range	Sweep rate	E_{cor}	$I_{O,\ init}$	R_p	$I_{O,\ Tafel}$	$i_{O,\ Tafel}$
		V vs. ESC	$mV \cdot s^{-1}$	V	A	$\Omega \cdot m^2$	A	$A \cdot m^{-2}$
1	3.10	–0.5 ÷ 5	50	-0.591	$3.418 \cdot 10^{-08}$	0.833	$4.831 \cdot 10^{-08}$	0.014
2	5.95	–0.5 ÷ 5	50	-0.588	$6.541 \cdot 10^{-08}$	0.435	$1.490 \cdot 10^{-07}$	0.044
3	10.60	–0.5 ÷ 5	50	-0.113	$5.837 \cdot 10^{-07}$	0.049	$1.012 \cdot 10^{-06}$	0.301

According to the results presented in Table 2, the most corrosive medium for *Al÷100 mM Na_2SO_4* system is the alkaline one, while in the acid medium, the corrosion current achieves the lowest value. The behavior of aluminum dissolution in aqueous solutions of sodium sulfate is opposed to that of *Al÷3.42 mM NaCl* system, thus emphasizing the influence of the chloride ion onto the dissolution process of aluminum.

Linear sweep and cyclic voltrammograms shown in Fig. 4 support this conclusion. Moreover, the passivation phenomenon at the alkaline pH has been pinpointed. Throughout the potential range where the anode becomes passivated, the mass transfer is the limiting dissolution rate. In acid range and near neutral value of pH, *Al÷100 mM Na_2SO_4* system becomes unstable at potential values higher than 1.5 V when current oscillates strongly.

Iron dissolution in diluted aqueous solution containing NaCl

In Fig. 5a are shown the linear sweep voltammograms obtained at iron dissolution in diluted aqueous solutions of NaCl at various pH values.

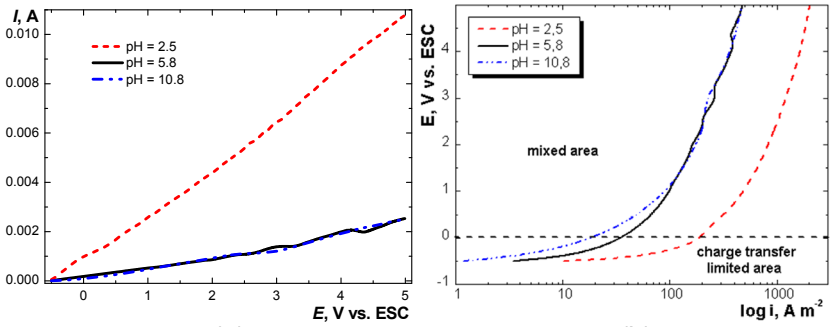

(a) (b)

Figure 5. Linear sweep voltammograms (a) and their semilogarithmic plots (b) at iron dissolution in aqueous solution of NaCl at different pH values. Potential ranges: -0.5 – 5 V/ESC and -0.5 – 5 -0.5 V/ESC; sweep rate 50 mV·s^{-1}; Resolution time 0.8 s, T = 298 K, anode diameter 2.6 mm

Fig. 5b points out two distinct areas on the investigated potential range. Thus, the first part is characteristic to the exchange transfer limiting rate, while the second part corresponds to a mixed area where current density increase accelerates with the increase of the potential values due to a more pronounced influence of mass transport over the dissolution rate.

Fig. 6 presents linear sweep voltammograms and Evans plots obtained at iron dissolution in diluted aqueous solutions of NaCl at different values of scan rate.

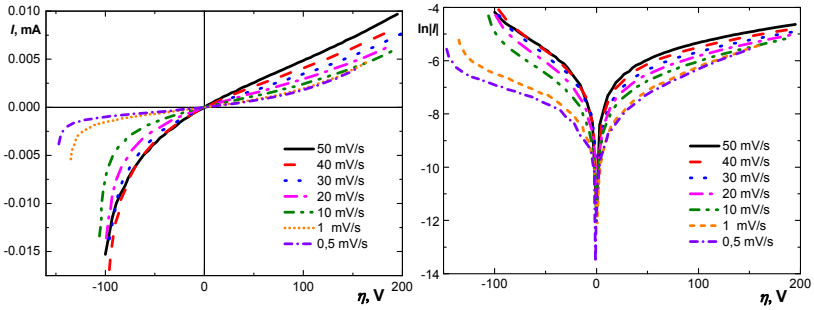

(a) (b)

Figure 6. Current-overpotential (a) and Evans (b) plots corresponding to iron dissolution in aqueous solutions of NaCl at different values of potential sweep rate, pH = 5.8. Potential range: -0.15 – 0.15 V/ESC, T = 298 K, anode diameter 2.6 mm

As in the case of aluminum dissolution, in the presence of chloride ions, iron dissolution takes also place with a positive influence of potential sweep rate over the corrosion current.

The values of corrosion parameters calculated for this system are presented in Table 3.

Table 3. Corrosion parameters of Fe÷3.42 mM NaCl system at different values of pH and sweep rates

Run No.	pH	Potential range	Sweep rate	E_{cor}	$I_{O,\,init}$	R_p	$I_{O,\,Tafel}$	$i_{O,\,Tafel}$
		V vs. ESC	$mV \cdot s^{-1}$	V	A	$\Omega \cdot m^2$	A	$A \cdot m^{-2}$
1	2.54	–0.5 ÷ 5	50	-0.555	$3.09 \cdot 10^{-06}$	0.022	$3.381 \cdot 10^{-06}$	0.637
2	5.80	–0.5 ÷ 5	50	-0.572	$7.35 \cdot 10^{-07}$	0.092	$5.129 \cdot 10^{-07}$	0.097
3	10.8	–0.5 ÷ 5	50	-0.542	$6.90 \cdot 10^{-07}$	0.097	$4.794 \cdot 10^{-07}$	0.090
4	5.8	–0.15 ÷ 0.15	50	-0.572	$7.347 \cdot 10^{-07}$	0.092	$5.129 \cdot 10^{-07}$	0.097
5	5.8	–0.15 ÷ 0.15	40	-0.589	$6.611 \cdot 10^{-07}$	0.102	$4.694 \cdot 10^{-07}$	0.088
6	5.8	–0.15 ÷ 0.15	30	-0.593	$5.720 \cdot 10^{-07}$	0.118	$3.958 \cdot 10^{-07}$	0.075
7	5.8	–0.15 ÷ 0.15	20	-0.593	$4.300 \cdot 10^{-07}$	0.156	$2.827 \cdot 10^{-07}$	0.053
8	5.8	–0.15 ÷ 0.15	10	-0.589	$3.083 \cdot 10^{-07}$	0.218	$2.225 \cdot 10^{-07}$	0.042
9	5.8	–0.15 ÷ 0.15	1	-0.560	$1.804 \cdot 10^{-07}$	0.373	$1.690 \cdot 10^{-07}$	0.032
10	5.8	–0.15 ÷ 0.15	0.5	-0.552	$1.509 \cdot 10^{-07}$	0.446	$1.587 \cdot 10^{-07}$	0.030

It can be noticed that the acid medium is the most corrosive one in case of steel. Also, it is emphasized a similar behavior of iron dissolution at pH = 5.8 and 10.8 respectively, which is supported by the values of corrosion current and polarization resistances as listed in Table 3.

In Fig. 7 is shown the variation of iron dissolution rate in the presence of chloride ions at different values of pH and current potential. Iron dissolution rate is proportional with the potential, the highest values corresponding to the acid values of pH.

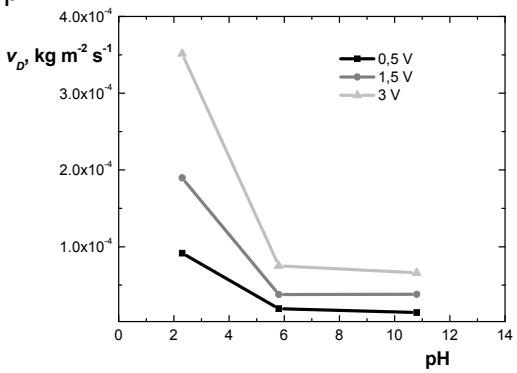

Figure 7. Dependence of iron dissolution rate on solution pH

Iron dissolution in diluted aqueous solution containing Na_2SO_4

Fig. 8 shows linear sweep and cyclic voltammograms measured at iron dissolution in aqueous solution of *100 mM* Na_2SO_4 at various values of pH and potential respectively.

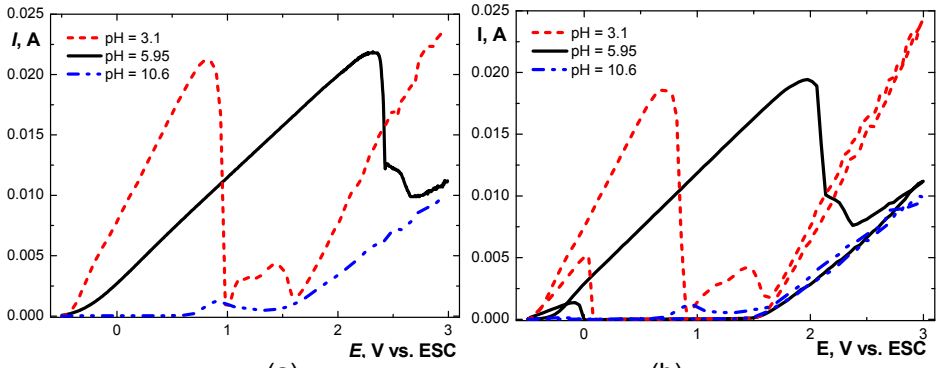

Figure 8. Linear sweep (a) and cyclic (b) voltrammograms obtained at iron dissolution in aqueous solutions of Na_2SO_4 at different values of pH. Potential ranges: -0.5 – 3 V/ESC and -0.5 – 3 -0.5 V/ESC; sweep rate 50 $mV \cdot s^{-1}$; Resolution time 0.8 s, T = 298 K, anode diameter 2.6 mm

It can be noticed the passivation of iron surface at the alkaline pH. Also, the mixed regime step is extended at higher values of the potential.

In Table 4 are presented the corrosion parameters corresponding to iron dissolution in aqueous solutions of *100 mM* Na_2SO_4 at different values of pH. These parameters were determined on the basis of linear sweep voltammograms and Evans plots shown in Fig. 9.

Table 4. Corrosion parameters of Fe÷100 mM Na_2SO_4 system at different values of pH

Run No.	pH	Potential range	Sweep rate	E_{cor}	$I_{O,\ init}$	R_p	$I_{O,\ Tafel}$	$i_{O,\ Tafel}$
		V vs. ESC	$mV \cdot s^{-1}$	V	A	$\Omega \cdot m^2$	A	$A \cdot m^{-2}$
1	3.10	–0.5 ÷ 5	50	-0.616	$3.72 \cdot 10^{-06}$	0.018	$2.677 \cdot 10^{-06}$	0.504
2	5.95	–0.5 ÷ 5	50	-0.522	$8.11 \cdot 10^{-07}$	0.083	$5.026 \cdot 10^{-07}$	0.095
3	10.60	–0.5 ÷ 5	50	-0.569	$9.62 \cdot 10^{-07}$	0.071	$5.943 \cdot 10^{-07}$	0.112

Acid medium favors the corrosion of iron in aqueous solutions of Na_2SO_4. However, compared to the system containing chloride ions, the passivation phenomenon occurs. In case of alkaline pH, the passivation is very strong, being recorded a peak of $1.22 \cdot 10^{-3}$ *A* at *0.9 V*, while in acid medium, the peak reaches the value of $2.1 \cdot 10^{-2}$ *A* at 0.8 V.

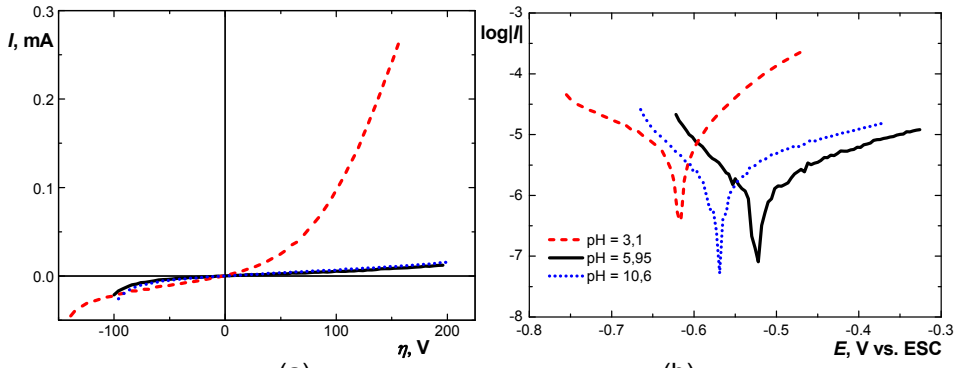

(a) (b)

Figure 9. Current-overpotential (a) and Evans (b) plots corresponding to iron dissolution in aqueous solutions of Na_2SO_4 at different sweep rates. Potential ranges: -0.15 – 0.15 V/ESC, T = 298 K, anode diameter 2.6 mm

CONCLUSIONS

Four different electrochemical systems were voltammetrically characterized. Several studies specific to processes taking place under kinetic and mixed regimes were performed. Thus, parameters such as current density at null potential, heterogeneous constant rate in mixed regime and dissolution rate were determined.

In order to describe the process of anodic dissolution of aluminum and iron respectively in diluted aqueous solutions, potentiodynamic polarization curves were measured on different potential ranges.

Based on linear sweep voltammograms measured on relatively small ranges of potential values, current density at null potential was determined by two different methods. These have allowed comparing the investigated systems in relation to anodic dissolution rate of aluminum and iron respectively at different values of pH, for two different support electrolytes. By widening the investigated potential range from -0.15-0.15 V to -0.5-5V, it was emphasized the influence of mass transport over the global rate of the dissolution rate of both aluminum and iron.

Considering the current values at different potentials, the dissolution rate of the four investigated systems were determined.

It was found that in case of aluminum dissolution in the presence of chloride ion, no passivation phenomenon occurs. At null potential, the alkaline pH favors most the corrosion process, while applying a potential difference, the dissolution process of aluminum in the presence of sulfate ion is influenced by the occurrence of the passivation phenomenon.

In case of iron dissolution into aqueous solutions of NaCl or Na_2SO_4 relatively close values were obtained at certain values of pH. However, in the presence of sulfate ion, the anode becomes passivated.

The obtained results emphasize the positive role played by the chloride ion in both aluminum and iron anodic dissolution processes.

EXPERIMENTAL SECTION

Materials and reagents

Electrode materials used in investigations were made of aluminum (*EN AW-1080A*, composition: *Al* min. *99.5%*, *Si 0.2%*, *Fe 0.2%*, *Zn 0.03*, *Mn 0.03)*, steel (*OL 32*, composition: *Fe* min. *99,14%*, *C* max *0.15*, *Mn* max. *0.6%*, *P* max *0.055%*, *S* max. *0.055%*), stainless steel (*X5CrNi18-10*, composition, *C 0.05%*, *Cr 18%*, *Ni 10 wt%*).

Aqueous solutions of 3.42 mM sodium chloride and 0.1 M sodium sulfate were prepared by dissolving *NaCl* A.R. and $Na_2SO_4 \cdot 10H_2O$ A.R. (Lachner, Czech Republik) into distilled water.

Adjustment of pH of aqueous solution was achieved by using 0.1 N and 1 N solutions of H_2SO_4 and NaOH respectively. These solutions were prepared by dissolving anhydrous NaOH A.R. (Fluka, Germany) and diluting H_2SO_4 98% solution (Merck, Germany) into distilled water.

Experimental Procedures

In order to measure the potentiodynamic polarization curves, the VoltaLab 32 (Radiometer Copenhagen) electrochemical installation, presented in Fig. 10, was employed.

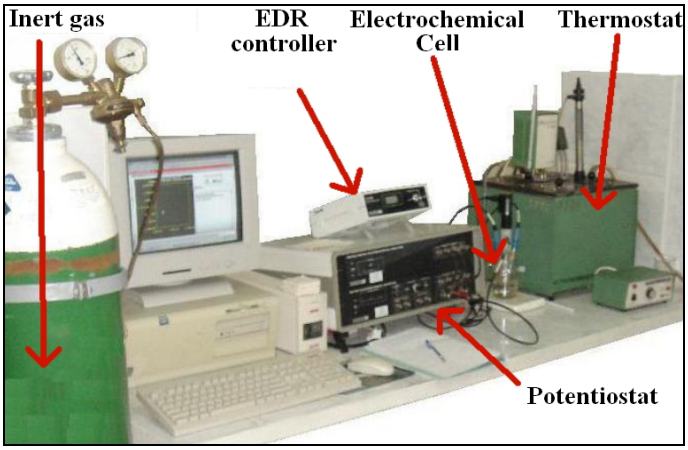

Figure 10. VoltaLab 32 electrochemical system

This electrochemical system is composed of a DEA-322 digital electrochemical analyzer potentiostat, an electrolytic cell with three electrodes provided with thermal coating and gas-sparging system, an IMT 102 data interface connected to a computer operated with Volta Master software.

CTV 101 (Radiometer Copenhagen) was employed for operating the rotating electrode in the range of 0-5000 RPM. The thermostating system consisted of a 657 MTA Kutesz controlled by 1031 MTA Kutesz regulator. For removing air from the electrolyte solution, a nitrogen gas bottle was used.

Cylindrical electrodes were fixed into Teflon (PTFE) supports for mechanical and electrical connection to the rotating device.

The electrolytic cell is composed of three electrodes according to a standard geometry and is provided with thermal coating. The three-electrode geometry varied as a function of the studied systems. Thus, there were employed discs of aluminum (disc of *2.07 mm*) or steel (disc of *2.6 mm*) as working electrode, a saturated calomel electrode as reference electrode, and a platinum electrode as counter-electrode. A volume of *30 mL* of electrolyte solution was used in the experimental investigations [21-23].

During the preliminary experiments it was found that the voltammograms of the investigated systems are highly reproducible.

ACKNOWLEDGMENTS

This work was supported by CNCSIS-UEFISCSU, PN II-RU No. 52/2010, COD 44.

REFERENCES

1. X.M. Chen, G.H. Chen, P.L. Yue, *Chemical Engineering Science*, **2002**, *57*, 2449.
2. P.K. Holt, G.W. Barton, M. Wark, C.A. Mitchell, *Colloids and Surfaces A: Physicochemical and Engineering Aspects*, **2002**, *211*, 233.
3. P.K. Holt, G.W. Barton, C.A. Mitchell, “6th World Congress of Chemical Engineering”, Conference Media CD (paper 518), Melbourne, Australia, **2001**, p. 518.
4. P. Canizares, M. Carmona, J. Lobato, F. Martinez, M.A. Rodrigo, *Industrial & Engineering Chemistry Research*, **2005**, *44*, 4178.
5. P. Canizares, F. Martınez, C. Jimenez, J. Lobato, M.A. Rodrigo, *Industrial & Engineering Chemistry Research*, **2006**, *45*, 8749.
6. P. Canizares, C. Jimenez, F. Martınez, C. Saez, M.A. Rodrigo, *Industrial & Engineering Chemistry Research*, **2007**, *46*, 6189.
7. M.Y.A. Mollah, P. Morkovsky, J.A.G. Gomes, M. Kesmez, J. Parga, D.L. Cocke, *Journal of Hazardous Materials*, **2004**, *114*, 199.
8. C. Noubactep, A. Schoner, *Journal of Hazardous Materials*, **2010**, *175*, 1075.
9. G. Mouedhen, M. Feki, M. de Petris Wery, H.F. Ayedi, *Journal of Hazardous Materials*, **2008**, *150*, 124.

10. M.S. Secula, I. Cretescu, S. Petrescu, *Desalination*, **2011**, *277*, 227.
11. R. Stefec, “Corrosion data from polarization measurements”, Ellis Horwood, New York, **1990**.
12. T. Visan, “Electrochimie şi coroziune pentru doctoranzii” ELCOR, vol. 1, Printech, Bucureşti, **2002**.
13. M. Stern, A.L. Geary, *Journal of the Electrochemical Society*, **1957**, *104*, 559.
14. H. Uhlig, “Corrosion and Corrosion Control”, John Wiley&Sons Inc., New York, **1971**.
15. F. Mansfeld, “The polarization resistance technique for measuring corrosion currents, Advances in Corrosion Science and Technology”, vol. VI, Plenum Press, New York, **1976**.
16. M. Stern, *Corrosion*, **1958**, *14*, 440.
17. J.M. West, “Basic corrosion and oxidation”, Ellis Horwood, New York, **1990**.
18. S. Petrescu, M.S. Secula, *Revista de Chimie*, **2005**, *56*, 977.
19. D.D. Macdonald, *Journal of the Electrochemical Society*, **1978**, *125*, 1443.
20. J.C. Donini, J. Kan, J. Szynkarczuk, T.A. Hassan, K.L. Kar, *Canadian Journal of Chemical Engineering*, **1994**, *72*, 1007.
21. S. Petrescu, M.S. Secula, I. Cretescu, Gh. Nemtoi, *Revista de Chimie*, **2009**, *60*, 462.
22. Gh. Nemtoi, M.S. Secula, I. Cretescu, S. Petrescu, *Revue Roumaine de Chimie*, **2007**, *52*, 655.
23. Gh. Nemtoi, M.S. Secula, I. Cretescu, S. Petrescu, *Revista de Chimie*, **2007**, *55*, 1216.

STUDIA UBB CHEMIA, LVII, 3, 2012 (p. 237 – 240)
(RECOMMENDED CITATION)

HOMEOSTASIS OF THE MATERNO-FETAL COMPLEX OF EXPERIMENTAL ANIMALS AFTER ETHANOL ADMINISTRATION. NOTE I. LIPID HOMEOSTASIS

ZENO GÂRBAN[1], PETRU-ROBERT VELCIOV[2], GABRIELA GÂRBAN[3], GEORGE-DANIEL GHIBU[1] , ELISABETA MITROI[1], CARMEN BĂRBAT[4]

ABSTRACT. Blood samples collected from pregnant Wistar strain rats randomized in three groups (C – control, E_1 – consumed 20% ethanol ad libitum in the drinking water during pregnancy for 20 days, E_2 – received 20 % ethanol ad libitum in the drinking water 20 days before pregnancy and for 20 days during pregnancy) reveal differences in serum total cholesterol, HDL-cholesterol, LDL-cholesterol and triacyglycerols, in the order E_2>E_1>C. These results differ from those obtained in our previous experiments where ethanol was directly injected into the animals.

Keywords: *ethanol consumption - Wistar rats; pregnancy - lipid biomarkers*

INTRODUCTION

Chronic ethanol consumption has complex influences on metabolism. Experimental animal models have offered valuable insight in this respect [1 - 5]. In animals ethanol is first oxidized to acetaldehyde via three different pathways, and then further oxidized to acetic acid by aldehyde dehydrogenase – AlDH [3]. At low ethanol intake, acetaldehyde is produced by alcohol dehydrogenase (ADH) and nicotinamide adenine dinucleotide, NAD^+, in the cytosol and mithocondria of hepatic cells. With larger amounts of ethanol, acetaldehyde production is taken over by NADPH and H_2O_2 or O_2. Here, we follow up on previous studies on the effects of alcohol upon the organism causing the alcohol embryo- and fetopathy [6 - 10].Our investigations pursue the evaluation of the biochemical homeostasis status of lipid metabolites after chronic ad libitum alcohol administration in pregnant Wistar strain rats. This first note presents results on biomarkers of lipid homeostasis.

[1] *Department of Biochemistry and Molecular Biology, Faculty of Food Products Techology, University of Agricultural Science and Veterinary Medicine Timişoara, Calea Aradului Nr. 119, RO-300657, Timişoara, Romania. E-mail: zeno.garban@yahoo.com*
[2] *Faculty of Chemistry and Environmental Engineering, University Politehnica Timişoara, Pta Victoriei, Nr.2, RO-300006 Timişoara, Romania*
[3] *Laboratory of Environment and Nutrition, National Institute of Public Health – Branch Timişoara, Blvd. Dr. V. Babeş Nr. 16, RO-300226 Timişoara, Romania*
[4] *Faculty of Sociology and Psychology, West University of Timişoara, Blvd. Vasile Pârvan Nr.4, RO-300223 Timişoara, Romania*

RESULTS AND DISCUSSION

Table 1 shows a synopsis of the animal model used in this research (cf. Experimental section). Serum concentrations were determined for total-cholesterol (T-C), high density lipoprotein-cholesterol (HDL-C), and triacylglycerols (TAG); the values of serum low density lipoprotein-cholesterol (LDL-C) were obtained using the Friedewald equation, cf. [11]. These are considered as biochemical markers of lipid metabolism [12 - 14].

Table 1. Synopsis of the animal experimental model

Grp	No. anim	Admin. subst.	Conc (%)	Adm. way	Quan-tity	Period of admin (days)	
						before pregnancy	pregnancy
C	8	tap water	-	per os	ad libitum	-	-
E_1	8	ethanol	20			-	20
E_2	8	ethanol	20			20	20

Table 2 shows that, in good agreement with previous literature data [15, 16], serum T-C, LDL-C and HDL-C were increased in both experimental groups (E_1 and E_2). For E_2 the individual values show a more remarkable variation, perceptible by the SD values. While HDL-C is considered a beneficial lipoprotein, as its large particles can remove cholesterol from atheroma and have a negative effect on the development of fatty liver., elevated LDL-C is known to promote atheroma formation on the arteries walls, a principal cause of cardiovascular diseases. [14, 17, 18]

Table 2. Concentrations of lipid biomarkers from the class of sterols

Group	No. anim	T-C (mg/dL) X ± SD	HDL-C (mg/dL) X ± SD	LDL-C (mg/dL) X ± SD
C	8	92.71± 8.27	36.14 ± 2.94	44.99 ± 4.17
E_1	8	103.83± 3.45**	39.61±5.88***	48.13±6.82***
ΔX_1		+ 11.12	+ 3.47	+ 3.14
E_2	8	114.86±11.34**	43.52 ± 4.19**	52.88 ± 5.09**
ΔX_2		+ 22.15	+ 7.38	+ 7.89

* statistically significant : ** $P < 0.01$; *** $P < 0.05$

Table 3. Concentrations of triacylglycerols

Group	No. anim	TAG (mg/dL) X ± SD
C	8	57.86 ± 6.12
E_1	8	80.41 ± 9.42**
ΔX_1		+ 22.55
E_2	8	92.28 ± 8.06*
ΔX_2		+ 34.42

* Significancy : * P < 0.001; ** P< 0.01

Values for triacylglycerols (TAG), as specific biomarkers for lipid metabolism, are presented in Table 3. E_1 showed an elevation by 38% and E_2 by 59%, in qualitative agreement with previous literature data [5, 19-21]. While serum TAG result mostly from dietary glycerides, ethanol increases the endogenous production of TAG, as liver cells eliminate the excess hydrogen formed from the breakdown of alcohol by utilizing it to form alpha-glycerophosphates and fatty acids.

CONCLUSIONS

Chronic ethanol consumption by pregnant female rats induces dyshomeostatic effects characterized by increases in total cholesterol, its lipoprotein derivatives HDL-C and LDL-C, and triacylglycerols (TAG). The effects are more notable in group E_2 (i.e., a longer period of consumption). Notably, these data differ from our own previous reports where alcohol was administered by injection,[3.6,7] as opposed to the ad libitum oral route followed here - an important methodological observation, that affects the meaningfulness of ethanol-related studies in animals.

EXPERIMENTAL SECTION

*A*nimals were randomly divided in one control (C) and two experimental groups (E_1 and E_2). Each group included 8 animals with an average body weight of 200 ± 20 g. Ethanol with a concentration of 20% in drinking water was provided ad libitum to animals of group E_1 during pregnancy. The same concentration of ethanol was provided 20 days before pregnancy and 20 days during pregnancy to the animals of group E_2 On the 20^{th} day of pregnancy all the animals were euthanized after ketanest anaesthesia. After laparotomy blood samples were obtained by puncture of vena cava caudalis and collected in clean non-heparinized centrifuge tubes. Blood was allowed to coagulate and the tubes were centrifuged for serum separation. Analytical determinations were made by using a LABSYSTEM-901 analyzer and specific Clinilab reagents. The method of Fossatti and Prencipe [22] was used for triacyglycerols and the method of Allain et al. [23] for total cholesterol determination. HDL-cholesterol were determined by the enzymatic method elaborated by Burnstein at al. [24] and perfected by Lopez-Virella et al. [25]. Spectrophotometric measurements were made at 505 nm. Values of LDL-C were calculated [29] according to the equation: LDL-C = T-C – [(HDL-C) – (TAG/5)]. Results are expressed as means (X) and standard deviation (SD) and the statistical significance as the *t* test was used as appropriate.

REFERENCES

1. G. Obe, H. Ristow, *Mutation Res*earch, **1979**, *65*, 229.
2. R. Sanchis, M. Sancho-Tello, M. Chirivella, C. Guerri, *Teratology*, **1987**, *36*, 199.
3. Z. Gârban, în *"Embrio- şi fetopatia alcoolică"* (Sandor S., Ed.), Editura Academiei Române Bucureşti, **1993**, 139-149.
4. L. Feinman, C.S. Lieber, *The American Journal of Clinical Nutrition*, **1999**, *70*, 791.
5. C.F. Daher, R.N. Berberi, G.M. Baroody, *Food and Chemical Toxicology*, **2003**, *41* (11), 1551.
6. S. Şandor, M. Checiu, I. Fazakas-Todea, Z. Gârban, "Advances in the Bioscience", Vol. 47: Advanced Concepts in Alcoholism (Ed. Tittmar H.G.), Pergamon Press, Oxford, **1984**, 13-43.
7. Z. Gârban, G. Daranyi, I. Borza-Ţeicu, R. Nemeş, V. Precob, *Romanian Journal of Morphology and Embryology,* **1989**, *4*, 289.
8. F. Majewski, "*Handbook of Alcoholism*" (Zernig G., Saria A., Kurz M., O'Malley S. Stephanie, Eds.), C.R.C. Press, Boca Raton, **2000**, 251-267.
9. F. Herrera, M. Llobera, "*Organ-directed toxicity, chemical indices and mechanisms*". IUPAC Pergamon Press, Oxford, **1981**, 11-83.
10. A. Raj, K.V. Praveen, Varghese Sheeba, J.K. Mukkadan, P.K. Joseph, *Indian Journal of Experimental Biology,* **2009**, *47*, 333.
11. W.T. Friedewald, R.I. Levy, D.S. Fredrickson, *Clin. Chem.*, **1972**, *18*, 499.
12. I. Mincu, N. Hâncu, *Dislipidemiile. Lipidologie clinică*, Ed. Medicală, Bucureşti, **1976**.
13. L.A. Kaplan, A.J. Pesce, C.S. Kazmierczak, C*linical Chemistry: Theory, analysis and correlation*, 4th ed., C.V. Mosby Comp., St. Louis, **2002**.
14. Margaret Sozio, D.W. Crabb, *American Journal of Physiology, Endocrinology and Metabolism*, **2008**, *295*, E10.
15. J.B. LaBorde, K.S. Wall, B. Bolon, T.S. Kumpe, R. Patton, Q. Zheng, R. Kodell, J.F. Young, *Laboratory Animals*, **1999**, *33*, 275.
16. Luisa M. Ojeda, M.J. Delgado-Villa, Ruth Llopis, Luisa M. Murillo, Olimpia Carreras, *Alcohol and Alcoholism*, **2008**, *43* (5), 544.
17. S.B. Hulley, S. Gorden, *Circulation,* **1981**, *64*, 57.
18. A. Lucas, B.A. Baker, M. Desai, C.N. Hales, *British Journal of Nutrition*, **1996**, *76*, 605.
19. J.S. Pennington, T.I. Shuvaeva, S.N. Pennington, *Alcohol Clinicial and Experimental Res*earch, **2002**, *26*, 848.
20. P.-R. Velciov, Gabriela Garban, Elisabeta-Mihaela Mitroi, Ada Gruescu, *"Proceedings of the 16th Symposium on Analytical and Environmental Problems"* (Ed. Galbács Z.), Publ. by SZAB, Szeged, **2009**, 195-197.
21. Gabriela Garban, P.-R. Velciov, Ariana-Bianca Velciov, "*Proceedings of the 17th Symposium on Analytical and Environmental Problems*" (Ed. Galbács Z.), Publ. by SZAB, Szeged, **2011**, 219-222.
22. P. Fossati, L. Prencipe, *Clinical Chem*istry, **1982**, *28*, 2077.
23. C.C. Allain, Lucy S. Poon, C.S. Chan, W. Richmond, P.C. Fu, *Clinical Chem*istry, **1974**, *20*, 470.
24. M. Burnstein, H.R. Scholnick, R. Morfin, *Journal of Lipid Res*earch, **1970**, *11*, 583.
25. M.F. Lopes-Virella, *Clinical Chem*istry, **1977**, *23*, 882.

STUDIA UBB CHEMIA, LVII, 3, 2012 (p. 241 – 248)
(RECOMMENDED CITATION)

CHARACTERIZATION OF HINDERED SETTLING IN CONCENTRATED SOLID-LIQUID SUSPENSIONS

ADINA GHIRIŞAN[1], SIMION DRĂGAN[1]

ABSTRACT. In order to characterize the hindered effect which appears by sedimentation of concentrated suspensions new experiments with quartz sand having equivalent size d_{90} = 170 μm and concentration 10 – 30 %, in volume, in ethylene glycol and aqueous solutions carboxymethylcellulose (CMC) 0.5%, 1.0%, in weight, were carried out. The drag coefficient, C_D, as a parameter which quantifies the hindered effect, was calculated with particle terminal settling velocity. The hindered settling velocities predicted by Richardson-Zaki's equation were founded comparable with experimental results.

Keywords: *drag coefficient, particle terminal settling velocity, hindered settling velocity, Richardson-Zaki's equation, sedimentation exponent*.

INTRODUCTION

By interacting surfaces in relative motion, as in the case of a moving solid object through a surrounding fluid or a moving fluid which flows on a solid, appears the friction. In many practical applications it is need to know the fluid dynamic drag (friction) on solid particles in process equipments (e.g., slurry pipelines, fixed and fluidized beds).

In settling processes, the fluid drag generated by the moving of solid particles in suspending liquid influences the particle terminal settling velocity. There are two components which define the fluid drag force, F_D, on a moving particle: the skin friction or viscous drag (due to viscous friction) and the form drag (due to the boundary layer separation in the wake of the particle movement).

The fluid drag force is often expressed by the dimensionless friction factor or drag coefficient C_D [1]:

$$\mathbf{C_D} = \frac{\mathbf{F_D}}{\left(\frac{1}{2}\boldsymbol{\rho}\mathbf{w}^2\right)\left(\frac{\boldsymbol{\pi}\mathbf{d}^2}{4}\right)} \tag{1}$$

where: ρ is the disperse liquid density (kg/m^3), w – the particle settling velocity (m/s) and d - the diameter of the solid particle (m).

[1] *Universitatea Babeş-Bolyai, Facultatea de Chimie şi Inginerie Chimică, Str. Kogălniceanu Nr. 1, RO-400084 Cluj-Napoca,Romania, ghirisan@chem.ubbcluj.ro*

Experimental measurements and dimensional analysis have lead to the conclusion that the moving sphere in a Newtonian fluid shows a dependence of drag coefficient on particle Reynolds number Re [2], as:

$$\mathbf{C_D} = \frac{24}{\mathrm{Re}} \tag{2}$$

in Stokes regime Re < 1 (0,2);

$$\mathbf{C_D} = \frac{18.5}{\mathrm{Re}^{0.6}} \tag{3}$$

in Allen regime: 1 < Re < 10^3; and

$$\mathbf{C_D} = 0.44 \tag{4}$$

in Newton regime: 10^3 < Re < $10^{5;}$

The particle Reynolds number is defined for Newtonian and Non-Newtonian fluids as equations (5) and (6) show [1]:

$$\mathrm{Re} = \frac{\boldsymbol{\rho} \cdot \mathbf{w_S} \cdot \mathbf{d}}{\boldsymbol{\eta}} \tag{5}$$

$$\mathrm{Re} = \frac{\boldsymbol{\rho} \cdot \mathbf{w_s^{2-n}} \cdot \mathbf{d^n}}{\mathbf{k}} \tag{6}$$

where: w_S is the terminal particle velocity for Newtonian or non-Newtonian (power-law) fluids (m/s), d - the average particle size (m), ρ - the disperse fluid density (kg/m^3), η - the viscosity of Newtonian liquid (Pa·s), *k* – the fluid consistency coefficient (Pa·s^n), *n* – the flow behavior index (-).

Dimensional analysis applied to the moving sphere in a Non-Newtonian fluid shows the dependence of drag coefficient on particle Reynolds number and on power-index [1]:

$$\mathbf{C_D} = \mathbf{f}(\mathrm{Re}, \mathbf{n}) \tag{7}$$

In creeping flow region (Re << 1) the numerical results shows that the drag coefficient obtained from Stokes' law may be expressed using a deviation factor, X(n) [1]:

$$\mathbf{C_D} = \frac{24}{\mathrm{Re}} \mathbf{X}(\mathbf{n}) \tag{8}$$

The numerical values of X(n) show that: shear-thinning causes drag increase X(n) > 1, and shear-thickening causes drag reduction X(n) < 1.

Relationship between drag coefficient and particle Reynolds number can be used in characterization of particle motion in suspending liquid (frequently, the liquid phase may exhibit complex non-Newtonian behavior) and in determination of particle terminal velocity, important parameter in pipeline design for slurry transport.

In the present study, in order to characterize the hindered effect which appears in settling of concentrated suspensions, the drag coefficient was calculated considering the single particle terminal velocity obtained from experimental data.

Hindered settling velocity of particles in concentrated suspension (called also zone settling or mass settling) experimentally determined by the height of descending interface between suspension and the clear liquid followed in time was compared with the Richardson and Zaki predicted values.

In agreement with the equation of Richardson and Zaki [3] (equation 9), the most used expression of hindered settling velocity, the particle settling was graphically determined by extrapolation of the velocity to the voidage equal 1:

$$\mathbf{w(c) = w_S\left(1 - C_v\right)^z = w_S \cdot \varepsilon^z} \tag{9}$$

where: *w(c)* is the hindered settling velocity (m/s), w_S - the single particle terminal settling velocity (m/s), C_v - the solid volume concentration (m^3/m^3), ε - the voidage or void fraction (m^3/m^3) and z – the sedimentation exponent (-).

Comparative to the single particle terminal settling velocity, graphically determined by extrapolation of yielded straight line log (w_{exp}) versus log (ε), by numerical simulation the terminal settling velocity of a spherical particle in Newtonian fluids, in creeping regime (Re_t < 2), can be evaluated by Stokes' equation:

$$\mathbf{w_s = \frac{g \cdot d^2(\rho_s - \rho)}{18 \cdot \eta}} \tag{10}$$

where: d is the equivalent particle size of particles (m), ρ_s – the solid density (kg/m^3), ρ - the disperse fluid density (kg/m^3), η - the fluid viscosity (Pa·s), g - the gravitational acceleration (m/s^2).

The theoretical terminal settling velocity of a particle in non-Newtonian fluids following power-law is estimated by equation (11) [1]:

$$\mathbf{w_s = \frac{g \cdot d^{n+1}(\rho_s - \rho)^{1/n}}{18 \cdot k \cdot X(n)}} \tag{11}$$

where: k is the fluid consistency coefficient ($Pa \cdot s^n$), *X(n)* - the deviation factor, a function of flow index n.

As equations (1) – (11) show the settling behavior of particles, in sedimentation processes of solid-liquid suspensions, is influenced by: size and density of particles, the presence of other neighboring particles in concentrated suspensions; and rheological parameters of suspending liquid.

The literature data show that the variation of sedimentation velocity with concentration for non-spherical particles is similar to the behavior of spherical particles [4].

RESULTS AND DISCUSSION

Experimental hindered settling velocities

Gravity sedimentation, a simple and direct method, is used in the present work in order to characterize experimentally the particles settling. The method is based on measure the descendent solid-liquid interface as a function of time, as describe previously [5].

As in the case of sedimentation quartz sand in 0.5% CMC and 1.0 % CMC solutions, the hindered settling velocities in ethylene glycol is determined by sedimentation curves, considering concentrated suspensions (volume concentration C_v between 10 and 30 %, Figure 1).

The incipient hindered settling velocities calculated show clearly the decrease of velocities with the increase of solid particle concentration.

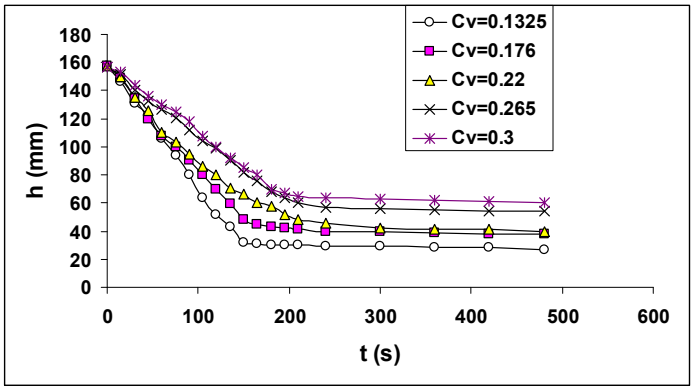

Figure 1. Sedimentation curves of quartz sand in ethylene glycol.

Single particle terminal settling velocity $w_{s(ex)}$ is determined by extrapolation to the voidage equal 1, when equation (9) is plotted on logarithmic coordinate (Figure 2). The obtained values are shown in Table 1.

As the slope of straight lines yielded in Figure 1 shows, the sedimentation exponent *z* determined by experimental data is comparable with Richardson-Zaki value (*z*=4.65).

Theoretical particle Stokes settling velocities $w_{S(s)}$ is calculated by Stokes' equation (10) or (11) for the equivalent size particle of d_{90} = 170 μm, and the liquid density and viscosity, or the rheological parameters *k* and *n* of suspending liquid shown in Table 1. The rheological parameters considered in the present work are from literature [6].

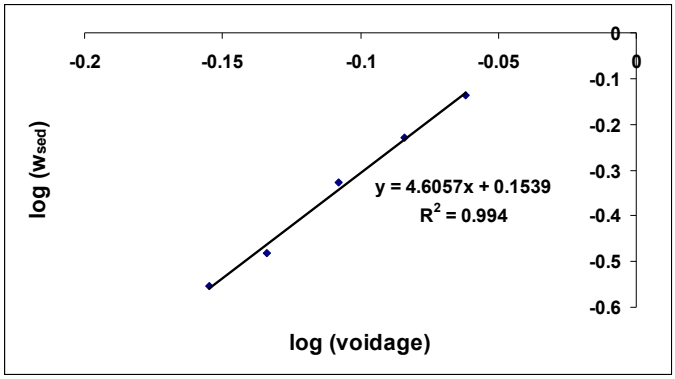

a.

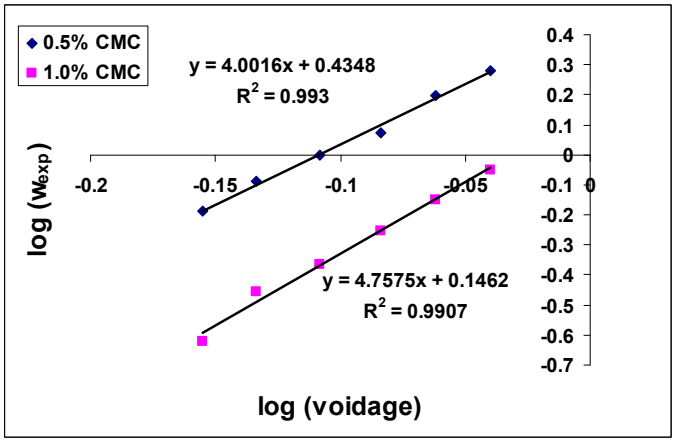

b.

Figure 2. Log-log plot of experimental settling velocity and voidage in ethylene glycol (a) and in CMC solutions (b).

The ration between $w_{S(s)}$ and $w_{S(ex)}$ varies from 0.98 to 1.26. If in the case of ethylene glycol, a typical Newtonian liquid, and 0.5 % CMC the values are comparable, in the case of 1.0 % CMC, a typical shear-thinning liquid [7], the predicted value showing a clear influence of rheological parameters, is larger that those determined by experimental data (see Table 1).

All particle Reynolds numbers calculated by equation (5) or (6) with corrected particle velocity $w_{S(ex)}$ are smaller than 1, which indicates particle terminal settling in a creeping regime, as it was considered.

The calculated drag coefficient shows comparable values in the case of sedimentation of quartz sand in ethylene glycol and 0.5 % CMC, and a higher value in 1.0 % CMC, as is expected for shear-thinning fluids.

The theoretical hindered settling velocities predicted by Richardson and Zaki's equation, noted $\mathbf{w_{t1}}$ when theoretical Stokes' velocity $\mathbf{w_{S(s)}}$ and $\mathbf{w_{t2}}$ when single particle terminal velocity $\mathbf{w_{S(ex)}}$ is used, are compared with experimental hindered settling velocities as a function of voidage in Figure 3.

Table 1. Comparison of single particle terminal velocity using experimental data and Stokes' equation

Suspending medium	Liquid parameters	$w_{S(ex)}$ (extrapolation) (mm/s)	$w_{S(s)}$ (Stokes' equation) (mm/s)	Re_t	C_D
Ethylene glycol	ρ=1112 (kg/m^3) η=16.1 (mPa·s)	1.425	1.50	0.0167	1437
0.5 % CMC	ρ=1002 (kg/m^3) k=29.275(mPa·s) n=0.9295	2.70	2.61	0.0191	1382
1.0 % CMC	ρ=1002 (kg/m^3) k=110.76(mPa·s) n=0.871	1.40	1.77	0.0028	10276

It can be seen a good correlation between experimental and predicted settling velocities when ethylene glycol was used as suspending liquid and some differences for the other two cases.

In the same time, an improving of theoretical Richardson-Zaki's prediction was observed in the present study comparative with the previous, due to the new rheological parameters and appropriate equivalent particle size considered.

The difference which appears between experimental and theoretical hindered settling velocities in the case of quartz sand sedimentation in 1.0 % CMC seems to by caused by the rheological behavior of CMC solution as a shear-thinning liquid (see Table 1), which generally induces particle aggregation.

The larger value of drag coefficient in the case of 1.0 % CMC indicating a higher friction between particles and suspending liquid causes a higher hindered effect and induces smaller hindered settling velocities, as experimental data show.

CONCLUSIONS

The particles settling in hindered regime in the case of quartz sand suspensions in ethylene glycol, 0.5 % CMC and 1.0 % CMC was experimentally determined.

The single particle terminal settling velocity w_S was determined by extrapolation of the experimental velocity to voidage equal 1 and by numerical prediction using Stokes' equation.

An improving of theoretical hindered settling velocities in non-Newtonian fluids was obtained reconsidering the new values of rheological parameters necessary to determine the particle terminal settling velocity by Stokes' law.

The hindered settling velocity can be predicted by Richardson-Zaki's equation, considering an appropriate value for the sedimentation exponent z.

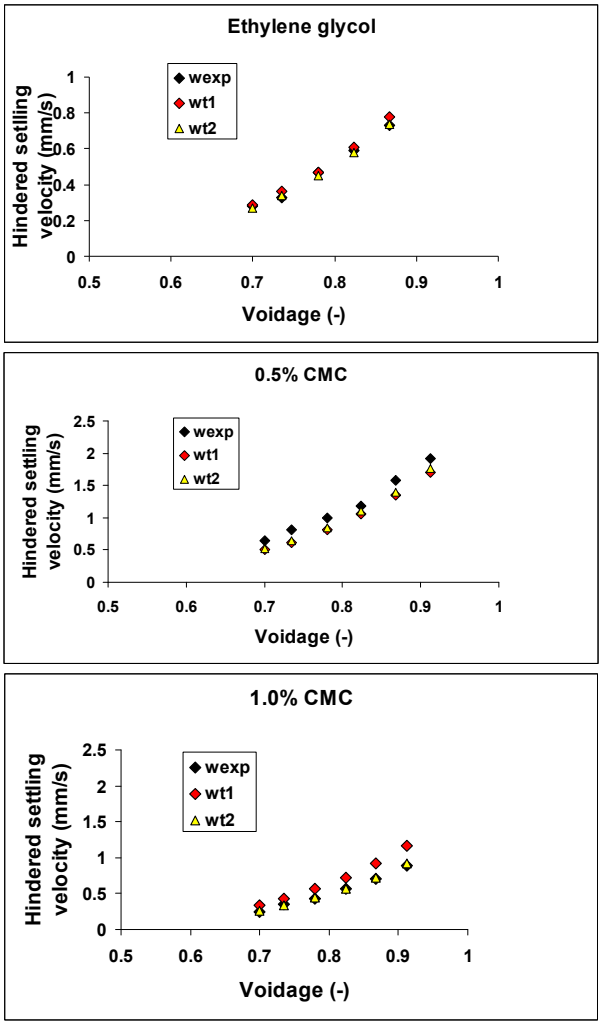

Figure 5. Experimental and theoretical hindered settling velocities vs. voidage.

The hindered effect on settling behavior was analyzed considering the drag coefficient. The drag coefficient and the hindered effect was higher in 1.0 % CMC, as for a shear-thinning fluid is expected.

EXPERIMENTAL SECTION

To get the particle size of sand quartz used for the experimental measurements, first a very narrow fraction of raw sand was prepared by sieving, and the sieve range 200 μm < d < 180 μm was removed. Sieve range refers to the range between material passing through 200 μm and retained on 180 μm. The separated fraction was than analyzed by wet sieving using the sieve series of 180, 163, 125, 90 and 71 μm, and compared with the analyze resulted using the Andreasen pipette which evaluated the particle settling velocities. By wet sieving and by sedimentation using the Andreasen pipette was determined the equivalent size of particle d_{90} =170 μm.

Experimental settling velocities were determined by collected data from batch settling tests. The suspensions with volume concentration between 10 % and 30 % have shown net sedimentation front during the whole settling process. The experimental runs were carried out in cylinders with internal diameter of 28 mm and 300 mm tall.

Prior each settling experiment, the blends were strongly mixed by shaking, directly in the cylinder were the tests are done, in order to obtain a well dispersed initial state. After mixing, the cylinder was allowed to stand, and the height of quartz sand was noted at regular intervals until no further sedimentation occurs. The boundary between the settling suspension and the supernatant phase were determined visually for each sample, as a function of time in order to establish the sedimentation curves. Each experiment was performed in triplicates.

REFERENCES

1. R.P. Chhabra, J.F. Richardson, "Non-Newtonian Flow in Process Industries. Fundamentals and Engineering Applications", Butterworth-Heinemann, Linacre House, Jordan Hill, Oxford OX2 8DP, **1999**.
2. R.B. Bird, W.E. Stewart, E.N. Lighfoot, "Transport Phenomena", 2nd edition, John Wiley & Sons Inc., New York, **2002**.
3. J.F. Richardson, W.N. Zaki, *Trans. Inst. Chem. Engrs.*, **1954**, *32*, 35.
4. R. Di Felice, R. Kehlenbeck, *Chem. Eng. Technol.*, **2000**, 23, 1123.
5. A. Ghirişan, S. Drăgan, *Studia UBB Chemia,* **2011**, *LVI*(2), 115.
6. M.A. Cancela, E. Alvarez, R. Maceiras, *Journal of Food*, **2005**, *71*(4), 419.
7. T.G. Mezger, "The Rheology Handbook", 2nd revised edition, Vincentz Network GmbH &Co. KG, Hannover, **2006**.

STUDIA UBB CHEMIA, LVII, 3, 2012 (p. 249 – 258)
(RECOMMENDED CITATION)

ASPECTS OF SUSTAINABLE DEVELOPMENT: FLY ASH DEPOSITS, BIOSOLIDS, CONTAMINATED BIOMASS

SMARANDA MASU[1], GEORGETA BURTICA[2], NICOLETA LUMINITA JURJ[2], MARIANA ALBULESCU[3, *]

ABSTRACT. Nowadays, barren and inert fly ash deposits result from power plants operating on fossil coal and occupy large areas of land. They change the landscape, altering ecosystems and dispersing pollutants by precipitations and deflations. On the other hand, from wastewater treatment results sludge waste (biosolids) rich in nutrients. Biosolids are fertilizers with many nutrients and could be recycled to improve soil productivity and stimulate plant growth. A solution was found for the capitalization of two wastes - biosolids and fly ash, both resulting in the same city, Timisoara, Romania. The use of biosolids in fly ash fertilization provides rapid efficiency in topsoil for plant growth. Plant species were chosen considering the possibilities to restrict the metal access in plants, *i.e. Lolium perenne* species*,* with reduced harvest, recycled as fodder or, on the contrary, to stimulate accumulation of metals *i.e. Onobrychis viciifolia* species*,* with increased harvest, but potentially toxic biomass, processes evidenced by a specific parameter, the coefficient of translocation. Pilot experiments was done in four versions, each in three replicates in a randomized block. The treatment were control and fertilized variant fot each plant species. The new crop installed presents characteristics depending on plant species: with accumulation of metals, i.e. Cr, Cu, Ni, in the shoots, such as in leguminous *Onobrychis viciifolia* species, resulting vegetation with waste regime. with smaller accumulations of heavy metals, such of grass *Lolium perenne,* with recycling possibilities in agro-zoo technical field.

Keywords: *biosolids, fly ash deposits, heavy metal bioavailability, Lolium perenne, Onobrychis viciifolia.*

INTRODUCTION

Thermal power plants operating on coal are the main sources of energy worldwide. Coal combustion produces solid residues resulting from the non-combustible fraction. Physical and chemical characteristics of residues are determined by the nature of coal used in combustion, by operating conditions and post combustion conditions [1-3]. Coal combustion leads to the formation in

[1] *National Research and Development Institute for Industrial Ecology- ECOIND, P-ta Regina Maria no.1 et 2, RO-300004, Timisoara, Romania*
[2] *"Politehnica" University of Timisoara, P-ta Victoriei no. 2, RO-300006, Timisoara, Romania*
[3] *West University of Timisoara, Pestalozzi no. 16, RO-300115, Timişoara, Romania*
[*] *E-mail: Malbulescu@yahoo.com*

time of huge wastes in the open - fly ash deposits. In coal combustion, about 70÷75% of the obtained fly ash is stored either on specially designated landfill (deposits) or in natural depressions [1,4]. These sites are devoid of vegetation, have the appearance of a deserted area and have the potential of spreading material in the form of fine particles in the atmosphere and/or soil, leaching, water percolation etc. [5-6]. Some stabilization/ remediation strategies using plant were developed. The process is simple, but several necessarily stages are required [7-11]. From municipal wastewater plants, results in large quantities, another waste material - the sewage sludge (biosolids), with high nutrient content. The disadvantages of biosolids use are due to smell, potential disease risk to humans or animals that are consumers of products/food from treated fields. Municipal sludge is stabilized (higienically) by one or more controlled processes, aerobic, anaerobic, liming, etc., to reduce pathogens and to remove the vectors drawn here: flies, rodents, birds etc. [12-13]. The literature reports that these biosolids may have an average content in nitrogen between 1 and 6%: low N content (1÷3% N), or high N content (3÷6% N) (while the manure contains 1.2÷4% N) and 1.5 P% (while the manure contains 0.3÷3.3%) [12]. The biosolids contain also other useful microelements like Fe, Mn, S, Ca, Mg, K, etc. [13-15]. Biosolids can be used in fertilizing forests, contaminated soil for phyto-remediation of the sterile materials deposits. Upper inert fly ash deposits are treated in advance to ensure a minimum nutrient, needed for the installation of healthy vegetation [15-19].

The aim of the study is to form on fly ash deposits a plant layer for particulate matter stabilization and furthermore for ecological restoration, by choosing proper plant species that generate biomass with recycling possibilities. Fly ash deposits of Timisoara, Romania, occupy hundreds of hectares of land with a moon aspect and with high risk of deflation, erosion, and leaching of stored material The whole process involves the use of another waste, available in large quantities, the municipal sludge. Also, from the Timisoara municipal water treatment plant, three tons of municipal sludge with 20% dries matter, or 12 tons with 5% dry matter result daily. Until now, for the two types of waste there is no sustainable management for recovery or ecological integration in the environment. In this paper we performed a research to integrate in the upper layers of fly ash deposits a pre-determined quantity of semi liquid biosolids for phytostabilization/phytoremediation of inert waste. The choices of plant species for this study were made either to lead to high biomass yields with metals bioaccumulated into, *i.e.* leguminous *Onobrychis viciifolia,* or to obtain reduced biomass including low quantities of metals, *i.e. Lolium perenne*. Pilot experiments was done in four versions, each in three replicates in a randomized block. The treatment were control and fertilized variant fot each plant species.

MATERIALS AND METHODS

Fly ash samples and biosolids analysis was done to determine the metal concentrations to according with the Romanian standardized methodology. 5g soil samples analysis (in triplicate) was done to determine the metals concentrations. Metals were extracted from the soil samples by heating with Aqua Regia for 2hrs, at reflux. After interrupting the heat, the system was left in stand-by for 16 hrs. Then the samples were diluted in a calibrated flask with deionized water to 50 ml. Plant sampling was done in agreement with the Romanian standardized methodology. Plant tissues were thoroughly washed with de ionized water to remove any soil particles attached to plant surfaces. 5g plant tissues were dried (105°C) to constant weight. Plant samples with precise weight are then brought to 550°C; to the residual materials 5ml of concentrated hydrochloric acid are added, samples are maintained 30 minutes on the dry sand bath. After filtering those in a paper filter with small porosity (type 640de Mackerel-Nagel Germany), were taken to a calibrated flask (25 mL) with hydrochloric acid 1:1 solution. Plant and soil extracts analysis was done using a spectrophotometer, Avanta AAS. The detection limit of the device for Cr, Cu, Fe, Mn, and Zn is of 0.05mg/L, for Ni is of 0.10 mg/L, for Pb is of 0.20 mg/L. The following were determined according to Romanian current laws: pH, DM, N_{Total} and P. The vegetation degree of coverage is established by Braun-Blanquet scale [18]. For in time monitoring of the metal bioaccumulation in the aerial parts of plants and the level of metals in upper layer of fly ash deposit, we analyzed: [18, 20-22]: 1. The amount of metals accumulated in aerial plant tissue, 2. The coefficient of metal translocation from roots to shoot of plants TC = Q_S/Q_R, where: Q_S - metal amount in the aerial tissue (mg/ kg D.M.), Q_R - amount of metal in roots (mg/ kg D.M.).

RESULTS AND DISCUSSION

1. Strategy research on experimental parcels

The study is carried out on four different experiments: 1. Non-treated fly ash parcel seeded with *Lolium perenne* grass species (C1); 2. Non-treated parcel fly ash seeded with *Onobrychis viciifolia* species (C2); 3. Fly ash parcel fertilized with municipal sludge (25 to/ha DM) and seeded with *Lolium perenne* grass species (C3); 4. Fly ash parcel fertilized with municipal sludge (25 to/ha DM) and seeded with *Onobrychis viciifolia* leguminous species (C4). The experimental parcels are randomized in an experimental block area. Each experimental parcel is carried out in triplicates. The area of each experimental parcel was 10 m^2. Agricultural work is done with ordinary farm equipment to prepare the experimental parcels for sowing, fertilization, and for plants harvesting. Was initiated and maintained a plant cover of grasses and leguminous species adapted to excessive drought conditions.

Harvesting and management of resulting biomass were done in concordance with their quality indicators.

2. Characterization of fly ash and biosolids

2.1. Fly ash characterization

From fossil coal combustion in power plants of Timisoara city, result the non-combustible fraction, fly ash. A field study was conducted at fly ash deposit during three years to assess the effect of biosolids treatment. Metal content of the upper layer of experimental parcels is presented in Table 1. C1 and C2 parcels correspond to fly ash experimental variants without biosolids and C3 and C4 parcels correspond to fertilized fly ash with organic fertilizer, biosolids. Fly ash has pH = 7.2 and does not contain nutrients, nitrogen and phosphorus; carbon content is present but in non-biodegradable form.

Table 1. Concentration of metals of the upper layer of experimental parcels; Values are means of 3 replicate samples±SE

No	Parcel	* Heavy metal content in the topsoil upper layer [mg/kg D.M.]						
		Cr	Cu	Fe	Mn	Ni	Pb	Zn
1	C1	64.2± 1.1	72.4± 2.5	1,860.0± 20.2	150.0± 3.6	68.6± 2.4	19.6± 3.1	124.0± 2.5
2	C2	93.6± 3.6	77.6± 2.1	1,903.0± 21.9	153.1± 4.4	68.8± 2.2	7.4± 0.4	82.6± 2.1
3	C3	99.0± 2.3	74.2± 2.9	1,878.0± 11.7	150.0± 4.6	54.6± 1.7	28.5± 3.8	122.7± 3.5
4	C4	99.6± 2.4	82.0± 2.0	1,892.0± 12.2	171.2± 4.3	60.1± 1.9	7.3± 0.7	79.5± 1.8

* mean values

2.2. Biosolids characterization

Biosolids result from Timisoara municipal water treatment plant. 25 to/ha D.M. of biosolids, having characteristics presented in Table 2, were used to prepare the fertile layer of vegetation covering the fly ash deposits, in Timisoara's vicinity. Other characteristics of biosolids: humidity= 90±0.5%, organic matter=26.4±0.6%, N_{Total} =2.5±0.2%, P=0.35±0.2%, pH = 7.1±0.3.

Table 2. Heavy metal content of used biosolids. Values are means of 12 samples±SE

Material	*Heavy metal content of used biosolids [mg/kg D.M]							
	Cr_{tot}	Cu	Cd	Fe	Mn	Ni	Pb	Zn
Biosolids	134.7±3.2	333.9±3.5	7.3± 0.1	2,003.7±12.2	75.0 ±1.8	27.4 ±0.3	157.8±12.0	304.6±13.6

* mean values

2.3. *Influence of fly ash with biosolids mixture on the mobilization of metals in parts of plants (roots and shoots)*

Vegetation strategy is selected for plant species leading to large amount of biomass, which contains in mature plants (harvested) bioaccumulated metals, or plant species leading to lower amounts of biomass and, as well, a lower level of accumulation of metals in the aerial parts. Because of the new vegetative cycle after harvesting, the young plants grown on non-treated soil will selectively accumulate metals in tissues, namely in the aerial parts. In Table 3 are presented the surfaces covered with plants and the amount of green mass harvested from cultivated experimental parcels.

Table 3. The biomass quantities and coverage degree based on Braun-Blanquet scale [18]

No	*n	Parcel	Plant species	**Biomass quantity [kg/ha]	Coverage degree (Braun-Blanquet scale)
1	3	C1	*Lolium perenne*	805.0 ±25.1	Level 2 small abundance, limited coverage degree 5-25%;
2	3	C2	*Onobrychis viciifolia*	25.0 ±3.2	Level 1 more individuals, but with small coverage degree under 5%;
3	3	C3	*Lolium perenne*	1,125.0 ±132.5	Level 4 abundant individuals and good coverage degree 50-75%;
4	3	C4	*Onobrychis viciifolia*	11,960.0 ±154.9	Level 4, abundant individuals, good coverage degree 50-75%;

* number of observations,* * mean values

The species *Lolium perenne* covers non-fertilized fly ash layer, C1, at level of coverage 2 on the Braun-Blanquet scale, up to 25%, the sown area. If the fly ash layer is fertilized with biosolids, C3, coverage with plants is higher, reaching level 4 on the Braun-Blanquet scale, but the quantity of biomass harvested from this experimental version is lower, about 1,125.0 kg/ha of green biomass. *Onobrychis viciifolia,* a leguminous species, did not grow on non-fertilized fly ash parcel, C2. Grown plants dry slowly. Fertilization of fly ash experimental parcels with biosolids, C4, determined the growth of a vegetable layer covering over 50% of the the sown area. This layer produced a quantity of plant biomass over 10 times higher than that obtained when grasses *Lolium perenne* was cultivated.

In Tables 4 and 5 are shown the amounts of metal accumulated in plant tissue at maturity (1st harvested biomass in July) and in young plants in the moment of the new vegetative cycle after harvesting.

The two species of plants grown on non fertilized experimental parcels accumulate in their mature phenophase similar amounts of heavy metals i.e.: Cu, Cr, Fe, Ni and Pb. Other hand, *Onobrychis viciifolia* species accumulates two times more Mn and 4 times more Zn versus *Lolium perenne*

species. The addition of organic fertilizer has determined that grass species accumulate lower amounts of metals, Cr, Fe and Zn up to 2 times lower, of Cu up to 4 times lower and Pb up to 12 times, versus the amount that was found in plants grown on untreated fly ash experimental parcel.It can be seen, from Table 4, that depending on the nature of the plant, accumulation of Cu, Fe, Pb, and Ni is 2-3 times higher than the amounts accumulated in mature plants.

Table 4. Metal content, in harvested biomass, mg/kg D.M.

* n	Parcel	Plant species	* * Metal content in (1st harvested biomass in July) [mg/kg D.M.]						
			Cr	Cu	Fe	Mn	Ni	Pb	Zn
3	C1	***Lolium perenne***	3.5 ±0.6	1.9 ±0.5	377.9 ±13.8	13.9 ±0.5	1.8 ±0.3	1.2 ±0.3	17.9 ±1.2
3	C2	***Onobrychis viciifolia***	3.4 ±0.6	1.8 ±0.6	378.0 ±15.7	25.0 ±0.8	1.6 ±0.3	1.3 ±0.3	19.2 ±2.2
3	C3	***Lolium perenne***	1.5 ±0.4	1.5 ±0.6	207.2 ±12.4	29.3 ±1.6	5.0 ±0.7	0.1	9.5 ±2.5
3	C4	***Onobrychis viciifolia***	3.7 ±0.6	2.5 ±0.7	199.6. ±12.2	35.5 ±2.5	7.5 ±0.9	0.2 ±0.1	12.0 ±2.7

* number of observations,* * mean values

In contrast, plants bio accumulate Mn and Ni up to 2 times more than in plant tissues grown on non-treated topsoil experimental parcel. If leguminous plants grown on treated experimental parcel with biosolids, bioaccumulation of heavy metals increases between 2-10 times for the quantity of most heavy metals accumulated in tissues versus plants grown on non-treated experimental parcels. There is one exception - lead; in this case, the bioaccumulation decreases in the aerial plant tissues. In conclusion, plants from grass species grown on experimental parcels fly ash fertilized with biosolids led to: 1) green mass productivity 10 times lower than leguminous species, 2) instead, grass species present lower degree of bioaccumulation of toxic metals like Cr and Pb, than leguminous species of plants, 3) the accumulation in the aerial part of the species *Lolium perenne* for Fe, Mn and Ni metals is within normal limits for grassland plants.

Plants grown on experimental parcels, fly ash fertilized with biosolids, in the vegetative phenophase, a new cycle, after harvesting, have significant differences in the degree of accumulation of toxic metals; addition of organic fertilizer led to a similar behaviour in the case of grass species for both phenophases analyzed in terms of quantities of metal bioaccumulations, see Table 5. The addition of organic fertilizer on the experimental parcels fly ash resulted in different behaviours regarding the bioaccumulation of heavy metals on the different phenophases in leguminous species, namely

young plants accumulate 3-4 times larger amounts of Cr, Cu, Fe, Ni versus the bioaccumulation of heavy metals in tissues of mature plants. The accumulation of metals in this species, both in young and mature plants, is several times larger than in the case of grass species, *i.e.* the addition of fertilizer limits the access of Pb in aerial tissues.

Table 5. Metal content, of young plant (the new vegetative cycle)

* n	Parcel	Plant species	* * Metal content (in new vegetative cycle) [mg/kg D.M.]						
			Cr	Cu	Fe	Mn	Ni	Pb	Zn
3	C1	***Lolium perenne***	4.5 ±0.5	4.5 ±0.2	672.5 ±32.6	15.2 ±3.7	7.2 ±0.5	2.8	25.5±2.5
3	C2	***Onobrychis viciifolia***	1.7 ±0.2	2.5 ±0.3	672.1 ±31.7	32.9 ±7.5	7.2 ±0.5	2.9	25.0±2.3
3	C3	***Lolium perenne***	1.6 ±0.2	4.3 ±0.3	312.5 ±22.3	65.4 ±6.5	5.7 ±0.7	-	44.8±3.3
3	C4	***Onobrychis viciifolia***	11.6 ±0.7	12.2±0.8	1,784.4 ±45.6	70.3 ±7.8	18.9±0.9	-	45.0±5.1

* number of observations,* * mean values

In figures 1 and 2, the translocation of metals from the roots in the shoots of the plant is presented. The means of translocation depend on many factors like: nature of plant species, plant phenophase development, the nature of soil and type of fertilization treatment thereof.

The two plant species selected for fly ash deposits vegetation allow passage of a limited amount of total metal accepted in root at maturity stage. Generally, the aerial part of plants accumulates small amounts of metal, so the translocation coefficient is lower than 1. Plants grown on non-fertilized fly ash have a TC between 0.17 and 0.5. An exception is in the case of lead where the amount of metal accumulated in the aerial part of plants exceeds 3 times the amount of metal accumulated in root. Addition of biosolids fertilizer determined to a series of metals the reducing of TC. But nickel ion is translocated in much higher quantity in *Lolium perenne* plants grown on experimental parcels fly ash fertilized. In the case of *Onobrychis viciifolia* young plants, biosolids addition determined the increase of translocation coefficient values by 6-9 times for some metals, like Pb, Zn, and Ni.

The addition of biosolids in the soil alters metal species availability, which then translocate and accumulate in the aerial part of plants. In *Lolium perenne* plants grown on experimental parcels fly ash treated with biosolids, in both phenophases, translocation coefficient was less than 0.3 for the group of metals Cr, Cu, Fe, and Mn. In the case of plants grown on non-treated fly ash experimental parcels, the translocation coefficient can reach values TC > 1.

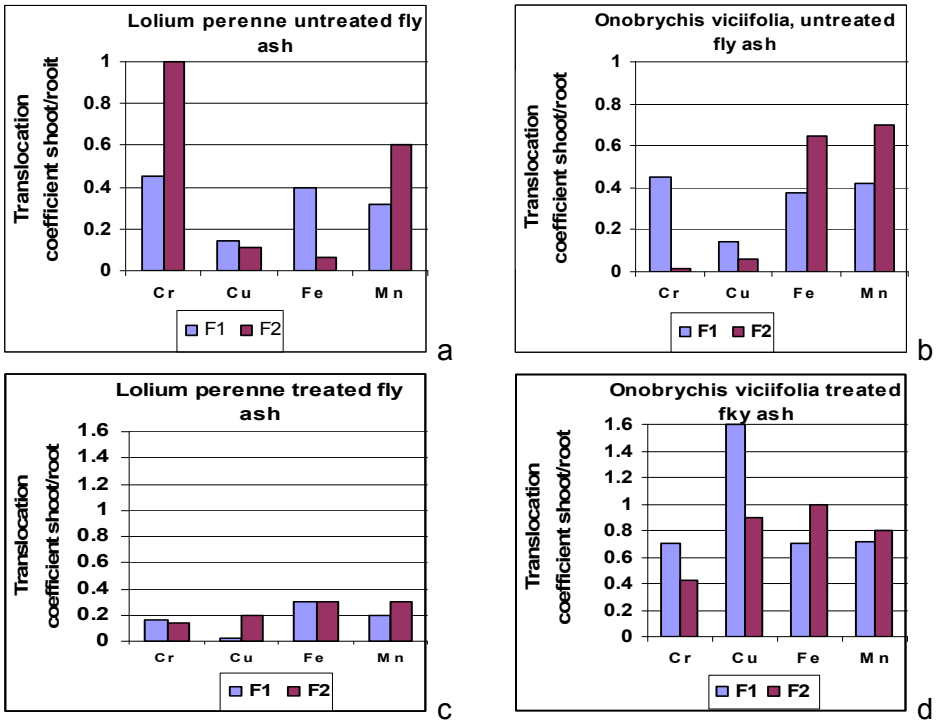

Figure 1. Cr, Cu, Fe, Mn , TC shoot/root: a) *Lolium spp.* non-treated fly ash, b) *Onobrychis spp.* non-treated fly ash, c) *Lolium spp.* fertilized fly ash, d) *Onobrychis spp.*fertilized fly ash. (F1-plants before harvest; F2-new cycle of plants).

For *Onobrychis viciifolia*, plants grown in non-fertilized topsoil of fly ash parcel, the TC was between 0.3 and 0.6. As can be seen, the addition of fertilizer may cause to some plant species the reducing of metal bioaccumulation in tissue, such as *Lolium perenne*, or increasing access of metals in the aerial part of plants as for the *Onobrychis viciifolia* species. For metals, such as Ni and Zn, biosolids addition alters the bioaccumulation in the aerial parts, especially in the phenophase of vegetative resumption in *Onobrychis spp.* species. *Onobrychis viciifolia* species accumulates in the aerial parts large quantities of these metals, in larger amounts than *Lolium perenne* species, in the same studied phenophases.

The TC for lead is greater in mature plants of *Lolium perenne* but is reduced below the detection to plants starting a new vegetative cycle. Addition of biosolids modifies metal access in plant tissue.

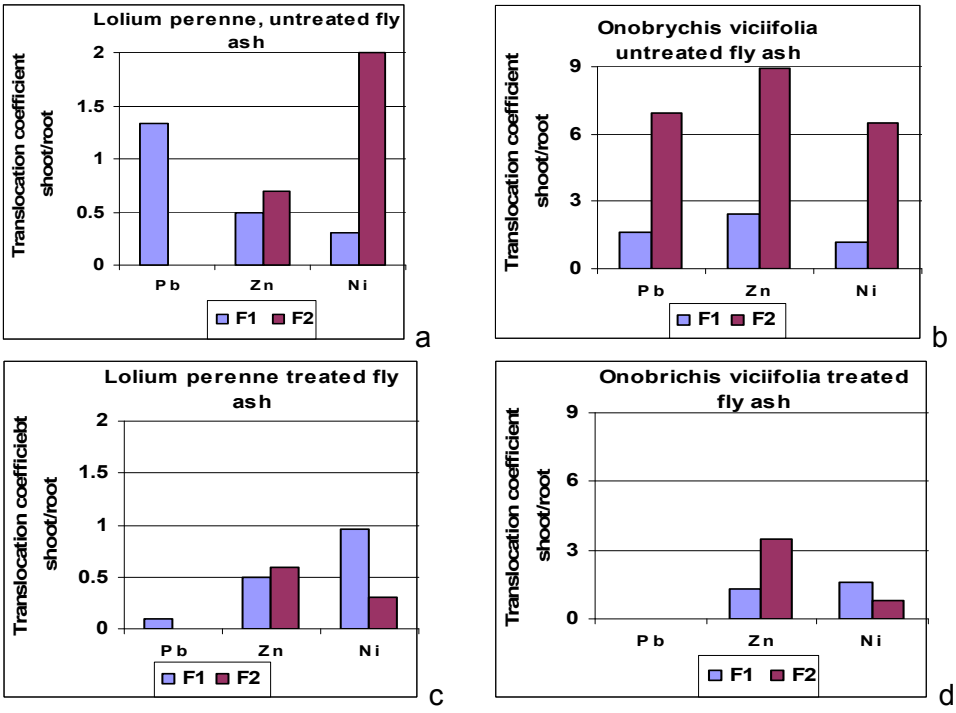

Figure 2. Pb, Zn, Ni translocation coefficient shoot/root: a) *Lolium spp.* non-treated fly ash, b) *Onobrychis spp.* non-treated fly ash, c*) Lolium spp.* fertilized fly ash, d) *Onobrychis spp.* fertilized fly ash; (F1-plants before harvest; F2-new cycle of plants).

CONCLUSIONS

Experimental studies based on to use of biosolids for fertilization of upper layers fly ash deposits (a waste lacking nutrients and resulting in burning lignite in power plants) led to the development of vegetation on these inert deposits. Pilot experiments confirmed a sustainable strategy for stabilizing/ phytoremediation of fly ash deposits, focused on capitalization of sludge waste, resulted in large amounts from municipal water treatment plants. The new crop installed presents characteristics depending on plant species: 1. Large biomass amount, but with accumulation of heavy metals, i.e. Cr, Cu, Ni, in the aerial parts of plants, such as in the case of leguminous *Onobrychis viciifolia* species, resulting vegetation with waste regime; 2. Lower biomass amount, with smaller accumulations of heavy metals, such as the case of grass *Lolium perenne,* with recycling possibilities in agro-zoo technical field (forage, bedding for animals, lignocelluloses support for compost). You can choose a path of rapid revegetation to restore the landscape with leguminous plants or a more slow vegetation of grasses, which can produce biomass without threatening the food chain.

REFERENCES

1. R.J. Haynes, *Journal Environmental Management,* **2009**, *90*, 43.
2. S. Jala, D. Goyal, *Bioresource Technology*, **2006**, *97,* 1136.
3. D.C. Adriano, A.L. Page, A.A. Elseewi. A.C. Chang, I. Straughan, *Journal of Environmental Quality,* **1980**, *9*, 333.
4. D. Elcock, N.L, Ranek, Coal Combustion Waste Management at Landfills and Surface Impoudment 1994-2004, US-Departament of Energy, US-EPA, Washington D.C., **2006**.
5. M. Ahmaruzzaman, *Progress in Energy and Combustion Science,* **2010,** *36,* 327.
6. V.C. Pandey, B. Singh, *Ecological Engineering,* **2012**, *49,* 190.
7. P. Pavlovic, M. Mitrovic, L. Djurgevici, G. Gajic, O. Kostic, S. Bojovic, *Polish Journal of Environmental Studies,* **2007**, *16,* 427.
8. L. Mitrovici, P. Pavlovici, D. Lakusic, L. Djurdjevic, B. Stevanovic, O. Kostic, G. Gajic, *Science of the Total Environment*, **2008,** *407,* 338.
9. D. Técher, P. Laval-Gilly, A. Bennasroune, S. Henry, C. Martinez-Chois, M. D'Innocenzo, J. Falla, *Industrial Crops and Products*, **2012**, *36,* 427.
10. V.C. Pandey, *Ecotoxicology and Environmental Safety*, **2012**, *82*, 8.
11. J. Bilski, K. Mclean, E. Mclean, F. Soumaila, M. Lander, *International Journal of Environmental Sciences*, **2011**, *1*, 2028.
12. *****U.S. Environmental Protection Agency, Biosolids, A plain English Guide to the EPA Part 503 Biosolide Rule, Cap. 1, Use of Disposal of Sewage Sludge Biosolids, Washington D.C.USA, **2006**.
13. .Q. Xu, R.L. Yu, X.Y Dong, G.R. Hu, X.S. Shang, Q. Wang, H.W. Li, *Journal of Hazardous Materials*, **2012**, *217-218,* 58.
14. R. Ikanpour, H.H.J. Cocs, P.J. Kearney, J.H. Clark, A.B. Pincince, G.T. Daigger, Regulations for Biosolids Land Application in U.S. and European Union, *Journal Residuals Science and Technology,* **2004**, *1,* 209.
15. M.J. McFarland, "Biosolids Engineering", Mc Graw Hill Inc., New York**,** chapter 1-15, **2000**.
16. M.M. Lasat, *Journal of Hazardous Substance Research*, **2000***, 2,* 1.
17. M. Mitrovic, S. Jaric, O. Kostic, G. Gajic, B. Karadzic, L. Djardjevic, L. Oblean, D. Pavlovic, M. Pavlovic, P. Pavlovic, *Polish Journal, Environmental Studies,* **2012**, *12,* 1339.
18. S. Mâşu, N. Dragomir, *Animal Science and Biotechnologies*, **2011**, *44*, 218.
19. G. Murtaza, R.J. Haynes, K.R. Kim, M.H. Zia, R. Naidu, O.N., Belyaeva, *Environmental Science Pollution Research Intitute,* **2012**, *19*, 636.
20. R. Singh, D.P. Singh, N. Kumar, S.K. Bhargava, S.C. Barman, *Journal of Environmental Biology,* **2010,** *31*, 421.
21. M. Ghosh, S.P. Singh, *Asian Journal on Energy and Environment*, **2005**, *6,* 214.
22. S.K. Maiti, J. Shishir, *Environmental Monitoring and Assessment*, **2008**, *136,* 355.

STUDIA UBB CHEMIA, LVII, 3, 2012 (p. 259 – 266)
(RECOMMENDED CITATION)

HARD CHEMICAL CONSTITUENT EVIDENCE IN FERROMANGANESE ALLOYED POWDER FeMn80C20

CRISTIAN SUCIU[1], GEORGE ARGHIR[1], PAUL BERE[2]

ABSTRACT. The mechanical properties of sintered steels are depending mainly on the powder microstructure. The paper presents studies of ferromanganese powder obtained by milling. The X-ray diffraction analysis evidenced two chemical compounds: the major compound is $FeMn_4$, and some traces of complex ferromanganese carbide $Fe_{1.1}Mn_{3.9}C_2$. The carbide hardness is 2365 $HV_{0.02}$. They are dispersed in the major micro structural constituent, α Mn phase. The observed microstructure prove that α Fe appears only as phase in a pearlite like eutectoid constituent. It appears as a grey lamellar micro structural constituent having an average grain size of 50 μm. This constituent feature present hardness values lower than 715 $HV_{0.02}$. Finally, we could conclude that the particle size do not affects the powder composition and micro structural constituents' distribution. The particle size affects only the technological properties as apparent density and the flow rate.

Keywords: *ferromanganese powder, hard compounds, phase distribution*

INTRODUCTION

The hard chemical and intermetallic compounds are intensively investigated in order to achieve a better wear resistance designed for a wide range of industrial and technical applications [1, 2]. Several methods for the surface hardening were found in the literature. Considering iron or low alloyed steel as the bulk base, the wear surface of the part needs an improved hardness. One of the current method used for surface hardness improvement is the coating with hard iron compounds with some different atomic species such Al, Ti, and some of the newest iron carbon fullerites [3 - 5]. The above mentioned studies reveal that a special microstructure occur during surface enrichment with Al. Ti based hard compounds formation are relative to surface nitrating or nitro - carburizing processes [6, 7]. Thus, it means that the alloying micro-structural components involved in the hardening layers play the most important role in the wear strength improvement success. The

[1] *Technical University of Cluj - Napoca, Faculty of Materials Science and Environmental Engineering, Muncii Ave., No. 103-105, RO-400641 Cluj-Napoca, Romania, suciucristianteo@yahoo.com*
[2] *Technical University of Cluj-Napoca, Faculty of Machine Building, Muncii Ave., No. 103-105, RO-400641 Cluj-Napoca, Romania*

hard compound development at micro-structural is very important but not enough for a proper wear strength improvement; this requires also a very good dispersion of the hard component grains among the bulk part microstructure. A well-controlled powder mixture allows a good wear resistance improvement via plasma spray coating as well as via powder metallurgy processes [8 - 10].

The most important hardening element in alloys is manganese due to its hard microstructure developed when is alloyed with iron. As it is known, manganese alloys are very suitable for automobile industry and military applications [11, 12]. Nowadays is a more pronounced tendency to replace expensive alloying elements with less expensive ones. Recent studies points out the manganese compounds importance in the powder metallurgy field [13, 14]. There were reported refined structures obtained by alloying during the sintering process as a consequence of atom species diffusion [13].

Considering the previously mentioned aspects as a pertinent hypothesis it results that the hardening effect in iron manganese alloys are strongly related with the micro-structural aspect of hard compound grains as well as their distribution. In such cases, the initial pre alloyed manganese powder is essential. Finally the aim of this research is to investigate the manganese hard compound distribution in the micro-structure of the FeMn80C20 pre alloyed powder.

RESULTS AND DISCUSSION

The initial FeMn80C20 powder was sieved according to the particle size class; the results are presented in Table 1. The predominant particle size class is situated between 125 ÷ 250 μm having almost 40 wt. % of the total powder amount. We would further refer to this value as average particle size.

Table 1. Powder particles size (wt. %)

Particle size (μm)	< 63	63 ÷ 71	71 ÷ 80	80 ÷ 100	100 ÷ 125	125 ÷ 250	250 ÷ 315	> 315
FeMn80C20,%	9.43	1.66	1.29	4.06	7.21	37.71	24.22	14.42

There are some particles with bigger size (around 38 %) distributed widely between 250 ÷ 315 μm. The refined particles are less represented in powder distribution; despite this we notice a significant amount of 9.43 wt % under 63 μm. These finest particles could be important enough in a further surface hardening due to their ability to be assimilate by the host microstructure.

The powder apparent density and the flow rate are presented in Table 2.

Table 2. Apparent density and flow rate of powder

Sample	Apparent density, (g/cm^3)	Flow rate, (sec/50 g)
FeMn80C20	3.38	37

Both technological parameters are affected by the micro structural particles distribution. The obtained values are in agreement with the observed distribution. The smaller particles fill up the spaces between the greater particles reducing empty spaces fact which increases the apparent density to a value closer to the bulk density. Still, we notice a significant difference due to the presence of the bigger particles. The flow rate is also affected by the particle size. The non-uniform particle distribution as presented in Table 1 conducts to a relatively good flow rate of the ferro manganese powder.

The chemical composition of the utilized powder is another important parameter which must to be followed. We performed a mass spectrometry determination for the initial powder in order to check the main elements. The results are in good agreement with the composition provided by the powder manufacturer is presented in the Table 3.

Table 3. Chemical composition of powder

Sample	C, (%)	Si, (%)	Fe, (%)	P, (%)	Mn, (%)
FeMn80C20	2.32	3.03	16.00	0.17	78.36

The ensemble view of the FeMn80C20 powder microstructure after polishing and nital chemical etching is presented in Figure 1a. Particles having polyhedral borders were identified. This fact proves the brittle nature of the powder which is close related to the high hardness. As mentioned in the experimental section the powder was produced by grinding, fact observed by the particle shape.

The chemical etching reveals the microstructure of the particle insight: larger white areas having around of 175 μm are surrounded by finest black grains which could be some intermediary compounds. Several darken areas are also observed close to the particles borders.

The microstructure observed at average magnification, Figure 1b, reveals more clearly the micro–constituents. There are observed few greater white grains surrounded with some lamellar areas having around of 50 μm average diameter. The structures of lamellar grains are pearlite like, which corresponds to the mentioned eutectoids in the Fe-Mn equilibrium diagram. There are also observed finest grains having over 20 μm diameter dark colored which could belongs to some complexes of FeMn or FeMnC compounds.

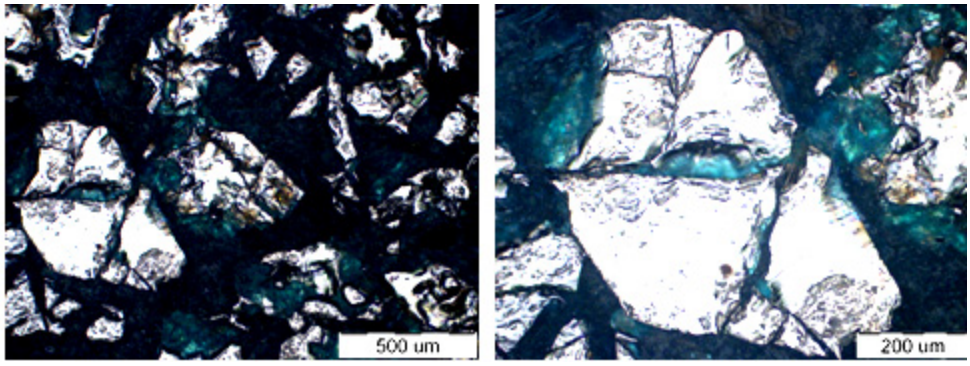

a) b)

Figure 1. The microstructure of FeMn80C20 powder:
a) low magnification and; b) average magnification. Nital 3%

Considering the equilibrium conditions for the FeMn binary system at the powder composition we have a mixed microstructure formed by α Mn grains very similar to ferrite in steels, and eutectoid grains formed by a fine mixture of α Mn and α Fe. The micro hardness results, Table 4, agrees the microstructural observations, α Mn (bright white grains) being harder than eutectoid grains.

Table 4. Micro hardness of the FeMn80C20 powder constituents

Grain type, colour	Average grain diameter, (μm)	Microhardness ($HV_{0.02}$)
Gray shade (lamellar compound)	50	715
Bright white (ferrite like)	175	1695
Dark	20	2365

The darken grains feature a higher hardness over the other microstructural compounds corresponding to the equilibrium diagram. Perhaps during alloying process and further cooling there were developed some chemical compounds corresponding to a non-equilibrium state. Such compounds appear often in alloyed steels at different thermal gradients [15].

The micro-structural characteristics must to be confronted with the crystalline phase analysis. The proper phase identification in the ferromanganese powder could be performed in optimum conditions only with the X-ray diffraction technique [16, 17]. Each particle class sample was subjected to the X-ray diffraction investigation. The resulted patterns are presented in Figure 2. All samples feature a pronounced crystalline aspect which is in concordance

with the micro-structural observations presented in Figure1. The diffractions peaks are well developed in full agreement with the polycrystalline aspect of metals and alloys. We observed, in Figure 2a, a significant influence of particle size class on the diffraction peaks shape. The greater particles conduct to a relative smooth baseline and vigorous peaks, case of Figure 2 a-c. This is due to their relative large surface which allows a good focalization of the incident X-ray. The average particles/grains, feature well developed XRD pattern along with a slightly tendency of "noise" at the baseline level, case of Figure 2 d-f. The smaller particles induce a significant "noise" at the pattern baseline due to their small size associated with a random orientation. Thus, the relevant peaks are more enhanced mainly because the finest and randomly oriented particles in the sample surface, case observed for Figure 2 g and h.

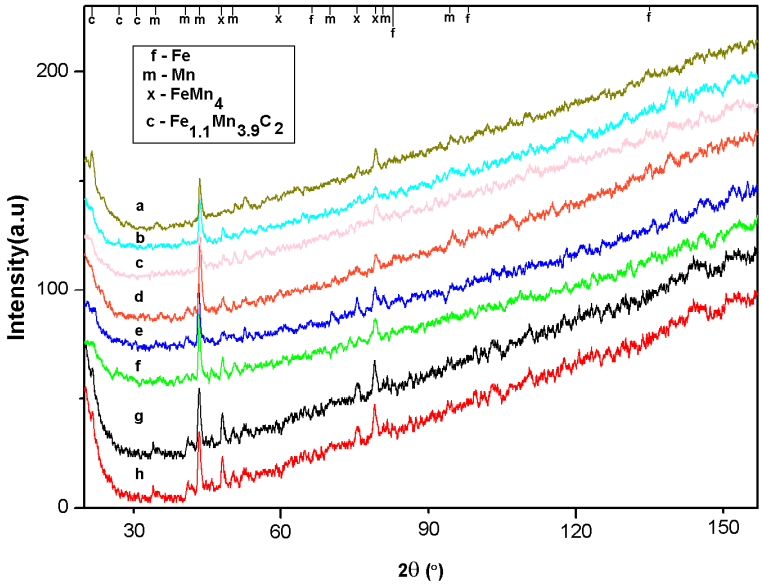

Figure 2. X-ray diffraction pattern for FeMn80C20 powder at different grain size: a) > 315 μm, b) 250 ÷ 315 μm, c) 125 ÷ 250 μm, d) 100 ÷ 125 μm, e) 80 ÷ 100 μm, f) 71 ÷ 80 μm, g) 63 ÷ 71 μm, and h) 0 ÷ 63 μm.

The XRD investigation of ferromanganese powder according to their particle size classes allows a full characterization of the considered material. We notice that relevant peaks appears in all obtained XRD patterns, relevant peaks appear in all obtained XRD patterns, Figure 2 only small variation of their relative intensity was observed. The diffraction angles do not varies with the particles size. All aspects reveal that the investigated ferromanganese powder is homogeneous from the point of view of phase composition.

The main phase component of the ferromanganese sample is the α Mn. Considering the relative intensities and the structure factor we could estimate that the amount of α Mn phase is around of 75 wt. %, which result in good agreement with the mass spectrometry results.

Other identified phase is the ferromanganese compound $FeMn_4$ which is well represented by four diffraction peaks with relative intensities ranging from 10% to 50%. This proves to be related to darken, hard compound revealed by microscopic investigation. This type of compound is mentioned in literature as results of the quenching process [18]. Its presence in the composition of the investigated ferromanganese powder could be explained only by some faster thermal gradients involved during the powder manufacturing. However, α Fe as single phase was identified only with weaker peaks under 25% relative intensity. This fact may confirm that a significant iron amount was consumed by the formation of $FeMn_4$ hard compound. The α Fe phase appears, in the investigated powder sample, only as component in the lamellar grey compound (eutectoid like).

Finally, the carbon was evidenced in the phase structure of the ferromanganese powder as $Fe_{1.1}Mn_{3.9}C_2$ carbide. This phase prove to be as trace levels the corresponding diffraction peaks being relatively weak. However, such carbide is also a hard compound which could locally increase the sample micro hardness.

The micro hardness tests confirm the connections between identified phases and the microstructure. The greater micro hardness result appears for the dark smallest spots in the microstructure (as report in Table 4). The weaker hardness appears on the pearlite like compound where free α Fe could be found.

CONCLUSIONS

The ferromanganese powder is very important for various applications where surface hardening is required mainly for the intensive wear surfaces. We investigate a commercial type of ferromanganese powder with 80% Mn in order to establish the hard chemical components or constituents.

The X-ray diffraction analysis evidenced two chemical compounds able to increase the sample hardness: the major compound is $FeMn_4$, it is followed by some traces of complex ferromanganese carbide $Fe_{1.1}Mn_{3.9}C_2$. This compounds are fine distributed in the α Mn phase, fact in good concordance with the microscopy investigation. The very hard dark spots have the grain size below 20 μm. Their micro hardness is 2365 $HV_{0.02}$.

Free α Fe phase was evidenced by the X-ray diffraction. The observed microstructure prove that α Fe appears only as phase in a pearlite like eutectoid constituent. It appears as a grey lamellar micro structural constituent having an average grain size of 50 μm. This constituent feature a hardness of 715 $HV_{0.02}$.

Finally, we could conclude that the particle size do not affects the powder composition and micro structural constituents' distribution. The particle size affects only the technological properties as apparent density and the flow rate.

EXPERIMENTAL SECTION

The ferromanganese powder FeMn80C20 was produced by Elkem Ferromanganese Sauda, Norway, according to the E.U. prescriptions. The samples were prepared according to their particle size class by sieving a roughly un-uniform FeMn80C20 ferromanganese powder. The powder sieving and distribution on the particle classes was performed according to the prescription European Union standards SR EN 2449. The apparent density was measured and calculated according to the prescriptions SR EN 23923, meanwhile the powder flow rate was determined according to ISO 4490, using a flow meter with a diameter of 2.54 mm.

The powder chemical composition was determined on an inductive coupled plasma mass spectrometer type Elan DRC (ICP-MS). For instance, the powder sample (e.g. 1 gram) was melted in a specific crucible as demanded by the spectrometer requirements.

The powder was integrated in resin samples for the microstructure analysis. The samples were polished and etched with 3% Nital, for metallographic investigations. The microstructural analysis and photography was done on an Olympus GX51 microscope. The micro-hardness $HV_{0.02}$ was measured on a Carl Zeiss Neophot 2 microscope with a micro-hardness tester.

The X-ray diffraction analysis was performed on a Dron 3 diffract meter equipped with data acquisition module. A monochrome Cu K_{α} radiation was used. The crystalline compounds were identified from the X-ray diffraction pattern using Match 1.0 Standard Database powered by Crystal Impact Company.

ACKNOWLEDGMENTS

This paper was supported by the project "Doctoral studies in engineering sciences for developing the knowledge based society-SIDOC" contract no. POSDRU/88/1.5/S/60078, project co-funded from European Social Fund through Sectorial Operational Program Human Resources 2007-2013 and by the project "Develop and support multidisciplinary postdoctoral programs in primordial technical areas of national strategy of the research - development - innovation" 4D-POSTDOC, contract nr. POSDRU/89/1.5/S/52603.

REFERENCES

1. Ni. Wangyang, Y.T. Cheng, D.S. Grummon, *Surface and Coatings Technology*, **2006**, *201*, 1053.
2. J.D. Bressan, R. Hesse, E.M. Silva, *Wear*, **2001**, *250*, 561.
3. D.E. Alman, J.A. Hawk, J.H. Tylczak, C.P. Dogan, R.D. Wilson, *Wear*, **2001**, *251*, 875.
4. S. PalDey, S.C. Deevi, *Materials Science and Engineering*, **2003**, *A342*, 58.
5. O.P. Tchernogorova, O.A. Bannykh, V.M. Blinov, E.I. Drozdova, A.A. Dityatev , N.N. Melnik, *Materials Science and Engineering*, **2001**, *A299*, 136.
6. L.L Pranevicius, P. Valatkevicius, V. Valincius, C. Templier, J.-P. Riviere, L. Pranevicius, *Surface and Coatings Technology*, **2002**, *156*, 219.
7. Ph. Roquiny, G. Mathot, G. Terwagne, F. Bodart, P. van den Brande, *Nuclear Instruments and Methods in Physics Research B*, **2000**, *161-163*, 600.
8. H. Eschnauer, E. Lugscheider, *Thin Solid Films*, **1984**, *118*, 421.
9. H. Bhat, H. Herman, *Thin Solid Films*, **1982**, *95*, 227.
10. A. Salak, M. Selecka, *Materials Science Forum*, **2011**, *672*, 55.
11. Y.N. Dastur, W. C. Leslie, *Metalurgical Transactions*, **1981**, *12A*, 749.
12. J. Tianfu, Z. Fucheng, *Materials Letters*, **1997**, *31*, 275.
13. M. Selecka, A. Salak, D. Jukubeczyova, *Materials Science Forum*, **2011**, *672*, 59.
14. A. Salak, M. Selecka, *Powder Metallurgy*, **2008**, *51*, 327.
15. P. Nurthen, O. Bergman, I. Hauer, *PM 2008 Word Congress*, Washinton, USA, **2008**.
16. G. Arghir, "Caracterizarea metalelor şi aliajelor prin difractie cu raze X", Litografia Universitaţi Tehnice din Cluj Napoca, **1993**.
17. A. Clearfield, H. Reibenspies, N. Bhuvanesh, "Principles and Applications of Powder Diffraction", Blackwell Publishing Ltd., **2008**.
18. A. Westgreen, G. Phragmen, *Z. Physics*, **1925**, *33*, 784.

STUDIA UBB CHEMIA, LVII, 3, 2012 (p. 267 – 282)
(RECOMMENDED CITATION)

LINEAR SOLVATION ENERGY RELATIONSHIPS FOR CHARACTERIZATION OF MLC SYSTEMS WITH SODIUM DODECYL SULPHATE MOBILE PHASES MODIFIED BY ALIPHATIC ALCOHOLS OR CARBOXYLIC ACIDS

VADYM V. MARKOV[1,*], ALEXANDER P. BOICHENKO[1, 2], LIDIA P. LOGINOVA[1]

ABSTRACT. The Linear Solvation Energy Relationships (LSER) have been successfully used for the modeling of partition and retention of the set of test compounds in different systems. The properties of micellar chromatographic systems with the mobile phases on the basis of sodium dodecylsulphate modified (ODS) by additives of aliphatic alcohols (1-butanol, 1-pentanol) or aliphatic carboxylic acids (butanoic, pentanoic) were characterized on the basis of comparison of calculated LSER coefficients. Principal component analysis (PCA) was used for the classification of studied systems.

Keywords: *Linear Solvation Energy Relationships (LSER), partition, modeling, micelle bounding, Micellar Liquid Chromatography (MLC), Principal Component Analysis (PCA)*

INTRODUCTION

During several last decades Linear Solvation Energy Relationships (LSER) have been widely used for describing the different processes such as partitioning in two-phase systems, chromatographic retention, reactivity, solubility, toxicity etc. [1].

The variety of non-covalent interactions such as dispersion, dipole-dipole, dipole-inducted dipole, forming of hydrogen bonds are the main factors, which are responsible for the partition of solutes in two-phase systems and their chromatographic retention. The attempts to apply thermodynamic equations for describing the potential energies of unspecific interactions and treating the partition processes when a limited number of congeneric solutes is used for modeling. Unfortunately, the strict thermodynamics cannot be used for the

[1] *Kharkov V.N. Karazin National University, Department of Chemical Metrology, Svoboda sq. 4, 61022 Kharkov, Ukraine, *markov.vadim@gmail.com*
[2] *University Centre for Pharmacy, Department of Analytical Biochemistry, A. Deusinglaan 1, 9713 AV Groningen, The Netherlands*

prediction of chemical properties and is useful only for understanding the relationships between them. Thermodynamics gives more “physical” information than “chemical” that prevents the analysis of the relationships between the molecular structure and the physical-chemical properties. Linear solvation energy relationships are extrathermodynamic free energy relationships which connect some physical-chemical properties with descriptors describing the molecules. In general, the relationship between the dependent variable such as partition constant or retention factor and independent variables (descriptors) can be represented by equation (1):

$$SP = const + eE + sS + aA + bB + vV \quad (1)$$

where *SP* is the dependent variable; *E,* the excess molar refraction; *S*, the polarity/polarizability; *A,* the hydrogen bond donor acidity; *B,* the hydrogen bond acceptor basicity; *V,* the McGowan volume. The notations *e, s, a, b,* and *v* represent the LSER coefficients.

Descriptors *S*, *A*, *B* are historically related with the solvatochromic parameters of the solvents (*π*, α, β*) (polarity, acidity and basicity) proposed by Camlet and Taft [2] and later converted to molecular descriptors by Abraham [3]. Excess molar refraction of a solute is its polarizability above that of alkane (often hypothetic) of the same molar volume. McGowan volume is related with molecular size. The validity of LSER has been many times proofed for different systems. Recently several works on re-evaluation of LSER coefficients for different two-phase systems have been published [4-8]. LSER are also successfully used for the investigation of the properties of gas and liquid chromatographic systems.

Micellar liquid chromatography (MLC) is a mode of reversed-phase high-performance liquid chromatography (RP-HPLC) in which the mobile phases are solutions of surfactants above the critical micelle concentration with small additives of organic solvents. The aliphatic alcohols are often used as mobile phase modifiers in this chromatographic mode. The pioneering work on the characterization of MLC systems and their comparison with aqueous-organic RP-HPLC systems has been published in 1995 by Yang and Khaledi [9]. The authors have obtained LSER coefficients by using the data on retention in MLC (mobile phases on the basis of SDS and tetradecyltrimethylammonium bromide modified by 1-propanol) and RP-HPLC mode (mobile phases on the basis of methanol or 2-propanol). MLC systems with C8 and C18 stationary phases and mobile phases based on sodium dodecylsulphate (SDS) and cetyltrimethylammonium bromide solutions modified by methanol, 1-propanol or 1-butanol were characterized by Garcia et al. [10-12]. In the work [13], the MLC systems with micellar mobile phases and aqueous-organic mobile phases were thoroughly compared by Torres-Lapasio et al. Authors concluded that the solute dipolarity/polarizability and hydrogen donor basicity decrease

the retention and solute volume increases the retention [10]. The data obtained in biopartitioning micellar chromatographic (BMC) mode (mobile phases on the basis of polyoxyethylene(23)lauryl ether (Brij35) were modeled by using LSER with addition term mean net charge per molecule by Lu et al. [14]. Recently Tian and Row have obtained the LSER coefficients for SDS mobile phases modified by methanol, 1-propanol or 1-butanol [15]. The BMC systems using monolithic column were characterized by Lu et al. [16] and compared with other physicochemical and biological processes. The similarity between BMC systems and biomembrane transport process was observed [16].

In our previous works aliphatic carboxylic acids have been proposed and successfully used as modifiers of micellar eluents [17, 18]. After the comprehensive investigation of the effect of aliphatic carboxylic acids on retention and efficiency it was concluded that they can be used as successful alternative to alcohols and provide the different selectivity in comparison with alcohols [17]. As we know there are no works on the characterization of MLC systems with new modifiers in terms of any free-energy relationships.

Thus, the main aim of this research is the characterization of the MLC systems with SDS micellar mobile phases modified by additives of aliphatic carboxylic acids or alcohols and their comparison with different two-phase and pseudophase systems.

RESULTS AND DISCUSSION

Thermodynamics of partition in two-phase systems and chromatographic retention

In most partition and chromatographic experiments, the concentration of distributed compound is small enough and the activity coefficient (γ) tends to unity. In this case the partition constant is described by the equation (2):

$$K = \frac{[\mathrm{A}]^{I}\gamma_{A}^{I}}{[\mathrm{A}]^{II}\gamma_{A}^{II}} \cong \frac{[\mathrm{A}]^{I}}{[\mathrm{A}]^{II}} \tag{2}$$

where: [A] represents equilibrium concentration of A.

The retention factor, k, can be directly related with the partition constant and the volume ratio of mobile and stationary phases, being expressed by equation (3):

$$k = \frac{n(\mathrm{A})_{s}}{n(\mathrm{A})_{m}} = K\frac{V_{s}}{V_{m}} \tag{3}$$

As a result, the coefficients (except the intercept) of LSER for two-phase and chromatographic systems could be compared and analyzed.

The solubilization of solutes by surfactant micelles is often presented by binding constant or partition constant. The last one is the same as partition in “real” two-phase system. The binding constant is related with the chemical reaction that can be used for representing the solute (A) solubilization by micelles (Mic), as follows:

$$\mathrm{A+Mic=AMic}$$

The equilibrium constant of this reaction is called binding constant, K_b, and can be represented by the equation (4):

$$K_b = \frac{\left[\mathrm{A}_{Mic}\right]_{tot}}{\left[\mathrm{A}_{aq}\right]_{tot}\left(c_s - cmc\right)} \tag{4}$$

where $\left[\mathrm{A}_{Mic}\right]_{tot}$ and $\left[\mathrm{A}_{aq}\right]_{tot}$ are equilibrium concentrations of A in micellar and bulk aqueous phase related to the total volume of solution, c_s is the micellized surfactant concentration, *cmc* is the critical micelle concentration.

If the volume of micelles is much lower than the total volume of solution, the partition constant for micellar pseudophase-water system can be obtained by simple transformation expressed by equation (5):

$$K_{MW} = \frac{\left[\mathrm{A}\right]_{Mic}}{\left[\mathrm{A}\right]_{aq}} = K_b \upsilon_S^{-1} \tag{5}$$

where K_{MW} is the partition constant of solute in micellar pseudophase-water system; $\left[\mathrm{A}\right]_{Mic}$ and $\left[\mathrm{A}\right]_{aq}$ are the equilibrium concentrations of *A* in micellar and bulk aqueous phase related to the volume of each phase; υ_S is the molar volume of surfactant.

Data on partition and retention of test compounds in different systems and LSER descriptors

The set of test compounds that was used in this work is consisted of 33 aliphatic and aromatic compounds with different hydrophobicities. The data on chromatographic retention was obtained for 26 of these compounds. Also the set of aliphatic carboxylic acids which partition has been studied earlier was added to the test set [19]. In Table 1 the literature values of logarithms of partition constants of compounds in 1-octanol-water, heptane-water, chloroform-water, and SDS pseudophase-water system are presented. In the last case we have collected all our available data, because it is known that micelle-water partition constants can accept different values depending on

the method used for their determination [19]. As there is no commonly accepted procedure, in further work we have used the mean value of partition constant in SDS micelles-water system.

The partition constants are changed on five orders of magnitude: the minimum value of log K_{ow} is -0.17 (acetic acid), and the maximum value is 5.52 (hexylbenzene). The corresponding minimum and maximum values for heptane-water system are -3.14 (chloroacetic acid) and 4.11 (pentylbenzene). The data for hexylbenzene were not found in literature. The retention factors obtained for the test set of compounds in MLC mode with SDS based mobile phase modified by 1-pentanol, 1-butanol, butanoic or pentanoic acid are presented in Table 2 as well as the LSER descriptors.

The adequate LSER coefficients for each system could be obtained if there are no strong inter-correlations between the descriptors for the chosen set of compounds. As can be seen from Table 3 the statistically significant correlations were obtained only between the descriptors *E* and *S* and *E* and *V*. These correlations could be explained by the relationship between the descriptors: *E* and *S* characterize the polarity of molecules, and *E* and *V* are functionally related [1, 20].

Table 1. Logarithms of partition constants of compounds from test set.

Compound	Log *K* (organic or micelle phase-water)			
	1-Octanol	SDS	Heptane	Chloroform
1,3,5-Trimethylbenzene	3.42 [21]	–	4.05 [22]	–
Monochloroacetic acid	–	–	-3.14 [23]	-1.35 [23]
1-Ethyl-4-nitrobenzene	2.94	2.63 [24]	–	–
2,3-Dichlorophenol	3.15 [25]	2.58 [26]; 2.52 [27] 2.57 [28]; 2.52 [29]	–	–
2,5-Dichlorophenol	3.06 [25]	2.52 [26]; 2.39 [27]; 2.46 [27]; 2.73 [29]	–	–
2,6-Dichlorophenol	2.64 [25]	2.33 [26]; 2.56 [29]	–	–
2-Nitroanisole	1.73 [30]	1.62 [31]	0.25 [22]	2.13 [32]
2-Nitrophenol	1.73 [21]	2.09 [33]; 2.17 [28]; 2.15 [28]	1.40[22]	2.54 [32]
3,4-Dichlorophenol	3.33 [25]	2.78 [26]; 2.70 [29]	–	–
3,5-Dichlorophenol	3.62 [25]	2.58 [26]; 2.60 [34]; 2.63 [35]; 2.59 [35]; 2.70 [27]; 2.82 [27]; 2.60 [29]	–	–
Trichloroacetic acid	–	–	-2.63 [22]	0.04 [36]
3-Chlorophenol	2.47 [21]	1.58 [37]	-0.08 [22]	1.02 [23]

Compound	Log *K* (organic or micelle phase-water)			
	1-Octanol	SDS	Heptane	Chloroform
3-Nitrophenol	2.00 [21]	2.07 [28]; 2.10 [28]	-1.40 [22]	0.41 [32]
4-Chlorophenol	2.44 [21]	2.10 [38]; 2.12 [34]; 2.35 [39]; 2.20 [35]; 2.09 [35]; 2.22 [27]; 2.28 [27]; 2.32 [40]; 3.03 [41]	-0.10 [22]	1.01 [23]
4-Nitrophenol	1.91 [21]	1.82 [42]; 1.45 [43]; 2.03 [33]; 1.89 [37]; 1.81 [34]; 1.89 [28]; 1.93 [28]	-2.00 [22]	0.17 [32]
Anisole	2.10 [21]	2.15 [40]; 1.49 [34]; 2.07 [44]; 2.15 [40]	2.10	1.33 [32]
Benzene	2.03 [21]	2.01 [38]; 1.93 [37]; 1.30 [45]; 1.99 [37]	2.22 [22]	2.80 [23]
Acetic acid	-0.17 [32]	–	-2.90 [23]	-1.56 [32]
Propanoic acid	0.33 [32]	1.00 [19]	-2.14 [23]	-0.79 [32]
Butanoic acid	0.79 [32]	1.28 [19]	-0.96 [23]	-0.27 [32]
Pentanoic acid	1.39 [32]	1.56 [19]	–	0.33 [32]
Hexanoic acid	1.92 [32]	2.02 [19]	0.24 [23]	0.95 [32]
Chlorobenzene	2.84 [46]	1.89 [45]; 2.52 [47]; 2.63[37]	2.92 [22]	3.46 [23]
Ethylbenzene	3.15 [46]	2.78 [38]; 2.23 [31]	3.43[22]	–
Fluorene	4.18[21]	3.11 [31]	–	–
Hexylbenzene	5.52 [46]	–	–	–
Naphtalene	3.59[21]	4.12 [48]; 2.53 [31]; 2.46 [45]	–	–
2-Nitroaniline	1.79 [21]	2.23 [24]	–	–
Pentylbenzene	4.90 [46]	3.96 [38]	4.11 [22]	–
Phenol	1.48 [21]	1.66 [40]; 1.64 [34]; 0.96 [45]; 1.60 [37]; 1.61 [49]; 1.51 [49]; 1.30 [34]; 1.47 [34]; 1.59 [44]; 1.78 [50]; 1.68 [51]; 1.60 [41]	-0.70 [22]	0.38 [32]
Phenanthrene	4.46 [21]	4.48 [34]; 3.79 [31]	–	–
p-Xylol	3.15 [21]	3.05 [34]; 2.27 [31]; 2.81 [39]	–	–
Toluene	2.73 [21]	2.42 [38]; 2.11 [34]; 1.85 [31]; 1.77 [45]; 2.48 [52]	2.75 [22]	3.41 [23]

Table 2. Logarithm of retention factors of test compounds and their LSER descriptors.

Compound	Log *k**	*E* / *S* / *A* / *B* / *V*	Ref.**
1,3,5-Trimethylbenzene	1.45 / 1.37 / 1.33 / 1.29	0.649 / 0.52 / 0 / 0.190 / 1.139	
Monochloroacetic acid	-	0.427 / 1.03 / 0.79 / 0.35 / 0.59	
1-Ethyl-4-nitrobenzene	1.09 / 1.04 / 0.96 / 0.94	-	
2,3-Dichlorophenol	0.73 / 0.80 / 0.65 / 0.66	0.96 / 0.94 / 0.480 / 0.20 / 1.02	[53]
2,5-Dichlorophenol	0.79 / 0.89 / 0.70 / 0.75	0.96 / 0.88 / 0.560 / 0.18 / 1.02	[53]
2,6-Dichlorophenol	0.72 / 0.78 / 0.62 / 0.65	0.90 / 0.90 / 0.380 / 0.24 / 1.02	[53]
2-Nitroanisole	0.54 / 0.44 / 0.43 / 0.36	0.97 / 1.42 / 0 / 0.360 / 1.09	[54]
2-Nitrophenol	0.72 / 0.67 / 0.64 / 0.59	1.015 / 1.05 / 0.05 / 0.37 / 0.949	[55]
3,4-Dichlorophenol	0.82 / 0.89 / 0.72 / 0.75	1.02 / 1.14 / 0.85 / 0.03 / 1.02	[53]
3,5-Dichlorophenol	0.90 / 1.00 / 0.82 / 0.85	1.02 / 1.10 / 0.83 / 0 / 1.02	
Trichloroacetic acid	-	0.524 / 1.21 / 1.01 / 0.26 / 0.83	[5]
3-Chlorophenol	0.64 / 0.71 / 0.56 / 0.59	0.91 / 1.06 / 0.69 / 0.15 / 0.898	[53]
3-Nitrophenol	0.36 / 0.45 / 0.30 / 0.36	1.05 / 1.57 / 0.79 / 0.23 / 0.949	[54]
4-Chlorophenol	0.62 / 0.67 / 0.55 / 0.55	0.915 / 1.08 / 0.67 / 0.2 / 0.898	[5]
4-Nitrophenol	0.35 / 0.42 / 0.25 / 0.31	1.07 / 1.72 / 0.82 / 0.26 / 0.949	[53]
Anisole	0.96 / 0.91 / 0.85 / 0.82	0.708 / 0.75 / 0 / 0.290 / 0.916	[54]
Benzene	1.05 / 1.02 / 0.95 / 0.93	0.61 / 0.52 / 0 / 0.14 / 0.716	[54]
Acetic acid	-	0.227 / 0.6 / 0.55 / 0.43 / 0.465	[57]
Propanoic acid	-	0.235 / 0.6 / 0.54 / 0.43 / 0.606	[57]
Butanoic acid	-	0.241 / 0.6 / 0.54 / 0.42 / 0.747	[57]
Pentanoic acid	-	0.247 / 0.6 / 0.54 / 0.41 / 0.887	[57]
Hexanoic acid	-	0.251 / 0.6 / 0.54 / 0.39 / 1.028	[57]
Chlorobenzene	1.34 / 1.28 / 1.23 / 1.19	0.718 / 0.65 / 0 / 0.07 / 0.839	[54]
Ethylbenzene	1.22 / 1.18 / 1.09 / 1.07	0.613 / 0.51 / 0 / 0.15 / 0.998	[5]
Fluorene	1.50 / 1.43 / 1.37 / 1.33	1.588 / 1.03 / 0 / 0.20 / 1.357	[56]
Hexylbenzene	1.64 / 1.49 / 1.58 / 1.47	0.591 / 0.50 / 0 / 0.150 / 1.562	[54]
Naphtalene	1.34 / 1.29 / 1.21 / 1.18	1.340 / 0.92 / 0 / 0.200 / 1.085	[54]
2-Nitroaniline	0.48 / 0.44 / 0.40 / 0.36	1.180 / 1.37 / 0.30 / 0.36 / 0.99	[16]
Pentylbenzene	1.57 / 1.46 / 1.50 / 1.42	0.594 / 0.520 / 0 / 0.14 / 1.421	[56]
Phenol	0.19 / 0.27 / 0.17 / 0.21	0.85 / 0.69 / 0.60 / 0.30 / 0.775	[54]
Phenanthrene	1.50 / 1.44 / 1.36 / 1.34	2.055 / 1.29 / 0 / 0.26 / 1.454	[56]
p-Xylol	1.37 / 1.31 / 1.24 / 1.21	0.613 / 0.52 / 0 / 0.16 / 0.998	[5]
Toluene	1.24 / 1.19 / 1.11 / 1.09	0.601 / 0.52 / 0 / 0.14 / 0.857	[58]

* log k (0.1 SDS 3% pentanoic acid) / log k (0.10 SDS 3% 1-pentanol) / log k (0.15 SDS 5% butanoic acid) / log k (0.15 SDS 5% 1-butanol).

** Reference to source of LSER descriptors.

Table 3. Correlation coefficients between the LSER descriptors of test compounds (the significant correlations are in bold).

Descriptors	Correlation coefficients
E – S	**0.62**
E – A	-0.19
E – B	-0.32
E – V	**0.55**
S – A	0.43
S – B	0.03
S – V	0.10
A – B	0.13
A – V	-0.45
B – V	-0.39

Literature data on LSER coefficients for selected systems

The interest to LSER results in a number of papers where the models of different processes are described in terms of LSER coefficients. In Table 4, the literature data on the coefficients for 1-octanol-water, SDS pseudophase-water, heptane-water, and chloroform-water systems are presented.

Table 4. Literature data on LSER coefficients for various systems.

Solvent or micellar mobile phase composition	log K = *const* + eE + sS + aA + bB + vV	*Ref.*
1-Octanol	log K^* = -0.03 + 0.49E - 1.05S - 0.028A - 4.23B +4.22V	[3]
SDS	log K = 0.54 - 0.58S - 0.37A - 1.65B + 3.02V	[59]
	log K = 1.20 + 0.54E - 0.40S - 0.13A - 1.58B + 2.79V	[42]
	log K = -0.62 + 0.32E - 0.57S - 0.08A - 1.84B + 3.25V	[60]
	log K = -1.87 - 0.25S - 0.16A - 1.79B + 4.00V	[61]
	log K = 1.327 + 0.37E + 0.41S - 0.13A - 1.98B + 2.98V	[8]
Heptane	log K = 0.325 + 0.67E - 2.06S - 3.32A - 4.73B + 4.54V	[3]
Chloroform	log K = 0.327 + 0.16E - 0.39S - 3.19A - 3.44B + 4.19V	[3]
SDS, 1-Pentanol (C18 Column)	log k^{**} = 0.20A - 0.50B + 0.26V	[62]
0.08 M SDS, 5% 1-Butanol (C18 Column)	log k = 0.46 + 0.27E - 0.49S - 0.44A - 1.38B + 1.18V	[11]
0.09 M SDS, 5% 1-Butanol (C18 Column)	log k = 1.25 + 0.17E - 0.88S - 0.22A - 0.73B + 1.05V	[15]
0.14 M SDS, 3% 1-Butanol (C8 Column)	log k = 0.91 + 0.53E - 0.40S - 0.28A - 0.81B + 0.67V	[10]

* Distribution constant
** Retention constant

It should be noted that our aim was not to bring all of the known coefficients of the LSER for each system. Only recent results for two-phase systems are shown except the SDS pseudophase-water system. The LSER

coefficients for MLC systems with SDS mobile phases which composition is close to the composition of mobile phases investigated in our work are also included in Table 5.

Description of experimental data by LSER

The application of LSER for the description of experimental data on the partition and retention of compounds in all studied systems results in high goodness-of-fit: squares of correlation coefficient are in the range 0.86-0.99. The prediction power of obtained models was examined by leave-one-out cross validation procedure. The lower values of R^2 and R^2_{cross} estimated for SDS pseudophase-water system could be explained by higher uncertainty in the values of partition constants.

Table 5. The LSER coefficients for various systems constructed on the basis of data presented in Table 1 and 2.

Solvent or micellar mobile phase composition	log *K* = *const* + *eE* + *sS* + *aA* + *bB* + *vV*	*n* / R^2 / R^2_{cross}
1-Octanol	log *K* = 0.17+ 0.51*E* - 0.92*S* + 0.09*A* - 4.36*B* + 3.84*V*	31 / 0.99 / 0.98
SDS	log *K* = 0.36+0.43*E* - 0.63*S* - 0.05*A* - 1.71*B* + 2.59*V*	26 / 0.89 / 0.75
Heptane	log *K* = 0.74 + 1.34*E* - 2.38*S* - 2.87*A* - 5.24*B* + 3.70*V*	20 / 0.98 / 0.91
Chloroform	log *K* = 1.01 + 0.12*E* - 0.57*S* - 2.33*A* - 5.85*B* + 3.68*V*	18 / 0.94 / 0.88
0.10 M SDS, 3% Pentanoic acid	log *k* = 0.94 + 0.20*E* - 0.18*S* - 0.80*A* - 2.37*B* + 0.68*V*	25 / 0.96 / 0.93
0.10 M SDS, 3% 1-Pentanol	log *k* = 0.97 + 0.28*E* - 0.26*S* - 0.58*A* - 2.31*B* + 0.57*V*	25 / 0.95 / 0.91
0.15 M SDS, 5% 1-Butanoic acid	log *k* = 0.79 + 0.18*E* - 0.23*S* - 0.71*A* - 2.17*B* + 0.72*V*	25 / 0.97 / 0.93
0.15 M SDS, 5% 1-Butanol	log *k* = 0.81 + 0.23*E* - 0.26*S* - 0.60*A* - 2.16*B* + 0.64*V*	25 / 0.96 / 0.91

The representativeness of chosen set of compounds for the estimation of LSER coefficients is also confirmed by comparing the LSER coefficients obtained in our work with literature data for the two-phase systems. The correlation coefficient between the literature values of LSER coefficients and those calculated are very high for 1-octanol-water and heptane-water systems and for most SDS pseudophase-water systems, excepting the data from paper [61]. The sign of the s coefficient presented in [8] differs from that presented in other works. The analysis of residuals shows no systematic dependences that indicates the adequacy of the constructed models.

Comparison of studied systems on basis of LSER coefficients

The principal component analysis (PCA) has been applied for the classification of the investigated systems. Figure 1 presents the projection of the first and second components obtained for literature data of LSER coefficients and the LSER coefficients estimated in our work for two-phase and chromatographic systems.

As can be seen from the Figure 1, the micellar chromatographic systems form a separate group that indicates their difference from “real” two-phase systems. The points related to SDS pseudophase-water systems have positive values of the first principal component and positive or negative values of the second principal component and they are distributed separately.

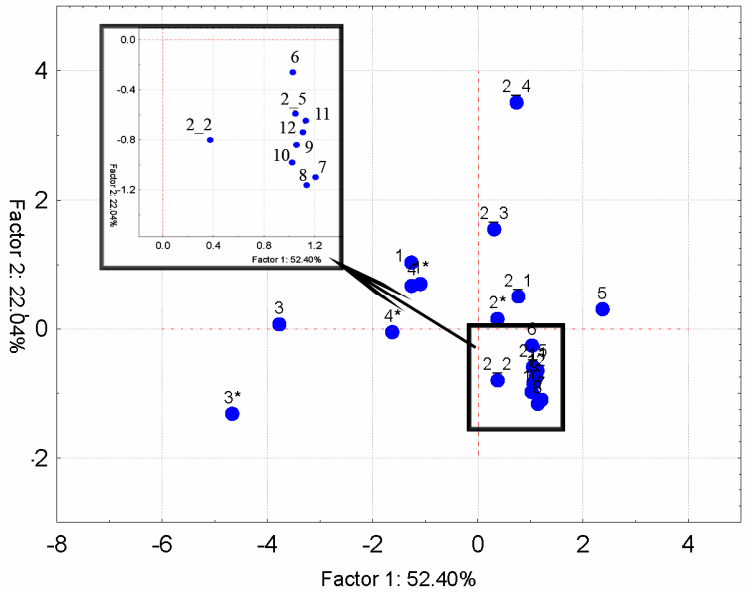

Figure 1. The projection of the first and second components on the surface. 1 – 1-octanol-water [3]; 2_1 – SDS-water [59]; 2_2 – SDS-water [42]; 2_3 – SDS-water [60]; 2_4 – SDS-water [61]; 2_5 – SDS-water [8]; 3 – heptane-water [3]; 4 – chloroform-water [3]; 5 – mobile phase SDS, 1-pentanol (Column C18) [62]; 6 – 0.08 M SDS, 5% 1-butanol (Column C18) [11]; 7 – 0.09 M SDS, 5% 1-butanol (Column C18) [15]; 8 – 0.14 M SDS, 3% 1-butanol (Column C8) [10]; 9 – 0.10 M SDS, 3% pentanoic acid; 10 – 0.10 M SDS, 3% 1-pentanol; 11 – 0.15 M SDS, 5% 1-butanoic acid; 12 – 0.15 M SDS, 5% 1-butanol; 1* – 1-octanol-water (our data); 2* – SDS-water (our data); 3* – heptane-water (our data); 4* – chloroform-water (our data); 5* – chloroform-water (our data); 10 – 0.10 M SDS, 3% pentanoic acid.

Figure 2 shows the histogram of LSER coefficients which could be used for comparing the properties of different systems. However, some points must be taken into account during the analysis of obtained coefficients. First, each coefficient shows the difference in the properties of two phases. Second, the coefficients *a* and *b* characterize the difference in basicity and acidity of phases correspondingly. The negative values of LSER coefficients indicate the shift of partition to aqueous phase.

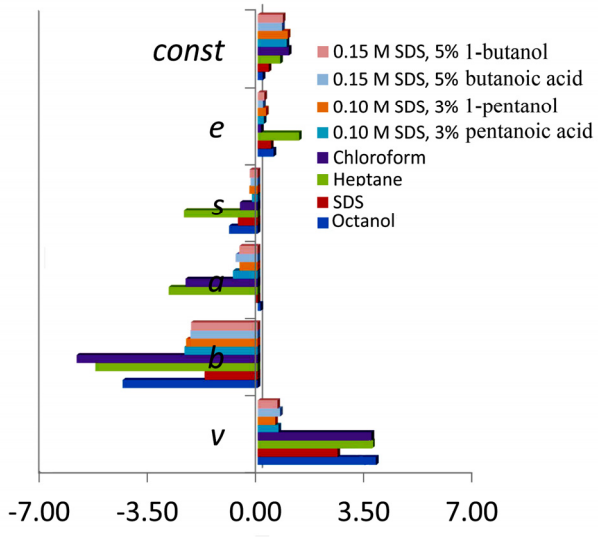

Figure 2. Histogram of LSER coefficients estimated in our work for the chromatographic systems: 1-octanol-water, heptane-water and SDS pseudophase-water.

As can be seen in Figure 2 the values of *s* are negative. This means that the polarity of 1-octanol, heptane, SDS pseudophase and C18 column modified by mobile phase components are lower in comparison with aqueous phase. The largest difference in polarity is observed for heptane-water. The difference in polarity of micellar mobile phase and dynamically modified stationary phase is lower than for SDS pseudophase-water system. This can be related with the formation of hemimicelles on the surface of stationary phases. Heptane has the lowest hydrogen bond donor (*b* = -5.24) and acceptor (*a* = -2.87) properties. Thus, the compounds with tendency to form hydrogen bonds are partitioned into the aqueous phase. The dynamically modified stationary phases and 1-octanol have low hydrogen bond donor capacity due to the absence of hydrogen bond donor groups in C18 bonded groups and SDS monomers. In contrast, each molecule of water has two hydrogen atoms which could form the hydrogen bonds. The less difference in the properties

of SDS pseudophase and water can be explained by the hydration of SDS micelles surface. Otherwise, hydrogen bond acceptor capacity of water, 1-octanol, and SDS pseudophase are almost equal. Such similarity of 1-octanol and SDS pseudophase properties can explain the correlation between partition constants in these systems for the congeneric compounds [25].

The size of the molecule has the largest contribution to the distribution of organic compounds into the non-aqueous phase and their retention. The *v* coefficient is related with the energy which is needed for forming the cavity inside the bulk phase. Intermolecular interactions are weaker in the heptane, 1-octanol and hydrophobic micelle core comparing with water which expels large hydrophobic molecules. The properties of mobile and stationary phase are less different in chromatographic systems due to the opportunity of direct partition of hydrophobic compounds into stationary phase from the micelles without transfer to the bulk aqueous phase.

The chromatographic systems with SDS mobile phases modified by acids show less difference in the polarity of mobile and stationary phases in comparison with mobile phases modified by alcohols. However the cavity formation in the stationary phase is energetically more favorable in the case of using of mobile phases modified by acids that result in stronger retention of highly hydrophobic compounds. Hydrogen bond donor properties of mobile and stationary phases modified by acid or alcohol with the same carbon chain length are quite similar. Despite the general similarity of MLC systems modified by acid or alcohol they provide different selectivity of compounds separation which is indicated by differences in coefficient values obtained for these MLC systems.

CONCLUSIONS

LSER is a useful tool for modeling the partition of two-phase and pseudophase systems and the retention in liquid chromatography with micellar mobile phases. The chosen set of test compounds allows obtaining adequate LSER coefficients and interpreting their chemical sense. The MLC chromatographic systems modified by different modifiers shows the similar properties in terms of LSER coefficients. However, the analysis of their absolute values differences can be used to move inside the mechanism of retention in MLC.

EXPERIMENTAL SECTION

Reagents

Mobile phases were prepared with sodium dodecylsulphate (≥97%, Fluka, Buchs, Switzerland or >98.5%, Sigma-Aldrich, L'Isle d'Abeau Chesnes, France), 1-butanol (>99%, Carlo Erba Reagents, Peypin, France), 1-butanoic

acid (>99%, for synthesis, Merck, Darmstadt, Germany), 1-pentanol (Aldrich), 1-pentanoic acid (99%, Janssen Chimica, Geel, Belgium). The standard buffer solution was prepared from NaH_2PO_4 (Prolabo, Paris, France) and H_3PO_4 (Fluka, Buchs, Switzerland).

The stock solutions of phenol from Prolabo (Paris, France) and 2,5-dichlorophenol (98%), 4-chlorophenol (99%), 2,3-dichlorophenol (98%), 3,4-dichlorophenol (99%), 3,5-dichlorophenol (97%), 3-nitrophenol (99%), 2-nitrophenol (98%), 4-nitrophenol (99%), 2,6-dichlorophenol from Aldrich, anisole (99%) from Janssen Chimica, benzene (99.5%), phenanthrene (97%) from Fluka, naphthalene (99%) from Aldrich, fluorene (97%) from Fluka, o-nitroaniline "pure" from Prolabo, hexylbenzene from Fluka, chlorobenzene (99%) from Merck, pentylbenzene (97%) from Fluka, ethylbenzene (99%) from Merck, p-xylol (99%) from Aldrich, 1,3,5-trimethylbenzene (99%) from Fluka, 1-ethyl-4-nitrobenzene (99%) from Fluka, 3-chlorophenol (98%) from Merck, toluene from Rectapur, and 2-nitroanisole (98%) from Fluka were prepared in methanol.

The working solutions of the test compounds were prepared by the dilution of standard solutions with micellar mobile phase.

Apparatus and chromatographic conditions

The Shimadzu HPLC system (Kyoto, Japan) was composed of a pump (model LC-10AS), a UV detector (model SPD-6A), a column oven (model CTO-6A) and an in-line Rheodyne 7010 valve with a 20 µl sample loop. The retention data were obtained by using isocratic conditions with the flow rate of 0.5 mL/min for the Zorbax Extend-C18 column (150 mm×3.0 mm i.d., 5 µm particle size diameter, Agilent, USA). After working with the micellar mobile phase, the columns were washed by water, water-acetonitrile (Prolabo, Paris, France) and water-methanol solutions and rinsed with pure methanol before storage. The two identical columns from the same batch were used for the collection of chromatographic data. The pH meter was a Mettler Toledo MP220 (Mettler, Virofly, France) equipped with a combination pH electrode which was calibrated with pH 4.0 and pH 7.0 standard buffer solutions. The Mettler Toledo AB204-S balance was used for the preparation of stock solution and phosphate buffer. An Elmasonic ultrasound bath (Elma Hans Schmidbauer GmbH & Co. KG, Stuttgart, Germany) was used for dissolution of samples.

REFERENCES

1. M. Vitha, P.W. Carr, *Journal of Chromatography* A, **2006**, *1126*, 143.
2. M.J. Kamlet, R.W. Taft, *Journal of the Chemical Society, Perkin Transactions,* **1979**, *2*, 337.
3. M.H. Abraham, A. Ibrahim, A.M. Zissimos, *Journal of Chromatography A*, **2004**, *1037*, 29.
4. L.M. Sprunger, J. Gibbs, W.E. Acree Jr., M.H. Abraham, *QSAR and Combinatorial Science*, **2009**, *28*, 72.
5. L.M. Sprunger, S.S. Achi, W.E. Acree Jr., M.H. Abraham, A.J. Leo, D. Hoekman, *Fluid Phase Equilibria*, **2009**, *281*, 144.
6. L.M. Sprunger, A. Proctor, W.E. Acree Jr., M.H. Abraham, N. Benjelloun-Dakhama, *Fluid Phase Equilibria*, **2008**, *270*, 30.
7. L.M. Sprunger, J. Gibbs, W.E. Acree Jr., M.H. Abraham, *Fluid Phase Equilibria*, **2008**, *273*, 78.
8. L. Sprunger, W.E. Acree Jr, M.H. Abraham, *Journal of Chemical Information and Modeling*, **2007**, *47*, 1808.
9. S. Yang, M.G. Khaledi, *Journal of Chromatography A*, **1995**, *692*, 301.
10. M.A. García, M.F Vitha, J Sandquist, K Mulville, M.L Marina, *Journal of Chromatography A*, **2001**, *918*, 1.
11. M.A. García, M.F. Vitha, M.L. Marina, *Journal of Liquid Chromatography & Related Technologies*, **2000**, *23*, 873.
12. M.A. García, M.F. Vitha, M.L. Marina, *Journal of Liquid Chromatography & Related Technologies,* **2000**, *23*(6), 873-895. Erratum: *23*(20). 3203-3205.
13. J.R. Torres-Lapasió, M.J. Ruiz-Ángel, M.C. García-Álvarez-Coque, M.H. Abraham, *Journal of Chromatography A*, **2008**, *1182*, 176.
14. R. Lu, J. Sun, Y. Wang, Z. He, *Chromatographia*, **2009**, *70*, 21.
15. M. Tian, K.H. Row, *Journal of Liquid Chromatography and Related Technologies*, **2009**, *32*, 772.
16. R. Lu, J. Sun, Y. Wang, H. Li, J. Liu, L. Fang, Z. He, *Journal of Chromatography A*, **2009**, *1216*, 5190.
17. A.P. Boichenko, A. Berthod, *Journal of Chromatography A*, **2010**, *1217*, 5665.
18. A.P. Boichenko, A.U. Kulikov, L.P. Loginova, A.L. Iwashchenko, *Journal of Chromatography A*, **2007**, *1157*, 252.
19. A. Boichenko, L. Dung, L. Loginova, *Journal of Solution Chemistry*, **2011**, *40*, 968.
20. K. Héberger, *Journal of Chromatography A*, **2007**, *1158*, 273.
21. A. Leo, C. Hansch, “Substituent constants for correlation analysis in chemistry and biology”, **1979**, New York: Wiley, sections 3-17.
22. Ya.I. Korenman, “Coefficients of distribution of organic compounds: compendium”, **1992**, Voronezh, chapter 2.

23. N. El Tayar, R.-S. Tsai, B. Testa, P.-A. Carrupt, A. Leo, *Journal of Pharmaceutical Sciences*, **1991**, *80*, 590.
24. E. Fuguet, C. Ràfols, E. Bosch, M. Rosés, *Langmuir*, **2002**, *19*, 55.
25. P. Camilleri, S.A. Watts, J.A. Boraston, *Journal of the Chemical Society, Perkin Transactions* **1988**, *2*, 1699.
26. C.-E. Lin, W.-C. Lin, W.-C. Chiou, *Journal of Chromatography A*, **1996**, *722*, 333.
27. A.S. Kord, J.K. Strasters, M.G. Khaledi, *Analytica Chimica Acta*, **1991**, *246*, 131-137.
28. A. Senz, H.E. Gsponer, *Journal of Colloid and Interface Science*, **1997**, *195*, 94.
29. V. Pino, F.J. Conde, J.H. Ayala, A.M. Afonso, V. González, *Journal of Chromatography A*, **2005**, *1099*, 64.
30. A. Leo, *Journal of the Chemical Society, Perkin Transactions 2*, **1983**(6), 825.
31. B.N. Woodrow, J.G. Dorsey, *Environmental Science and Technology*, **1997**, *31*, 2812.
32. A. Leo, C. Hansch, D. Elkins, *Chemical Reviews*, **1971**, *71*, 525.
33. T. Saitoh, N. Ojima, H. Hoshino, T. Yotsuyanagiet, *Microchimica Acta*, **1992**, *106*, 91.
34. K.T. Valsaraj, L.J. Thibodeaux, *Separation Science and Technology*, **1990**, *25*, 369.
35. E. Pramauro, G. Saini, E. Pelizzetti, *Analytica Chimica Acta*, **1984**, *166*, 233.
36. ***, “Handbook of Chemist. Analytical Chemistry. Spectral Analysis. Refractiv Indexes”, Leningrad: Chemistry, **1967**, vol. 4.
37. A. Berthod, M.C. García-Alvarez-Coque, “Micellar Liquid Chromatography. Chromatographic Science Series”, **2000**, New York, Basel: Marcel Dekker, Appendix III.
38. M.F. Vitha, A.J. Dallas, P.W. Carr, *The Journal of Physical Chemistry*, **1996**, *100*, 5050.
39. F. Mutelet, M.H. Guermouche, M. Rogalski, *Chromatographia*, **2003**, *57*, 729.
40. K.A. Kelly, S.T. Burns, M.G. Khaledi, *Analytical Chemistry*, **2001**, *73*, 6057.
41. H. Fujiwara, K. Kanzaki, T. Kano, A. Kimura, K. Tanaka, Y. Da, *Journal of the Chemical Society, Chemical Communications*, **1992**(10) 736.
42. M.H. Abraham, H.S. Chadha, J.P. Dixon, C. Rafols, C. Treiner, *Journal of the Chemical Society, Perkin Transactions 2*, **1995**(5), 887.
43. D.W. Armstrong, G.Y. Stine, *Journal of the American Chemical Society*, **1983**, *105*, 2962.
44. F.P. Tomasella, L.J. Cline Love, *Analytical Chemistry*, **1990**, *62*, 1315.
45. M.A. Garcна, J.C. Dhez-Masa, M.L. Marina, *Journal of Chromatography A*, **1996**, *742*, 251.
46. J. Sangster, *Journal of Physical and Chemical Reference Data*, **1989**, *8*, 1111.
47. M.L. Marina, S. Vera, A.R. Rodriguez, *Chromatographia*, **1989**, *28*, 379.
48. A. Mohamed, A.-S.M. Mahfoodh, *Colloids and Surfaces A: Physicochemical and Engineering Aspects*, **2006**, *287*, 44.

49. E. Pramauro, E. Pelizzetti, *Analytica Chimica Acta*, **1983**, *154*, 153.
50. W.A. Massad, P. Repossi, G.A. Argüello, *Journal of Colloid and Interface Science*, **2002**, *255*, 189.
51. A. Berthod, A. Roussel, *Journal of Chromatography A*, **1988**, *449*, 349.
52. M.A. Garcia, S. Vera, M.L. Marina, *Chromatographia*, **1991**, *32*, 148.
53. M.H. Abraham et al., *Journal of the Chemical Society. Perkin Transactions 2*, **1997**(1) 19.
54. J. Jiskra et al., *Journal of Chromatography A*, **2002**, *977*, 193.
55. M. Roses, D. Bolliet, C.F. Poole, *Journal of Chromatography A*, **1998**, *829*, 29.
56. C. West, E. Lesellier, *Journal of Chromatography A*, **2006**, *1115*, 233.
57. M.J. Kamlet et al., *Journal of Physical Chemistry*, **1988**, *92*, 5244.
58. A. Wang, L.C. Tan, P.W. Carr, *Journal of Chromatography A*, **1999**, *848*, 21.
59. M.F. Vitha, A.J. Dallas, P.W. Carr, *Journal of Colloid and Interface Science*, **1997**, *187*, 179.
60. F.H. Quina, E.O. Alonso, J.P.S. Farah, *Journal of Physical Chemistry*, **1995**, *99*, 11708.
61. S. Yang, M.G. Khaledi, *Analytical Chemistry*, **1995**, *67*, 499.
62. M. Gil-Agustí, J. Esteve-Romero, M.H. Abraham, *Journal of Chromatography A*, **2006**, *1117*, 47.

STUDIA UBB CHEMIA, LVII, 3, 2012 (p. 283)
(RECOMMENDED CITATION)

==ERRATUM==

1. STUDIA UBB CHEMIA, Volume 56 (LVI), no. 4, 2011, pp. 243-248,
Title: DEGRADATION KINETICS OF ANTHOCYANINS FROM CRUDE ETHANOLIC EXTRACT FROM SOUR CHERRIES,
Author(s): BIANCA MOLDOVAN, LUMINIŢA DAVID, ROXANA DONCA, CRISTIAN CHIŞBORA
He also appeared in STUDIA UBB CHEMIA, Volume 56 (LVI), no. 2, 2011, pp. 189-194. Remains the article published in Volume 56 (LVI), no. 2, 2011, pp. 189-194. Article published in Volume 56 (LVI), no. 4, 2011, pp. 243-248 is withdrawn.

2. STUDIA UBB CHEMIA, Volume 56 (LVI), no. 2, 2011, pp. 133-140,
Title: EFFECT OF DIFFERENT SUBSTRATE TEMPERATURE ON GROWTH OF NANO CRYSTALLINE DIAMOND BY HFCVD TECHNINQUE
Author(s): HASTI ATEFI, MAHMOOD GHORANNEVISS, ZAHRA KHALAJ, MIRCEA V. DIUDEA
He also appeared in STUDIA UBB CHEMIA, Volume 56 (LVI), no. 3, 2011, pp. 171-178. Remains the article published in Volume 56 (LVI), no. 2, 2011, pp. 133-140. Article published in Volume 56 (LVI), no. 3, 2011, pp. 171-178 is withdrawn.

3. STUDIA UBB CHEMIA, Volume 56 (LVI), no. 2, 2011, pp. 141-148,
Title: EFFECT OF CATALYST LAYER THICKNESS ON GROWTH OF CVD DIAMOND
Author(s): FATEMEH SHAHSAVARI, MAHMOOD GHORANNEVISS, ZAHRA KHALAJ, MIRCEA V. DIUDEA
He also appeared in STUDIA UBB CHEMIA, Volume 56 (LVI), no. 3, 2011, pp. 257-264. Remains the article published in Volume 56 (LVI), no. 2, 2011, pp. 141-148. Article published in Volume 56 (LVI), no. 3, 2011, pp. 257-264 is withdrawn.